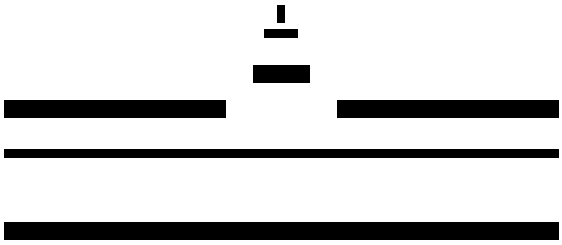

Properties of the Potential Energy Landscape under Shear

Markus Blank-Burian

- 2018 -

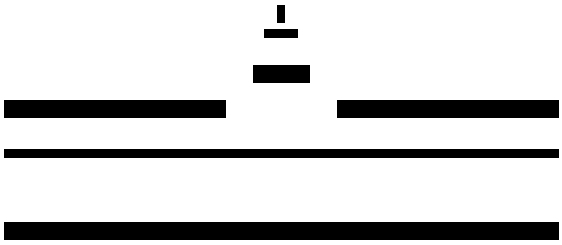

Theoretische Physik

Properties of the Potential Energy Landscape under Shear

Inaugural-Dissertation
zur Erlangung des Doktorgrades
der Naturwissenschaften im Fachbereich Physik der
Mathematisch-Naturwissenschaftlichen Fakultät
der Westfälischen Wilhelms-Universität Münster

vorgelegt von
Markus Blank-Burian
aus Münster
- 2018 -

Dekan:	Prof. Dr. Michael Klasen
Erster Gutachter:	Prof. Dr. Andreas Heuer
Zweiter Gutachter:	Prof. Dr. Nikos Doltsinis
Tag der mündlichen Prüfung:	03.07.2018
Tag der Promotion:	03.07.2018

Abstract

English

The aim of this thesis is to explore the behavior of a model glass former under an applied shear in the context of the potential energy landscape (PEL). While the rheological features of glasses have been explored for a long time, the microscopical origins, for example the process of yielding during the stress overshoot, are topic of active research.

In this thesis, we define the new concept of minimized structures (MS), which is basically an extension of inherent structures (IS) to the sheared system. The importance of MS transitions to the dynamics, can be seen in comparison with other plastic events, which turn out to be more local and small than MS transitions. We find that the first MS transition plays an important role in the stress overshoot and at yielding. Looking at the statistics of the first MS transition, we find a crossover position, that defines the average onset of irreversible transitions and thus naturally defines a yield point. Furthermore, we can show that using only MS energies, we are able to successfully predict the height of the reversal overshoot and give a good estimate on the reversal shear modulus.

The concept of metabasins, used in the PEL picture, can be extended to the sheared system in a simple way, by replacing inherent structures with minimized structures in the definition. Thus, metabasins are defined in a consistent way for the whole crossover regime, between the shear dominated and the temperature dominated regime and our results are consistent with previous work focusing on the quiescent system. Using metabasins and minimized structures, we are able give a good approximation of the diffusion constant and the structural contribution to the viscosity in the crossover regime.

Last we explore the connection of equilibrium fluctuations to the sheared system. After providing a way to calculate per-particle statistics in spherical coordinates using structural information and the force fields, we focus on the connection between the stress and the anisotropy. We find, that the structural anisotropy scales perfectly with the stress, shows a very similar overshoot at start-up shear and a nearly identical flow curve.

In summary, the present work shows how a careful and innovative analysis of the results of computer simulations can contribute to the physical understanding of sheared glass-forming systems.

Deutsch

Das Ziel dieser Dissertation ist die Untersuchung eines Modell-Glasbildners unter Scherung im Kontext der potentiellen Energielandschaft (PEL). Obwohl die generellen rheologischen Eigenschaften von Gläsern schon längere Zeit erforscht sind, sind die mikroskopischen Ursprünge, zum Beispiel im Fall der Fließgrenze Teil der aktiven Forschung.

In dieser Dissertation definieren wir als neues Konzept die minimierten Strukturen (MS), die im Prinzip eine Erweiterung der inhärenten Strukturen (IS) sind, wie sie in der Beschreibung im PEL-Bild benutzt werden. Die Wichtigkeit der MS-Übergänge in der dynamischen Beschreibung des Systems sieht man insbesondere im Vergleich mit anderen plastischen Übergängen, die dazu vergleichsweise lokal und klein sind. Unter anderem beim Spannungsüberschuss und bei der Bestimmung der Fließgrenze spielt der erste MS-Übergang eine große Rolle. In der Statistik der ersten MS-Übergänge finden wir einen ausgezeichneten Punkt, der im Durchschnitt das Einsetzen von irreversiblen Übergängen und damit auf natürliche Weise die Fließgrenze beschreibt. Außerdem können wir zeigen, dass unter Umkehr der Scherrichtung, der rückwärtige Spannungsüberschuss eindeutig vorhersagbar von der MS-Energie abhängt. Ebenso erlaubt uns die MS-Energie eine gute Vorhersage des Schermodulus direkt nach der Umkehr.

Das Konzept von Metabasins aus der PEL-Beschreibung kann auf einfache Art auf das gescherte System übertragen werden, indem in der Definition inhärente Strukturen durch minimierte Strukturen ersetzt werden. Damit sind Metabasins auf konsistente Art und Weise innerhalb des Übergangs zwischen scherungs- und temperaturdominiertem Bereich definiert und die Ergebnisse konsistent mit Ergebnissen aus älteren Arbeiten am ungescherten System. Mittels Metabasins und minimierten Strukturen sind wir in der Lage eine gute Näherung der Diffusionskonstante und ebenso dem strukturellen Beitrag zur Viskosität im Übergangsbereich zu geben.

Zuletzt untersuchen wir die Verbindung zwischen Equilibriumsfluktuationen und dem gescherten System. Nachdem wir einen Weg zur Berechnung der Statistik auf Teilchenebene in Kugelkoordinaten dargestellt haben, der Informationen über die Struktur und das Kraftfeld benötigt, fokussieren wir unsere Analyse auf die Verbindung von Spannung und Anisotropie. Wir sehen, dass die strukturelle Anisotropie, ebenso wie die radiale Verteilungsfunktion, ideal mit der Spannung skaliert und ebenso wie die Spannung einen Anisotropie-Überschuss und eine nahezu identische Flusskurve aufzeigt.

Zusammenfassend zeigt diese Arbeit, wie eine sorgfältige und innovative Analyse von Ergebnissen aus Computersimulationen zum physikalischen Verständnis von glassbildenden Systemen unter Scherung beitragen kann.

Contents

Chapter 1

Introduction

In our everyday life, we are surrounded by amorphous materials, which change their rheological properties with the applied shear rate. Typical examples of such materials are ketchup, whipped cream, toothpaste, foams. It is also common, that the preparation history of such a material has a large impact on its properties. Many of these materials, showing very similar rheological behavior, have very different microscopic properties, e.g. being colloids, polymers or metallic glasses. However, there is currently no complete microscopic theory explaining this similarity. We refer to [Bonn et al., 2017] for a review of current research.

In this work, we will analyze the rheological properties of a model glass former, an 80-20 binary mixture of Lennard-Jones particles, which models a $Ni_{80}P_{20}$ metallic glass [Kob and Andersen, 1994] under pure shear. At start-up shear, our model system exhibits a stress overshoot, which depends on the preparation history, the shear rate and the temperature [Varnik et al., 2004]. This overshoot characterizes a crossover from elastic behavior to fluid behavior, as initially, the stress depends only on the strain, but after the overshoot, the stress depends on the shear rate. In this so called flow regime, this dependency can be characterized by the Hershel-Bulkley law [Herschel and Bulkley, 1926].

To analyze the microscopic behavior of our model glass, we employ the method of Stillinger and Weber [Stillinger and Weber, 1983]. This method was developed to describe the movement a quiescent systems through phase space as a hopping process at sufficiently low temperature near the glass transition at T_g. The points, between this hopping process takes place, are minima in the *Potential Energy Landscape* (PEL). In later works, this method has been refined to describe the alpha-relaxation and diffusion of the quiescent system near T_g using a continuous time random walk through a series of traps. A review of the methods and results can be found in [Heuer, 2008]. Recently, there has also been progress on the description of diffusion in systems, which are driven by a single particle in terms of an effective temperature [Schroer, 2015].

Here, we will apply methods of the PEL analysis to the sheared system. However, the sheared potential energy landscape looks quite different, than the quiescent one [Lacks, 2001]. The strain acts as some kind of control parameter, which leads to fold catastrophes [Maloney and Lacks, 2006, Chung and Lacks, 2012b], thereby continuously changing the PEL. Nevertheless, we find a way to characterize movement through the PEL, by associating each minimum in the PEL to its equivalent in the unsheared PEL. This gives us the access to the same tools and methods as for the quiescent system.

For the PEL analysis, we are forced to look at small systems, as the energy is most informative only there. As a simple example, one might look at the sum of the energy for two equal independent systems, where both systems have only two states. This energy would fluctuate between three states. In the limit of big systems, the informative value of the energy would vanish, as by combinatoric arguments the average energy of all possible states of the subsystems has the highest probability in the combined system. Previously, a system size of $N = 65$ was used for the analysis of the quiescent three dimensional system, whereby even this small system could be regarded as the superposition of at least two subsystems [Heuer et al., 2005]. However, for the analysis of the sheared system, we use a slightly bigger system ($N = 130$), as the spatial extent of the stress correlations [Chowdhury et al., 2016] causes strong finite size effects. The comparison with big systems is done in the ensemble average, as some characteristic rheological features, like the stress overshoot or the Hershel-Bulkley behavior of the flow curve appear already, when summing over single trajectories. The single trajectories consist of piecewise linear sections interrupted by plastic events [Dubey et al., 2016b]. This immediately shows, that the apparent flow of the system, with a constant shear stress can also be described as the interplay of elastic strains and plastic events. For a description in the PEL picture, we will therefore investigate the statistics of these elastic strains and their shear modulus as well as the plastic events. Similarly, we will discover that the stress overshoot is equally well described in this simple superposition of subsystems and can be explained in terms of a decorrelation of the single trajectories. Despite the reproduction of some rheological features, such as the stress overshoot and flow stress behavior, there is also evidence from studies of large systems, that yielding regions behave sufficiently independent [Patinet et al., 2016]. However, there are also limitations in the use of small systems, as for example shear banding [Divoux et al., 2016] cannot be described. Hope lies in mesoscopic models, to fill the gap and provide the remaining link between the small and the large system [Rehwald and Heuer, 2012, Martens et al., 2012].

This work is structured as follows: First, in chapter 2, we will describe our simulation and analysis methods in detail. After this, in chapter 3, we will establish the link between the quiescent energy landscape and the sheared one, introducing the new concept of *minimized structures* (MS). In this chapter, we will also analyze some key statistics of both landscapes, which are needed for later discussion of our results. Chapter 4 will then focus on the description of the overshoot in terms of the PEL. Interestingly, we will find a crossover point which in many aspects compares to the yield point found in cyclic shear in large systems. Therefore in chapter 5, we will take a closer look at the PEL properties of our small system under cyclic shear. We see, that small temperatures are enough to break limit cycles and reproduce the crossover. Additionally, in chapter 5, we explain the height of the reversal overshoot in terms of the energy landscape. After the discussion of the flow curves in chapter 6, we introduce an effective temperature, from which we find that zero temperature shear simulations are comparable with temperatures around $1.8T_g$. Similar to the idea in [Chattoraj et al., 2010], we then introduce a rate model, describing the metabasin waiting times in the crossover from the temperature to the shear dominated regime in good approximation. Also in this chapter, we analyze the MS shear modulus from the flow regime. Using this new information and employing a simplified model, we can reproduce most of the contribution of the inherent stress to the apparent viscosity. We also see, how the diffusion is influenced by the waiting times defined in the PEL picture. Last, in chapter 7, we explore the connection of equilibrium fluctuations to the sheared system. Using spherical coordinates, we show an easy way to calculate the per-contact and per-particle statistics for common observables. We find, that due to equilibrium fluctuations, states with anisotropy are visited and there is linear dependence of the system stress on the anisotropy, thus providing a possible link between the equilibrium and the sheared system.

Chapter 2

Simulation

In this chapter we will give insights into the basics of our simulation, detailing the algorithmic challenges of simulating a sheared system. When necessary, we point out changes to previously used algorithms, such as some subtle details in the construction of metabasin. We will also give a short overview, of how we select our starting structures for equilibrium and for low temperature simulations. The focus will be mainly on algorithms and technical details and we leave most of the scientific insights for the following chapters.

2.1 Simulation software

For simulating the sheared system, we developed our own MD simulation software. While all code was written completely from scratch, we based some algorithms on previously used ones. For example, the equilibration routine was changed, allowing for faster equilibration times. Also the minimization procedure, which was used to calculate potential energy minima, was rewritten to use the GSL library [Gough, 2009]. Care was taken, to test the simulation results for obvious errors, such as non-constant energies in the NVE ensemble or a non-constant temperature in the NVT ensemble. Furthermore, we reproduced key results from the $N = 65$ system, to check for any deviations. Special treatment was necessary for the center of mass. We kept the center of mass constant by enforcing a zero center of mass velocity. Additionally, we removed the center of mass on all spatial comparisons in our analyses, as it may change during minimization.

For future use beyond the sheared system, we prepared the simulation code for support of arbitrary potentials, extensions of the per-particle data and kept most of the code very modular. In the near future, this allows the research of an electrically driven small system with differently charged particles, employing an additional Yukawa potential as well as an electric field. Also, we prepared for the analysis of a micro-rheologically driven system using a single particle in a harmonic potential, which moves with constant velocity.

$$\sigma_{np} = \begin{pmatrix} 1.0 & 0.8 \\ 0.8 & 0.88 \end{pmatrix}, \quad \epsilon_{np} = \begin{pmatrix} 1.0 & 1.5 \\ 1.5 & 0.5 \end{pmatrix}, \qquad \rho = 1.2, \quad \frac{N_A}{N_B} = \frac{80}{20}, \qquad m_A = m_B = 1$$

Table 2.1: Parameters of the Kob-Anderson potential for a binary mixture of Lennard-Jones particles.

N	65	130	260	520
L	3.78	4.77	6.01	7.57
V	54.2	108.3	216.7	433.3

Table 2.2: Lengths and volumes in natural units for different system sizes at $\rho = 1.2$

2.2 Potential and Force

The potential, used in our simulations, is based on the popular Kob-Anderson potential [Kob and Andersen, 1994] for a binary mixture of Lennard-Jones particles. The parameters, which are given in table 2.1, make the potential similar to the one used in [Stillinger and Weber, 1983], which has been used to simulate an amorphous metallic $Ni_{80}P_{20}$ alloy. In their work, Kob and Anderson used a cutoff radius $r_c = 2.5$ and shifted the potential to be continuous at r_c (see eq. (2.2)).

$$V_{pn}^{\mathrm{LJ}}(r) = 4\epsilon_{pn}\left(\left(\frac{\sigma_{pn}}{r}\right)^{12} - \left(\frac{\sigma_{pn}}{r}\right)^{6}\right) \tag{2.1}$$

$$V_{pn}^{\mathrm{KA}}(r) = V_{pn}^{\mathrm{LJ}}(r) - V_{pn}^{\mathrm{LJ}}(r_c) \tag{2.2}$$

The indices p and n reference the particle type and the neighbor type, commonly called "A" and "B" type particles.

As we simulate small systems, down to a size of $N = 65$, we have to reduce our cutoff radius to $r_c = 1.8$, because we use the minimum image convention with periodic boundary conditions for our simulations. The minimum image convention means, that no particle appears twice as a neighbor of a single other particle. For this, the cutoff radius has to be half the box size. At a density of $\rho = 1.2$ and $N = 65$ particles, the box length is about $L = 3.78$ (see table 2.2).

When doing molecular dynamics simulations, there should be no jump in the first derivative at the cutoff. Otherwise, there would a small but finite force appearing out of nowhere when the particles reach the interaction distance. Therefore, we made the potential smooth also in the first derivative at $r = r_c$ by adding a term linear in r [1] (see eq. (2.3)). This type of potential has already been used in many publications, e.g. [Büchner and Heuer, 2000, Doliwa and Heuer, 2003d, Heuer, 2008, Rehwald et al., 2010, Schroer and Heuer, 2013].

$$V_{pn}^{\mathrm{cutoff}}(r) = V_{pn}^{\mathrm{LJ}}(r) - (r - r_c)\mathbf{F}_{pn}^{\mathrm{LJ}}(r_c) \cdot \mathbf{e}_r - V_{pn}^{\mathrm{LJ}}(r) \tag{2.3}$$

$$\tag{2.4}$$

In this work, we add another modification to the potential. In our tests, we found that the minimization results, at least when doing minimization of $V(\mathbf{x}, \gamma)$ (see section 3.2), are very

[1] The sign of the force is chosen in that way, that it points into the right direction when calculating the force of a neighbor particle n at distance r on a central particle p.

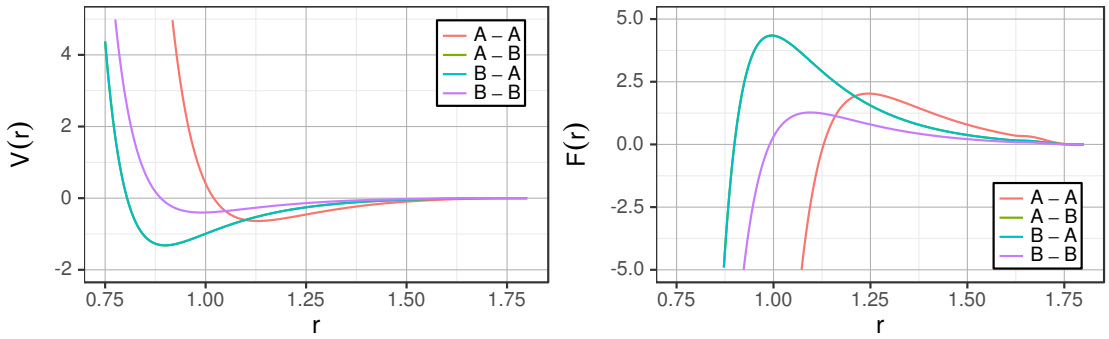

(a) Potential Energy

(b) Force

Figure 2.1: Form of the potential and the forced used in the simulations for this work.

sensitive on the chosen algorithm and parameters. From [Maloney and Lemaître, 2006], we also know that the minimization procedure is sensitive to jumps in the second derivative of the potential. Due to those reasons, they chose to add a term, quadratic in r, to their potential. However, we want our simulation results to be comparable to previous work. So we opt to multiply the potential $V_{pn}^{\text{cutoff}}(r)$ with a standard interpolation polynomial $I_{\text{poly}}(r)$ of 5th order (eq. (2.6)). We limit the interpolation to the outer 10% of the interaction range, in order to keep the minimum at the same position.

$$V_{pn}(r) = V_{pn}^{\text{cutoff}}(r) I_{\text{poly}}(d(r)) \tag{2.5}$$

$$I_{\text{poly}}(d) = \begin{cases} 1 & \text{if } d < 0 \\ -6d^5 + 15d^4 - 10d^3 + 1 & \text{if } d \in [0,1] \\ 0 & \text{if } d > 1 \end{cases} \tag{2.6}$$

$$d(r) = (r - r_s)/(r_c - r_s), \qquad r_s = 0.9 r_c \tag{2.7}$$

The resulting potential is shown in fig. 2.1. The change of the slope in the potential is nearly invisible with the eye, while the force shows a small range at the start of the interpolation, where it is nearly constant for a small distance. We did extensive tests on many observables in equilibrium simulations (e.g. the waiting time distribution, energy distribution, diffusion constant), but found no deviation in the results.

2.3 Lees-Edwards-Boundaries

Our simulations have periodic boundaries on all sides. As we shear our system, these periodic boxes have to move as well. This sheared periodic boundary conditions are also called Lees-Edwards boundary conditions, as they were first described in [Lees and Edwards, 1972]. In short, we move the periodic boxes in our simulation with a velocity of $v_{\text{box}} = y_{\text{box}}\dot{\gamma}$. A sketch of these boundary conditions can be seen in fig. 2.2.

We will quickly go through the process of finding a neighbor with these boundary conditions, as it is a central, potentially time consuming piece of the simulation but very prone to programming errors and not well documented in whole.

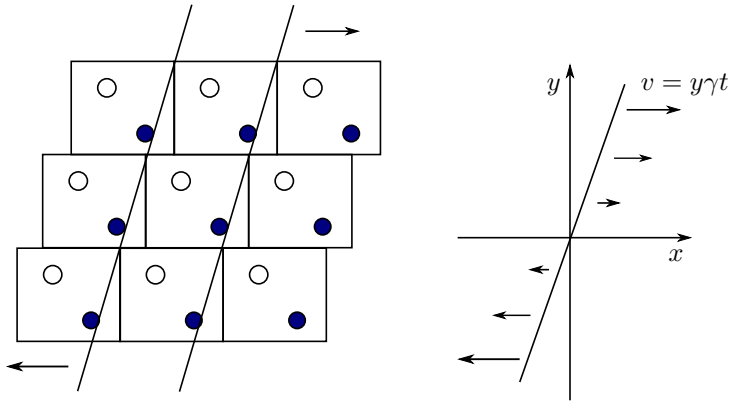

Figure 2.2: Sketch of Lees-Edwards boundary conditions.

2.3.1 Finding Neighbors with a Sheared Cell List

First of all, we construct a cell list [Frenkel and Smit, 2001], containing all particles mapped to positions in the box at the origin. This gives us $O(1)$ access to all the particles, as the cell number should be increased when increasing the box length, keeping the particle number per cell roughly constant. So for every particle in the list, we have only a constant number of neighboring cells. For small system sizes, this becomes mostly irrelevant, as the number of neighbors of a particle is a large fraction of the system size. [2]. As suggested in [Frenkel and Smit, 2001], we chose to add a small tolerance radius of r_c^{tol} for the procedure of finding neighbors to reduce the number of neighbor list updates.

The search for neighboring cells must of course be adjusted to the Lees-Edwards boundary conditions [Evans and Morriss, 1984b]. Normally a cell index [3] to a position $\mathbf{r}$ is found via:

$$i_{\text{cell}}(\mathbf{r}) = \sum_{d=0}^{D-1} (n_{\text{cells}})^d \lfloor (\frac{r_d}{L_d} - \lfloor \frac{r_d}{L_d} \rfloor) n_{\text{cells}} \rfloor \tag{2.8}$$

with the box size $\vec{L}$ in D dimensions and the number of cells in each dimension n_{cells}. With a shear rate $\dot{\gamma} > 0$, we have to adjust $\mathbf{r}$ by the box offset [4] at the given y:

$$r_x \to r_x - \lfloor \frac{r_y}{L_y} \rfloor \gamma L_x \tag{2.9}$$

This function is used first to determine the cell index of each particle to build the cell list. In search for a neighbor, this function is also used to find all neighbor cells in a search box around a given position [5]. The search box length is given by $r_s = r_c + r_c^{\text{tol}}$. We note that the tolerance has to be decreased as we shear the system, as the neighboring boxes are moved against each other. Assuming, that resting particles represent the worst case, one can safely reduce the tolerance by $\Delta r_c^{\text{tol}} = L_y \Delta\gamma$ per time step.

[2] At $N = 65$ and a cutoff of $r_c = 1.8$, our search radius is roughly half the simulation box
[3] Linear number of a cell in the periodic box
[4] Origin of the copy of the periodic box, where the particle currently resides in
[5] For the neighbor search, this function is implemented partly unrolled to save temporary calculations within the same copy of the periodic box.

In passing, we note that we are using the minimum image convention [Frenkel and Smit, 2001]. This makes no particle appear twice as a neighbor of another particle. As we use a fixed cutoff $r_c = 1.8$ for the potential (see section 2.2), the tolerance for the search radius has to be chosen, so that $r_s \leq \min\{L_x, L_y, L_z\}$.

Until now, we have searched all neighboring particles in a surrounding box. Therefore, as a last step, we filter out all particles not within the search radius around the position $\mathbf{r}$.

The distance $\mathbf{d}$, a neighboring particle $\mathbf{n}$ has to be moved from its current position, to be closest to a particle residing at $\mathbf{r}$ is normally given by [Frenkel and Smit, 2001]:

$$\mathbf{d}_d = L_d \cdot \text{round}(\frac{r_d - n_d}{L_d}) \tag{2.10}$$

This equation only holds using minimum image convention and modifies the distance of the particles by a maximum of half a box length in each direction. When using Lees-Edwards boundary conditions, we have to modify d_x after having evaluated eq. (2.10):

$$d_x \to L_x \cdot \text{round}(\frac{r_x - n_x - d_y\gamma}{L_x}) + d_y\gamma \tag{2.11}$$

So after calculating d_y, which is not affected by shear, we can shear the periodic box at this height back for the current γ and calculate the corresponding offset. This equation is best verified for two particles, one in the center of the box at the origin and one in the center of the box above at $r_x = n_x$ and $d_y = r_y - n_y = -L_y$. Then d_x has to flip at $\gamma = \frac{1}{2}$ before it is sheared back to its original strain, thereby still modifying the distance by only a maximum of half a box length.

Using this distance $\mathbf{d}$, we can now finally calculate the closest distance of a particle to one of its neighbors and therefore filter for all particles within the search radius r_s.

2.4 SLLOD

Normally, it suffices to modify the neighbor list calculations to implement shear in an MD simulation. By moving the periodic images, a strain gradient forms automatically. With a constant shear rate, this gradient is expected to be constant across the whole system after an initial settling time. For small systems ($N = 65, N = 130$) and shear rates $\dot{\gamma} \geq 1$, the system splits up at the boundaries forming blocks sliding along each other. This can be seen in fig. 2.3a, where at $\dot{\gamma} = 1$, the strain gradient is effectively zero. Even at lower shear rates, there is an effect visible at the boundary, requiring at least shear rates smaller than 10^{-2}. Also, by driving the shear only at the boundaries, a change in the shear rates at the boundaries takes approximately the speed of sound to traverse the system [Rottler and Robbins, 2003], inducing an effect depending on the box size.

For these two reasons, we opt to use the SLLOD algorithm [Evans and Morriss, 1984a, Evans and Morriss, 2013]. In planar Couette flow, SLLOD puts the momenta into a co-moving coordinate frame. In contrast to the very similar DOLLS tensor method, SLLOD cannot be derived from a Hamiltonian, but similarly fulfills Green-Kubo relations, e.g. predicting the shear and bulk viscosity from equilibrium fluctuations. However, it's equations of motion eqs. (2.12) and (2.13) give an exact representation to the planar Couette flow:

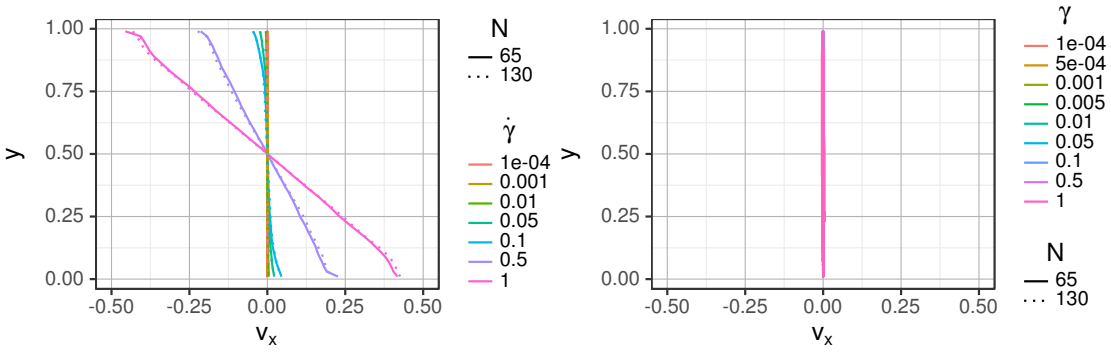

(a) Without SLLOD

(b) With SLLOD

Figure 2.3: Horizontal velocity at $T = 0.01$, relative to the ideal constant velocity gradient, induced by a constant $\dot{\gamma}$. The vertical direction y and the velocity v_x have been scaled by the box height/width, so they are comparable at different system sizes.

$$\dot{\mathbf{q}}_i = \frac{\mathbf{p}_i}{m_i} + \gamma q_{ix}\mathbf{e}_x \qquad (2.12) \qquad\qquad \dot{\mathbf{p}}_i = \mathbf{F}_i - \gamma p_{iy}\mathbf{e}_x \qquad (2.13)$$

These equations of motions can be further modified to include support a thermostat [Evans and Morriss, 2013], like the commonly used Nosé-Hoover thermostat [Nosé, 1984], which is known to reproduce the canonical ensemble. The latter has been used in our group for some time in a variant using a thermostat chain [Martyna et al., 1992].

2.5 Metabasins

In supercooled liquids near the glass transition, the particle movements consists mostly of oscillations around stable configurations, with occasional jumps between those [Schrøder et al., 2000]. These stable structures are called *inherent structures* (IS). The method of calculating these inherent structures at equidistant points in the particle trajectory goes back to [Stillinger and Weber, 1983]. Near the glass transition temperature, the movement can be divided into two processes [Stillinger, 1995]. The first is characterized by a hopping process in a set of IS and the second process jumps between different sets of IS. A set of inherent structures is called *metabasin* (MB). Here, we will describe the algorithmic detection of inherent structures and metabasins. For a physical description see section 3.1.

The concepts of IS and MB are illustrated in fig. 2.4, which shows an example IS energy trajectory. This trajectory features the typical forward-backward hopping between IS of same energy, as well a transition to a region with a completely different set of IS energies. IS with the same energy can be combined into intervals, marking the first and last occurrence of a unique energy. These intervals may then be merged into metabasins.

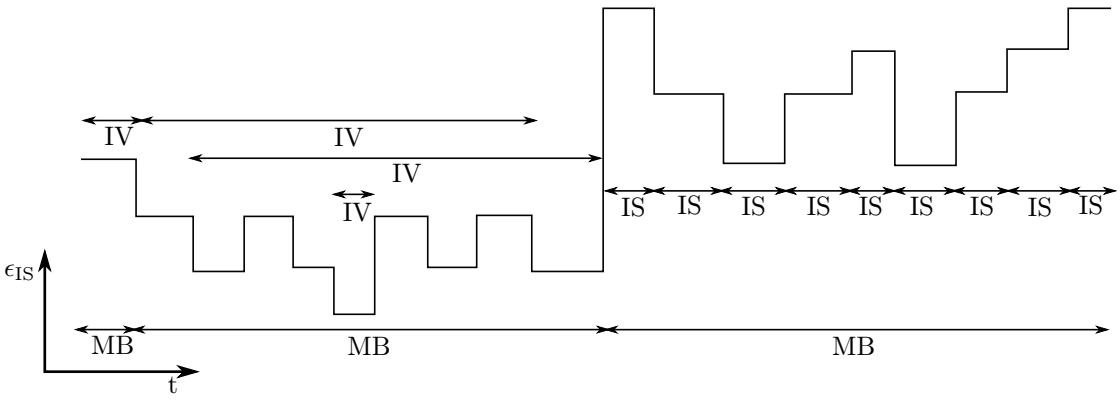

Figure 2.4: Sketch of an IS energy trajectory, illustrating the concepts of inherent structures (IS) and metabasins (MB). For the leftmost two metabasins, we also show intervals of same energy (IV).

$\Delta\epsilon_{\text{small}}$	$\Delta\epsilon_{\text{big}}$	Δd_{small}	Δd_{big}
10^{-5}	10^{-3}	$5 \cdot 10^{-3}$	10^{-2}

Table 2.3: Tolerances used for constructing metabasins

2.5.1 Metabasin construction

We will now describe in detail, how several IS can be combined into so called metabasins. More information about the use of metabasins can be found in chapter 3. The algorithm 2.1 has first been described in [Doliwa and Heuer, 2003a].

However, there are some subtleties in the implementation, which we will now explain.

Already the first step has to be evaluated with care: The energies and positions for a single IS fluctuate due to the minimization process. Therefore, when building the interval list, it is not guaranteed, that the first unknown IS lies in the middle of the fluctuations. A simple choice would be to double tolerances, which in turn might combine different, but very close IS to a single interval. Instead of simply doubling the tolerance, we use two tolerances instead. If the value is within the smaller tolerance to a previously found IS, we extend the previous interval. If instead the value is within the bigger tolerance, we extend the previous interval, but also open up a new interval with the new IS. This method gives us more intervals than the naive implementation, but may pick up more data points at the border of the intervals. By construction, these additional intervals overlap greatly, so they are combined in the later steps of the metabasin construction. The downside of this algorithm is seen, when there are only two data points available, which lie on both the far ends of the fluctuation spectrum. These would be considered to belong to different IS. However, we have carefully evaluated many single trajectories and metabasin lifetime statistics, to check if our tolerances (table 2.3) produce sensible results, which are within reasonable error to previous work.

After generating intervals, each interval is assigned to unique metabasin. These metabasins are then merged, according to the rules specified in algorithm 2.1. In fig. 2.5, we illustrate the elementary steps of this metabasin construction algorithm. The most simple case is depicted in fig. 2.5a, where disjunct intervals would be kept in different metabasins. In fig. 2.5b and fig. 2.5c

Algorithm 2.1 Metabasin construction algorithm using intervals with same IS.

1. Determine all intervals $[t_{\text{start}}, t_{\text{end}}] \in I$ where t_{start} is the first occurrence of an single IS and t_{end} is the last occurrence in the trajectory. Two IS are considered equal within the tolerance (particle distance) of the algorithm used to minimize the potential energy.
2. Start with a set of metabasins M, each containing one such interval:
   $M \leftarrow \{\{i\} | i \in I\}$
3. Enlarge every $m \in M$ by all intervals, which overlap more than 50% with any interval in m:
   $\forall m \in M : m \leftarrow m \cup \{[t'_{\text{start}}, t'_{\text{end}}] | [t_{\text{start}}, t_{\text{end}}] \in m, [t'_{\text{start}}, t'_{\text{end}}] \in I,$
   $(t'_{\text{start}} > t_{\text{start}} \wedge t'_{\text{end}} < t_{\text{end}}) \vee$
   $(t_{\text{start}} > t'_{\text{start}} \wedge t_{\text{end}} < t'_{\text{end}}) \vee$
   $(t_{\text{start}} < t'_{\text{start}} \wedge t_{\text{end}} > t'_{\text{start}} \wedge \frac{t_{\text{end}} - t'_{\text{start}}}{\min\{t_{\text{end}} - t_{\text{start}}, t'_{\text{end}} - t'_{\text{start}}\}} \geq 0.5) \vee$
   $(t'_{\text{start}} < t_{\text{start}} \wedge t'_{\text{end}} > t_{\text{start}} \wedge \frac{t'_{\text{end}} - t_{\text{start}}}{\min\{t_{\text{end}} - t_{\text{start}}, t'_{\text{end}} - t'_{\text{start}}\}} \geq 0.5)\}$
4. Merge metabasins containing same intervals:
   (a) Enlarge M by merging metabasins containing same intervals:
   $M \leftarrow \{m \cup m' | m \in M, m' \in M : m \cap m' \neq \emptyset\}$
   (b) Remove from M all metabasins completely contained in others:
   $M \leftarrow M \setminus \{m | m \in M, m' \in M : m \subset m' \wedge m' \not\subset m\}$
5. Build a set of still overlapping metabasins:
   $O \leftarrow \{(m_1, m_2) | m_1 \in M, m_2 \in M, i_1 \in m_1, i_2 \in m_2, t_{\text{start}}(i_1) < t_{\text{start}}(i_2), i_1 \cap i_2 \neq \emptyset\}$
6. Randomly choose to cut the overlapping part from the left or the right metabasin
   (a) $\forall (m_1, m_2) \in O, \forall i_1 \in m_1 : t_{\text{end}}(i_1) \leftarrow \min\{t_{\text{end}}(i_1), \min\{t_{\text{start}} i_2 | i_2 \in m_2\}\}$
   (b) $\forall (m_1, m_2) \in O, \forall i_2 \in m_2 : t_{\text{start}}(i_2) \leftarrow \max\{t_{\text{start}}(i_2), \max\{t_{\text{end}} i_1 | i_1 \in m_1\}\}$

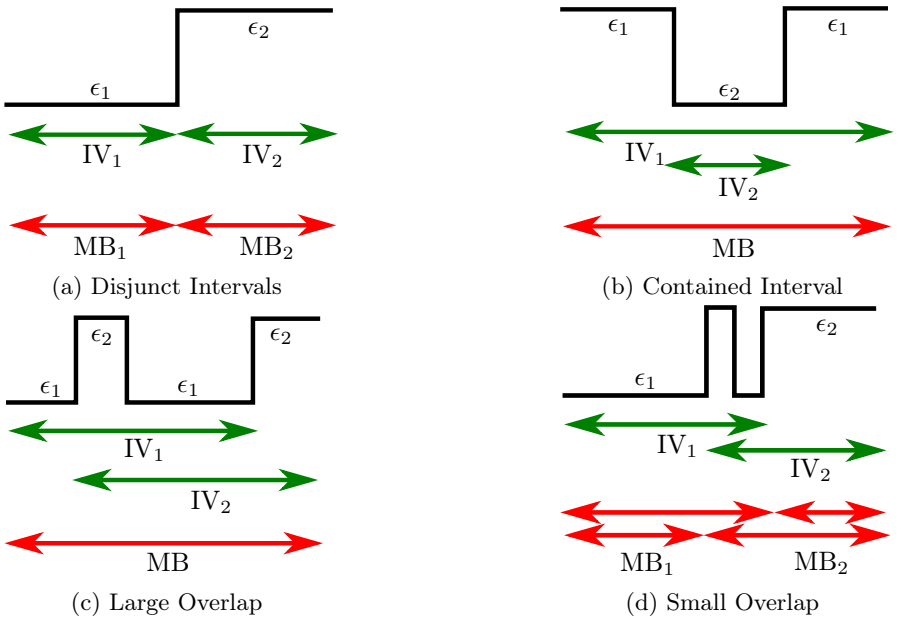

(a) Disjunct Intervals (b) Contained Interval

(c) Large Overlap (d) Small Overlap

Figure 2.5: Sketches of typical IS energy trajectories, illustrating the elementary steps of the metabasin construction algorithm.

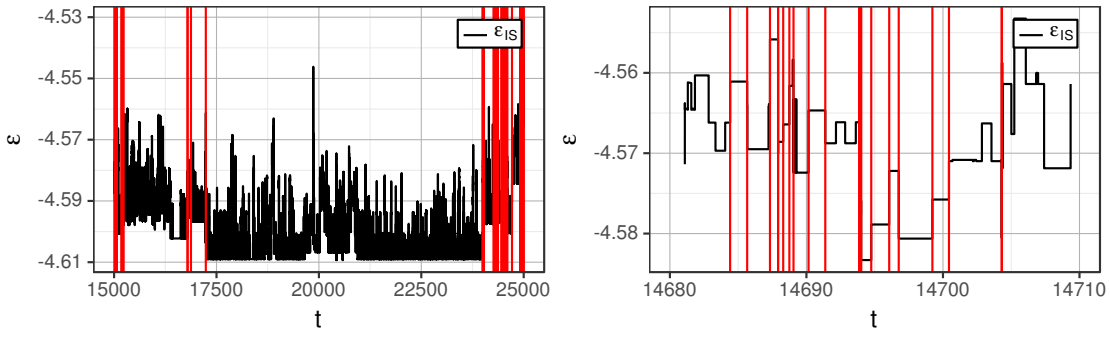

(a) (b)

Figure 2.6: Sample trajectories, simulated at $T = 0.435$ and $N = 130$. Red lines mark the borders of metabasins, which were constructed using algorithm 2.1.

the metabasins containing the respective intervals are merged.

At low temperatures and energies near the glass transition, the dynamics of the IS is dominated by jumps between neighboring IS, which are visited multiple times, giving rise to trajectories like those in fig. 2.5c and fig. 2.5d. If the intervals overlap at least 50%, their metabasins are merged. We note in passing, that a slight change in this number has no significant influence on the results. During the whole process, each metabasins keeps an inventory of all its intervals. Furthermore, all comparisons of overlaps are carried out only on intervals and never on some intermediate metabasins. This guarantees, that there is no dependence on the of merge operations. For example, if we would start merging metabasins from the left and compare the overlap between the merged metabasin size and the next one to the right, the merged metabasin size may soon reach a critical point, where following intervals would always have an overlap smaller than 50%.

After all the merge processes have finished, the last part of the algorithm, consists of stripping small overlaps, as shown in fig. 2.5d. This step is nondeterministic, as it uses random data. However, for reproducibility, we use only seeded pseudo-random-numbers in our algorithm. We decided against a 50-50 splitting of the overlap, as in this case the position of the MB transition would not coincide with an IS transition, which however is necessary for later analysis of MB jumps.

The energy and structure associated with a metabasin is usually the one with the lowest energy, as it matches the idea of the trap model [Monthus and Bouchaud, 1996]. In equilibrium simulations, the interval with lowest energy is usually the longest within a single metabasin.

In fig. 2.6, we see how the algorithm successfully merges a long range of inherent structures into a long metabasin. However, at the borders of metabasins, there may be many IS of different energies, so there are no overlapping intervals. These intermittent regions occur largely at high energies and have short duration. As we will see in section 3.1.1, the metabasin lifetime distribution is smooth even for high energies and shows no additional peak at small timescales, so these regions need no special treatment here.

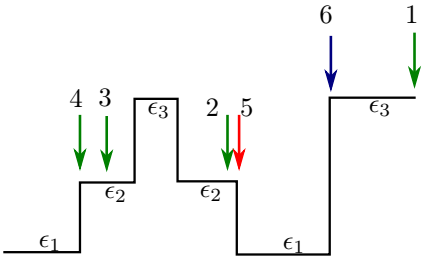

Figure 2.7: Sketch illustrating the problems using a simple binary search algorithm for detecting IS transitions. The green arrows mark the points, which are evaluated by the the first bisectioning procedure. After point 4 is found, the next bisection could continue with either points 4 and 1 or points 2 and 1. In both cases, we would find point 5 next, thereby skipping the first region with ϵ_3.

2.5.2 Detecting Jumps in the IS trajectory

Up until now, we have talked about how to combine several IS into metabasins. However, we have yet to clarify, how we detect the transitions or "jumps" between IS. The basic idea of this algorithm is not new, but for this work, we have made some changes to optimize its performance and accuracy, so it will be described in more detail. The current IS for a given point in the trajectory, i.e. the structure we are oscillating around at low temperatures, is found by minimizing the potential energy $V(\mathbf{x})$.

As we simulate the trajectory, we save a copy of all particle positions into a buffer of size n_{buffer}. The safest way to find IS transitions, would be to minimize every point in the trajectory, separated by the simulation time step. As the processing cost of the minimization is very high (sometimes over a few thousand minimization steps), and trajectories at small temperatures are very long ($\approx 3 \cdot 10^7$ steps), this is no viable alternative. A better alternative is using a binary search over the buffer, to determine the jump point. However, due to the nature of the dynamics near the glass transition, there are many forward-backward jumps between same energies. Therefore, using a binary search might give wrong results, if we accidentally find an energy of the same value in the middle of our buffer, although there were different energies before that point. The sketch in Figure 2.7 illustrates this problem.

In fig. 2.8a, we see that the buffer size indeed influences the resulting metabasin length, which is derived from the IS transition data. We see, that using a the simple bisectioning algorithm, this observable is very sensitive to the buffer size n_{buffer}, even up to small multiples of the time step. Hence, we need an algorithm which can resolve IS lifetimes, as small as a single time step, while still doing only few minimizations at longer intervals of same energy.

To provide both accuracy and speed at a configurable parameter, algorithm 2.2 does a stochastic test within intervals for the same energy. After checking via normal binary search, it additionally checks using CacheAndCheckInterval if n_{equi} equidistant points in this interval have the same energy. This gives a high probability, that all values within this interval have the same energy. Each time an energy gets evaluated for a given structure in the trajectory, the energy value is also cached. These cached values are used to quickly identify ranges of same energy, greatly improving the performance of the algorithm. Furthermore, no interval is blindly skipped, but rather checked with CacheAndCheckInterval. In fig. 2.8b, we see that already for $n_{\text{equi}} = 1$, except for the highest energy, there is no difference in τ_{MB}. With this knowledge, we conservatively choose a

Algorithm 2.2 Algorithmic pseudocode for evaluating a buffer of trajectory data. All energy evaluations are cached, so searching through the buffer has the side-effect that each call to this function with the same First and Last value will have different results.

```
function ProcessBuffer(First, Last)
    if First = Last then return
    end if
    LastSame ← FindLastSame(First, Last)
    if CacheAndCheckInterval(First, LastSame) then
        FirstDifferent ← FindFirstDifferent(LastSame, Last)
        if CacheAndCheckInterval(First, LastSame) then
            Write out interval between First and LastSame
            ProcessBuffer(LastSame+1, Last)
        else
            ProcessBuffer(First, Last)
        end if
    else
        ProcessBuffer(First, Last)
    end if
end function
function FindLastSame(First, Last)
    return Position of last energy in cached values between First and Last, with same value as First
end function
function FindFirstDifferent(First, Last)
    return Position of first energy in cached values between First and Last, with different value as First
end function
function CacheAndCheckInterval(First, Last)
    Calculate energy at n_equi equidistant points between first and last state
    if All points have same energy then
        return True
    else
        return False
    end if
end function
```

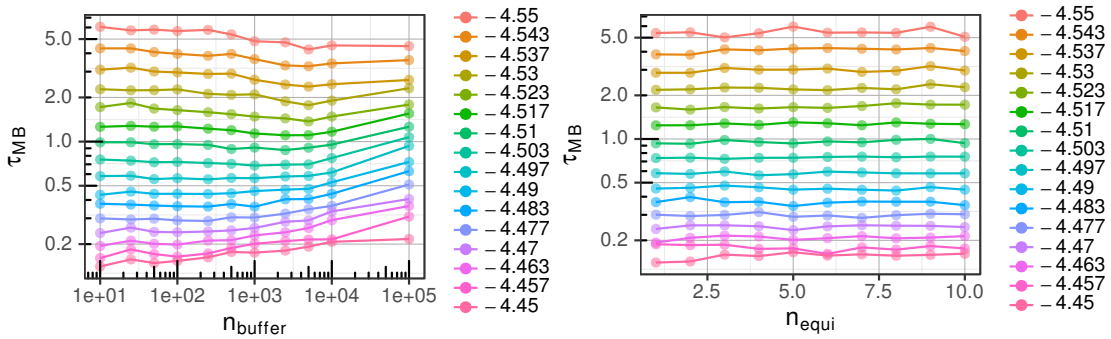

(a) Simple binary search

(b) With interval search

Figure 2.8: Metabasin lifetime τ_{MB} at $T = 0.55$ and $N = 130$ for different energies ϵ_{MB} at (a) different buffer sizes n_{buffer} and (b) different numbers of equidistant tests n_{equi}. The results are used to select optimal parameters n_{buffer} and n_{equi} for the IS jump detection algorithm.

value of $n_{\mathrm{equi}} = 5$ for all our simulations and can safely use a buffer size of $n_{\mathrm{buffer}} = 100000$ for optimal performance.

2.6 Starting Structures for Low Temperature Simulations

2.6.1 Simulations in Equilibrium at $T > T_g$

The starting structures for equilibrium simulations are prepared using a simple protocol, which is similar to the one used in [Rehwald, 2012] and [Schroer, 2015]. Starting form a random configuration and zero velocities, we use our normal Nosé-Hoover integration scheme [Nosé, 1984]. As the particle distances are random, some may be very close to each other, resulting in very high forces, which may also result in ∞ values, as the repulsive force in a Lennard-Jones potential scales with r^{-13}. This may result in artificially high particle velocities, sometimes translating to a NaN temperature. Once we encounter such a temperature, we use an Andersen thermostat to reset the particle velocities and reset all internal variables of our integrator, i.e. the bath particle velocities. Still, the velocities might still be very high and therefore some kind of dampening has to be applied. However, some kind movement is necessary, to bring the particles from their initial random positions to a normal glassy structure.

Naturally, due to our small system sizes (e.g. $N = 130$), the temperature fluctuates even with normal simulations after being properly equilibrated. However, we can safely choose a critical temperature T_{crit} of four times our equilibration temperature, which should never be reached in an equilibrated system. In case of crossing this temperature, we use a velocity scaling thermostat to reduce particle velocities and also reset our integrator to prevent the internal variables of the Nosé-Hoover thermostat to acquire high velocities. The same procedure is used, if our forces

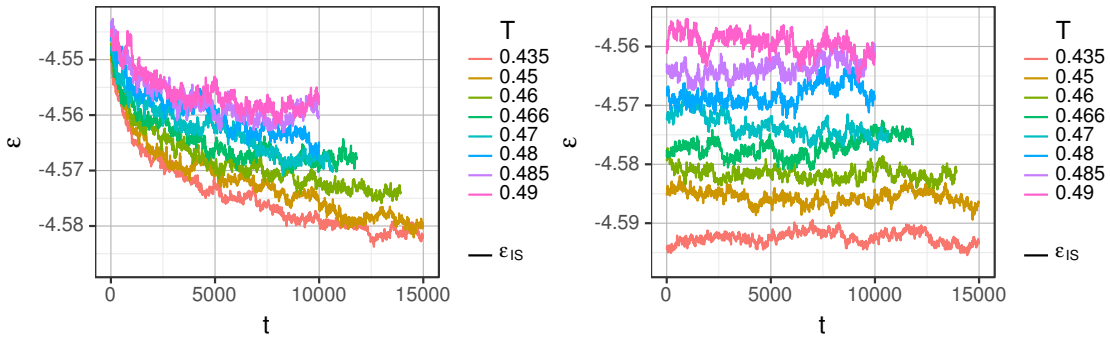

(a) $\Delta t_{\text{good}} = 500$

(b) After sufficiently large equilibration time

cross a critical force, which we derive from the critical temperature by:

$$F_{\text{crit}} = \frac{p_{\text{crit}}}{\Delta t m} \tag{2.14}$$

$$p_{\text{crit}} = \sqrt{2 m E_{\text{crit}}} \tag{2.15}$$

$$E_{\text{crit}} = \frac{1}{2} k_{\text{B}} T_{\text{crit}} \tag{2.16}$$

Furthermore, we limit the maximum force applied to the system by this force, thereby limiting particle movement during a single time step to sane values. If no reset happens for a number of n_{good} time steps, we assume that we have reached equilibrium. For equilibration, we choose a slightly higher time step $\Delta t_{\text{equi}} = 0.005$, as we do not need greater accuracy. In fig. 2.9a we see what happens, if we would choose $n_{\text{good}} = 100000$, which equals to $\Delta t_{\text{good}} = 500$. From this plot, we can approximate the waiting time before reaching equilibrium. For example at $T \approx 0.46$, the simulation needs at least $\Delta t_{\text{good}} = 15000$. We use this data to determine lower limits for our equilibration time. For the actual equilibration time, we use 5 times the lower limit. An example of properly equilibrated data can be seen in fig. 2.9b.

2.6.2 Simulations below T_g

For simulations below T_g, we choose a special method to select starting structures. First, in our equilibrium simulations, we calculate metabasins (see section 2.5.1), and find their characteristic structures, i.e. the contained IS with the lowest energy. Then, we employ two methods of selecting a subset of these IS to define our starting structures.

For method I, we sort the characteristic IS from simulations at $T = 0.5$ by their energy, starting with the lowest. From them, we pick the first 256 structures, which have an Euclidean distance of at least $d = 40$. As two IS inside a single metabasin have a maximum distance of $d_{\max} \approx \frac{1}{2}\sqrt{N}$ (see section 3.1.2), and our maximum particle number for simulations with minimization is $N = 260$, this should give us sufficiently independent configurations. In fig. 2.10a we see the energy density of the resulting set of starting structures. By construction, the distribution is not symmetric and has a larger amount of low energetic structures. It corresponds to a sample of the outer left wing of $\phi(\epsilon_{\text{MB}})$ (see section 3.1.1). The advantage of this method is, that we can simulate an aged glass, generated from the deepest of our accessible states. However, in fig. 2.10b, we find that the average value shifts to higher energies, as low energy states have lower probabilities in larger systems.

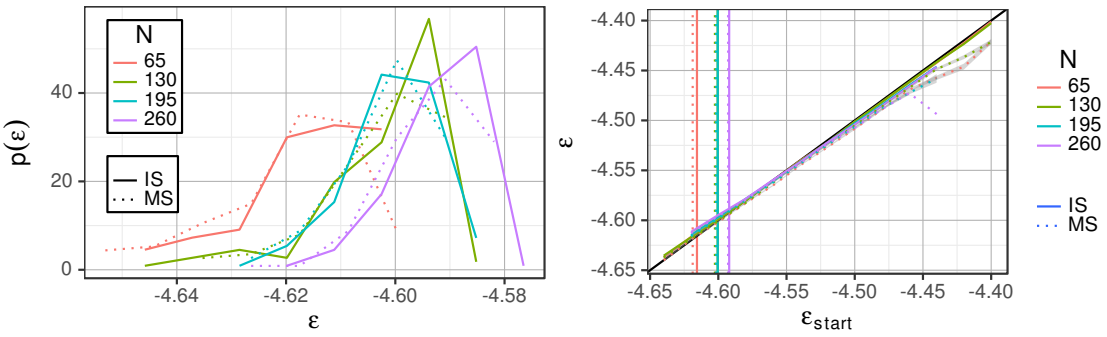

(a) Density (b) Mean energy

Figure 2.10: In (a), we show the density of the starting structures, generated by method I for various system sizes. (b) shows the mean energy of the starting structures, generated with method II. The vertical lines show the mean values energies for method I.

In method II, we select characteristic metabasin structures by their energy from simulations with $T \in [0.435, 0.625]$. For selected energies $\epsilon_{\text{start}} \in [-4.64, -4.4]$, we search metabasins with a maximum distance of $|\epsilon_{\text{start}} - \epsilon_{\text{MB}}| \leq 0.01$. For each ϵ_{start}, we now select a random sample without replacement, where each metabasin is weighted by its length τ_{MB}. This should give us a representative sample of metabasins for an aged glass at each ϵ_{start}. As can be seen in fig. 2.10b, the deviation of the average value from the expected ϵ_{start} in our samples is very small, even for very high energies. We note, that also the minimized structures, which are associated to the starting inherent structures (see section 3.2), are in close proximity to their respective IS. This small discrepancy is explained by residual stresses in the system, which is apparently small for IS near the bottom of the metabasin. In our case, the residual stress is caused by finite size effects, however it is also seen when looking at small parts of large systems [Tsamados et al., 2009, Abraham and Harrowell, 2012].

The number of starting configurations acquired using both of these methods is relatively low. Using a total number of 512 runs serving as our input, we have only generated less than 160 independent configurations per ϵ_{start} using method II. To increase our statistics in shear simulations at low temperatures, we opt to shear our starting structure into different directions [6]. As we have 3 independent planes in our cubic system and we can shear into 2 different directions per plane, we have 6 additional shear directions in total. For all these 6 directions, this method creates a different stress-strain curve.

[6] In our actual implementation, instead of choosing alternative shear directions, we rotate our system so that we can always shear in the x-y plane of our lab system, as it makes the analysis scripts much simpler.

Chapter 3

The Sheared Energy Landscape

As temperatures reach the vicinity of the glass transition temperatures, the topology of the potential energy landscape (PEL) becomes important to particle movement. In this chapter, we will give a short recap on the important concepts of the PEL analysis, like the definition of *inherent structures* or *metabasins*. At the same time, we compare the results of our new simulations at $N = 130$ with previous analysis at $N = 65$, providing a few new insights into system size scaling. Then we will extend the PEL analysis to the sheared system by introducing *minimized structures* (MS), which are intended to replace inherent structures in the definition of metabasins in the sheared PEL. Finally, we will elaborate more on the differences between IS and MS.

3.1 Equilibrium Metabasin Statistics

As temperatures reach the vicinity of the glass transition temperatures, the topology of the potential energy landscape (PEL) becomes important to particle movement [Sastry et al., 1998]. In this regime, the dynamics of the system can be divided into harmonic oscillations around a nearby energy minimum and a hopping process between minima. The concept of describing the dynamics statistically, using transitions between the associated nearby energy minima, goes back to [Stillinger and Weber, 1983]. Nearby minima are found by quenching the current particle configuration to zero temperature, which is usually done using a conjugate gradient minimization of the potential energy $V(\mathbf{x})$. These minima in the PEL are called *inherent structures* (IS).

Below a crossover temperature of approximately $T = 0.8$, two relaxation times become visible in the self-intermediate-scattering function [Kob and Andersen, 1994, Kob and Andersen, 1995b]. Therefore, the hopping dynamics at low temperatures can be divided into two processes [Stillinger, 1995]. The first process is described by hopping between a constrained set of inherent structures. During this process, some inherent structures are visited many times and others are visited rarely. The other process describes an irreversible transition to another region in phase space. After this point, no previously visited IS is seen again and the first process resumes with another set of IS. This set of IS, which is visited during the first process is called *metabasin* (MB) and we call the second process an *irreversible* jump between metabasins. Figure 3.1 illustrates these processes and definitions.

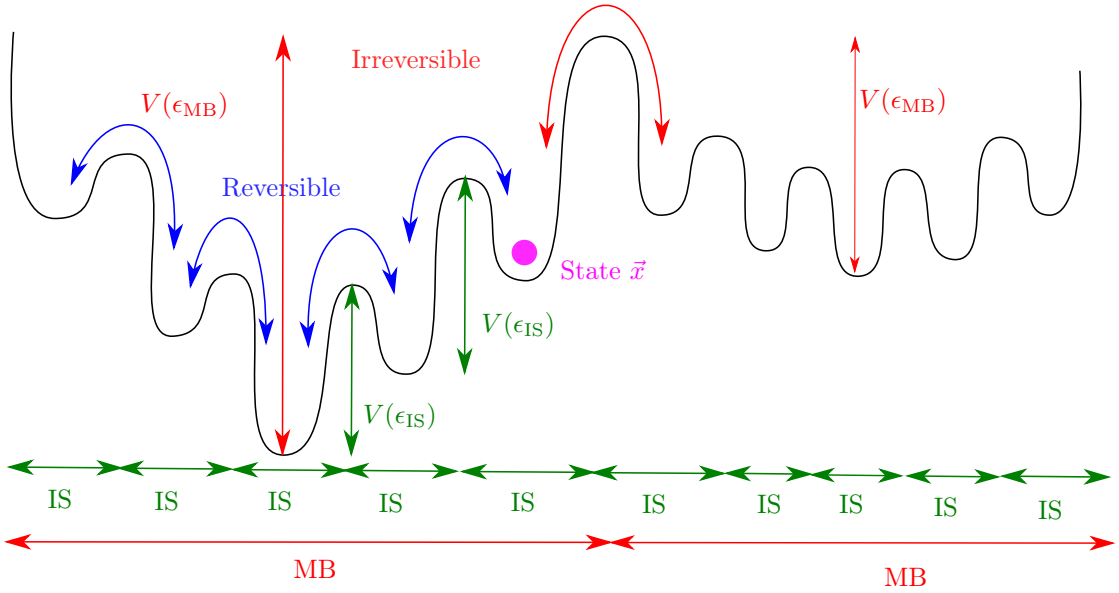

Figure 3.1: Sketch of the energy landscape, illustrating the concepts the potential energy landscape analysis via inherent structures and metabasins.

Metabasin jumps can be described as a temperature activated process, because the average waiting times between jumps, so called metabasin *lifetimes*, show an Arrhenius behavior of the form $\langle \tau_{\mathrm{MB}} | \epsilon_{\mathrm{MB}}; T \rangle = \tau_0(\epsilon_{\mathrm{MB}}) \mathrm{e}^{\beta V(\epsilon_{\mathrm{MB}})}$. Herein $\beta = \frac{1}{\mathrm{k_B} T}$ is the inverse temperature and $V(\epsilon_{\mathrm{MB}})$ the height of the energy barrier between metabasins. We recognize, that the waiting times and the barrier heights depend on the metabasin energy, which is defined as the lowest energy found in the metabasins. As we are in thermal equilibrium, this usually corresponds to the absolute energy minimum of the metabasin, at which the system resides most of the time. In case of a sheared system, this might be completely different, as the system is far from equilibrium [Isner and Lacks, 2006]. Jumps between inherent structures are themselves also activated processes. However, as we will see in section 3.1.1, they have a constant average barrier height for all energies. Using the statistics of metabasin jumps it is easily possible to describe diffusion [Doliwa and Heuer, 2003d] and also the structural relaxation process [Rubner and Heuer, 2008] as a *continuous time random walk* (CTRW). Many important results of the energy landscape analysis via metabasins have been summarized in a comprehensive review article by [Heuer, 2008].

The whole picture of activated processes can also be described by the extended trap model [Heuer et al., 2005], which is based on the work of [Monthus and Bouchaud, 1996]. In short, the whole system is seen as a superposition of a small number of high-dimensional traps with random energies. The barriers of the traps are defined as the $V(\epsilon_{\mathrm{MB}})$, measured in simulations. One of the key results is, that the number of trap-like subsystems in a $N = 65$ system is approximately 2. The extension of this model to even bigger systems can then be achieved via a scalar coupling mechanism [Rehwald and Heuer, 2012], which can successfully reproduce the finite size scaling of the structural relaxation time.

Crossing over from equilibrium to non-equilibrium, the PEL approach was recently used to characterize diffusion [Schroer and Heuer, 2013, Schroer and Heuer, 2015] for a small system under the influence of a single particle, driven by a constant force. In section 6.2, we will make

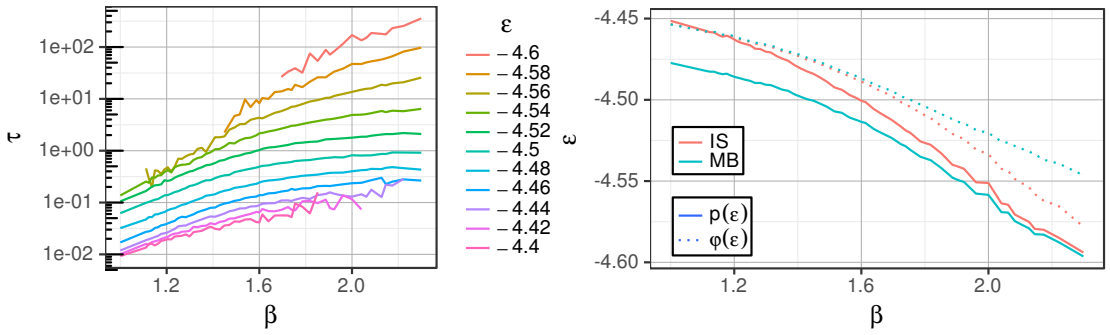

(a) Metabasin lifetime

(b) Metabasin energy

Figure 3.2: (a) Metabasin lifetimes with respect to the distribution $\phi(\epsilon_{\mathrm{MB}})$. (b) Mean IS and MB energies. Both plots show data from equilibrium simulations at $N = 130$.

use of a similar approach to characterize the crossover between equilibrium and non-equilibrium in the sheared system.

3.1.1 Energy Barriers

In proximity of the glass transition temperature, the metabasin lifetimes, conditioned on the respective energy, follow an Arrhenius behavior, which is characteristic of an activated process. This temperature range coincides approximately with the range, for which the the power-law prediction of the mode-coupling-theory $\tau \propto (T - T_c)^{\gamma}$ holds [Kob and Andersen, 1994]. For a system size of $N = 65$, this has been studied intensively in [Doliwa and Heuer, 2003a]. However, to simulate the sheared system with only small finite size effects, we have to use a slightly bigger system with $N = 130$. A comparison between the $N = 65$ and the $N = 130$ system in terms of metabasins but without shear can be found in [Doliwa and Heuer, 2003b]. One of the main findings is, that the system with 130 particles may be regarded as a superposition of two independent subsystems in terms of the waiting times. As the authors point out in their discussion, this might break down in the limit of very low temperatures near T_g, as the cooperative length scales increase.

We plot the MB waiting times for $N = 130$ in fig. 3.2a for the full range of temperatures, we have accessible. It becomes clear, that Arrhenius behavior is only found for $\beta \geq 1.8$. Comparing our data with previous results, our Arrhenius temperature range is much shorter than in [Doliwa and Heuer, 2003a]. At this point, we can only speculate, if this is maybe the result of the Langevin-Thermostat, as our results, using MD with a Nosé-Hoover thermostat, are consistent with [Schroer, 2015]. A similar difference at high temperatures is found in the mean energy fig. 3.2b, where our data is equally consistent with [Rehwald, 2012] and [Schroer, 2015]. In comparison of our data for $N = 65$ and $N = 103$, we remark that the data at $N = 130$ and $\epsilon_{\mathrm{MB}} > -4.5$ our data displays a small slope in the Arrhenius regime, which is not seen in $N = 65$ simulations. However, these energies are quite rare in low temperature equilibrium simulations and have only little effect on our statistical analysis.

In passing, we mention the two fundamental energy distributions $\varphi(\epsilon_{\mathrm{MB}})$ and $p(\epsilon_{\mathrm{MB}})$, commonly used to describe metabasin dynamics [Doliwa and Heuer, 2003a]. The first one, $\phi(\epsilon_{\mathrm{MB}})$ describes the probability of an energy at a metabasin transition. In contrast, $p(\epsilon_{\mathrm{MB}})$ describes

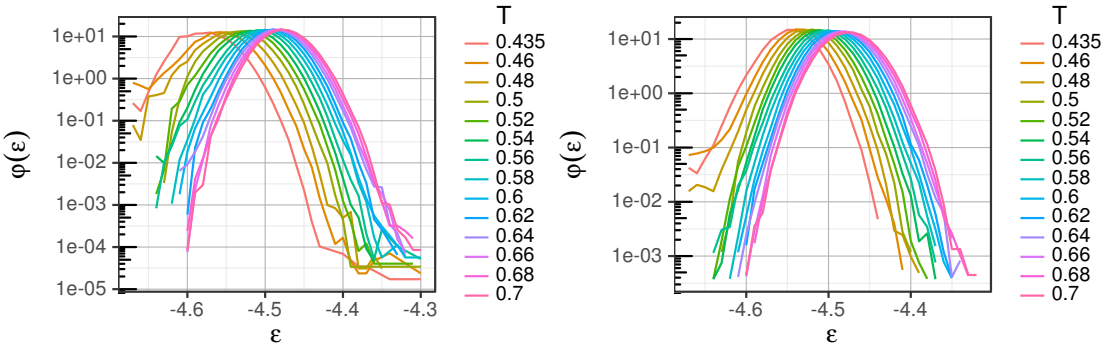

(a) IS (b) MB

Figure 3.3: Energy distribution according to distribution $\varphi(\epsilon)$ at $N = 130$.

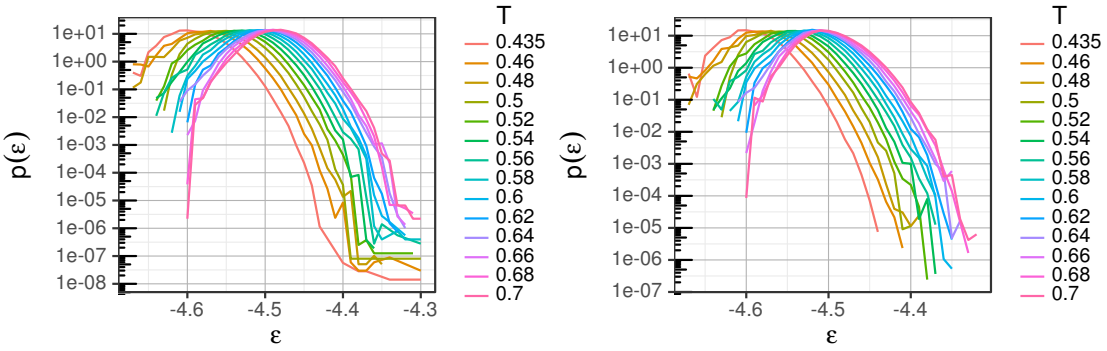

(a) IS (b) MB

Figure 3.4: Energy distribution according to distribution $p(\epsilon)$ at $N = 130$.

the probability of an energy for an arbitrary selected time. Both probabilities are connected via:

$$p(\epsilon_{\mathrm{MB}}; T) = \frac{\langle \tau_{\mathrm{MB}} | \epsilon_{\mathrm{MB}}; T \rangle}{\langle \tau_{\mathrm{MB}}; T \rangle} \varphi(\epsilon_{\mathrm{MB}}; T) \tag{3.1}$$

For reference, we plot both distributions in fig. 3.3 and fig. 3.4. In all plots, we see a perfect Gaussian shape in the range $\beta \geq 1.8$, which corresponds to $T < 0.56$. Slight deviations with an increase in higher energies occur for higher energies only in $p(\epsilon)$. Furthermore, we notice that the distributions for $p(\epsilon)$ show a more pronounced cutoff at low temperatures, while keeping a Gaussian shape for the remainder of the data.

Similar to the energies, we can express every MB-relevant quantity in terms of an arbitrary selected time by simple weighting of the distribution:

$$p(X_{\mathrm{MB}}; T) = \frac{\langle \tau_{\mathrm{MB}} | X; T \rangle}{\langle \tau_{\mathrm{MB}}; T \rangle} \varphi(X_{\mathrm{MB}}; T) \tag{3.2}$$

For example, X_{MB} can be the curvature via the lowest eigenvalue λ or the shear modulus G.

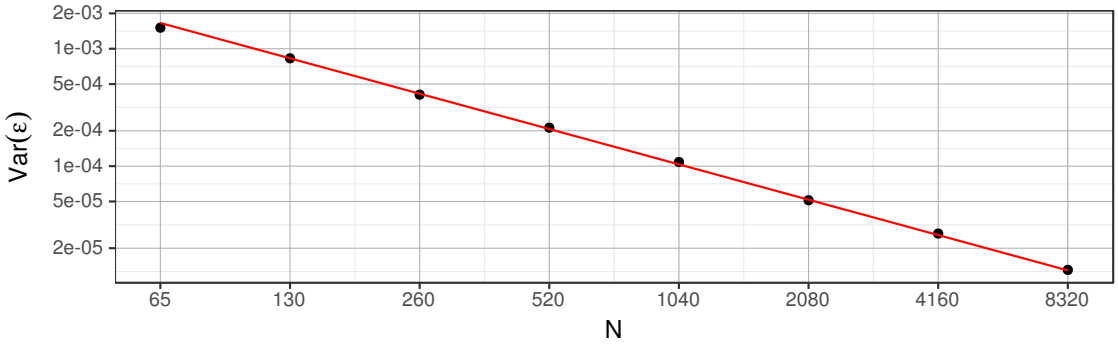

Figure 3.5: System size scaling of the inherent structure energy fluctuations at a temperature of $T = 0.5$. The red line was fitted with a fixed slope of -1 in log-space and has an intercept of 0.108, which corresponds to $\mathrm{Var}(\epsilon)$ at $N = 1$.

Choosing the metabasin waiting times $X_{\mathrm{MB}} = \tau_{\mathrm{MB}}$, we find in the average:

$$\langle \tau_{\mathrm{MB}}; T\rangle_{\tau_{\mathrm{MB}}} = \frac{1}{\langle \tau_{\mathrm{MB}}; T\rangle} \int \tau_{\mathrm{MB}} \langle \tau_{\mathrm{MB}} | \tau_{\mathrm{MB}}; T\rangle \varphi(\tau_{\mathrm{MB}}; T) \mathrm{d}\tau_{\mathrm{MB}} = \frac{\langle \tau_{\mathrm{MB}}^2; T\rangle}{\langle \tau_{\mathrm{MB}}; T\rangle} \tag{3.3}$$

Herein, we have denoted the time-weighted average with an index τ_{MB}. This value specifies the average length of a metabasin for a randomly chosen time. However, when interested in the *remaining* time of a metabasin, we have to select a uniformly distributed random point in the metabasin. The remaining time in a metabasin, also called the *persistence time* τ_ξ is then given by exactly half of this value:

$$\tau_\alpha = \tau_\xi = \frac{\langle \tau_{\mathrm{MB}}^2; T\rangle}{2\langle \tau_{\mathrm{MB}}; T\rangle} \tag{3.4}$$

This result was previously derived in a slightly different way in [Heuer et al., 2005], while the identification with the α-relaxation time has been made in [Berthier et al., 2005]. We note that the system size scaling of the α-relaxation time was analyzed in [Karmakar et al., 2009]. The authors found a strong system size dependence for systems with $N < 300$, however with a mostly identical scaling for all temperatures $T \leq 0.6$.

Naturally, with an increase in the system size, the fluctuations of the system energy decrease, as it is defined as sum over all particle contacts: $\epsilon = \frac{1}{2}\sum_{ij} V_{ij}^{pn}(r_{ij})$. As can be seen in fig. 3.5, we observe perfect N^{-1} scaling for the IS energies at $T = 0.5$. However, as we noted earlier in this section, this scaling might break down at lower temperatures due to increased cooperative length scales.

Due to the Arrhenius behavior at $\beta \geq 1.8$, we can extract the barrier height $V(\epsilon_{\mathrm{MB}})$ for the activated process with respect to the metabasin energy with a linear fit to $\log\langle \tau_{\mathrm{MB}} | \epsilon_{\mathrm{MB}}; T\rangle$. The results can be seen in fig. 3.6. Naturally, we have a higher error at small/high energies with the $N = 130$ system than with the $N = 65$, as the smaller system shows much wider energy fluctuations, and also is much faster to simulate. Nevertheless, we observe a nearly linear behavior for the $\epsilon < -4.5$ regime. Following [Doliwa and Heuer, 2003b], there might be a small curvature in the activation energy, which results directly from a superposition of the transition rates for two independent $N = 65$ systems. We recognize, that our error is still too high to verify this assumption.

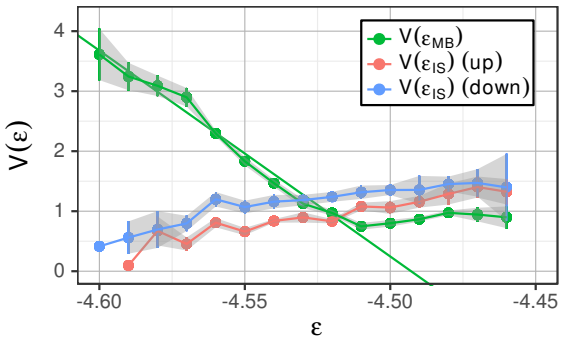

Figure 3.6: Energy barriers determined via Arrhenius-Fit of the metabasin lifetimes $\langle \tau_{\mathrm{MB}} | \epsilon_{\mathrm{MB}}; T \rangle$ as well as the inherent structure lifetimes $\langle \tau_{\mathrm{IS}} | \epsilon_{\mathrm{IS}}; T \rangle$. At the IS level, we differentiate between upwards and downwards jumps, i.e. to higher or lower IS energies. The solid green line represents a fit for the MB barriers with $\epsilon_{\mathrm{MB}} \leq -4.54$. The plot shows data from equilibrium simulations at $N = 130$.

In addition to the MB barriers, we can also calculate the IS barriers from the IS lifetimes, which we also show in fig. 3.6. However, the actual values have to be read with care, as there is a slight systematic curvature in our underlying data (not shown). At $N = 65$, this curvature is not seen, and the IS barriers keep constant for high and low energies, being slightly above 1 for upward jumps and slightly below 1 for downward jumps. This means that IS behave similar across the whole energy range, while metabasins, being constructed out of inherent structures, have an energy dependent barrier. This is an important feature of the potential energy landscape, which we make use of in section 6.3.

To gain further understanding on the IS dynamics, we again distinguish between upwards and downward jumps, i.e. IS jumps to a higher/lower IS energy after the jump. First, we look at the probabilities for upward/downward jumps (fig. 3.7a). We see an increase in downward jumps at high energies and an increase in upward jumps at low energies. Therefore, on average, the system will jump towards an equilibrium point, where the probability of an upward jump is equal to the probability of a downward jump ($p(\mathrm{up}|\epsilon_{\mathrm{IS}}; T) = p(\mathrm{down}|\epsilon_{\mathrm{IS}}; T) = 0.5$). The energy at this point is always slightly above the average IS energy under distribution $\phi(\epsilon_{\mathrm{IS}})$. To analyze the origin of this discrepancy further, we look at the mean energy change $\Delta\epsilon_{\mathrm{IS}}$ at an IS transition. We see, that only the energy change at upward jumps is dependent on the temperature. At downward jumps, $\Delta\epsilon_{\mathrm{IS}}$ shows no temperature dependence at all. The temperature dependence at the upward jumps is most likely caused by the higher number possible next states, which increases at higher temperatures. In contrast, most downward jumps are also backward jumps, as we will show in section 3.1.4, thereby limiting the number of available states. However, the average change in energy per jump, and especially the difference between upward and downward jumps is much too small, to explain the shift between the mean IS energy and the point where $p(\mathrm{down}|\epsilon_{\mathrm{IS}}; T) = 0.5$. Therefore, we look at the distribution of energies. To explain the shift, we should see an asymmetry in the distribution between high and low ϵ_{IS} before the transition. And indeed, in fig. 3.7c we see this asymmetry. All distributions have exponential tails. However, the distributions show a change of slope in their downward tail, most pronounced higher energies. This asymmetry occasionally results in direct jumps from high energies to low energies, thereby trapping the system. This characteristic effect in the downward tails is not observed in any upward tail. We remark, that a similar effect is seen in the stress drop distribution at IS transitions in section 3.2.7, pointing at a strong connection of the sheared energy landscape to

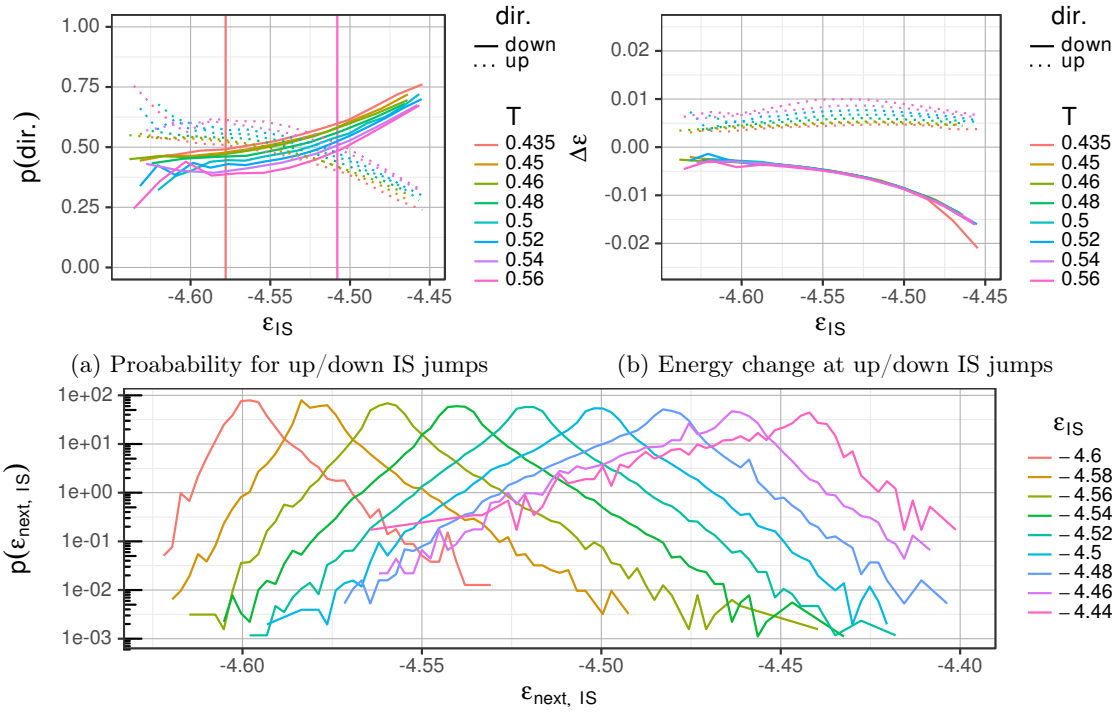

(a) Proabability for up/down IS jumps

(b) Energy change at up/down IS jumps

(c) Distribution of $\epsilon_{\text{next,IS}}$

Figure 3.7: (a) Probability to have an upward/downward jump with respect to the current IS energy and the temperature. Vertical lines show the mean IS energy for the distribution $\phi(\epsilon_{\text{IS}})$ at $T = 0.435$ and $T = 0.56$. (b) Average IS energy difference at upward/downward jumps with respect to the current IS energy and the temperature. Both plots show data from equilibrium simulations at $N = 130$. (c) Distribution of IS energies after an IS transition $p(\epsilon_{\text{next}}|\epsilon_{\text{IS}};T)$ at $N = 130$ and $T = 0.5$.

the quiescent one.

Last in this section, in fig. 3.8, we show the underlying distributions for τ_{IS} and τ_{MB}, whose mean values show Arrhenius behavior for low energies. In contrast to [Doliwa and Heuer, 2003c], we show the waiting time distribution not only in dependence of the temperature, but also of the IS/MB energy. We notice, that the distributions, especially in the case of metabasins, show deviations from power-law behavior. However, the crossover between two different decays is still prominent. Also, the tail after the crossover is still responsible for most of the average waiting time $\langle\tau|\epsilon;T\rangle$ between IS/MB for all energies. We remark, that in the average over all energies, the metabasin waiting time has a log-normal distribution [Denny et al., 2003].

3.1.2 Maximum Diameter

Of special interest for us is the spacial extent of a single metabasin, as it gives us information about the *structural* properties of metabasins. As we define a metabasin via its dynamics (see section 2.5), the mean diameter of metabasins visited in equilibrium is expected to change with temperature. In this section we define the diameter d as the mean euclidean distance between

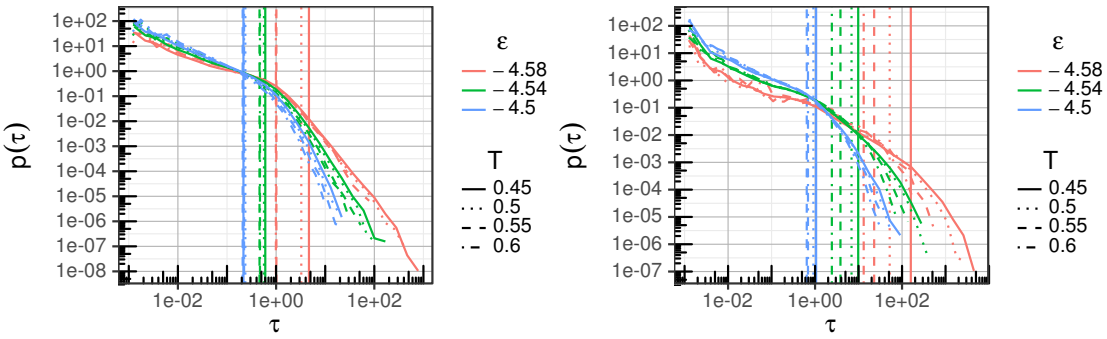

(a) IS (b) MB

Figure 3.8: Waiting time distribution $p(\tau|\epsilon;T)$ for (a) inherent structures and (b) metabasins at $N = 130$. The straight vertical lines mark the waiting times τ^*, where $\int_{\tau^*}^{\infty} \tau p(\tau|\epsilon;T)\mathrm{d}\tau = 0.9\langle\tau|\epsilon;T\rangle$

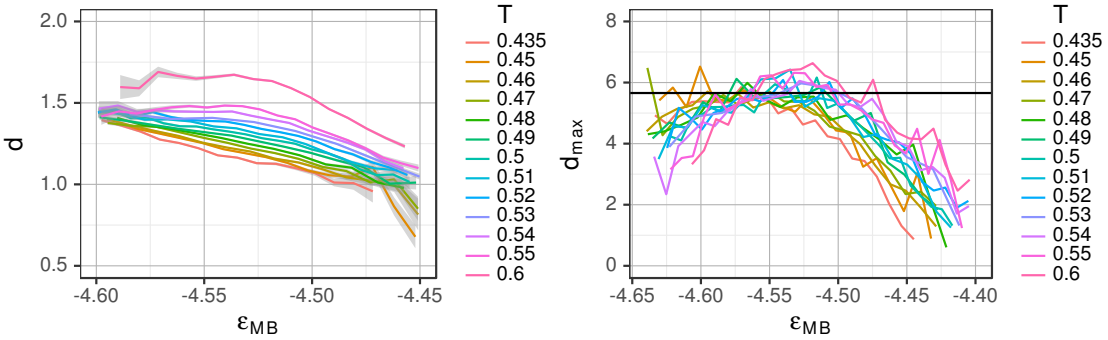

(a) (b)

Figure 3.9: (a) Mean and (b) maximum distance of different IS within a single MB of energy ϵ_{MB}. The horizontal line in (b) represents $d_{\max} = 4\sqrt{\frac{130}{65}}$, as we have simulated at $N = 130$.

the different inherent structures of a given metabasin. In fig. 3.9a, this temperature dependence vanishes for deep metabasins with energies $\epsilon_{\mathrm{MB}} \approx -4.6$. We can hereby ignore the behavior of temperatures $T \geq 0.55$, as there are already systematic deviations from Arrhenius behavior in the MB waiting times at these temperatures (see section 3.1.1). This temperature independence raises from the systems ability to visit many relevant IS at these deep metabasins. We note, that there is an exponential rise in the number of different IS in the escape path towards deeper MB (see section 3.1.3). Therefore, there is a high probability of returning to the bottom or any other low IS within the MB (see section 3.1.4). Even for $T = 0.55$ and $\epsilon_{\mathrm{IS}} = -4.6$, the probability of returning to a previously visited IS is still $p_{\mathrm{visited}} > 0.75$. Therefore, there is a good sampling of deep energetic IS for deep energetic MB. We conclude that most of the IS within the metabasin lie at the inner part of the MB, as IS energies at the MB borders increase.

Additionally, in fig. 3.9b, we show the maximum euclidean distance $d_{\max}$ of different IS visited within a MB. It decreases at low ϵ_{MB} with increasing temperatures, showing that the sampling of the border of the low energetic MB gets worse for increased temperature. However, for temperatures around T_g and low ϵ_{MB}, it levels off at around the maximum diameter seen for all

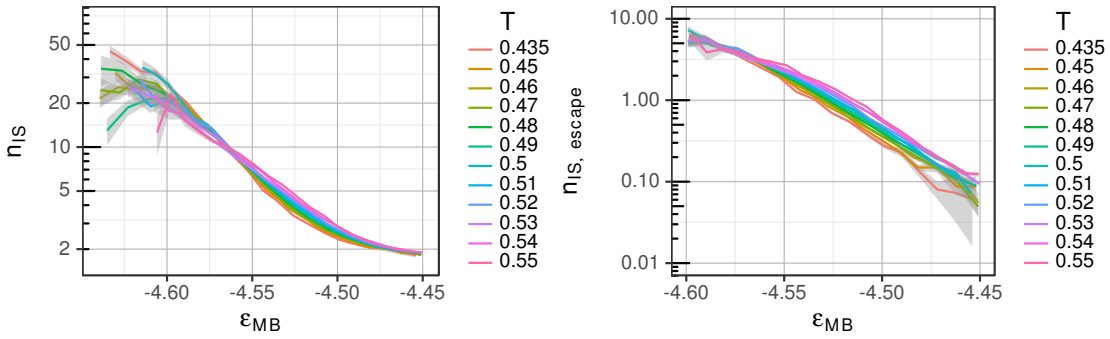

(a) (b)

Figure 3.10: (a) Number of inherent structures within a single metabasin and (b) Number of IS on the escape path from a single metabasin

simulations. This maximum distance was determined to be $d_{\max} = 4$ for $N = 65$ in [Doliwa and Heuer, 2003a]. Correcting for system size scaling, we have:

$$d_{\max} = 4\sqrt{\frac{N}{65}} \approx 0.5\sqrt{N} \tag{3.5}$$

As can be seen in fig. 3.9b, this is a very good approximation for our data. From the value of $d_{\max}$, being around 4 times larger, than the average d, this supports our previous argument, that most of the IS are not at the border of the metabasins.

Algorithmically, the maximum MB diameter can be used as an easy abort criterion, e.g. during escape runs, as the distance between distinct IS of a single MB can never be larger than $d_{\max}$ [1].

We remark, that in the context of the sheared energy landscape, distance comparisons of distinct IS are most meaningful only at similar boundary conditions, for example an unsheared reference frame [Maloney and Lemaître, 2004b], which has to be identical for both IS.

3.1.3 Number of IS

As metabasins are defined via the dynamics of the system, i.e. we count all IS between repeatedly visited IS to the same metabasin (see section 2.5), one might think that there is a strong temperature dependence in the number of visited unique IS n_{IS} for a given metabasin. However, as we see in fig. 3.10a, the temperature dependence is quite small and only leads to changes of $\frac{\Delta n_{\mathrm{IS}}}{n_{\mathrm{IS}}} < 67\%$. Nevertheless, this small dependence may be enough to explain the slightly growing MB diameter with increasing temperature (see section 3.1.2), since there are only a few IS per MB ($n_{\mathrm{IS}} \leq 8$) for $\epsilon_{\mathrm{MB}} \geq -4.55$. Apart from this small temperature dependence, n_{IS} mainly rises exponentially, going to deep ϵ_{MB}. We conclude, that even though our definition of the metabasins is defined via dynamics, the metabasin energy still defines most of its properties.

In section 3.1.2, we have seen that the diameter of the metabasin changes only slightly with the energy, while the number of IS increases exponentially when going to deeper energies. This

[1] We actually prefer to use a value of $d_{\max} = 10$ as abort criterion, keeping an additional buffer

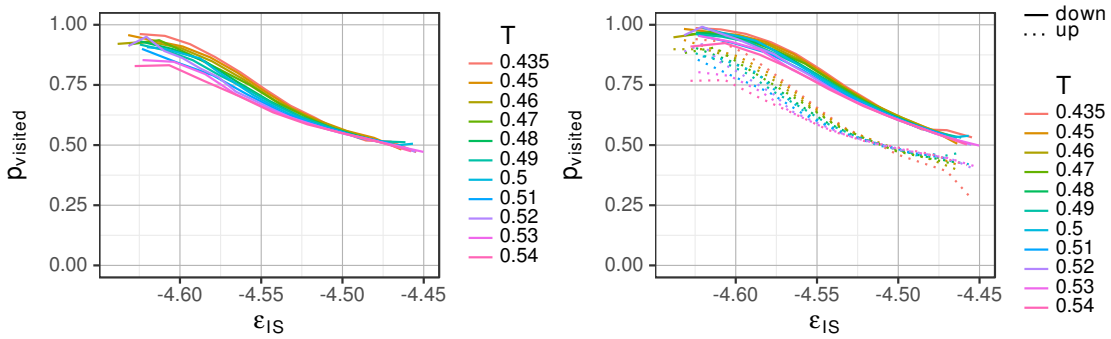

(a) (b)

Figure 3.11: Probability of having visited the same IS at an earlier time in the same trajectory. In (b) we distinguish between upward and downward IS jumps, i.e. transitions to a higher or lower energy.

means that all of these additional structures, that deep energetic metabasins consist of, are in close proximity of each other.

This also translates well to the number of different IS on the exit path of a metabasin, which is shown in fig. 3.10b. This number is calculated by determining number of different IS *between* the last occurrence of the characteristic IS for the current MB and the first IS of the next MB. In this data, we also see a mostly exponential dependence on the metabasin energy, and only a small temperature dependence, which becomes visible at $\epsilon_{\mathrm{MB}} \geq -4.55$. This tells us, that the length of the exit path is mainly given by the depth of the metabasin.

3.1.4 Backward Jumps

At low temperatures near T_g, the IS trajectory is dominated by jumps to previously visited inherent structures. In [Doliwa and Heuer, 2003a], the probabilities for returning to the ground state p_{back} were analyzed for a set of sample IS at the border of a metabasin using escape runs. The farther away the IS is from the ground state, the lower was the probability of a return. It was found that a return probability of $p_{\mathrm{back}} = 0.5$ was a good criterion to characterize the border of a metabasin. A probability $p_{\mathrm{back}} < 0.5$ would characterize the system as being free.

To determine p_{back}, one has to perform escape runs from several inherent states within a single metabasin. However, we want to extract a similar observable from our data without having to perform escape runs. Therefore, we define a similar quantity p_{visited}, which gives to probability at an IS transitions, to return to a previously visited IS. Similarly, this value should be $p_{\mathrm{visited}} = 0.5$ at the border of a metabasin.

In fig. 3.11a, we show that p_{visited} reaches the value 0.5 for energies of approximately -4.475. This corresponds roughly to the crossover energy from section 3.1.1, where the energy barriers of metabasins become 1. Furthermore, we notice, that the temperature dependence of p_{visited} vanishes for $\epsilon_{\mathrm{MB}} \geq -4.5$.

In section 3.1.1, we also showed, that there is a higher probability at high ϵ_{IS} to fall down to low ϵ_{IS}, than to climb from low ϵ_{IS} to high ϵ_{IS}. So it makes sense to distinguish between up- and downward jumps when determining p_{visited}. Indeed, we see in fig. 3.11b, that p_{visited} for

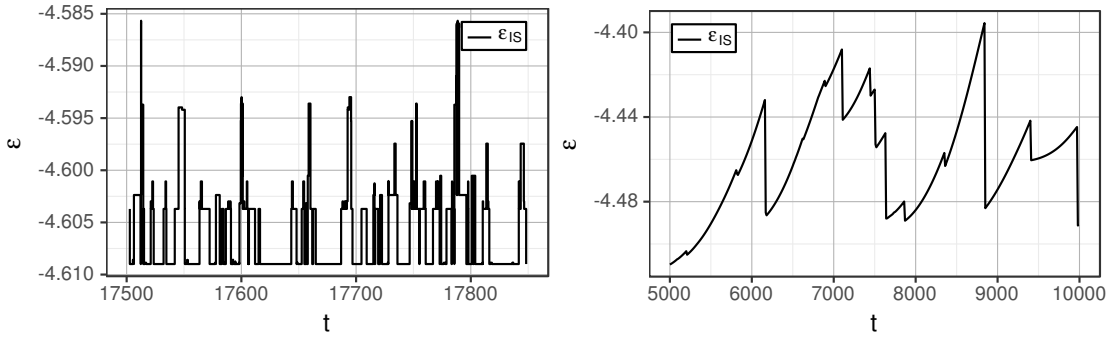

(a) $\dot{\gamma} = 0$, $T = 0.435$ (b) $\dot{\gamma} = 0.001$, $T = 0.01$

Figure 3.12: Exemplary parts of single trajectories without shear (a) and with a non-zero shear rate (b).

upward jumps crosses the value 0.5 lightly below $\epsilon_{\mathrm{MB}} = -4.5$, this time in absolutely perfect agreement with the crossover seen in the metabasin barriers. This means, that a system can be regarded as free, when it reaches energies of $\epsilon_{\mathrm{MB}} \geq -4.5$, where after an upward jump, it can now leave the metabasin with a 50% probability. This energy and its interpretation compares well with the crossover energy in the energy barrier heights seen in section 3.1.1. For energies above this crossover energy, the systems dynamics are non-activated and fluid-like [Heuer et al., 2005]. In contrast, for energies below this crossover, the system dynamics is activated and can be described by the trap model.

3.2 From Inherent Structures to Minimized Structures

3.2.1 IS Transitions

In equilibrium simulations without shear, we define metabasins via forward-backward jumps between inherent structures (see section 2.5). This is no longer be possible in case of a non-zero shear rate $\dot{\gamma} \neq 0$. Figure 3.12 shows how the form of the trajectories change, if we apply shear. While without shear, the energy stays constant between IS jumps, we notice a smooth change of the IS energy with $\dot{\gamma} \neq 0$. This is connected to the deformation of the potential energy landscape, which has been studied intensively by David Lacks and coworkers, e.g. [Malandro and Lacks, 1999, Lacks and Osborne, 2004, Maloney and Lacks, 2006]. As a basic picture, it turns out that applying a strain to the system acts like a tilt on the energy landscape. Thereby, not only the IS energies increase, but also the energy barriers between adjacent IS drop. In fig. 3.13c, we show a deformed $\sin^2 x$ potential with the control parameter γ, to explain the process. Assuming we start at $\gamma = 0$, the potential is symmetric. At low temperature, our system oscillates around the minimum at $x = 0$. This symmetry is broken, once we start to shear our system. However, despite the change in the minimum energy and the barrier height, the curvature around the minimum and its position change only slowly. In the limit of $\gamma \to \gamma_{\mathrm{c}} = 1$, the barrier goes to zero. At this point the minimum vanishes while the energy barrier shows a scaling of $V(\gamma) \approx (\gamma_{\mathrm{c}} - \gamma)^{\frac{3}{2}}$, which is typical for molecular systems [Maloney and Lacks, 2006]. For these systems, this scaling is valid for at least $\gamma_{\mathrm{c}} - \gamma = 10^{-2}$ [Karmakar et al., 2010b], and can be used to predict the stresses in the flow regime at temperatures below $T < \frac{3}{4} T_g$ [Chattoraj et al., 2010]. We examine the

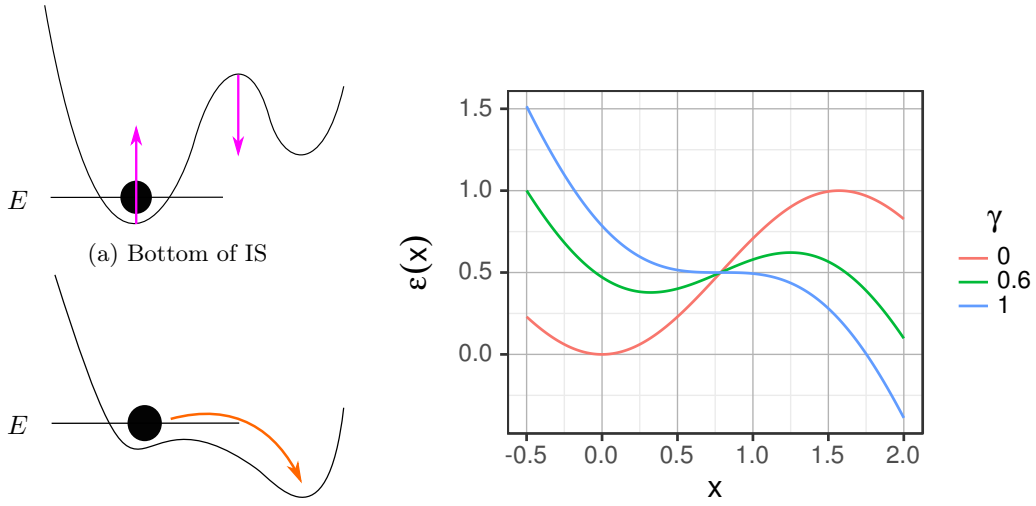

(a) Bottom of IS

(b) At jump

(c) $\sin^2(x)$ Energy Landscape

Figure 3.13: Sketch of the deformation of an inherent structure in the potential energy landscape. (a) and (b) show a sketch of the system far away from a jump and just before a jump. In (c) we plot as an example the 1-dimensional model PEL potential $\epsilon(x) = \sin^2(x) - \gamma(x - \frac{\pi}{4})$ for various γ, showing the same behavior.

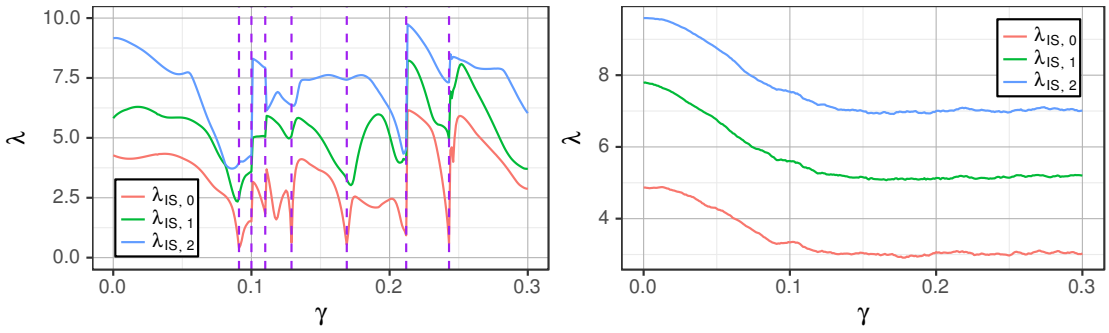

(a) Single trajectory

(b) Ensemble average

Figure 3.14: Lowest eigenvalues of the Hessian matrix, calculated from structures in the IS trajectory at $T = 0.01$, $N = 130$ and $\dot{\gamma} = 0.0001$. (a) shows a single trajectory and (b) the ensemble average over 768 runs. Vertical lines in (a) represent jumps in the $D_{\min,\mathrm{IS}}(t)$ trajectory (see section 3.2.2).

barrier scaling for different models of energy landscapes in more detail in section 6.3.7.

As the minimum vanishes, the curvature at the minimum also goes to zero [Malandro and Lacks, 1999]. The curvature is determined by the lowest eigenvalue λ_0 of the Hessian matrix for a given structure. Therefore, IS transitions induced by shear are characterized by the lowest eigenvalue going to zero, i.e. $\lambda_0 = 0$. The corresponding eigenvector represents the direction, in which the system moves during oscillations in this direction. During the jump, the particle rearrangements are largely correlated with this lowest eigenvector [Maloney and Lemaître, 2004b]. However, in fig. 3.14a, we see that λ_0 drops only in the vicinity of a jumps, making it hard to predict

the motion of the particles at the jump [Mosayebi et al., 2014, Gartner and Lerner, 2016b]. We remark, that in the case of equilibrium α relaxation, the particle movement over at least $200\tau_\alpha$ can be predicted by lowest eigenvectors [Widmer-Cooper et al., 2008, Widmer-Cooper and Harrowell, 2006]. As these describe the lowest curvatures in the highly multidimensional energy landscape, they are also called soft modes.

3.2.2 Detection of IS transitions

To detect regions without an IS transition, we have to find criteria, which tell us if a selected part of the trajectory is smooth. In addition to the energy in the IS trajectory $\Delta\epsilon_{\mathrm{IS}}(t)$, we can also monitor the Euclidean distance $\Delta d_{\mathrm{IS}}(t)$, the stress $\Delta\sigma_{\mathrm{IS}}(t)$ and the non-affine displacement $D_{\mathrm{min,IS}}(t)$.

The non-affine displacement was introduced in [Falk and Langer, 1998] and describes the non-affine displacement of neighboring particles. We slightly deviate from their notation, as we investigate the displacement in the interval $[t, t+\Delta t]$.

$$D_i^2(t) = \sum_j \left|\mathbf{r}_{ij}(t+\Delta t) - (\boldsymbol{I}+\boldsymbol{\epsilon}_i)(\mathbf{r}_{ij}(t))\right|^2, \qquad \text{with} \quad \mathbf{r}_{ij} = \mathbf{r}_j(t) - \mathbf{r}_i(t) \tag{3.6}$$

Minimizing the value of $D_i^2(t)$ with respect to the components of the affine displacement tensor $\boldsymbol{\epsilon}_i$ results in a set of equations needed for calculating the actual value of $D_i^2(t)$ at the minimum.

$$\boldsymbol{X}_i = \sum_j \mathbf{r}_{ij}(t+\Delta t)\mathbf{r}_{ij}(t), \qquad \boldsymbol{Y}_i = \sum_j \mathbf{r}_{ij}(t)\mathbf{r}_{ij}(t) \tag{3.7}$$

$$\boldsymbol{\epsilon}_i = \boldsymbol{X}_i\boldsymbol{Y}_i^{-1} - \boldsymbol{I} \tag{3.8}$$

We now take the sum over all non-affine displacements to define $D_{\min}(t) \coloneqq \sqrt{\sum_i D_{i,\min}^2(t)}$.

For the jump analysis, we write out data at a rate of $\Delta\gamma = 10^{-3}$, which is a common choice for AQS simulations [Lacks, 2002, Fiocco et al., 2013]. As we are limited by disk space, doing scans of large parameter ranges, we were unable to choose a higher rate. The only regions in the trajectories, where the write rate affects the detection of jumps, is where several transitions are in close proximity to each other. This happens only at large energy/stress drops. In AQS simulations, the behavior at these large transitions is reasonably good resolved, as the system simulated in the zero temperature limit by minimizing every time step. However, as we are simulating at a finite temperature, the stress relaxation time plays a major role after stress drops (see section 6.1). Therefore, after relaxation events, the IS trajectory sometimes touches neighboring IS before it settles for a final one. This makes it very hard to decide, whether to count every possible IS transition as a real transition or count an adjacent region of multiple transition as one. For that reason, an increased resolution would bring no further insights at these transitions. Conclusively, we decided to ignore IS with a length of our write rate $\Delta\gamma$ to count such quick transitions as a single one.

To find peaks in the trajectories, we found that a simple threshold is not good enough, as the observables span a large range of values. For example, the energy drops follow a power law distribution [Maloney and Lemaître, 2004a], making it sometimes difficult to distinguish noise from actual jumps. The situation is slightly better for the stress drops, as they show a

Jump Type	d	$D_{\min}$	ϵ	σ
Threshold	1.0	0.25	10.0	1.0

Table 3.1: Thresholds used for peak detection algorithm. These values define the minimum relative height of a peak, after a convolution with a Laplace distribution.

$P(Y\|X)$	d	$D_{\min}$	ϵ	σ
d		0.887	0.915	0.900
$D_{\min}$	0.997		0.946	0.945
ϵ	0.754	0.686		0.729
σ	0.856	0.790	0.841	

Table 3.2: Probabilities that a jump of type X is detected at the position of a jump of type Y in the IS trajectory, determined at $T = 0.01$, $N = 130$, $\dot{\gamma} = 0.0001$. X is given in horizontal and Y in vertical direction. (d : Euclidean distance of all particles, $D_{\min}$: Non-affine displacement of neighboring particles, ϵ : Energy, σ : Stress).

distinguished peak in their distribution [Dubey et al., 2016a]. However, a resolution of events up to an accuracy of at least $\Delta\sigma = 10^{-2}$ is necessary. For the suppression of small noise, we have convoluted the trajectories with a non-normalized Laplace distribution with standard deviation of $\sigma = \sqrt{2}$, acting as a smoothing filter [2]. First, the peak detection algorithm finds all positions, where a value is bigger than the two neighboring values at both sides. Then, the value is compared to the average of the five values. For each jump type, we defined a minimum relative peak height, serving as relative threshold for the algorithm. The corresponding thresholds are found in table 3.1.

However, using the peak detection method describe above, we find that not all kinds of jumps are correlated, which is a clear limitation of our method and a result of our chosen cutoffs. This situation cannot be improved much by lowering the relative thresholds, as we would then start to wrongly detect jumps at positions without plastic events, which was determined by careful inspection of the trajectories. In table 3.2 we list the probabilities of finding a jump of type Y at a position where a jump of type X was detected. Comparing the given probabilities, we find that by using $D_{\min}$ jumps, we can detect all other jump types with a probability of over 94%. Therefore, when we refer to IS jumps in sheared systems, they were detected by looking at the $D_{\min,\mathrm{IS}}(t)$ trajectory. In fig. 3.15, we analyze one example trajectory, showing the positions of the $D_{\min,\mathrm{IS}}$ jumps in comparison to the lowest eigenvalue, $D_{\min,\mathrm{IS}}$, the energy and the stress. As plastic events correlate with the lowest eigenvalue going to zero, we must find every transition up to our write-out resolution of $\Delta\gamma = 10^{-3}$ in fig. 3.15a with a relatively sharp drop. We remark, that at IS transitions, the eigenvalue trajectories shown in fig. 3.15a would actually display zero values at high enough write-out resolution [Maloney and Lacks, 2006]. Overall, we find that the detected peaks in $D_{\min,\mathrm{IS}}$, as indicated by the vertical lines, are reliably correlated with those drops. However, this is not the case for energy or stress drops. For example, looking at the 4th event, we see no visible change in the energy, but a slight stress drop. Furthermore, at the 5th event, we don't even see any change in the energy and stress, but only in the MS trajectory (see section 3.2.3). This does *not* mean, that there is no change in stress or energy, but that these changes are so small, that they cannot be used reliably, to detect a plastic event.

[2] To be precise, we use the `SciPy` function `general_gaussian` generating a window function with a maximum of 1, choosing a width of 51 samples and using `sig` = 0.5 [Jones et al., 2001].

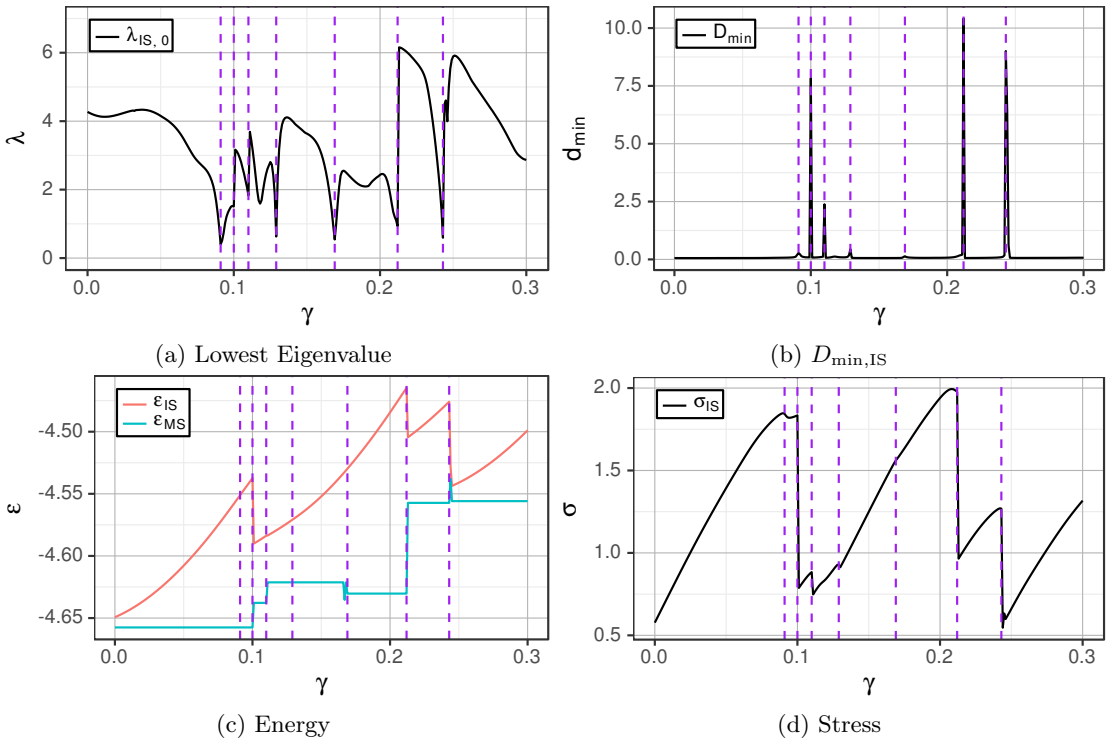

(a) Lowest Eigenvalue

(b) $D_{\min,\mathrm{IS}}$

(c) Energy

(d) Stress

Figure 3.15: Example trajectory to visualize the jump detection. We show (a) the lowest eigenvalue, (b) $D_{\min,\mathrm{IS}}$, (c) the energy and (d) the shear stress. The vertical lines show the positions, where peaks in the $D_{\min,\mathrm{IS}}$ trajectory have been detected. The write-out resolution for data points shown in these plots was $\Delta\gamma = 10^{-3}$.

3.2.3 Minimized Structures

The ϵ_{IS} trajectories between jumps is not only smooth, but also curved, as we have seen in fig. 3.12b. As a reference point, which could be associated to all points on this curve, the most obvious choice would be the minimum at the parabolic continuation to low γ. Detecting the curvature on an arbitrary short section of the trajectory is difficult, which poses a major problem as we increase the temperature (sections get shorter) and lower the shear rate (curvature gets smaller). As a solution to this problem, we change our minimization procedure slightly.

In unsheared simulations, we minimize $V(\mathbf{x})$ to find the inherent structures at $\mathbf{x}_{\mathrm{IS}}$ section 2.5.2. For the sheared system, we add another minimization step, allowing the strain γ to vary. The simple choice, i.e. minimizing $V(\mathbf{x}, \gamma)$ is problematic, because a change in γ results only in particle movement at the boundary plane, where periodic images slide over each other. In this case, particles near the boundaries have much higher changes in energies, than the other particles. Therefore, we opt to minimize $V(\boldsymbol{S}(\gamma)\mathbf{x}_0 + \Delta\mathbf{x}, \gamma_0 + \Delta\gamma)$, where $\boldsymbol{S}(\gamma)$ is an affine transformation in the shear plane, $(\mathbf{x}_0, \gamma_0)$ is the state before the minimization and $(\Delta\mathbf{x}, \Delta\gamma)$ is the change of state during minimization. This results in a much smoother energy distribution during each minimization step and still allows the minimizer to follow all degrees of freedom. We remark, that this new minimization procedure is equivalent to an athermal quasistatic (AQS) simulation (see [Lacks, 2002]) with a infinitesimal small shear steps into the direction of the lowest energy.

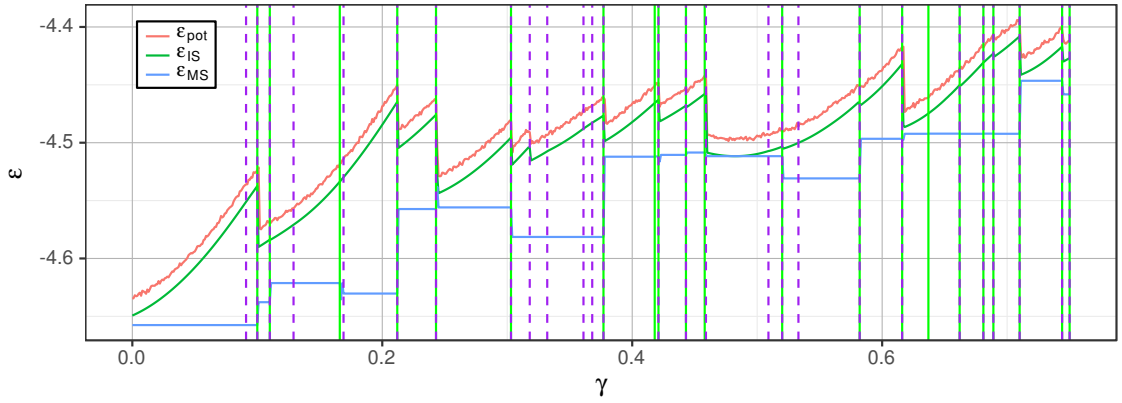

(a) Energy

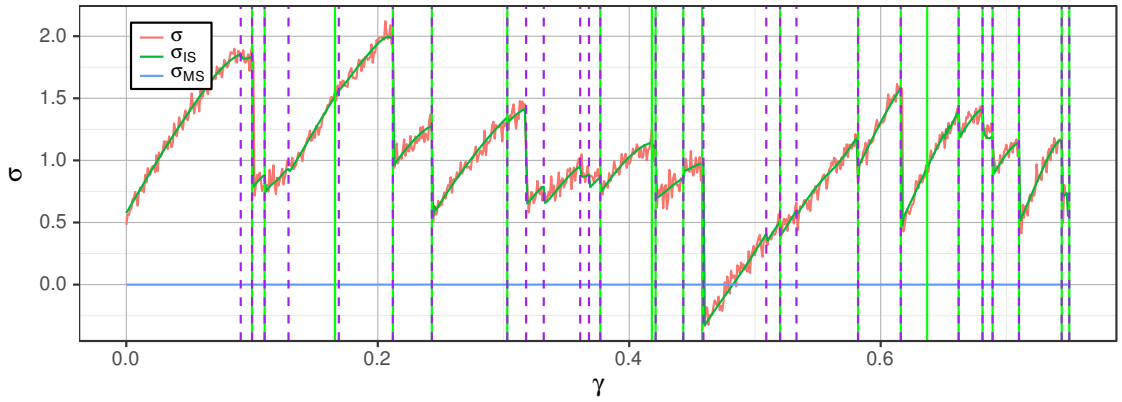

(b) Stress

Figure 3.16: Sample trajectory showing the evolution of (a) the potential energy, the IS energy and the MS energy and (b) the trajectory stress, the IS stress and the MS stress from the start of a simulation at $T = 0.01$, $N = 130$, $\dot{\gamma} = 0.0001$. Solid greed lines mark jumps in the MS trajectory and dashed purple line mark jumps in the IS trajectory, detected by $D_{\min,\mathrm{IS}}$ jumps.

In the example trajectory fig. 3.16, we see that the algorithm indeed finds a stable configuration for each smooth path. We call this configuration *minimized structure* or MS. At the minimized structures we always have a zero shear stress σ. This is not by incident but rather follows directly from the form of the pressure tensor [Evans and Morriss, 1984a] for planar Couette flow:

$$V\sigma = \sum_i \frac{p_{i,x}p_{i,y}}{m_i} - \frac{1}{2}\sum_{i\neq j} r_{ij,y}F_{ij,x} \tag{3.9}$$

$$\tag{3.10}$$

Here, V is the volume of our simulation cell, while V_{ij} represents the potential energy between particles i and j. For the quenched state, the momentum of all particles is zero, and therefore:

$$V\sigma = \frac{1}{2}\sum_{i\neq j}\frac{\mathrm{d}V_{ij}}{\mathrm{d}r_{ij,x}}\frac{\mathrm{d}r_{ij,x}}{\mathrm{d}\gamma} = \frac{\mathrm{d}}{\mathrm{d}\gamma}\left(\frac{1}{2}\sum_{i\neq j}V_{ij}\right) = \frac{\mathrm{d}}{\mathrm{d}\gamma}V(\mathbf{x},\gamma) = 0 \tag{3.11}$$

We made use of the fact, that $\frac{\mathrm{d}r_{ij,x}}{\mathrm{d}\gamma} = r_{ij,y}$ for a pure shear deformation in the x-y plane, i.e. constant y.

As we previously used the IS trajectory in the quiescent state to define metabasins, the MS trajectory in the sheared system may now provide an equivalent option. We note, that in the quiescent state, the inherent structures still have a residual stress, which causes the high starting stress in fig. 3.16b and also explains the slight energy difference between IS and MS in our low temperature starting structures (see section 2.6).

3.2.4 Minimized Structures in the Energy Landscape

To explain the ϵ_{IS} and ϵ_{MS} trajectory in the potential energy landscape, we imagine a one-dimensional version of the PEL, as sketched in fig. 3.17. In this picture, the typical exit path from a minimized structure at zero temperature is demonstrated. The minimized structure acts as a local minimum with respect to all spatial coordinates and the shear direction. By increasing the strain, we follow the path of the lowest energy with respect to only the spatial coordinates, i.e. the inherent structure. Looking at the slices in x-direction at constant γ, we see the appearance of a double-well potential, where at one point ($\gamma = 4.35$ in this example), the right minimum vanishes. At this point, the next local minimum along the x-direction is chosen. This corresponds to an IS jump in the IS trajectory. However, when we change our shear direction, even after this jump, we will return to the start MS. As the vertical landscape is a double well potential, by shearing backwards, the system will stay in the left minimum until this minimum vanishes at another point ($\gamma = 1.25$ in this example). The system will then return to the right minimum until it returns to the starting MS.

Our minimization process, described in section 3.2.3, does exactly that: It follows the IS trajectory to the direction of smaller energies, until the next MS is found. As noted there, this is equivalent to an AQS simulation, which consists of small affine transformations, followed by an energy minimization procedure at constant strain. So as long as we are able to find the same MS again, it means that our applied shear is *reversible* under slow shearing at zero temperature. In chapter 5, we will analyze the impact of this reversibility further.

In addition to the previously explained IS transitions within the same MS, there are two other kinds of transitions possible. The first one is the most simple one, where we have simultaneous

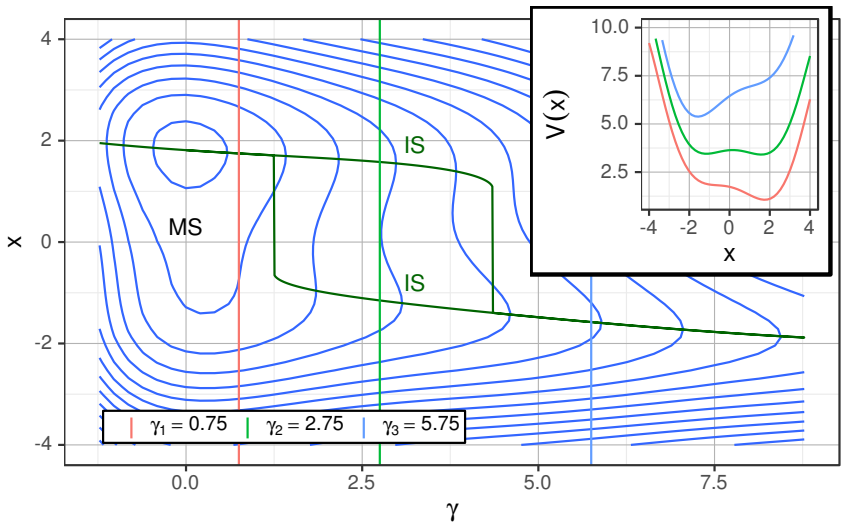

Figure 3.17: Sketch of the sheared potential energy landscape. The landscape in this figure is a 6th order polynomial, which was constructed by interpolation of a 7×7 array containing energy values. In the inset we draw vertical slices through the landscape. The positions of these slices are marked as vertical lines in the main plot.

IS and MS transition, which happens most of the time, when there is a MS transition. The second kind occurs very infrequent in the low-energy regime, being an MS transition without an IS transition. In the picture of the PEL, this means that there is a smooth path in the energy landscape connecting two minima by varying the shear strain γ. Looking at fig. 3.16, there is one such event at $\gamma \approx 0.625$, although the energy difference in the MS trajectory is invisible with the eye. In terms of the PEL, this kind of transition can be explained by a valley connecting two minimized structures.

3.2.5 Relation between MS and Metabasins

Our previous definition of metabasins used the detection of forward-backward jumps in the IS trajectory (see section 2.5.1). We will now slightly extend this definition, to include the sheared system, by simply replacing the IS trajectory with the MS trajectory. In equilibrium, this change has only a few implications. First, as we simulate small systems, there is always a non-zero residual stress in the IS, which is not present in the MS. As a result, the configurations differ slightly and the energy of the MS is slightly lower. Actual values for this difference can be seen in our analysis of the starting structures in section 2.6. Furthermore, there is a n-to-1 association between IS and MS at $\dot{\gamma} = 0$. As we have seen in section 3.2.4, there may be several IS connected to the same MS at the same strain. At the construction of the metabasins, this even proves beneficial, as these two states, which are clearly associated with the same superstructure, would be automatically associated with the same metabasin, without the need for forward-backward jumps.

In the limit of zero temperature and a non-zero shear rate, the definition would also be valid, as the system visits different MS. However, a metabasin would consist only of a single MS, as there is no jump to a previously visited MS. This poses no problem, as our definition of the metabasin

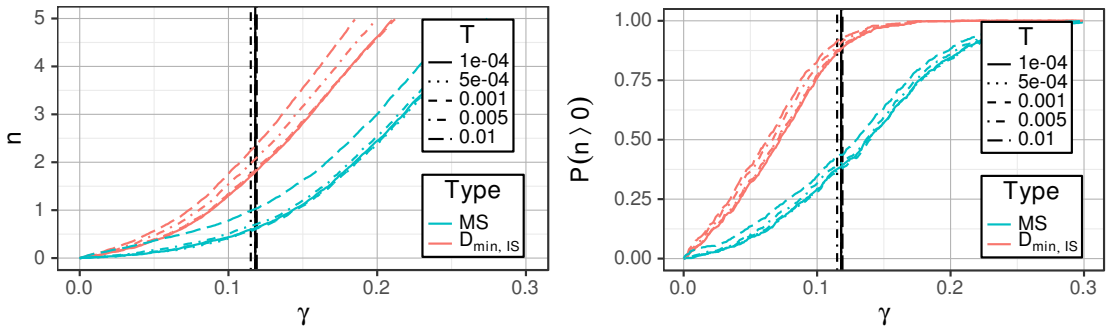

(a) Number of transitions

(b) Cumulative probability of first transition

Figure 3.18: Comparison of (a) the number of IS/MS transitions and (b) the position of the first IS/MS transition. Vertical lines mark the position of the stress overshoot. As explained in section 3.2.2, we use jumps in the $D_{\min,\mathrm{IS}}$ trajectory, to detect IS transitions. We deliberately do not show transitions in the stress, energy and Euclidean distance, since they behave similar to the IS transitions.

is a *dynamic* quantity. We note, that this is similar to high temperatures, where metabasins may also consist of single IS/MS (see section 3.1.3).

In contrast to other methods [Jaiswal et al., 2016], our definition can be used to properly calculate metabasin lifetimes for single trajectories. Furthermore, and most importantly, our definition of metabasins is consistent in the crossover region between the shear dominated regime and the temperature dominated regime, as the MS is always well-defined by the minimization of $V(\epsilon, \gamma)$. In section 6.2 and section 6.3 we will make use of this property, to calculate an effective temperature and metabasin lifetimes in the crossover region to the shear-thinning regime.

However, in terms of *structure*, the picture is quite complicated, and should only be used with care. Performing escape runs in the quiescent system at finite temperature $T > T_g$ from a single metabasin, the number of IS on the exit paths has only a slight dependence on the temperature (see section 3.1.3). But shearing a system at zero temperature, starting at the bottom of a metabasin, we might visit a completely different exit path, imposed by the shear direction, sampling a specific subset of IS during the exit. Similar to the different exit paths at different temperature. Furthermore, during this exit, we experience a change in the substructure, making energy minima vanish or appear, causing IS and MS jumps. This makes it complicated to find direct structural connections between a metabasin structure measured at high temperature and zero shear rate with the IS/MS jumps at zero temperature. However, in chapter 4, we see at multiple times the relevance of the metabasin energy of the starting structure for key observables like the stress overshoot height during yielding or the position of the first MS transition.

3.2.6 Number of IS and MS transitions

In this short section, we will clarify, how many IS and MS are visited when we start to shear a quiescent system. From fig. 3.18, it becomes immediately clear, that IS transitions occur much earlier than MS transitions. Looking at the position of the stress overshoot, there has been approximately one IS transition at that point, but only a 40% chance of a MS transition. It is even possible to have the first MS transition far beyond the stress overshoot, up until $\gamma \approx 0.3$. This

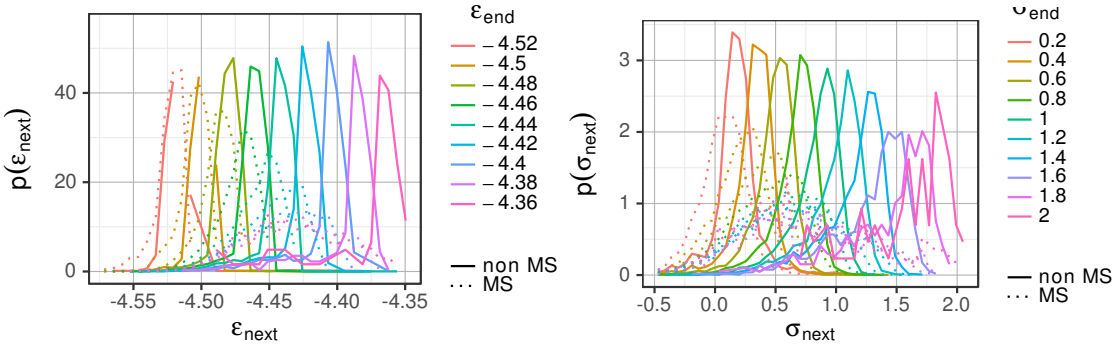

(a) Energy (b) Stress

Figure 3.19: (a) Energy and (b) stress in the IS trajectory of the whole simulation box after MS and non-MS transitions. IS transitions are detected using jumps in the $D_{\min,\mathrm{IS}}$ trajectory. The data in this plot is generated from simulation runs at $T = 0.01$, $\dot{\gamma} = 10^{-4}$ in strain interval $\gamma \in [0.0, 1.0]$ with a write rate of $\Delta\gamma = 10^{-3}$ and using a number of fixed $\epsilon_{\mathrm{start}} \in [-4.64, -4.4]$.

means, that there are few systems in our ensemble, for which it is possible, to shear back reversibly using AQS simulations to the same MS, we found for the starting configuration, although there have been many IS transitions at that strain. For more details on the first MS transition and its connection to reversibility, we refer to chapter 5.

It would be interesting, to bring the actual slopes in fig. 3.18a in connection to the diffusion constants, as there exists a Stokes-Einstein like connection between the viscosity and the shear modulus for low temperatures [Lacks, 2002]. However, as we have written earlier, having finite temperature and stress relaxation times sometimes causes multiple events to appear at a larger transition. Together with a constant write rate of $\Delta\gamma = 10^{-3}$ this gives a bad resolution of the actual number $n_{\mathrm{IS}}/n_{\mathrm{MS}}$ of transitions at high γ. Therefore, in chapter 6, when we analyze the flow regime in detail, we base our analysis on the MS lifetimes, generated using a bisection algorithm, which greatly increases accuracy.

3.2.7 Difference between MS and non-MS transitions

Besides the obvious difference between MS and non-MS transitions, i.e. that at MS transitions the MS energy changes, we now ask ourselves, if there is any other significant difference.

First, we start by analyzing the energies and stresses after a transition. In fig. 3.19 we binned the energy/stress before the transition, here denoted by END, and calculated the density of the resulting energy/stress after the transition, denoted by NEXT. Non-MS transitions show a systematic distribution of the energy/stress after the transition around the previous value. MS transitions behave very similar for low ϵ_{end}, σ_{end}. The difference between MS and non-MS transitions becomes most obvious at high $\epsilon_{\mathrm{end}}/\sigma_{\mathrm{end}}$, where we see evidence of a limiting distribution. As we have a small system, it is natural to think of a maximum possible rearrangement in the system, i.e. all particles change their energy/stress values. Therefore, as a next step, we want to find out, what part of the system is participating in a transition.

As stresses and energies behave quite the same, we will now focus only on the stress. Remembering, that the stress is calculated as a sum of the neighbor interactions [Evans and Morriss, 2013],

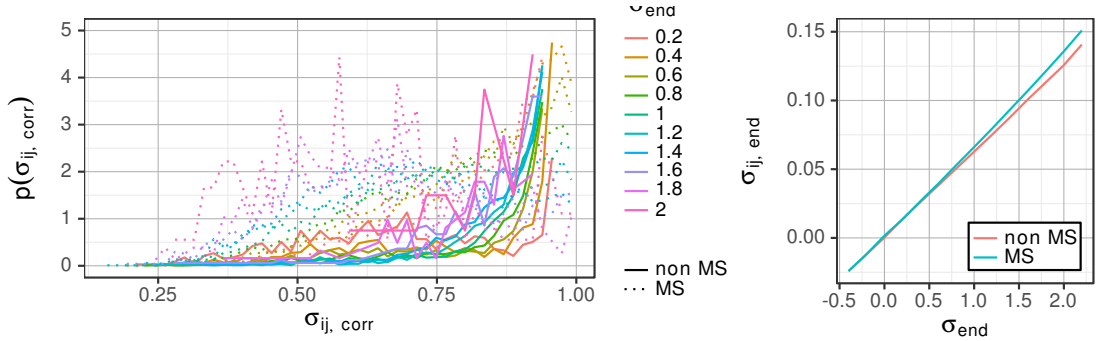

(a) Change in σ_{ij}

(b) Average $\sigma_{ij,\mathrm{end}}$

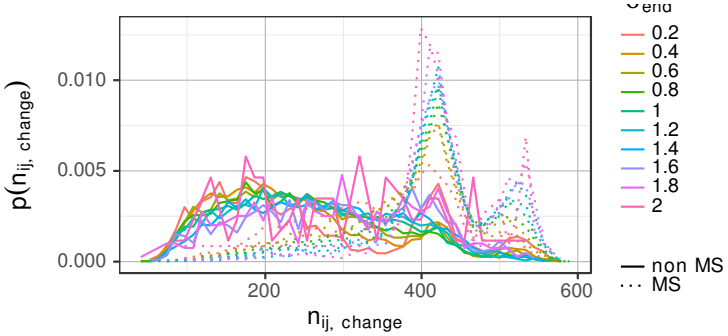

(c) Number of Contacts

Figure 3.20: Amount of change involved in an IS transition. IS transitions are divided into MS and non-MS transitions. (a) Change in contact stresses before and after a jump. (b) Average contact stress before a jump. (c) Number of contacts with a relative change $\geq 50\%$.

we will define two quantities based on the particle contacts: The relative before/after change in stress $\sigma_{ij,\mathrm{change}}$, which is defined with similarity to a correlation and the number of changing contacts $n_{ij,\mathrm{change}}$. For each jump, we calculate them via the following equations, averaging over all contacts which exist before and after the jump:

$$\sigma_{ij,\mathrm{change}} = \frac{\langle \sigma_{ij,\mathrm{end}} \sigma_{ij,\mathrm{next}} \rangle}{\sqrt{\left\langle \sigma_{ij,\mathrm{end}}^2 \right\rangle \langle \sigma_{ij,\mathrm{next}}^2 \rangle}} \tag{3.12}$$

$$n_{ij,\mathrm{change}} = \frac{1}{2} \left| \{(i,j)| \left| \frac{\sigma_{ij,\mathrm{end}} - \sigma_{ij,\mathrm{next}}}{\sigma_{ij,\mathrm{end}}} \right| > \frac{1}{2} \} \right| \tag{3.13}$$

We ignore the contacts, gained and lost during a transition, as they contribute only a small part (less than 10%) in stress and energy, when compared to the other contacts.

The definition of $\sigma_{ij,\mathrm{change}}$ is chosen, so that if $\sigma_{ij,\mathrm{next}}$ is randomly distributed, then $\sigma_{ij,\mathrm{change}} = 0$. Otherwise, if $\sigma_{ij,\mathrm{next}}$ always equal to $\sigma_{ij,\mathrm{end}}$, the resulting value is $\sigma_{ij,\mathrm{change}} = 1$. Therefore, it acts as a measure of the change in σ_{ij}. However, a comparison between MS jumps and non-MS jumps is only possible, if the average values of $\sigma_{ij,\mathrm{end}}$ is equal for both jump types. This property is validated in fig. 3.20b. The results for $\sigma_{ij,\mathrm{change}}$, shown in fig. 3.20, display a very clear difference between MS and non-MS jumps. We see that $\sigma_{ij,\mathrm{change}}$ in case of high stresses ($\sigma \geq 1.0$) is lower than 0.75 at MS transitions (down to 0.64 at $\sigma = 2.0$), whereas it is more than

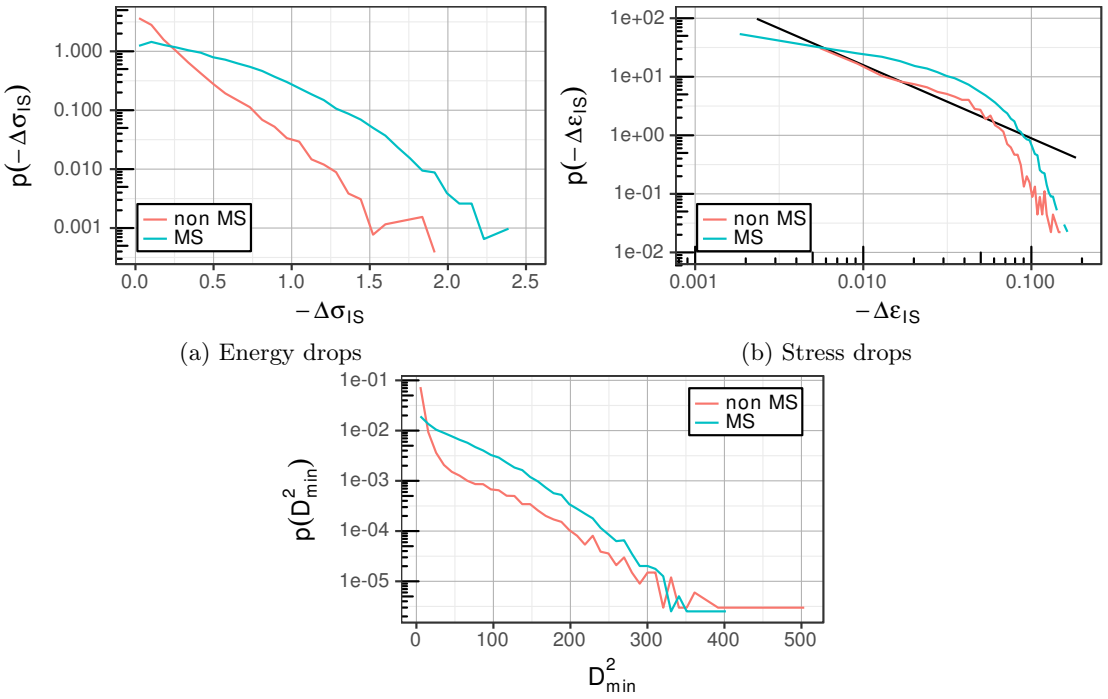

(a) Energy drops

(b) Stress drops

(c) $D_{\min}$ at transition

Figure 3.21: (a) Energy, (b) stress drop and (c) $D_{\min}$ distribution in the IS trajectory at MS and non-MS transitions. In (a) and (c) we use a log-normal plot, as the data is mostly exponentially distributed, whereas we use a log-log plot in (b) to see a small part of a power-law distribution for small energy drops. The solid straight line in (b) shows the theoretical value of $\frac{5}{4}$, which was given in [Dubey et al., 2016a].

0.9 for non-MS transitions. This shows us directly, that many stress contacts stay at similar values for non-MS transitions, whereby a much larger part of the stress contacts change at MS transitions.

The second definition, named $n_{ij,\text{change}}$, gives us another measure of how many contacts are involved in the transition. We effectively count the number of contacts, which have a relative change of more than 50%. This number of contacts, shown in fig. 3.20c, differentiates even more between MS and non-MS transitions. For MS transitions at $\sigma \geq 1.0$, the variable $n_{ij,\text{change}}$ averages to more than 220 contacts and shows a nearly identical distribution for the different σ_{end}, with a strong peak at $n_{ij,\text{change}} \approx 230$. On the other hand, for non-MS transitions, the distribution looks almost flat with a maximum at $n_{ij,\text{change}} \approx 90$.

Energy/stress drops are also a very important subject in the analysis of avalanches [Leishangthem et al., 2017], as they display a typical power law behavior for big systems [Maloney and Lemaître, 2004a]. Avalanches in glasses can be modeled by the spatial propagation of shear stresses, caused by elementary events [Liu et al., 2016]. However, the scaling behavior of stress drops is subject to finite size scaling, shortening the range of power-law behavior [Dubey et al., 2016a]. Therefore, at our system size, we see no power-law behavior for the stress drops and a short range of power law behavior for energy drops (see fig. 3.21). The power law exponent for the energy drops

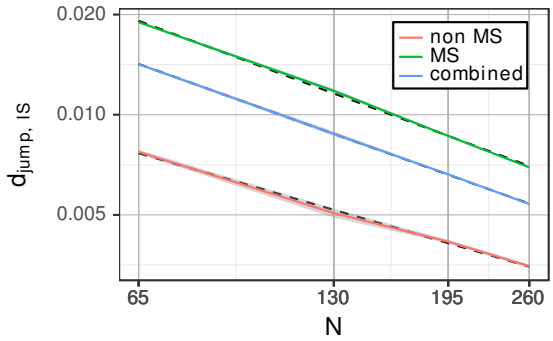

Figure 3.22: Euclidean jump distance in dependence of the transition type. We differentiate between MS transitions, non-MS transitions and also show the values for a combination of both transition types. The dashed black lines represent power law fits to the data. The exponents, as determined by these fits, are: -0.724(15) for MS transitions, -0.566(18) for non-MS transitions and -0.6968(24) for both transitions types combined.

compares well to [Dubey et al., 2016a]. Now, comparing MS and non-MS transitions, we see a similar shape in the distributions for high energy/stress drops. However, the probability for having small drops is much lower at MS transitions than for non-MS transitions. As can be seen in fig. 3.21c, the non-affine displacement at MS transitions is also much bigger than at non-MS transitions (3.4 times bigger on average).

Last, we check the system size dependence of the euclidean distance at transitions in the IS trajectory. In fig. 3.22 we see power law behavior, as is expected from the study of avalanches [Leishangthem et al., 2017]. Although in this paper, the energy and cluster size dependence are studied, the power law exponents show a characteristic system size dependence. Within good agreement, we also find an exponent of $\frac{1}{3}$ for IS transitions [3]. In addition, we see a similar system size dependence for both MS transitions and non-MS transitions, whereas MS transitions cause more than twice the movement in particles compared with non MS transitions in the shown system size range.

Overall we come to the conclusion, that a MS transition involves a much larger part of the system, causing a larger effect on the system, than an IS transition.

3.2.8 A Toy-Model for the Stress Drop Distribution

We would now like to introduce a toy model, which can reproduce several features of the stress drop distribution fig. 3.19b. However in this case, we look at the combined distribution of MS and non-MS transitions fig. 3.23a. The toy model to reproduce this data consists of a number N of random variables σ_i, which may be associated with the stress of particles, particle-particle contacts or simply small regions of our system. We assume that all variables are identically distributed. To simplify our model, we further assume a Gaussian shape, although in section 7.1, we see that the distribution of the stress contacts for example is strongly non Gaussian. However, by using the central limit theorem, the distribution of a sum of contact-stresses would be Gaussian in the limit of many contacts, as the contact distribution itself is not stable.

[3] In our plot, we show distances per particle and therefore we have to add 1 to the exponent for comparison.

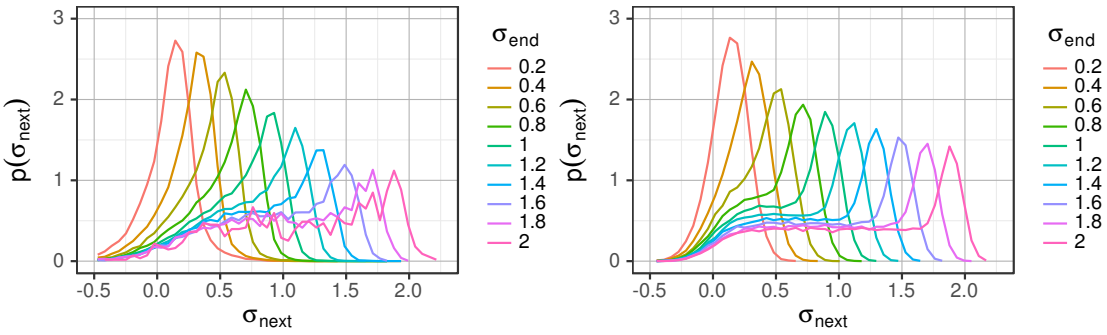

(a) Simulation (b) Model

Figure 3.23: Stress distribution after IS transitions, including all MS transitions. The color encodes the IS stress before the transition. In (a) we calculated the distribution from our simulations and in (b) we used a simple toy model.

Our model starts with all N variables randomly distributed around a mean value of the stress before the IS transition. We choose a fixed standard deviation of 1.8. Then we randomly choose a minimum number $1 \leq n \leq N$ of variables from a uniform distribution, which change during the transition. Additionally, we look at the current sample of random variables and select a subset of small variables with $|\sigma_i| < 1.0$. The number of small variables n_{small} number naturally changes with total stress $\sigma = \sum_i \sigma_i$ of the system. Finally, we select new values according to our Gaussian distribution for the subset of small variables, for the variable with the highest stress and also for a uniformly distributed random subset of the remaining variables, until we have reached a total of n variables.

Comparing our toy model with simulation data in fig. 3.23, we can reproduce the major features of the stress distribution after an IS transition. The plateau in this distribution is caused by the random number of variables involved in the transition. By always changing variables with small stress, we cause the peak at the upper end of the distribution to appear. The change in height of the plateau and the change in width of the peak is caused by the automatic scaling of the number of variables with small stress.

Although this model produces quite good results, its connection to the physical system still needs further exploration.

First of all, our model cannot be valid on the lowest level, the stress can be broken down to, i.e. the particle-particle contact stress. The contact stress distribution is strongly non-Gaussian, as we will see in section 7.1 and changes in the overall system stress result in a lightly skewed distribution, rather than a moved one, as in our model. However, adding the sum of some contacts and looking at spatial regions may be the key to understanding the physical correspondence. Here, we take only some preliminary steps, analyzing the contact stress in more detail and leave the spatial examination for future work.

If our model was correct for individual contact stresses, this would be visible immediately in the contact stress drop distribution fig. 3.24a. For the contact stress after the stress drop, there would be a high peak at the value before the transitions and a central peak for changing contacts. This is clearly not the case. However, the distribution for zero stress contacts before the transition looks similar to the equilibrium contact stress distribution section 7.1. This may be an analogy to

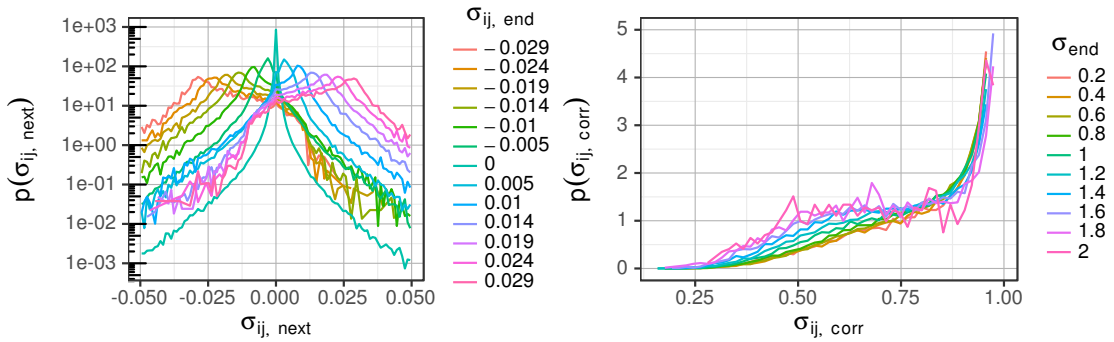

(a) Contact stress drop distribution

(b) Contact stress correlation

Figure 3.24: (a) Distribution of contact stresses after an IS transition. The stress before the transition was $\sigma_{\text{end}} = 1.8$. (b) Correlation of contact stresses before and after an IS transition. For both plots, we did not treat MS transitions separately.

our model, where we redistribute variables with small stresses. The number of particles having a stress around zero is quite high, also in the case of high stresses, as the contact stress distribution is only slightly skewed. We see an additional interesting property: The distribution is symmetric. Even though the system has a lot of stress, the relaxation event affects negative stress contacts in the same way as positive ones. This may be related to the symmetry of the spatial stress propagation operator for a single plastic event [Picard et al., 2004], which has a 4-fold rotational symmetry. However, we see no contacts at rest during an event, all exhibiting some form of change, mostly towards 0 stress.

In section 3.2.7 we looked at the particle contact stress correlation $\sigma_{ij,\text{change}}$ during MS and non-MS transitions, to describe the part of the system, which is involved in a transition. At high stresses ($\sigma_{\text{end}} \geq 1.8$), $\sigma_{ij,\text{change}}$ exhibits a long plateau, when combining MS and non-MS transitions (fig. 3.24b), while still retaining a peak at high correlations. Although this deserves further analysis, the plateau may be somehow related to our uniformly distributed number of changing contacts, while the peak of high correlation could in relation to our minimum number of small stress particles involved at a transition.

3.3 Summary

In the first part of this chapter, we have done a short recap on the description of glass forming systems near the glass transition with the concept of *inherent structures* (IS) and *metabasins* (MB) in the picture of the *potential energy landscape*. We found that the results from the $N = 65$ system translate well to the $N = 130$ system, which can be described as a superposition of two independent $N = 65$ systems in a first order approximation. This is why we found a similar crossover in the activation energies at $\epsilon \approx -4.5$, which marks the highest point in the energy landscape, where our system can be described in terms of metabasins. Also at this crossover energy, as the probability to return to a previously visited IS at an upward jump, drops below 0.5. This means, that above this crossover, where all IS have the same barrier height, the dynamics can be characterized as free. We also explored some additional structural features of metabasins, such as the metabasin diameter and the number of inherent structures in a metabasin, both of help in the interpretation of the results in chapter 4.

The second part of this chapter focuses on the sheared system at low temperatures. With an applied strain inherent structures are constantly changing, and can no longer be used to properly define a metabasin. However, in order to transfer the concept of metabasins to the sheared energy landscape, we introduced the new definition of *minimized structures*. To each inherent structure, we can assign via a n-to-1 mapping a minimized structure, representing an associated configuration in an unstressed system. Using the trajectory of minimized structures, it is now possible to transfer the definition of metabasin replacing inherent structures with minimized structures. This also works well for the quiescent system resulting only in a slight change of energies.

Then, we analyzed in more detail the differences between plastic events at IS transitions, which we detected by peaks in the $D_{\min}$ trajectory and plastic events at MS transitions. We found that there are more non-MS than MS transitions during start-up shear, but also that MS transitions have a much larger impact on the energy- and stress-drops and also the euclidean distance during a transition than non-MS transitions. In the euclidean distance we found an avalanche like system scaling for both MS and non-MS transitions. However, since also a larger amount of particles contributes to the MS transition, we interpret non-MS transitions as being more local and small in comparison to MS transitions.

Last, we looked at stress drops in the sheared system at zero temperature and found a similar asymmetry as for the energy drops in the quiescent system, thus showing the influence of the PEL. On the system scale, we could reproduce the stress drop distribution in very good agreement by a simple toy model.

Chapter 4

The Stress Overshoot

During the start-up phase of a sheared system under constant strain, we first observe nearly elastic behavior, resulting in an approximately linear stress increase with the strain, which can be characterized with a constant shear modulus $\Delta\sigma = G\Delta\gamma$. However, due to strong non-linear behavior and plastic events, the stress eventually shows a maximum and then decreases until it levels off at a constant value. This maximum is also called the *stress overshoot*. The height, position and existence of this maximum is affected by numerous parameters, like the temperature, the aging history and the shear rate [Shrivastav et al., 2016a]. This maximum in the system stress is also called *stress overshoot*. For a small review of experimental and simulations results for different materials, we refer to [Bonn et al., 2017].

In fig. 4.1a and fig. 4.1b we show the dependence of the overshoot on the temperature and the initial system energy. We find, that there is a very strong temperature dependence of the overshoot position for $T > 0.1$, while there is only a very slight dependence on the initial energy. As we are interested in the connection of the stress overshoot to the energy landscape, we immediately compare these observations with the energy during the overshoot in fig. 4.1c and fig. 4.1d. Our first observation is, that the IS energies undergo a change in slope, close to the position of the stress overshoot. For a single athermal system, between plastic events, the stress and energy are related via the non-linear connection:

$$\sigma = \frac{\mathrm{d}U}{\mathrm{d}\gamma} = \frac{\partial U}{\partial \gamma} \tag{4.1}$$

$$\frac{\mathrm{d}^2U}{\mathrm{d}\gamma^2} = \frac{\partial^2 U}{\partial \gamma^2} - \vec{\Xi} \cdot \mathcal{H}^{-1} \cdot \vec{\Xi} \tag{4.2}$$

In the last equation, $\mathcal{H}$ refers to the Hessian matrix, $\vec{\Xi} = \frac{\partial^2 \mathring{U}}{\partial \vec{\mathring{r}} \partial \gamma}$ and $\mathring{\vec{r}}$ is the position of the particles in a non-sheared reference frame. We note, that $\mathring{U}(\mathring{\vec{r}}, \gamma) \coloneqq U(F(\gamma) \cdot \mathring{\vec{r}}, \gamma) = U(\vec{r}, \gamma)$, where F is an affine transformation from the non-sheared reference frame to the sheared one. For a more detailed discussion, we refer to [Maloney and Lemaître, 2004b] and [Lemaître and Maloney, 2006]. This would explain the observed effect in the regime before the overshoot, if there were no plastic events. We remark, that using this formalism, a series expansion of σ can successfully predict the next point of failure [Karmakar et al., 2010a], however it cannot hold in the thermodynamic limit, due to the broad distribution of plastic events. As we will see later, there are already many plastic events before the stress overshoot and therefore, further analysis

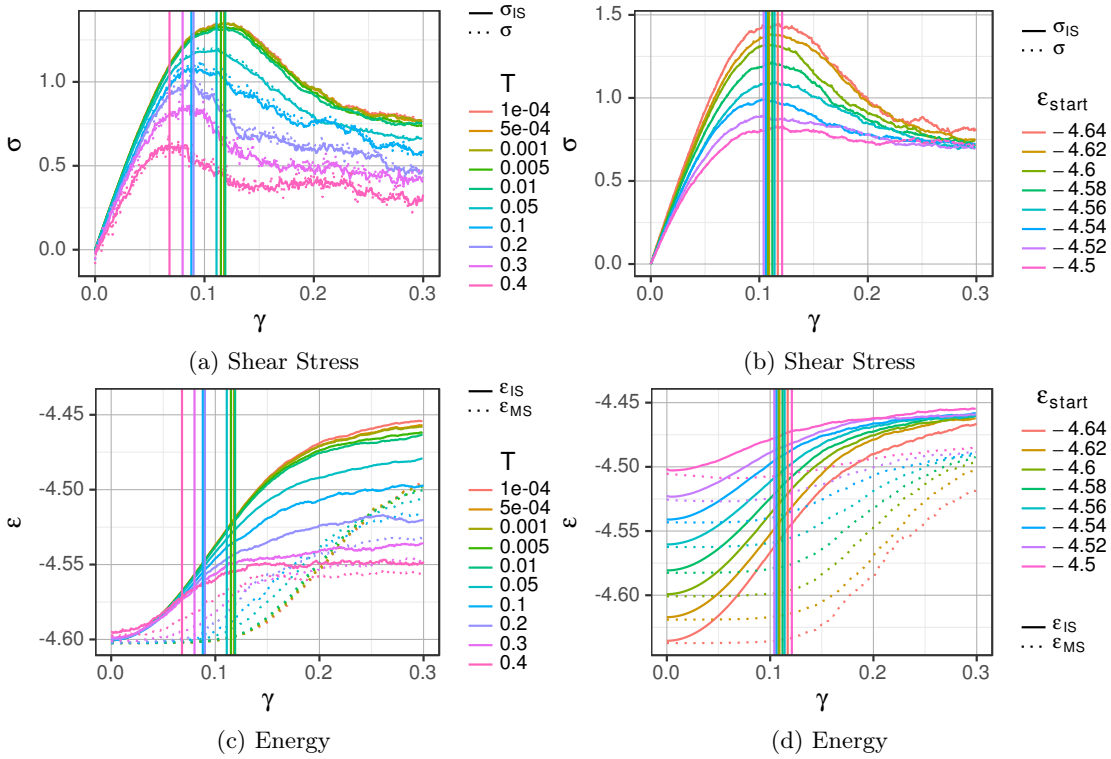

(a) Shear Stress

(b) Shear Stress

(c) Energy

(d) Energy

Figure 4.1: (a), (b) Shear Stress and (c), (d) energy during the start-up regime of a sheared system with $N = 130$ and $\dot{\gamma} = 10^{-4}$. In (a) and (c), we used a fixed initial energy of $\epsilon_{\text{start}} = -4.6$ and in (b) and (d) we used a fixed temperature of $T = 0.01$. The vertical lines show the position of the stress overshoot for the respective temperature T or initial energy ϵ_{start}.

has to be made, why the change in slope is still in the vicinity of the stress overshoot. In fig. 4.1, we also see the energy of our newly defined minimized structures ϵ_{MS}. On a qualitative level, we immediately notice the similarities in the temperature and initial energy dependence in the onset of changes in ϵ_{MS} and the overshoot position. A more quantitative analysis of the first MS transitions and its connection to the stress overshoot follows in section 4.2 and section 4.4.

First, we will demonstrate some more surprising similarities between PEL properties and the overshoot. For low temperatures, in the *flow regime*, we find that the average MS energy is around $\epsilon_{\text{MS}} = -4.48$ (see fig. 6.4b). This energy is similar to the crossover energy, we see in the activation energies for metabasin barriers in the equilibrium (see section 3.1.1 and fig. 4.2b). At $N = 65$, the crossover energy is even closer [Doliwa and Heuer, 2003b]. As the energy barriers above this crossover are approximately constant, dynamics resemble non-activated fluid-like dynamics, while below, the dynamics behave as activated process between traps [Heuer et al., 2005]. Therefore, at zero temperature, an applied shear brings our system energy-wise exactly to this crossover point. This process is also called *mechanical rejuvenation* [Utz et al., 2000, Lacks and Osborne, 2004], as the system is to a state, which resemble that of higher temperatures [Chung and Lacks, 2012a, Rodney and Schuh, 2009]. The dynamics during this exit from the starting trap, must by tightly coupled to its properties, most prominently the trap depth, which is dependent on the starting MS energy ϵ_{start}. We remark, that the ensemble of MS configurations,

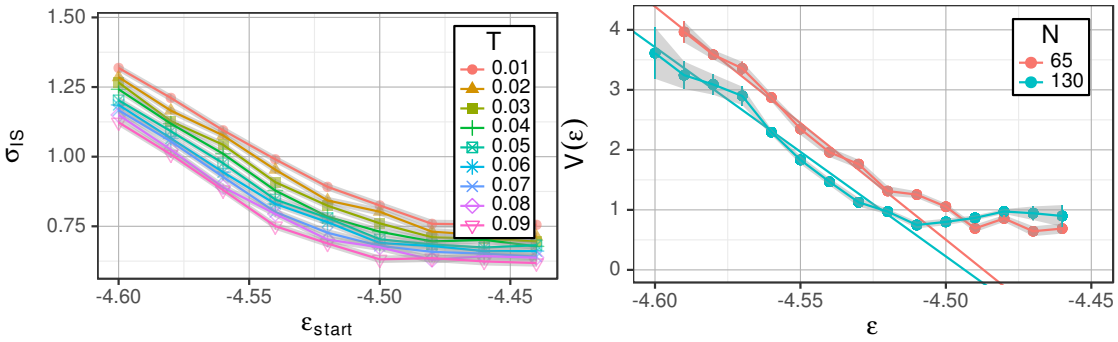

(a) Stress Peak

(b) Barrier Height

Figure 4.2: (a) Height of the stress overshoot peak with respect to the initial energy ϵ_{start} and the temperature at $N = 130$ and $\dot{\gamma} = 10^{-4}$. (b) Metabasin barrier height, calculated at equilibrium for temperatures $2.2 \leq \beta \leq 1.8$.

we access via shear at zero temperature is *not* identical with the ensemble of MS configurations, which is accessed by the non-sheared system in thermal equilibrium with the same average MS energy [Isner and Lacks, 2006]. The former is rather a specific sub-ensemble of the latter, as thermal fluctuations enable the system to access nearby states with similar energy, which are inaccessible by pure shear.

As we are transitioning from the bottom of a metabasin to the flow regime, it is not surprising, that the IS energy at the overshoot is directly linked to the starting energy. However, we find at low temperatures, that also the overshoot height is linearly connected the initial trap depth / barrier height (see fig. 4.2). This result is quite interesting, as on average, there are already some IS and MS transitions (on average 2 and 0.5, see section 3.2.6, fig. 3.18a), associated with stress drops. In literature, this effect has been observed in the context of aging, where the aging time τ_w has a logarithmic effect on ϵ_{pot} and therefore also ϵ_{IS} in the energy landscape influenced regime [Shrivastav et al., 2016a]. A similar dependence was also found in [Varnik et al., 2004, Rottler and Robbins, 2005, Rottler and Warren, 2008], where the effect was explained in terms of Eyring's model of stress-assisted thermal activation over free energy barriers [Eyring, 1936].

$$\sigma_{\text{peak}} = C(\dot{\gamma}, T) + A(T)\log(\dot{\gamma}\tau_w) = C(\dot{\gamma}, T) + A(T)(\log(\dot{\gamma}) + \log(\tau_w)) \tag{4.3}$$

Replacing $\log(\tau_w)$ by ϵ_{start} reproduces our energy dependence of the stress overshoot. This analogy makes it tempting to associate yielding with the exit of the initial metabasin. In this picture, the shear would apply to not only the IS within the metabasin, but also the whole metabasin simultaneously. During the exit of the metabasin, the system would cross several IS barriers, seen as IS and MS jumps in the trajectory. In the following sections, we will see the importance of the first MS transition and its connection to the exit of the initial metabasin.

4.1 IS Transitions in Single MS

Before we get into the details of the first transition, we now look at what happens during an average single MS. As we have shown in section 3.2.6, there are typically more IS transitions than MS transitions. Therefore, we have now averaged the IS stress and energy with respect

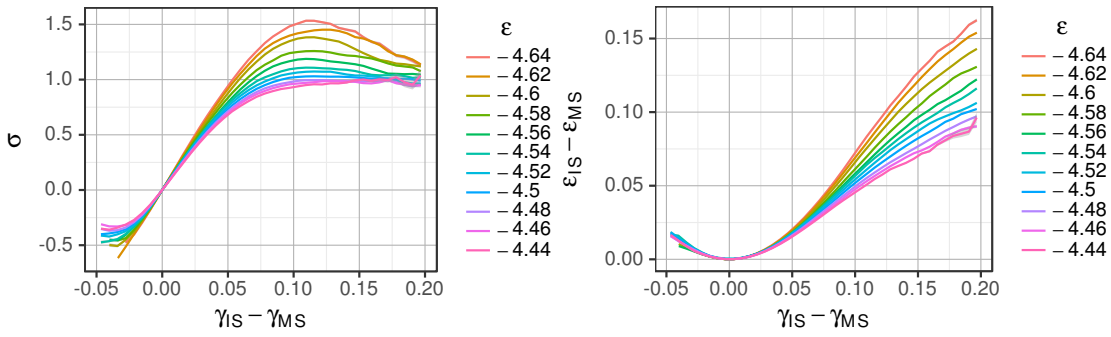

(a) Stress (b) Energy

Figure 4.3: (a) IS stress σ_{IS} and (b) energy difference between IS and MS $\epsilon_{\mathrm{IS}} - \epsilon_{\mathrm{MS}}$ with respect to the strain offset between IS strain and MS strain $\Delta\gamma = \gamma_{\mathrm{IS}} - \gamma_{\mathrm{MS}}$. We used data from start-up simulations at different initial energies $\epsilon_{\mathrm{start}}$ as well as data from the flow regime to increase statistics over a broad energy spectrum. All simulations had a low temperature $T = 0.01$ and $N = 130$.

to the underlying MS. The results can be seen in fig. 4.3. Similar to the normal behavior at the start-up, we also see a stress overshoot within a single MS. However, for the average value for large strains, is at $\sigma = 1.0$ in contrast to the flow regime, where we have $\sigma \approx 0.75$. This means, that we have a similar distribution of IS events, as in the case of the normal overshoot, but this time the drops are somewhat smaller (see also section 3.2.7), so that a higher stress is maintained, which is eventually released at the next MS transition. For completeness, we also show the average energies during a single MS in fig. 4.3b, which also behaves similar to what can be seen during the overshoot. We remark, that despite this overshoot behavior, IS transitions within a MS do not affect reversibility. As we pointed out in section 3.2.4, we find the MS by a process, which is equivalent of an AQS simulation in the reverse shear direction. Similarly to our findings, it is even possible to detect fully reversible avalanches in cyclic shear [Fiocco et al., 2014].

4.2 Two kinds of MS Transitions

Despite the findings of the last section, where we have seen, that even within a single MS, we find a stress overshoot caused by IS transitions, we will now look at the relevance of the first MS transition. We call the position of the first MS transition γ^1_{MS}. Looking at the change of properties at γ^1_{MS} in fig. 4.4, we immediately notice that some crossover behavior appears in the vicinity of $\gamma^1_{\mathrm{MS}} \approx 0.1 =: \gamma_{\mathrm{c}}$. To increase statistics, we simulated at multiple low temperatures, where we see no immediate temperature dependence. First, we notice, that before γ_{c}, the change in the MS energy at the transition is negligible, while it rises linearly afterwards. Similarly, the strain difference between the first and second MS is very small and then rises linearly at $\gamma^1_{\mathrm{MS}} > \gamma_{\mathrm{c}}$. Here, we repeat that the MS represents the state, which is also found by doing an AQS simulation in the direction of the lowest stress, thereby completely releasing the stress in the system. Therefore, if we regard the IS as a sheared state of the MS, then the MS strain gives us the amount, we have strained our system. As both the MS energy and the MS strain are more or less equal for $\gamma^1_{\mathrm{MS}} < \gamma_{\mathrm{c}}$, we would expect that these two MS are very close to each other in

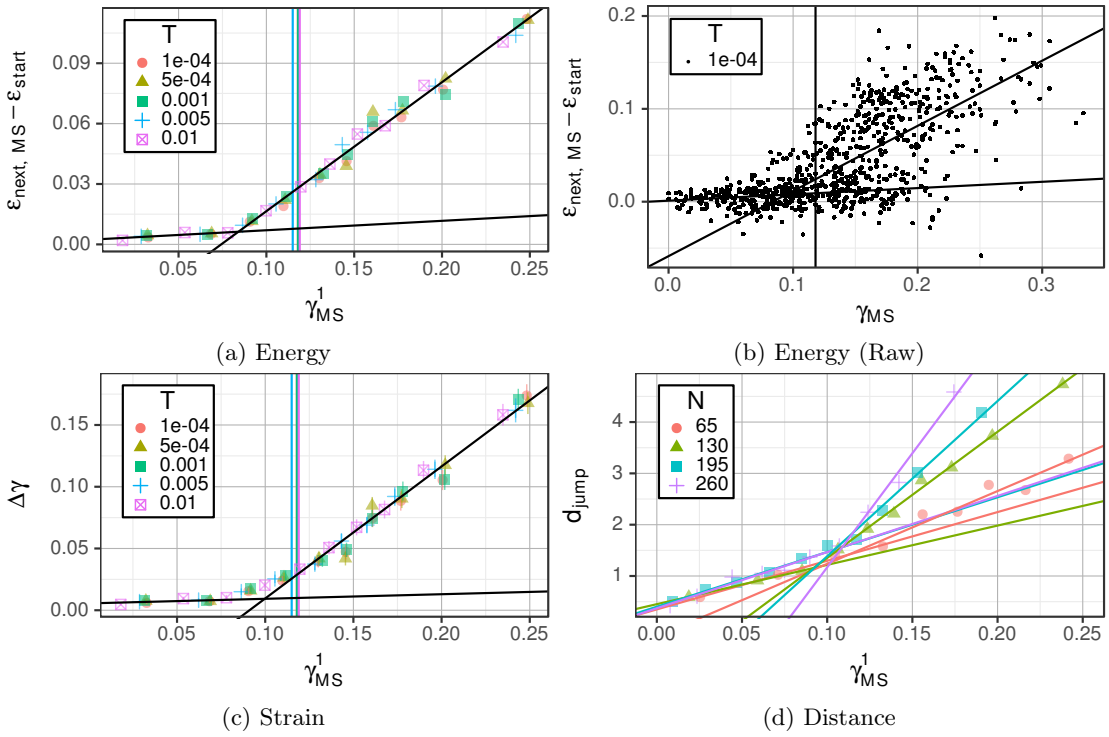

(a) Energy

(b) Energy (Raw)

(c) Strain

(d) Distance

Figure 4.4: Change of MS-properties at γ^1_{MS}, i.e. the position of the first MS-transition. (a) Change in MS energy. Intersection point: $\gamma^1_{\text{MS}} = 0.08$. (b) Raw data of (a) without averaging per γ^1_{MS}. (c) Change in MS strain. Intersection point: $\gamma^1_{\text{MS}} = 0.10$. In (a)-(c), the vertical lines show the position of the stress overshoot maximum. The other black lines show linear fits for $\gamma^1_{\text{MS}} \leq 0.075$ and $\gamma^1_{\text{MS}} \in [0.1, 0.25]$. (d) Euclidean distance between first and second MS. Intersection point: $\gamma^1_{\text{MS}} = 0.10$. The solid colored lines represent fits to $\gamma^1_{\text{MS}} \leq 0.09$ and $d_{\text{jump}} \geq 1.5$. The jump distance after the intersection point scales roughly by N, where the slope is given by $m = 0.183(13)N$. Unless specified otherwise, simulations have been performed at low $T \leq 0.01$, $N = 130$ and $\dot{\gamma} = 10^{-4}$ having $\epsilon_{\text{start}} = -4.6$.

the energy landscape and have similar properties, especially regarding the shear modulus.

Looking at the raw data in fig. 4.4b, we find that only by averaging the energy difference as a function of γ^1_{MS}, we see a sharp transition at γ_{c}. Otherwise, we see a rather long crossover regime, where both kinds of transitions seem to mix. For a good statistical evaluation of an absolute lower limit, where we start to see events which significantly change the MS energy, we have not enough data available. However, it might be slightly lower than the average crossover value γ_{c}.

Lastly, we look at the euclidean distance between the first two MS, where we find a similar crossover at γ_{c}. By showing the data for different system sizes, we see not only, that the crossover position is constant across all tested N, but also that the system size dependence vanishes for $\gamma^1_{\mathrm{MS}} < \gamma_{\mathrm{c}}$. For $\gamma^1_{\mathrm{MS}} > \gamma_{\mathrm{c}}$, the system size dependence is almost trivial, as the scope scales trivially with $m = 0.183(13)N$.

Overall, our analysis gives rise to two different kinds of MS transitions, one significant for the further evolution of the system and an insignificant one. At γ_{c}, which is before the stress overshoot peak position, we see that the significant transitions take over the overall average behavior of key observables. The existence of an early crossover before the overshoot point reminds us of simulations and experiments of cyclic shear ([Fiocco et al., 2013], [Kawasaki and Berthier, 2016], [Regev et al., 2015], [Leishangthem et al., 2017]). In a cyclic shear simulation, the system may enter a limit cycle after a number of cycles, which is in turn dependent on the system size. In the limit of large systems and many realizations, there exists a lower limit of γ_{max}, where limit cycles are always found. We call this strain γ_{nl}, which is typically around 0.07 for our model glass former [Leishangthem et al., 2017]. Other models and methods yield values around 0.115 [Regev et al., 2015] and 0.0885 [Kawasaki and Berthier, 2016]. We refer to chapter section 5.4 for a more detailed analysis of γ_{nl} and its system size scaling.

Previously, we argued, that slightly before γ_{c}, there is a point where no MS transition seems to have an impact on the relevant PEL properties. This point could be directly connected to γ_{nl}, as it marks the lowest limit for limit cycles. Another similarity between both crossovers besides the position and the semantics is the system size dependence. In [Regev et al., 2015] and [Leishangthem et al., 2017], a strong change in the system size dependence has been observed at γ_{nl}, which is attributed to avalanches. The authors made the connection to avalanches via an observed change in the system size scaling of the average cluster size during a transition, changing from a constant to a $N^{\frac{1}{3}}$ scaling. However, although we have not analyzed the cluster size dependence at the MS transitions, we find a similar strong change in the system size dependence in the euclidean distance from a constant to N (see fig. 4.4d).

With respect to the properties of the sheared energy landscape, we further note, that a similar value for d_{jump} at γ_{c} was also found in section 3.1.2, which was the average distance between IS for metabasins with $\epsilon_{\mathrm{MB}} = -4.6$. The comparison for particle positions in two different MS before and after a jump is valid, as due to $\Delta\gamma \approx 0$ at γ_{c} we are in a similar reference frame. We argued, that IS with a distance of $d < 1.5$ to the deepest IS of a metabasin, are still in the energetically low center of the metabasin, supporting our findings here for transitions with $\gamma_{\mathrm{MS}} < \gamma_{\mathrm{c}}$.

One special property of our simulations is the starting structure, as all simulations were started at the bottom of metabasins (see section 2.6). Therefore, they show no relaxation behavior towards lower energies, which in turn can be observed when starting at higher energies [Fiocco et al., 2013]. In our picture, this kind of relaxation would trivially be associated with a structure changing MS transition, thus changing or removing the crossover when starting at other configurations as

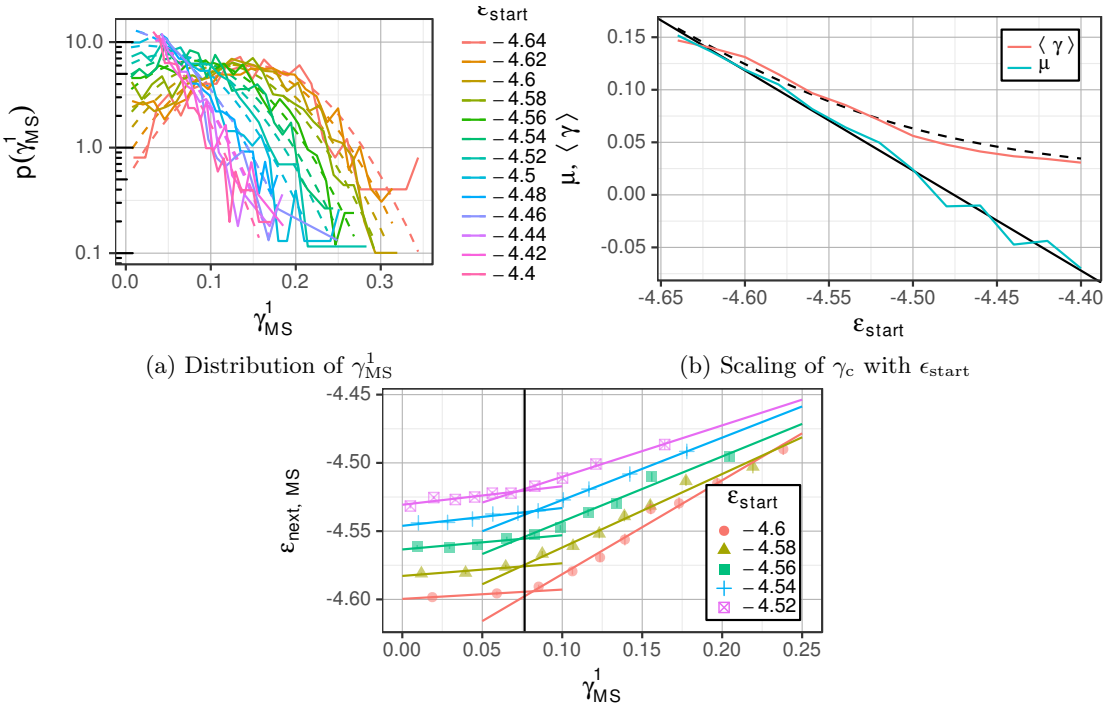

(a) Distribution of γ^1_{MS}

(b) Scaling of γ_c with $\epsilon_{\mathrm{start}}$

(c) Energy after a MS transition at γ^1_{MS}

Figure 4.5: (a) Distribution of γ^1_{MS}. The solid colored curves represent fits with a cut off Gaussian distribution to the data. (b) Parameterization of the γ^1_{MS} distribution. The blue line shows the fit parameter μ. The black straight line represents a fit to these values with a slope of $-0.953(28)$ and an intercept of $-4.26(13)$. The red line shows the average value of γ_{MS}, calculated directly from the distribution. From the linear fit of μ, we also calculated the average γ_{MS}, which is shown as the black dashed line. For all cut off Gaussian distributions, we used a fixed $\sigma = 0.0675$, which we determined as the mean fit parameter for the lowest $\epsilon_{\mathrm{start}}$. (c) Euclidean jump distance at γ_{MS} in the MS trajectory for different initial energies $\epsilon_{\mathrm{start}}$. The vertical line marks the position of the average crossover at $\gamma = 0.0765(46)$.

the bottoms of metabasin.

We close this section with a remark, that the detection of γ_{nl} requires finding a limit cycle and the time to find such a cycle diverges at γ_{nl}. Therefore, it might prove advantageous to further study γ_c, as it only requires simulations of small systems during the overshoot, i.e. $\gamma \leq 0.5$.

4.3 Crossover Scaling

This short section will describe the scaling behavior of the γ_c for different initial energies $\epsilon_{\mathrm{start}}$. First, we look at the distribution of γ^1_{MS} in fig. 4.5a. We see, that the distribution for each $\epsilon_{\mathrm{start}}$ resembles a Gaussian, which is cut off at $\gamma^1_{\mathrm{MS}} = 0$, as obviously the first transition occurs afterwards. Therefore, we have fitted the data with Gaussian distribution, which is cut off to the left and normalized properly, leading to the position of a maximum μ and a scaling parameter

σ. The parameter μ has a linear dependency on ϵ_{start}, as can be seen convincingly in fig. 4.5b. Furthermore, in the same plot, we show the average position first MS transition, which also clearly scales with the starting energy. On the other hand, looking at fig. 4.5c, we find no such strong scaling for the crossover position in the energy data.

In terms of the PEL we know that the number of states increases approximately exponentially towards higher energies [Doliwa and Heuer, 2003b]. This explains easily the scaling of μ towards earlier MS transitions at higher energies. However the constant position of the energy crossover may be attributed to the MB size, as we found in section 3.1.2 that the MB size changes only slightly with the energy.

4.4 Yielding

In literature, there exist different definitions of the yield point. For stress controlled measurements, the yield point can simply be defined as the point where the strain rate at constant stress becomes non-zero. The yield stress would then be defined as the stress at this discontinuity [Bonn et al., 2017]. At least for metallic glasses, it follows the relationship $\sigma_y = G\gamma_y$, with the shear modulus G and a yield strain of $\gamma_y = 0.0267(20)$ [Johnson and Samwer, 2005], which may however be temperature dependent. For colloids this kind of yielding can be described in terms of a percolation transition, where clusters of particles with large non-affine displacement form a percolated network on yielding [Ghosh et al., 2017].

In strain controlled experiments and simulations, it is much more difficult to define a yield point, as there is no such pronounced discontinuity. As there is a crossover from elastic to flowing behavior, the yield point should happen during the overshoot. So the first and most easily accessible observable here is the position γ_{ov} and height of the stress overshoot σ_{ov}. However, elasticity is characterized mainly by reversibility, so when shearing back an elastic system, all particles should be at the same positions. In oscillatory shear, it can be shown that irreversible plastic events happen before γ_{ov} [Leishangthem et al., 2017], making other definitions of a yield point necessary.

The first candidate for a yield point, is a rheological crossover γ_{rh}, which is found in oscillatory sheared systems as the point where the storage and loss modulus are equal. It was reported, that an anisotropy appears in the structure factor at $\gamma_{\text{max}} > \gamma_{\text{rh}}$ [Denisov et al., 2015], which could not be reproduced by simulations [Kawasaki and Berthier, 2016]. The latter work compared different methods of detecting yield points in oscillatory shear and found, that three different methods find approximately the same value. The first method uses the previously described γ_{nl}, the second finds the divergence point of the waiting time for a limit cycle as a function of the oscillatory amplitude γ_{max} and the third one finds the maximum stress amplitude in response to a given γ_{max}. In all cases, γ_{nl} was much smaller than γ_{rh}.

Another recent approach was given in [Jaiswal et al., 2016] and [Parisi et al., 2017], where the yield point was defined via an overlap function Q. Starting from an initial ensemble of states within close proximity[1], the yield point was defined as the position when half of the population have stopped overlapping, which was seen in the distribution of Q. This method can be seen in

[1] The authors describe this as a *metabasin* without giving a definition, or bringing this in context with previous definitions of metabasins. The preparation procedure brings these structures close together without the possibility of normal structural relaxation. However, as they start at a strong non-equilibrium condition, they have to observe some form of aging during their preparation. As aging by itself is an irreversible process, their initial structures could span different metabasins using our definition.

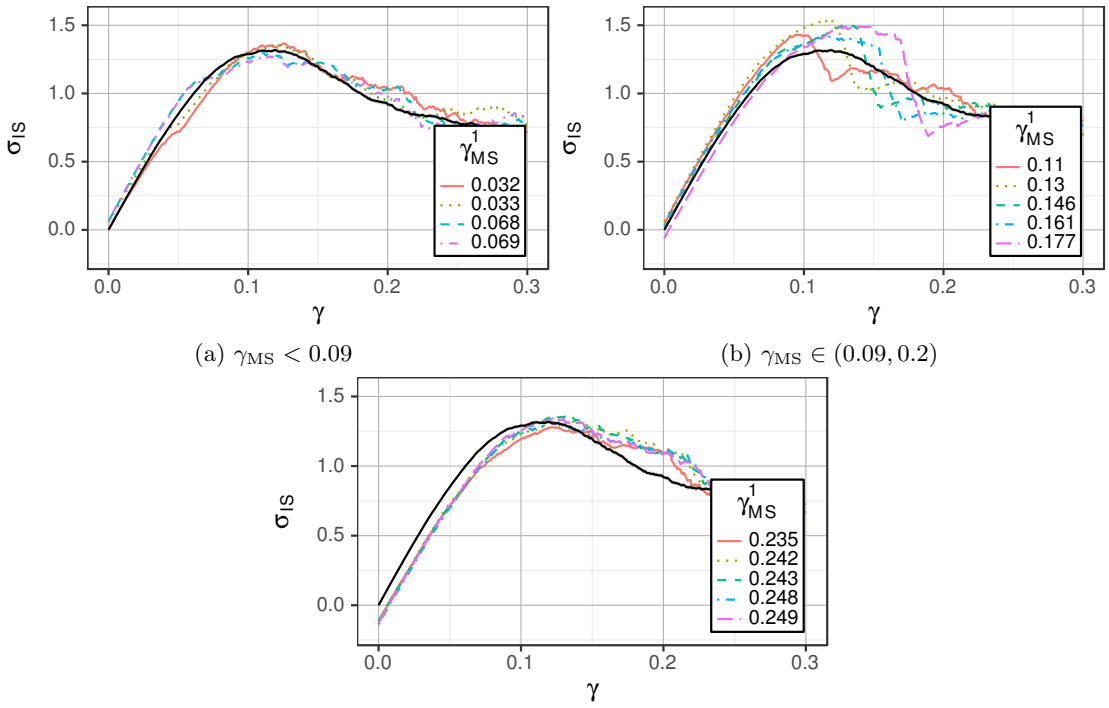

(a) $\gamma_{\mathrm{MS}} < 0.09$

(b) $\gamma_{\mathrm{MS}} \in (0.09, 0.2)$

(c) $\gamma_{\mathrm{MS}} > 0.21$

Figure 4.6: a) Stress of sub-ensembles with a given strain $\gamma_{\mathrm{MS}} < 0.09$. Show are trajectories for temperatures $T \in \{1 \cdot 10^{-4}, 5 \cdot 10^{-4}\}$. b) The same for $\gamma_{\mathrm{MS}} \in (0.09, 0.2)$ and $T = 10^{-4}$. c) For $\gamma_{\mathrm{MS}} > 0.21$ we plot all available values for $T \in [10^{-4}, 10^{-2}]$. The solid black curve shows the ensemble average at $T = 0.01$, $N = 130$ and $\dot{\gamma} = 10^{-4}$ as a reference.

resemblance to the method of analyzing chaotic systems with a Lyapunov exponent. As a result, the yield point marks a position, where the starting configurations begin to drift apart from other configurations in the same initial ensemble. One can observe, that there are strong finite size effects involved using this method even at systems as large as $N = 10000$ in 2D. In the [Procaccia et al., 2017], a scaling with $\sqrt{N}$ has been reported, which places the yield point at a position unrelated to the overshoot position (see [Procaccia et al., 2017] FIG. 6 and FIG. 8).

Similar to the findings for colloids in stress controlled experiments, a directed percolation transition was also observed in strain controlled simulations of Lennard-Jones particles [Shrivastav et al., 2016b], which can also be identified as a yield point with $\gamma_{\mathrm{perc}} \approx 0.07$. They also found, that this percolation transition precedes shear band formation and going further into the flow regime, further percolation transitions happen at a constant rate.

In comparison to these definitions of yield points, we will now look closer at what happens with the stress at the first MS transition γ^1_{MS}. Therefore, we analyze for each γ^1_{MS} the specific sub-ensemble of trajectories. The results are shown in fig. 4.6. For $\gamma^1_{\mathrm{MS}} < \gamma_c$, we notice that the stress in the sub-ensembles is very similar to the complete ensemble average. This means, that the later evolution of the system stress is unrelated to the early MS transitions, which further strengthens our argumentation from the last section. Furthermore, the stress drop at the MS transition has to be similar to a normal IS transition. This is in contrast to the normal case,

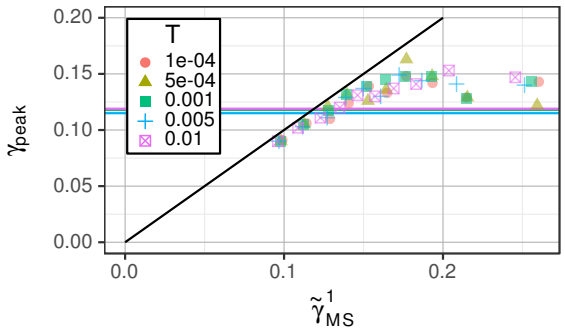

Figure 4.7: Average stress overshoot peak position for all trajectories with $\tilde{\gamma}^1_{\mathrm{MS}}$ at a given strain. The solid black line reflects the diagonal as a guide for the eye. Each point in this plot represents 10% of the trajectories for a given temperature.

where there is usually a large stress drop associated with a MS transition compared to the IS transitions (see section 3.2.7). However, for $\gamma_c < \gamma^1_{\mathrm{MS}} < 0.2$, we see the strong correlation of a stress drop at approximately the position of γ_{MS}. Also, we observe that the stresses are kept at a high level before the final stress relaxation occurs. At even higher stresses, it is also possible to see a slight stress overshoot. Both findings are compatible with our results in section 4.1, where we saw that a stress overshoot might occur from IS transitions alone and that the average stress for high $\Delta\gamma$ within the same MS is 1.

The analysis of the sub-ensembles brings us into a position, where we can analyze the position of the stress peak for each sub-ensemble with respect to γ^1_{MS}. We explicitly exclude MS transitions with $\gamma^1_{\mathrm{MS}} < \gamma_c$, as we determined that on average, they have no significant impact on the overshoot [2]. Instead, we will search the first MS transition with $\gamma^1_{\mathrm{MS}} > \gamma_c$ for each trajectory and call it $\tilde{\gamma}^1_{\mathrm{MS}}$. The resulting stress overshoot peak position with respect to $\tilde{\gamma}^1_{\mathrm{MS}}$ can be seen in fig. 4.7. We see that the peak for early $\tilde{\gamma}^1_{\mathrm{MS}}$ is approximately at the same position as the MS transition. However proceeding to larger $\tilde{\gamma}^1_{\mathrm{MS}}$, we start to see the stronger influence of IS transitions, causing an overshoot to appear and finally limiting the overshoot position to approximately $\gamma_{\mathrm{peak}} = 0.15$, which is above peak position of the ensemble average. As pointed out in section 4.1, this overshoot does *not* contradict reversibility.

In conclusion, we can describe the process of yielding via the properties of the extended PEL $V(\mathbf{x}, \gamma)$. MS transitions are an irreversible process in terms of AQS shear and can be used do define the yield point. However, we have seen that there are some MS transitions which are insignificant, as they change neither the MS energy, nor the MS strain and have no impact on the stress overshoot. On average, the significant MS transitions become relevant at a strain of $\gamma_c = 0.1$, which is slightly before the ensemble averaged stress overshoot peak position. The influence of MS transitions on the stress overshoot, however, is more complex and also involves the evaluation of IS stress drops within a single MS. This is seen especially for late MS transitions with $\gamma_{\mathrm{MS}} > 0.15$, which display a broad stress overshoot but are completely reversible.

[2] As we have seen in section 4.2, there may be earlier MS with a significant transition and later events with an insignificant transition, but they do not seem to have a large impact on our statistics.

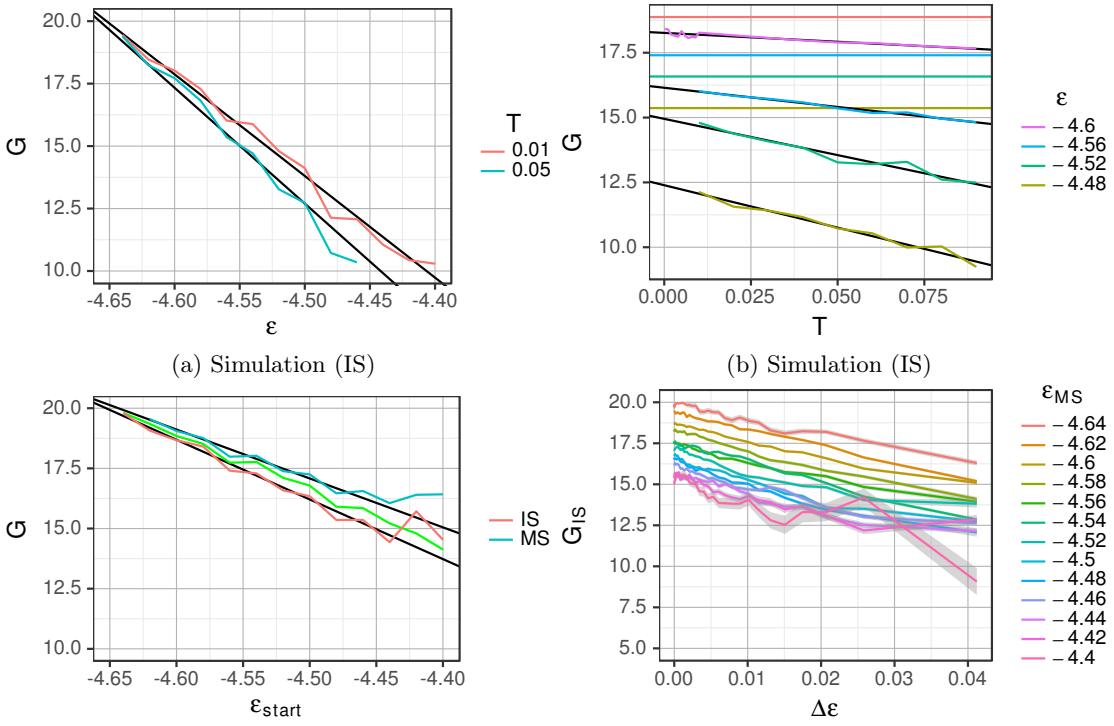

(a) Simulation (IS)

(b) Simulation (IS)

(c) AQS (first IS/MS)

(d) AQS (start+flow)

Figure 4.8: Shear modulus for different starting energies and temperatures. (a) G determined by linear fit to IS stress-strain curve at start of simulation ($\gamma \in [0, 0.01]$) with fixed ϵ_{start} at low temperature. The black lines represent linear fits to the data. (b) Temperature dependence of G at different ϵ_{start}. The smallest simulated temperature is $T = 0.0001$ for $\epsilon_{\text{start}} \approx -4.6$. The black lines are linear fits to the data and the horizontal colored lines show the IS strain as calculated in (c). (c) G computed using the AQS protocol, i.e. an affine transformation ($\gamma \in [-0.001, 0.001]$) followed by minimization. The green line shows the expected G_{IS}, by correcting G_{MS} by multiplying the mean energy difference $\langle \epsilon_{\text{IS}} - \epsilon_{\text{MS}} | \epsilon_{\text{start}} \rangle$ with the fitted slope from (d). (d) Dependence of G on the energy difference $\Delta\epsilon$ between IS and MS. In this last plot, we included startup data from all low temperature runs with $\gamma \in [0, 0.05]$ for statistical reasons and show only data points with more than 20 samples per bin. The mean slope of G_{IS} for $\delta\epsilon \in [0, 0.02]$ and $\epsilon_{\text{MS}} \leq -4.5$ is $-121.5(3.5)$.

4.4.1 Shear Modulus

The shear modulus for start-up shear is strongly affected by the preparation of our start structures in the equilibrium and therefore depends on the starting energy ϵ_{start}. We will now compare two different methods for the calculation of the modulus and also analyze the temperature dependence of the modulus. The first method uses the first part of the simulation run $\gamma \in [0, 0.01]$ and determines the slope of the stress-strain curve via linear fit. To exclude effects from the fit, we verified that for a maximum $\gamma_{\text{max}} \in [0.002, 0.015]$ the shear modulus remains constant. We use stress from the IS trajectory instead of the complete stress term to exclude effects from stress fluctuations caused by the temperature, which is already very low at $T = 0.01$. Shown in fig. 4.8a is the linear dependence of G on the starting IS energy ϵ_{start}. The stiffening towards lower ϵ_{start}

is expected and compares well to experiments [Wang, 2012], as the starting energy not only corresponds the the temperature before the quench [Lacks and Osborne, 2004], but also to the age of the system [Shrivastav et al., 2016a]. As we can see, there is still a small temperature effect, probably caused by minor IS jumps (see section 4.1) within the first MS, thereby reducing the stress and leading to a smaller G. We note in passing, that the systematic fluctuations in fig. 4.8a are caused by using the same starting configurations for all temperatures.

The effect of temperature is further analyzed in fig. 4.8b. We see a linear behavior of G on the temperature, with only minor changes, when approaching $T = 0$, compared to $T = 0.1$. However, this maximum modulus is still smaller than what would be expected in AQS simulations, which corresponds to the zero-temperature limit. Therefore, our second method for calculating the modulus will be a method involving AQS shear. In AQS simulations, the stress-strain curve is determined by an affine transformation, followed by a minimization. We used 4 samples with a maximum strain difference $\Delta\gamma = 0.001$ to determine G with a linear fit, which is sufficient for our purpose. This distance between the AQS modulus and the simulation determined zero-temperature modulus grows with higher ϵ_{start}. We believe that this softening is caused by the distance of the starting IS to the MS including IS transitions and non-linear behavior.

The results for the AQS method are explored systematically in fig. 4.8c. There, we see a similar linear dependence on ϵ_{start}. However, we also explore the shear modulus at the first minimized structure, calculated from the first IS. There is a systematic difference between the G_{IS} and G_{MS}, increasing with the starting energy.

Even for our small system, the shear modulus changes with energy. This change is linear, as can be seen in fig. 4.8d. We have plotted data from the start of our simulations, as there might be some differences between data from the startup and in the flow regime. In section 2.6, we calculated the energy difference between IS and MS of our starting structures. Using this mean energy difference $\langle \epsilon_{\text{IS}} - \epsilon_{\text{MB}} | \epsilon_{\text{start}} \rangle$, we can now calculate the effect of the change in G with energy on the MS shear modulus. The result is shown in fig. 4.8c. It turns out, that this difference would account for approximately half of the difference in G.

We remark, that the IS used in fig. 4.8c are found by equilibrium simulations, whereas in fig. 4.8d we naturally include IS found by shearing the initial IS. Experimental values for the temperature dependence of the shear modulus in the $Ni_{80}P_{20}$ metallic glass, which is our model glass former is based on, are hard to find. For example, [Wang et al., 2003] and [Johnson and Samwer, 2005] both report the shear modulus for different metallic glasses. For the $Ni_{80}P_{20}$ metallic glass, a shear modulus of 36.9 GPa has been derived from ultrasonic measurements at room temperature using the Debye-model. This value corresponds to 31.9 in reduced units and is thereby approximately twice as high, as we would expect from our data. For a Zr based bulk metallic glass (BMG), the temperature dependence was reported in [Wang et al., 2003] and for a Ce based BMG in [Zhang et al., 2007]. However for these glasses, the shear modulus is only temperature dependent for $T > 0.9T_g$, which differs from our findings. The deviations of our simulation data and experiments are yet unclear and still need further research. We believe, that it may originate in the different derivation methods of the shear modulus.

4.5 A Toy Model for the Stress Overshoot

A model to characterize the stress overshoot based on *free-volume theory* [Spaepen, 1977] and *shear transformation zones* (STZ) [Argon, 1979] is given in [Jiang et al., 2015]. This model, being

an extension of previous works, for example [Lemaître, 2002, Falk and Langer, 1998], describes to a very good degree the shape of the stress overshoot as well as other rheological features of metallic glasses and other amorphous materials. At this point, however, we are interested in a description of the stress overshoot in terms of the potential energy landscape, as we have no direct access to free volume with our Lennard-Jones glass former. Our model will be purely based on the new concept of MS transitions, and therefore reveals how much of the information of the stress overshoot is already contained in the MS transitions and how much is missing from having ignored IS transitions.

In the most simple version of our model, we increase the stress linearly with the strain, according to a shear modulus, which is selected with respect to the initial energy. With a probability of $p(\gamma_{\mathrm{MS}})$, we would then have a transition. In section 4.3, we found that the distribution $p(\gamma_{\mathrm{MS}})$ is a cut off Gaussian distribution and already determined the fit parameters. After the MS transition, we assume that all trajectories completely decorrelated and have a stress of $\sigma_{\mathrm{flow}} = 0.75$. As a shear modulus, we use the *effective* shear modulus, which depends on the initial energy. We use the respective data and fit from section 4.4.1, where we have analyzed the effective shear modulus at the start of shear simulations. The parameters for the linear fit of the modulus with respect to $\epsilon_{\mathrm{start}}$ are slope $= -42.5(1.7)$ and intercept $= -177.6(7.6)$. The equation for the time evolution for the ensemble average of $\sigma(\gamma)$ then looks like:

$$\langle\sigma|\gamma\rangle = \langle G|\epsilon_{\mathrm{start}}\rangle\gamma p(\gamma < \gamma_{\mathrm{MS}}) + \sigma_{\mathrm{flow}} p(\gamma \geq \gamma_{\mathrm{MS}}) \tag{4.4}$$

The results from this equation are shown in fig. 4.9a. We see, that the height of the overshoot is slightly overestimated, as would be expected from the fact that there are unaccounted IS transitions within the first MS, which we described in section 4.1. Furthermore, the influence of the shear modulus at the start of the simulations is very low and we see a strong dependence of the overshoot position on $\epsilon_{\mathrm{start}}$, which is not consistent with the real overshoot simulation data. However, the length and the form of the overshoot is well resolved, even in this very simple model.

In our most simple version of the model, we have assumed, that all systems are perfectly decorrelated after the first MS transition and specified a fixed σ_{flow}. Now, we make a slight variation of this model. We start the simulation of a single trajectory at $\sigma = 0$ and $\epsilon_{\mathrm{MS}} = \epsilon_{\mathrm{start}}$. Then, we select the points of MS transitions for this single trajectory randomly via $p(\gamma_{\mathrm{MS}})$. After the first transition, we assume, that we have already reached the flow regime for this trajectory, and select $\epsilon_{\mathrm{MS}} = -4.5$. We also reset σ to zero. Between MS transitions, we assume that, the stress rises according linearly with respect to the shear modulus. However, this time we select the AQS shear modulus. The parameters for the linear fit of the modulus with respect to $\epsilon_{\mathrm{start}}$ are slope $= -20.5(1.3)$ and intercept $= -75.3(6.0)$. After evaluating 2^{15} trajectories, we arrive at the ensemble average shown in fig. 4.9b. We find in contrast to the first model, this one captures the initial effective shear modulus better and also removes the overshoot for $\epsilon_{\mathrm{start}} < -4.5$. Also, it produces equally well the form of the overshoot while automatically finding a good approximation of the flow stress. However the overshoot height is still overestimated, as IS transitions during a single MS reduce the stress. These transitions also move the overshoot position, removing the overshoot position dependence, which is still visible for high $\epsilon_{\mathrm{start}}$. We remark, that reducing the stress to zero after each transitions, is in strong contrast to simulations at $N = 130$, where the stress after a transition usually starts at a random value with a mean of $\sigma_{\mathrm{next}} = 0.38$. However, going forward to the flow regime, we will find another example in section 6.5, where we can neglect σ_{next} with a possible explanation.

Overall, we find that both models reproduce the energy dependence of the stress overshoot quite well without having further adjustable parameters.

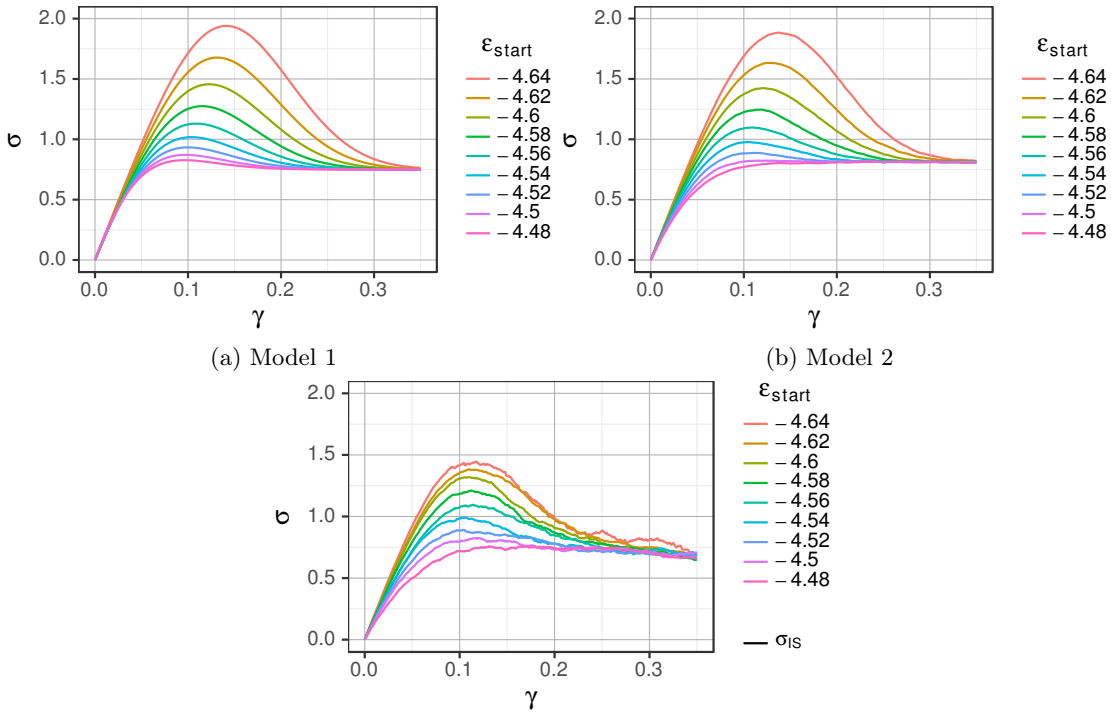

(a) Model 1

(b) Model 2

(c) Simulation

Figure 4.9: (a) and (b): Two variations of a simple model reproducing the stress overshoot using $p(\gamma_{\mathrm{MS}})$ and $\langle G|\epsilon_{\mathrm{MS}}\rangle$. See text for a description of each model. As a reference, we plot in (c) simulation data for $T = 0.1$, $N = 130$, and $\dot{\gamma} = 10^{-4}$.

4.6 Summary

In summary, we could show, that the energy landscape has a strong influence on the overshoot and on yielding in general. With regard to the stress overshoot, we have seen that the overshoot height depends linearly on the initial energy. This connection was reported in literature in terms of aging and explained by Eyring's model of stress-assisted activation, which is very similar to the picture of the sheared energy landscape.

Furthermore, we could show that the first MS transition during start-up shear already has a large influence on the overshoot and yielding. It specifies the exact point per trajectory, where the system can not return to the starting structure via AQS shear in the reverse shear direction. Furthermore, we found that there are two kinds of MS transitions, differing by their influence on the MS energy, the MS strain and the particle movement. In particular, the MS energy and MS strain are mostly unaffected by the first kind of MS transition. Also, these MS transitions have no effect on the resulting stress-strain curve. Thereby, these transitions are irrelevant in terms of yielding. The underlying cause for these irrelevant transitions have to be multiple nearby IS at the bottom of the metabasin with similar properties. The distribution of the first MS transition was identified with a cut off Gaussian distribution, with showed a linear dependence of the position with the maximum probability on $\epsilon_{\mathrm{start}}$. We attributed this dependence on the increased number of states at high energies. In contrast, the average crossover between both

types of MS transitions shows no strong dependence on the initial energy ϵ_{start}. This behavior may be related to other structural properties of the PEL, e.g. the MB diameter. In comparison with cyclic shear, we can say that if at zero temperature there is no *relevant* MS transition in either shear direction up to a γ_{max}, the system behaves fully reversible and produces limit cycles. We note, that during cyclic shear, there may be multiple MS transitions, before a limit cycle is reached. If the MS transition happens late, i.e. at $\gamma_{\text{MS}} = 0.15$, there may also appear a stress overshoot within the first MS, which is broader than usual. However, this is caused by stress/energy relaxations at IS transitions and is fully reversible. Furthermore, we looked at the shear modulus at the start of the simulations and found not only a strong dependence on the temperature and the starting energy, but it also differed much, if the shear modulus was analyzed at the initial MS or in the ensemble average over the IS trajectories. We concluded that there must be non-linear effects or plastic events already between the starting IS configuration and the starting MS.

Finally, we presented a simplified toy model, which could reproduce key features of the stress overshoot using only the parameterization of the γ_{MS} distribution and a linear energy dependence of the MS shear modulus.

Chapter 5

Cyclic Shear

In chapter 4, we have compared the first MS transition with the results from cyclic shear. In this chapter, we will therefore analyze cyclic shear for our $N = 130$ system in more detail. Our interest lies in particular on the PEL properties of the reversal point and their predictive power on the reverse overshoot. Furthermore, we will compare the cycle statistics for low temperature cyclic shear with AQS statistics, finding that already small temperatures break the limit cycles. In the last section, we further explore reversibility after the first MS transition by using AQS shear.

5.1 Cyclic Shear Simulations

Cyclic shear simulations are very similar to our simulations for shear start-up. For all simulations, we have used a fixed initial energy $\epsilon_{\text{start}} = -4.6$ and a constant strain rate $|\dot{\gamma}| = 10^{-4}$. However at a given $\gamma = \gamma_{\text{max}}$, we reverse the shear direction and the system then evolves in the reverse direction. This change in direction happens immediately, as we are using the SLLOD algorithm and all momenta are stored relative to the sheared frame. When the strain reaches $\gamma = -\gamma_{\text{max}}$, the shear direction is reversed again. Similar to [Fiocco et al., 2013], we define the *accumulated*

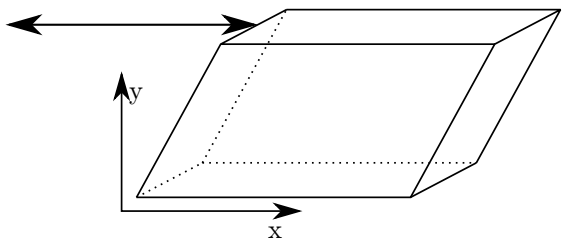

Figure 5.1: Sketch showing the deformation of the simulation box during cyclic shear. With a fixed x-z plane at the bottom, the top x-z plane moves in x direction.

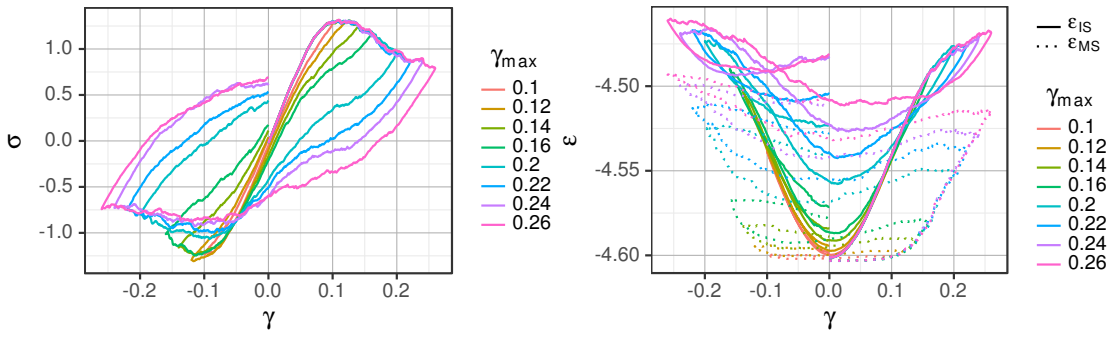

(a) (b)

Figure 5.2: Stress-strain curve (a) and energy-strain curve (b) for sheared runs at $T = 0.01$, $N = 130$, $\dot{\gamma} = 10^{-4}$, reversing the shear directions at $\gamma_{\max}$. The runs start at $\gamma = 0$ with a positive $\dot{\gamma}$. At $\gamma = \gamma_{\max}$, the sign of $\dot{\gamma}$ changes until $\gamma = -\gamma_{\max}$ is reached. At this point the sign of $\dot{\gamma}$ changes again.

strain γ_{acc} as the absolute sum over the strain:

$$\gamma_{\text{acc}} = \int_0^t |\dot{\gamma}| t \mathrm{d}t' \tag{5.1}$$

With this definition, a whole cycle is reached at $\gamma_{\text{acc}} = 4\gamma_{\max}$. This definition is useful, as it scales with respect to the time and also the shear rate, just like γ in non-cyclic shear.

5.2 Reverse Overshoot

When a system is sheared, starting from equilibrium configurations, we see a stress overshoot. We have seen in chapter 4, that the height of this overshoot depends on the starting energy ϵ_{start}. Reversing the shear direction at a fixed $\gamma_{\max}$ results in yet another overshoot with negative σ. The height of this overshoot depends greatly on the chosen $\gamma_{\max}$ and, of course, on the initial ϵ_{start}. In [Lacks and Osborne, 2004] this effect was described qualitatively in terms of aging and mechanical rejuvenation using the IS energy. We will now use the additional information of the MS energy, to give a quantitative prediction of the reversal overshoot.

In fig. 5.2a, we see the dependence of the reversal overshoot on $\gamma_{\max}$ in the stress-strain curve of the ensemble averaged stress. Comparing with the energy-strain curve, we notice, that the minimum energy after the reversal depends also strongly on $\gamma_{\max}$. A possible explanation would be, that only a subset of systems has performed a substantial MS jump, similar to the results from section 4.2. Upon reversing the strain, there should be no MS transition until we reach $\gamma = 0$, as we are simulating at low temperature ($T = 0.01$). However, looking at fig. 5.2, this is not completely true, as there is a slight drop in the MS energies. Ideally, if the overshoot only depends on the MS energy at $\gamma = 0$ and not some further history of the sheared system, we can predict the height of the reversal overshoot just from knowledge of the energy. Neglecting the small change in ϵ_{MS} during the reversal, we use the MS energy at the reversal point ϵ_{rev} when comparing the normal overshoot height with the reversal overshoot height in fig. 5.3a. We see a perfect agreement between the reversal overshoot height and the normal overshoot height.

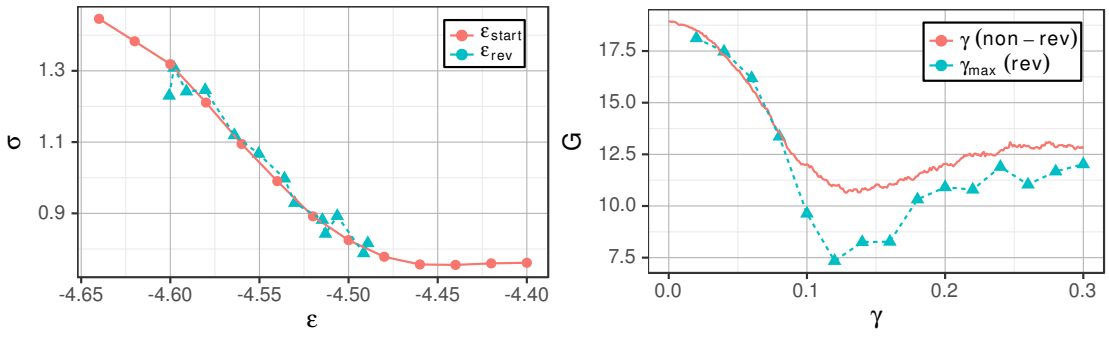

(a) (b)

Figure 5.3: (a) Height of the overshoot after reversing the shear direction in dependence of the mean MS energy at the reversal (blue), compared to the height of the normal non-reversal overshoot in dependence on the starting MS energy (red). Each data point represents an ensemble of runs with fixed $\gamma_{\max}$ and ϵ_{start}. In general, higher $\gamma_{\max}$ correspond to higher ϵ_{rev}, as can be seen in fig. 5.2b. For this plot, we excluded runs with $\gamma_{\max} < 0.1$, as they show no overshoot upon reversal. (b) Shear modulus G directly after the reversal (blue), compared to the mean IS shear modulus in non-reversal simulations. For reversal simulations, the shear modulus is determined via a linear fit on the ensemble averaged stress with a maximum distance of $\Delta\gamma = 0.02$ to the reversal point. The shear modulus for non-reversal simulations is evaluated by a linear fit of the stress-strain curve generated via AQS strain ($\Delta\gamma \leq 0.001$) of particle positions in individual trajectories. The starting energy for the reversal runs in (a) and (b) is $\epsilon_{\text{start}} \approx -4.6$ (see section 2.6). The common parameters for all simulation runs are: $T = 0.01$, $N = 130$, $\dot{\gamma} = 10^{-4}$.

Therefore, we can conclude that the knowledge of ϵ_{rev} alone is sufficient to completely describe the reversal overshoot height.

Next, we look at the shear modulus upon reversing the shear direction. Directly after the reversal, we would expect the number of IS transitions to be small. Therefore, the shear modulus measured by the slope of the stress-strain curve in the ensemble average should be identical to the mean shear modulus, determined via the AQS method for each individual trajectory. In fig. 5.3b, we see that this assumption holds to a good degree. However, in the range $\gamma_{\max} \in [0.1, 0.18]$, the mean AQS shear modulus is approximately 50% higher. We remark, that due to fluctuations, we had to use a much larger interval for the measurement of the ensemble averaged stress-strain curve: $\Delta\gamma \leq 0.02$ compared to $\Delta\gamma \leq 0.001$. This leads to the conclusion, that for single trajectories, the stress during the reversal within this larger interval has to be higher than expected from the AQS shear modulus. Indeed, looking at single trajectories (not shown), we see that the stress may show a plateau or even rise for a short period after an initial drop. This corresponds to the region of $\gamma \approx 0.1$ in the stress-strain curve fig. 5.2a, where the slope is minimal for all $\gamma_{\max}$. Remarkably, this position corresponds well to the average position of the first MS transition from section 4.2.

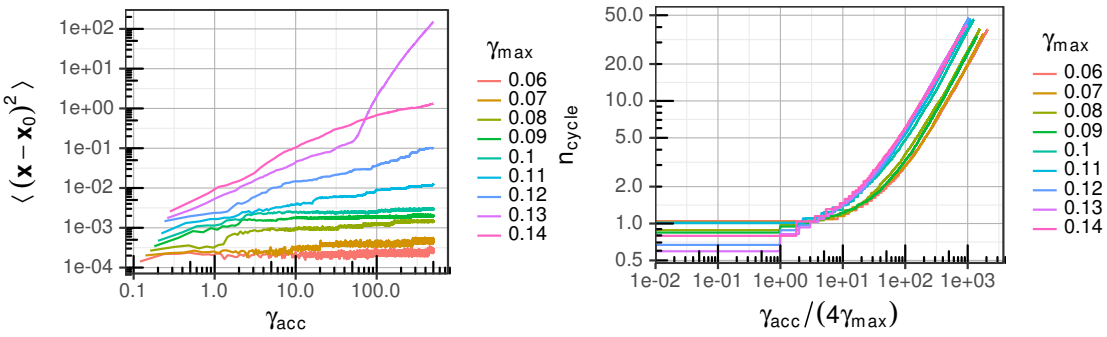

(a) Mean Squared Displacement

(b) Number of Distinct Cycles

Figure 5.4: (a) Mean squared displacement in the IS trajectory along the z axis for reversal runs in dependence of $\gamma_{\max}$. We only show data points for full cycles at $\gamma_{\text{acc}} = n_{\text{cycle}} \cdot 4\gamma_{\max}$. (b) Number of distinct cycles in dependence of the cycle number. Simulation data was generated at $T = 0.01$, $N = 130$ and $\dot{\gamma} = 10^{-3}$.

5.3 Cycle Analysis

5.3.1 Temperature Effects

[Fiocco et al., 2013] and [Kawasaki and Berthier, 2016] have shown that oscillating shear in AQS simulations and near-zero temperature over-damped Langevin dynamics can produce limit cycles in the trajectory. Furthermore, it was shown in [Fiocco et al., 2014] that this effect is also seen in the Random-NK model [Isner and Lacks, 2006]. If and when a limit cycle is entered depends largely on the system size N and the maximum strain amplitude $\gamma_{\max}$. Once a limit cycle is encountered, the system is caught in this cycle indefinitely, as the temperature is zero. However, we will now show that in MD simulations, even a temperature as small as $T = 0.01$ is sufficient to break these cycles.

First, we take a look at the mean squared displacement of the particle positions from the start of the simulation (see fig. 5.4a). To exclude small temperature fluctuations, we use position data from the IS trajectory. From [Fiocco et al., 2013] and [Kawasaki and Berthier, 2016], we would expect all of the MSD curves to become constant quickly, leading to a zero diffusion constant, as our system size at $N = 130$ is very small. However, even for $\gamma_{\max} = 0.06$, we still see some small diffusion. This gives rise to the question, if this is a temperature induced effect. If it is, we should see cycles in our data, which are eventually left. This kind of behavior is completely impossible in AQS simulations. We remark, that due to the low temperature, the actual value of the diffusion constant cannot be estimated from this data, as our runs are too short. This is seen well at $\gamma_{\max} = 0.13$ in fig. 5.4a, where have reached higher energies at $\gamma_{\text{acc}} = 60$, displaying faster diffusion, than at $\gamma_{\max} = 0.14$.

Now, in fig. 5.4b, we show the number of distinct cycles n_{cycle}, the system has encountered so far with respect to the number of oscillations. For all $\gamma_{\max}$, we see that the systems jump between different cycles, eventually leading to diffusion. Despite our small temperature of $T = 0.01$, this diffusion is caused purely as a temperature effect, as otherwise a cycles would be repeated indefinitely. In fig. 5.4b we see slight partition of the data with $\gamma_{\max}$ between 0.09 and 0.1. To explore this a little bit further, we gather some statistics about the cycles, we encounter in the

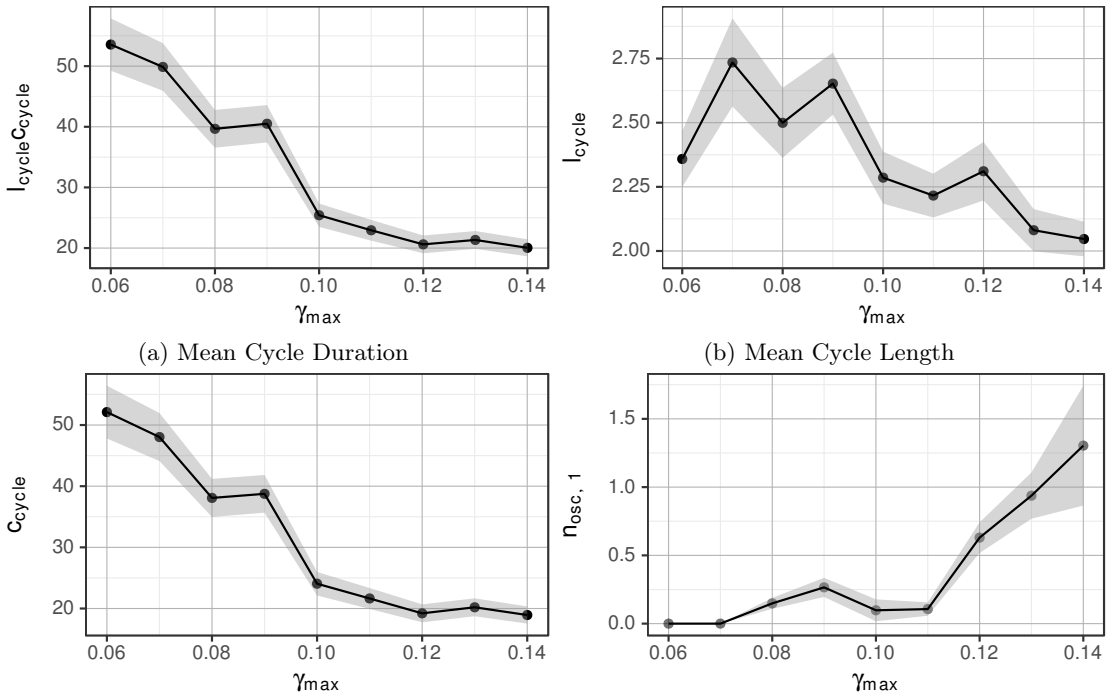

(a) Mean Cycle Duration

(b) Mean Cycle Length

(c) Mean Cycle Count

(d) First Cycle Start

Figure 5.5: (a) Mean duration of a cycle (amount of times, $\gamma = 0$ is crossed until the current cycle is left). (b) Mean length of a cycle (number of different states at $\gamma = 0$ until repetition of the cycle) at a given $\gamma_{\max}$. (c) Mean count of cycle repetitions until a cycle is left. (d) Starting γ_{acc} of the first detected cycle.

IS trajectory.

The highest probability to leave a cycle due to the temperature is near $\gamma_{\max}$, where we have the highest strain. If there is a transition, it is unlikely, that there will be another in close succession, as the system is not strained much further in the same direction. Therefore, we expect n_{cycle} to be a function of $\mathrm{n}_{\text{osc}} \coloneqq \frac{\gamma_{\text{acc}}}{\gamma_{\max}}$ instead of γ_{acc}, which is seen in fig. 5.4b. Furthermore, n_{cycle} is roughly proportional to the mean duration, the system stays within a cycle. This duration accounts for the shift of the curves in fig. 5.4b. It is the product of the length of the cycle l_{cycle}, i.e. the number of different states encountered at $\gamma = 0$ *during* this cycle, and c_{cycle}, which is defined as the count of *successive repetitions* of such a cycle. We show this cycle duration in fig. 5.5a, where we see two different regimes, with a crossover at $\gamma_{\max} \approx 0.1$. We note, that the slight partition in fig. 5.4b, may actually arise from a single outlier at $\gamma_{\max} = 0.09$, which does not affect the crossover point. As we find in fig. 5.5b, l_{cycle} alone shows only fluctuations of about 0.25 in that region. In contrast, c_{cycle} shows exactly the same behavior as the duration (see fig. 5.5c). A similar value for this crossover position has already been encountered as the yield strain in section 4.2 and the strain of the lowest shear modulus upon reversal in section 5.2. However, at this point, we have to leave the question of a possible connection between those observables open for further research.

Next, we look at the mean number of oscillations before the first cycle starts $\mathrm{n}_{\text{osc},1} \coloneqq \frac{\gamma_{\text{start},1}}{4\gamma_{\max}}$.

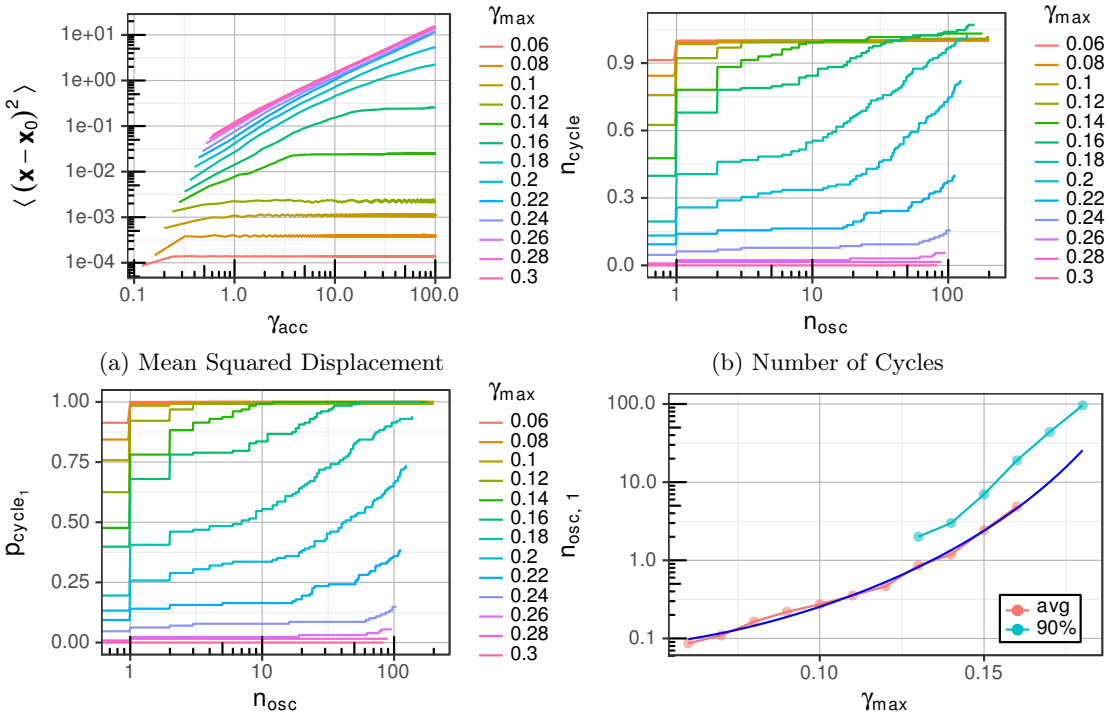

(a) Mean Squared Displacement

(b) Number of Cycles

(c) Probability to Enter Cycle

(d) Duration of Non-Cyclic Regime

Figure 5.6: (a) Mean squared displacement in the IS trajectory along the z axis for reversal runs in dependence of γ_{max}. (b) Average number of distinct cycles in dependence of the number of oscillations n_{osc}. (c) Probability to enter a limit cycle at a given n_{osc}. (d) Red points: Average value of $n_{osc,1}$, where a limit cycle is entered as a function of γ_{max}. We only show values, where at least 99% of all simulated trajectories have reached a limit cycle. The dark blue line denotes a power law fit of the form $\gamma_{start,1} = c \cdot (\gamma_{nl} - \gamma_{max})^{\delta}$ on the start of the first cycle with the fit parameters $c = 1.44 \cdot 10^{-6}$, $\delta = -5.49$ and $\gamma_{nl} = 0.231$. Blue points: The value of $n_{osc,1}$ where 90% of all simulations have entered a limit cycle. We used AQS simulations with $N = 130$ and $\Delta\gamma = 10^{-3}$ to generate the data shown in (a)-(d).

In our data (fig. 5.5d), we see mostly early cycle starts until $\gamma_{max} = 0.12$, where the number of oscillations starts to rise. This shows, that at the crossover position, it starts to be more difficult to find limit cycles. The same value was analyzed in [Kawasaki and Berthier, 2016] for a system with zero temperature. It was reported that the start of the first cycle diverges with $\frac{\gamma_{start,1}}{\gamma_{max}} \propto (\gamma_{dyn} - \gamma_{max})^{-\alpha}$, whereby γ_{dyn} is a fit parameter and T the oscillation period. Due to finite size effects, γ_{dyn} changes strongly with the system size for small systems ($N < 1000$) and is likely to be much higher than our sampled parameter range.

5.3.2 Athermal Quasistatic Simulations

In this section we used an athermal quasistatic integration scheme together with cyclic shear, to suppress all temperature effects. As noted previously, a limit cycle in cyclic AQS shear cannot be left by normal means. However, in fig. 5.6b, we plot the number of distinct cycles for AQS

simulations at $\Delta\gamma = 10^{-3}$, which we have chosen as in [Fiocco et al., 2013] for the smallest system size. One can observe, however, that a slight number of trajectories change their cycles, achieving a cycle count higher than 1. Inspection of single trajectories showed, that this happens mainly at the plastic events. Therefore, this must be a non-deterministic effect, caused by numerical errors. On one hand, every energy and force calculation is parallelized by multi-threading, which causes very small numerical differences during the addition of the individual per-particle results. On the other hand, it is much more likely, that the bigger effect comes from the fact, that after a whole cycle the input positions might be slightly different than for the last cycle, thereby causing rare switches between limit cycles. This shows us the high sensitivity of the system to small perturbations. In fig. 5.6c, we show for comparison the probability that the system has entered a cycle. This value is not affected by the aforementioned numerical issues. Here, we find as expected, for small values of $\gamma_{\max}$ already after a few cycles the system is in a limit cycle with basically 100% probability whereas in the opposite limit of large values only a tiny fraction has managed to reach a limit cycle for $n_{osc} = 100$.

As AQS simulations never leave their limit cycles, the most important property is the start of the first cycle. In fig. 5.6d, we plot the average value of the position and also the position, where 90% of all trajectories have reached a limit cycle. One can clearly see that the average accumulated strain strongly increases with increasing value of $\gamma_{\max}$. Using a power law fit, we find a divergence at $\gamma_{nl} = 0.231$. This value is in very good agreement with the system size scaling reported in [Kawasaki and Berthier, 2016], although the onset of the divergence in the analyzed range of $\gamma_{\max}$-values, where we derived γ_{nl} from, is quite weak. Furthermore, we also show when 90% of all simulations have entered a limit cycle. Comparison with the average value indicates that the heterogeneity becomes larger for larger $\gamma_{\max}$.

5.4 Reversibility of MS Transitions

In the introduction to minimized structures in section 3.2.4, we have described that the MS, corresponding to the current state of the system, can also be found by AQS simulations in the direction of zero shear stress. Therefore, we can say that a sheared state is reversible to another state, if they belong the same MS. However, the opposite is not always true: If two states belong to different MS, they can still be connected by AQS shear as well. The situation is even more complicated under oscillatory shear, where we can find limit cycles of higher order.

To analyze the reversibility of MS transitions further, we look at the probability to return to the starting MS by quasistatic shear in the reverse direction (fig. 5.7a). These simulations start at the inherent structure, visited directly after the first MS transition. We account for some hysteresis effects around $\gamma = 0$ by shearing up to $\gamma = -0.3$. First, we note that MS transitions really mark the onset of irreversible transitions, as even for very early transitions, the return probability is only around 75%. However, in section 4.2, we found that the MS after these early transitions may still be very close to the starting MS. Furthermore, we find that the return probability is approximately 50% at $\gamma_{MS} = 0.1$, marking the average onset of irreversible MS transitions. We remark, that this position compares well to the crossover position, where we see the average start of significant MS transitions. However, as we can see in fig. 5.7b, irreversibility and significance are not correlated. Lastly, the extrapolated return probability crosses zero at around $\gamma_{\max} = 0.28$. This value compares well to our previous findings, as for $\gamma_{\max} \geq 0.29$, we found that less than 1% of our trajectories entered limit cycles over the observed time window (see fig. 5.6c). At this high $\gamma_{\max}$ there should be at least one MS transition with $\gamma_{MS} < \gamma_{\max}$

(see fig. 4.5a). Therefore, this extrapolation may be a good predictor maximum $\gamma_{\max}$ in cyclic shear, where limit cycles may be found. We remark, that in cyclic shear, the simulation time diverges at this crossover, making it extremely difficult provide an exact value, whereas our new method has no such problems. Like in section 5.3.2, the system size dependence is expected in analogy to [Kawasaki and Berthier, 2016].

In close relation to p_{return} is the probability to find a limit cycle directly at the start of the simulation $p_{\text{cycle},1}$ (see fig. 5.8). To find a limit cycle directly at the start, there must be either no MS transition or a reversible one in both shear directions. We approximate this probability with the expression:

$$\begin{aligned} p_{\text{cycle},1}(\gamma_{\max}) \approx\ & P(\gamma_{\text{MS}} > \gamma_{\max}) \\ & + P(\gamma_{\text{MS}} \leq \gamma_{\max}) p_{\text{return}}(\gamma_{\max}) \left[P(\gamma_{\text{MS}} > \gamma_{\max}) + P(\gamma_{\text{MS}} \leq \gamma_{\max}) p_{\text{return}}(\gamma_{\max})\right] \end{aligned} \tag{5.2}$$

The first term dominates $p_{\text{cycle},1}(\gamma_{\max})$, while all further terms account for small corrections. The complete expression can be rationalized as follows: If there is no MS transition until $\gamma_{\max}$, we

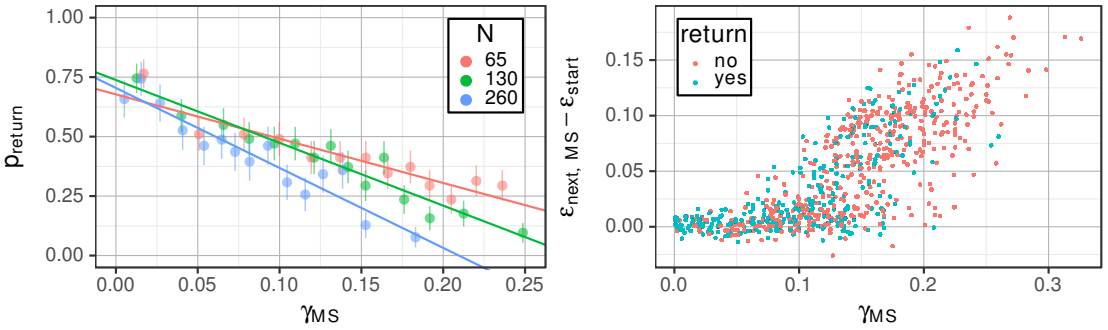

(a) (b)

Figure 5.7: (a) Probability to visit the starting MS by AQS shear in the reverse direction after the first MS transition. The solid lines represent a linear fits to the data and has a slope of $-2.64(20)$ and an intercept of $0.738(29)$ for $N = 130$. By extrapolation, p_{return} is zero for $\gamma_{\text{MS}} \geq 0.279(10)$. (b) Energy change at MS first transition. The color indicates, if the starting MS could be found by AQS shear in the reverse direction after first MS transition.

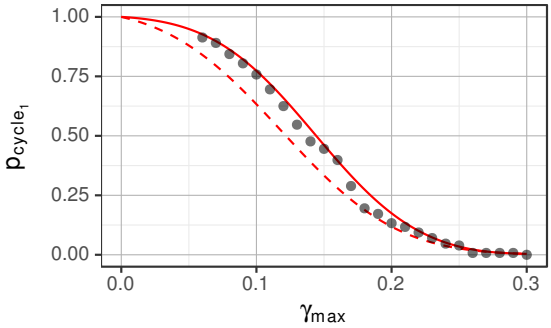

Figure 5.8: Probability to be already in a limit cycle at the start of a cyclic AQS simulation at $N = 130$. The solid red line represents approximation using MS statistics (see text). For comparison the dashed red line shows $P(\gamma_{\text{MS}} > \gamma_{\max})$.

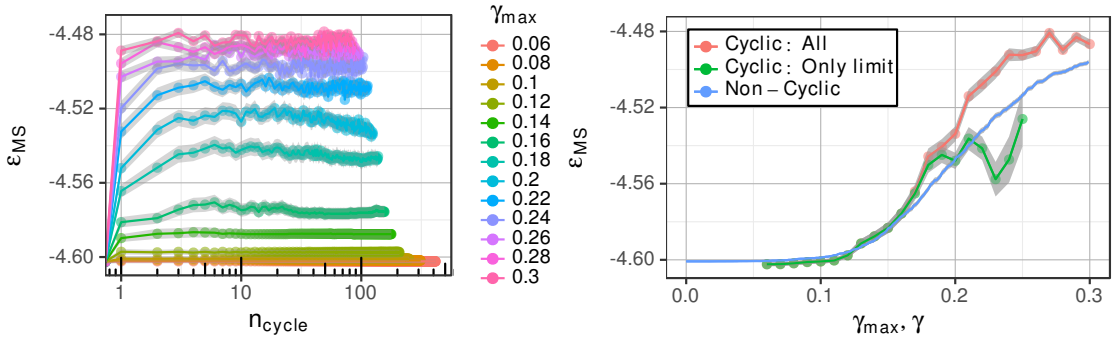

(a) (b)

Figure 5.9: (a) The average MS energy after n_{cycle} cycles for different values of $\gamma_{\max}$. (b) The final MS energy after 100 AQS cyclic shear simulations together with the final MS energy under the condition that the system is in a limit cycle after 100 cycles. Additionally the ensemble averaged MS energy, as shown in fig. 4.1d is included.

also expect no MS transition in the reverse direction. As we start with $\gamma_{\text{MS}} \neq 0$, this is only valid for small $\gamma_{\max}$. However at high $\gamma_{\max}$, there is a high probability of MS transitions earlier than $\gamma_{\max}$, thus dominating $p_{\text{cycle},1}$. Because there may be multiple MS transitions before reaching $\gamma_{\max}$, we assume that the last transition is close to $\gamma_{\max}$. Furthermore, if the last transition is reversible, than the others before have also been reversible and p_{return} for the last transition should have the same value, as if it was the first transition. Therefore, we can use $p_{\text{return}}(\gamma_{\max})$ instead of a more complicated term. If there was an MS transition on the forward direction, we assume that there may also be MS transitions on the backward direction, which may also be irreversible, forcing us to evaluate $P(\gamma_{\text{MS}} > \gamma_{\max})$ again. For the evaluation of the p_{return} in the reverse direction, the same argumentation as for the forward direction holds. Overall, we see a very good agreement between this approximation and the simulation data in fig. 5.8.

Finally, it is instructive to connect the observation of limit cycles with the underlying PEL properties and to compare it with the corresponding results in [Fiocco et al., 2013]. As shown in FIG. 5.9a, already after a few oscillations the limiting energy is reached. One roughly finds that around $\gamma_{\max} = 0.2$ it takes the longest time (approx. 7 oscillations) to reach the maximum energy. In contrast, in [Fiocco et al., 2013] it took for the $N = 4000$ system more than approximately 50 oscillations to reach the final energy value for $\gamma_{\max} = 0.08$. This shows for the large system how the elastic interaction among different subunits gives rise to a slow increase of energy in contrast to the results for small systems.

Furthermore, it turns out that the final energy, shown in FIG. 5.9b as a function of $\gamma_{\max}$, closely resembles the MS energies. Here we distinguish whether or not after 100 cycles the system has reached a limit cycle or not. We can distinguish three γ-regimes. For $\gamma_{\max} \leq 0.16$ the energy at the turning point $\gamma = \gamma_{\max}$ in the first cycle is the same as the energy in the 100th cycle. Among others this implies that the approx. 60% trajectories which for $\gamma_{\max} = 0.16$ did not start in a limit cycle (see FIG. 5.8) hardly increase their MS energy upon reaching a limit cycle in the course of oscillatory shearing. For $0.17 \leq \gamma_{\max} \leq 0.19$ by far the most trajectories still end up in a limit cycle so that the final MS energy after 100 cycles hardly changes upon restriction to the subset of trajectories with a limit cycle. However, the MS energies are now significantly higher than in the first cycle. Finally, for $\gamma_{\max} \geq 0.20$ the MS energies remain constant within statistical uncertainty, only taking into account the trajectories in a limit cycle. This suggests

that the energy of approx. -4.55 is a kind of crossover energy in the PEL. Once the system has significantly crossed this energy, the chance to enter a limit cycle approaches zero, independent of the applied amplitude $\gamma_{\max}$. Remarkably, this energy cutoff is lower than the average energy at the turning point of the first cycle (for $\gamma_{\max} \geq 0.22$). Thus, already after one cycle most of the trajectories have left the phase space where a limit cycle is still possible.

We would like to point out that the increase of the MS energy as a function of $\gamma_{\max}$ (taking the average over all trajectories after 100 cycles) is very continuous. In contrast, for the $N = 4000$-particle system in [Fiocco et al., 2013] one finds a discontinuous behavior when crossing the value of $\gamma_{\max}$ where limit cycles start to become relevant (between 0.08 and 0.09 for the large system). This is consistent with our previous observation in FIG. 5.9a that for all values of $\gamma_{\max}$ the final energy is reached after a few cycles so that there is not much space for a significant increase of energy for trajectories which do not enter a limit cycle so early (or at all). Thus, also the strong increase of energy with the number of cycles in [Fiocco et al., 2013] can be related to the elastic coupling of the different subsystems.

5.5 Summary

In our cyclic shear simulations, we have reproduced the effect of mechanical rejuvenation as well as memory effects in form of limit cycles. First, we looked at the reversal overshoot, whose height could be perfectly predicted by knowing the MS energy at the reversal point. By the analysis of the MS shear modulus at the reversal point, we could also give an approximation of the effective shear modulus at the start of the reversal.

Furthermore, we looked at the cycle statistics for low-temperature simulations at $T = 0.01$ and compared them to AQS simulations. As expected from literature, the AQS simulations found limit cycles up to high $\gamma_{\max}$, since we simulated at a very small system size $N = 130$. Also, as described in literature, we found a power-law behavior of the average $\gamma_{\text{start},1}$, where limit cycles are found with respect to $\gamma_{\max}$. Furthermore, we determined $\gamma_{\text{nl}} = 0.231$ at $N = 130$, which compares well to literature values.

In contrast to athermal simulation, we found that low-temperature MD simulations can break limit cycles already at temperatures as low as $T = 0.01$. Although the mean squared displacement showed, that our run length was too short to determine a proper diffusion constant, we found a power-law behavior with a slope of 1 in the number of distinct cycles for all tested $\gamma_{\max}$. A closer look at the cycle statistics revealed, that there is a crossover in the mean cycle count with a dependence on $\gamma_{\max}$. This crossover point coincides well with the crossover position of the first MS transition, we have found in section 4.2. However, to further evaluate the connection of both crossovers, more reversal simulations with different ϵ_{start} have to be made.

In the last section, we looked at the reversibility of MS transitions in terms of AQS shear and found that on average they become irreversible at $\gamma_{\text{MS}} = 0.1$. Although there is no direct correlation between irreversibility and our previously defined significance of MS transitions, this result compares well to average start of significant MS transitions in section 4.2. By extrapolating our data from non-cyclic simulations, we could easily approximate the maximum $\gamma_{\max}$ beyond which no limit cycles can be found in cyclic AQS simulations. This point is usually hard to determine as the simulation times in cyclic simulations diverge. As an application of the MS statistics, together with our data about to reversibility, we were able to give a very good approximation for the probability to be in a limit cycle at the start of the simulation.

Lastly, we looked at the MS energy in limit cycles. We found that for large $\gamma_{\max}$, the average MS energy of limit cycles was capped at about $\epsilon_{\mathrm{MS}} = -4.55$. In comparison with the earlier determined average MS energy, we found that at a crossover at $\gamma_{\max} \approx 0.22$ the majority of systems becomes unable to enter a limit cycle. This also compares well with our previously found $\gamma_{\mathrm{nl}} = 0.231$.

Chapter 6

The Flow Regime

In this chapter, we will focus on the analysis of the flow regime in terms of the sheared potential energy landscape. With the term *flow regime*, we hereby refer to the steady state after the stress overshoot. After a close look on the flow curves and determining the range of the energy landscape influenced regime, we will make use of the newly introduced *minimized structures* (MS) to define *metabasins* (MB). Of most interest is the *crossover regime* between the shear rate dominated and the temperature dominated regime, as both limits are well understood in literature. Using the metabasin energy distribution, we can, in comparison with data from quiescent simulations, easily define an effective temperature in this crossover regime and compare our findings to literature. Then we will introduce a rate model to approximate the average metabasin waiting time. This rate model is based on the simple assumption, that the energy barrier of the current minimum in the energy landscape is lowered as a function of the strain rate. Last in this chapter, we will apply our findings and make predictions of the apparent viscosity and the diffusion. Both of these observables have been studied intensively, but are still not well understood in the crossover regime [Shi et al., 2013, Lacks, 2002].

6.1 Flow Curve

The stress in the flow regime is commonly characterized with a Hershel-Bulkley law [Herschel and Bulkley, 1926]:

$$\sigma = \sigma_y + K\dot{\gamma}^n \tag{6.1}$$

This form describes a constant yield stress σ_y in the limit of zero shear stress. The exponent n is usually in the range of $0.2 - 0.8$. A comprehensive summary of experimental and theoretical results for the form and description of flow curves is found in [Bonn et al., 2017].

We will discuss the features of this flow curve in terms of the energy landscape, using inherent structures and minimized structures. In fig. 6.1a, we see that for our small system, the stress still follows a Hershel-Bulkey law for our trajectory data. However, the parameters show a strong temperature dependence.

Similar to the analysis in [Lacks, 2001], we now divide the stress into a component from the inherent structure and the vibrational part. Here, we find that for the inherent structures, the

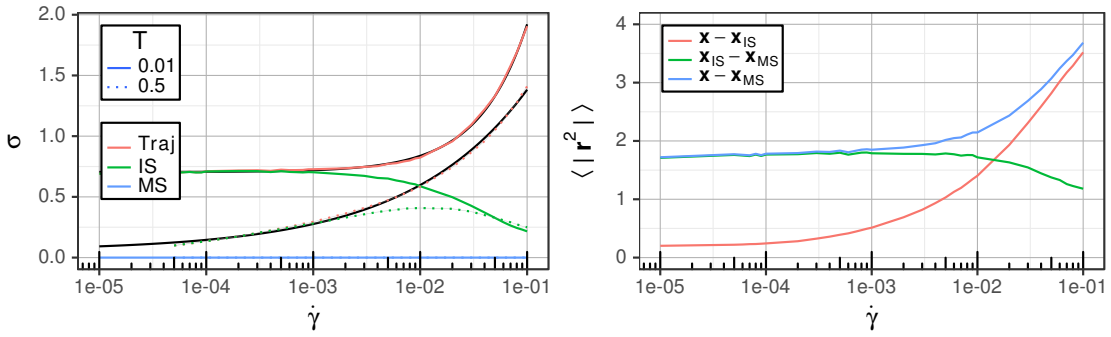

(a) Shear Stress (b) Distances

Figure 6.1: (a) Mean shear stress in the flow regime for $N = 130$ in the particle trajectory, the inherent structure trajectory and the minimized structure trajectory. The black line represent a fits to the Herschel-Bulkley equation. For $T = 0.01$, we determined to parameters $\sigma = 0.71 + 11\dot{\gamma}^{0.96}$ and for $T = 0.5$ we found $\sigma = 0.056 + 3.3\dot{\gamma}^{0.39}$. (b) Mean distance between coordinate vectors in the different trajectories at $T = 0.01$ and $N = 130$.

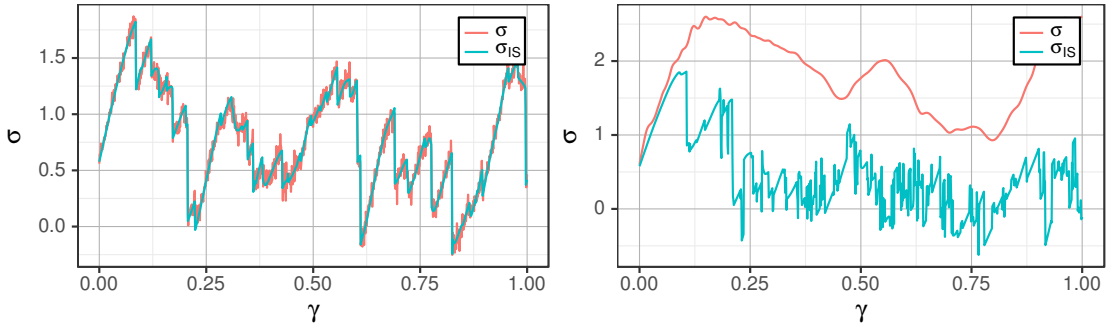

(a) $\dot{\gamma} = 10^{-4}$ (b) $\dot{\gamma} = 10^{-1}$

Figure 6.2: Stress in the real trajectory and the IS trajectory at low temperature ($T = 0.01$) for a low shear rate (a) and a high shear rate (b).

behavior of the stress is opposite: At high shear rates, the inherent structure stress drops! This can be explained immediately by looking at single trajectories (fig. 6.2). At high shear rates, we see a clear departure of the real trajectory from the inherent structure trajectory, similar to the behavior at high temperatures. We have confirmed, that the energies behave similarly for high shear rates. In contrast, at low shear rates, the real trajectory follows very closely the inherent structures. Therefore, from fig. 6.1a we can determine that the influence of the energy landscape, or at least of the inherent structures, starts to become weaker at $\dot{\gamma} = 10^{-3}$ for $T = 0.01$. To further understand this limit, we look at the mean squared displacement (fig. 6.3a) in direction of the z-axis, which is not directly affected by the shear. For short times, we see identical behavior for all shear rates. In fact, when plotting the curves with respect to the time Δt (not shown), they completely overlap during the ballistic regime until a time of approximately $\Delta t = 0.1$. However, the length of the caging regime is limited by a maximum *strain*, which is identical for all shear rates. Its value is between $10^{-4} < \Delta\gamma < 10^{-3}$. Therefore, the caging regime vanishes at a shear rate between 10^{-3} and 10^{-2}. We can safely assume, that for sufficiently low shear rates, diffusive motion in z direction is induced on the timescale of the

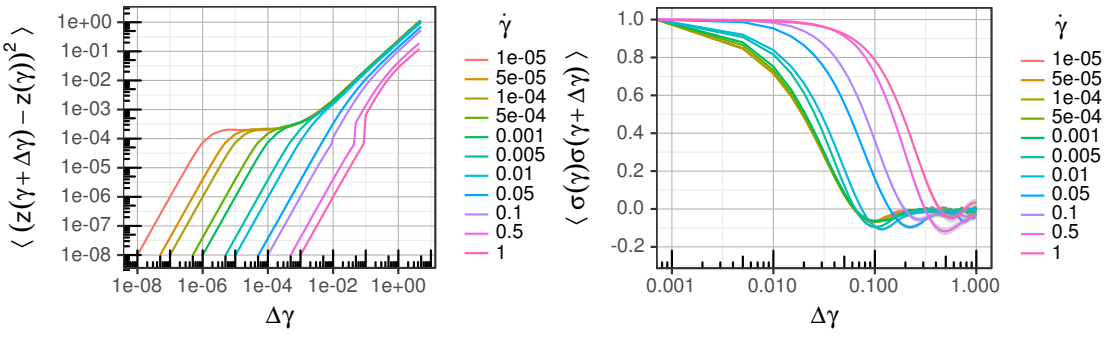

(a) MSD

(b) Stress Correlation

Figure 6.3: (a) Mean squared displacement of type A particles in z-direction at various shear rates. (b) Stress-stress autocorrelation with respect to γ. Both plots show simulation data at $T = 0.01$ and $N = 130$.

shear, as the temperature is too low for any other kind of activated jumps[1]. In addition to that, the curves in the MSD plot merge completely in the limit of high strains, when plotted against the strain instead of the time, showing that the shear rate provides the relevant timescale for this regime. Therefore, this means that as the caging regime vanishes, the ballistic timescale and the shear rate induced timescale are identical. At even higher shear rates, it becomes impossible for the system to relax between yield events, as the ballistic motion on short timescales dominates, causing the observed behavior in fig. 6.2b. We remark, that the sharpness of the transition in fig. 6.3a is influenced by the thermostat masses, as the system may adjust quicker between the two regimes at a higher oscillation frequency. However, despite different thermostat masses, the position of this transition stays constant for a given $\dot{\gamma}$, showing that it is not an artifact of the thermostat[2].

In literature, we found an attempt of adding dampened ballistic motion to quasistatic simulations in order to reproduce this effect, however they focused their work on avalanche statistics [Salerno et al., 2012, Salerno and Robbins, 2013]. A strong dampening results in closely following the energy landscape, while at low dampening, the system keeps moving ballistically for a longer time period. This mimics well the interplay of the shear rate with the intrinsic ballistic timescale.

The timescale of the yield events can be determined from the system stress autocorrelation in fig. 6.3b. For low shear rates, the curves overlap completely. In this regime, most of the events happen at a strain of $10^{-2} \leq \Delta\gamma \leq 10^{-1}$. This result is compatible with the MSD data (fig. 6.3a), where see the crossover between the caging and the diffusive regime ending at $\Delta\gamma = 10^{-2}$. At higher shear rates, stresses are correlated for much longer $\Delta\gamma$. Again, this is caused by the constant length of the ballistic regime and the direct crossover to diffusion.

The departure from the energy landscape can also be seen directly in the distance of the particle coordinates between the normal trajectory and the inherent structures (fig. 6.1b). However, we find very similar behavior of the shear stress to the distances from the minimized structure. The distance between the real trajectory coordinates and the corresponding MS coordinates $|\mathbf{x} - \mathbf{x}_{\mathrm{MS}}|$

[1] Any temperature facilitated aging events should also happen on the timescale of the shear, as small temperatures shift the yield point only slightly [Chattoraj et al., 2010].

[2] Our default thermostat masses are chosen for an oscillation frequency of $\omega_{\mathrm{Th}} = 7.56$.

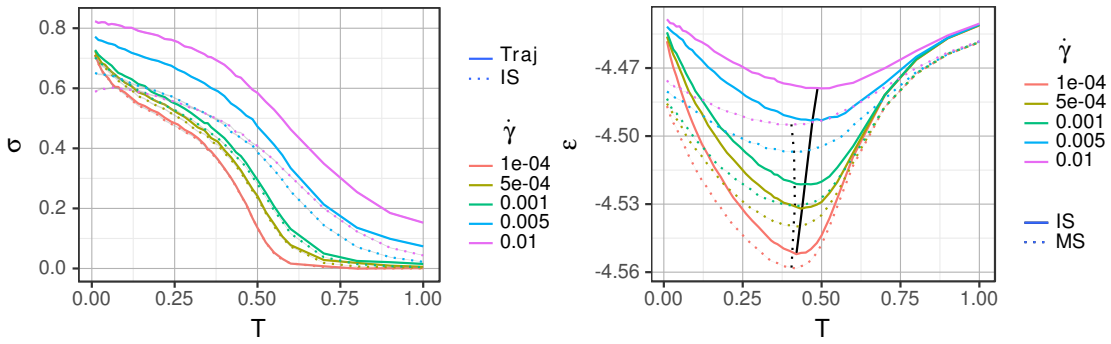

(a) Stress (b) Energy

Figure 6.4: Temperature dependence of the average stress (a) and energy (b) in the flow regime for the real trajectory, the inherent structure trajectory and the minimized structure trajectories. In (b), the black lines visualize the position of the minimum energy.

rises with the shear rate very similar to the shear stress σ. The same is true for $|\mathbf{x}_{\mathrm{IS}} - \mathbf{x}_{\mathrm{MS}}|$ compared to σ_{IS}. Therefore, contrary to the IS, we expect that the MS plays a significant role even at high shear rates $\dot{\gamma} \geq 10^{-3}$.

The connection between the system stress and the distance can be understood qualitatively in terms of anisotropy. We recall, that the MS represents the unsheared state with zero stress. The neighbor distribution $g(r)$ around this base state should be completely isotropic[3]. Shearing a system results in non-linear particle movement, which also induces an anisotropy $g(r)$ [Koumakis et al., 2012]. This anisotropy in turn is directly connected to the system stress, as we will show in more detail in section 7.5.

Last in this section, we will look at the temperature dependence of the stress and the energy in the flow regime (see fig. 6.4). In the low temperature regime $T < \frac{3}{4}T_g$, the behavior of the stress has been successfully described by [Chattoraj et al., 2010] for a 2D binary Lennard-Jones glass former. They used a method similar to the one described in section 6.3 to calculate a temperature based offset to the yield strain. Combined with a shear modulus, this leads to a finite stress offset, which can be added to the stress in the zero temperature limit. This method works well for the shear dominated regime. However, in the vicinity of the glass transition temperature T_g, there is a much more difficult interplay of the shear and the temperature.

For a qualitative description in the picture of the energy landscape, we look at the IS and MS energies in fig. 6.4b. We need to take into account various processes with different time scales. At temperatures above T_g, we see that temperature effects dominate mostly. Towards T_g, the α relaxation time grows exponentially [Berthier and Biroli, 2011] and the system explores energetically lower parts of the energy landscape while maintaining thermodynamic equilibrium. As temperature-activated transitions reset the system stress, the average stress is small in this regime. In contrast, at temperatures $T_g \to 0$, stresses are quite high, as they are only reset during yield events. The average stress here should be approximately half of the yield stress in individual trajectories. Similarly, the energies are also quite high, as yield events select energies that are strongly out of thermodynamic equilibrium. However, as the temperature increases towards T_g, the system is driven more and more towards thermodynamic equilibrium which is at

[3]In section 7.5, we will see that with our definition of anisotropy, there still remains a very small average anisotropy in the MS in the flow regime.

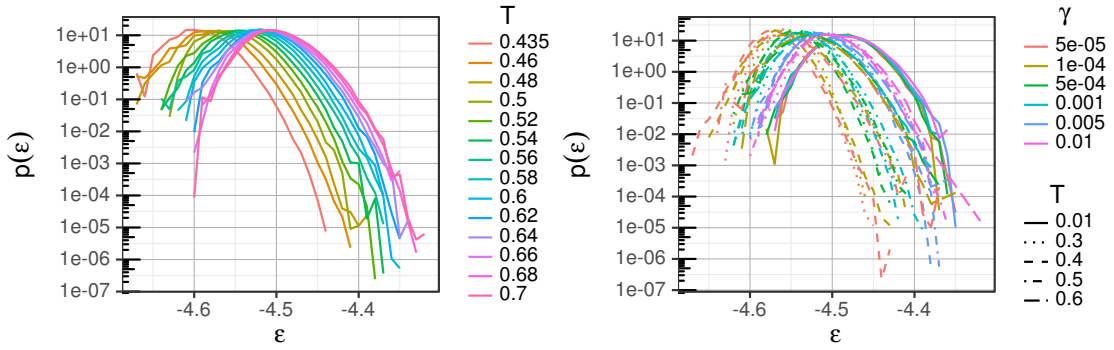

(a) $p(\epsilon_{\mathrm{MB}}; T)$ (b) $p(\epsilon_{\mathrm{MB}}; T, \dot{\gamma})$

Figure 6.5: Distribution of metabasin energies for (a) the quiescent state and (b) the flow regime.

low energies. As equilibration is not possible below T_g, the lowest energies are therefore found at T_g. Remarkably, the energetic minimum for the minimized structure is independent of the shear rate at $T_{\mathrm{min}} \approx 0.41$.

6.2 Effective Temperature

In this section we will derive an effective temperature from the energy distribution of the sheared potential energy landscape. Previously, in section 3.1.1, we have seen that the energy distribution $p(\epsilon_{\mathrm{MB}}; T)$ has a Gaussian form with a cutoff at low energies. At temperatures above $T = 0.6$, the shape starts to deviate from the Gaussian form, as the influence of the energy landscape lessens. In the case of a sheared system in the flow regime, the energy distribution is identical for low $\dot{\gamma}$ (fig. 6.5b). Similar to the case of high temperatures, the energy distribution also deviates from the Gaussian shape at $\dot{\gamma} = 0.01$. As we have seen in section 6.1, the trajectory does not follow the energy landscape anymore at these shear rates, similar to what happens at high temperatures. We would now like to analyze this correspondence further by introducing an effective thermodynamic temperature.

A similar concept has also been used in [Schroer and Heuer, 2015] for a small system, driven by a single particle under a constant *force*. However, care must be taken when comparing the results, as our sheared system is strain controlled, which would compare better to a system, driven by a single particle with constant *velocity*. The probability to have an energy ϵ_{MB} in the quiescent state is given via the density of states $G(\epsilon_{\mathrm{MB}})$:

$$p(\epsilon_{\mathrm{MB}}; \beta) \propto G(\epsilon_{\mathrm{MB}}) \mathrm{e}^{-\beta \epsilon_{\mathrm{MB}} N} \tag{6.2}$$

Our idea is basically, that the density of states reflects a structural property, which should not change, as the energy landscape is sheared. At least, it should be similar when strained back to $\sigma = 0$, as has been described in section 3.2, which forms the basis for the definition of ϵ_{MB} in the sheared PEL. However, at finite $\dot{\gamma}$, minima of the energy landscape eventually vanish, which adds another process of activation besides the temperature. Because of this, and also because we have still a Gaussian distribution $p(\epsilon_{\mathrm{MB}}; \beta, \dot{\gamma})$, we extend eq. (6.2) by introducing an effective temperature $\beta_{\mathrm{eff}}(\beta, \dot{\gamma})$, where $\beta_{\mathrm{eff}}(\beta, \dot{\gamma} = 0) = \beta$:

$$p(\epsilon_{\mathrm{MB}}; \beta, \dot{\gamma}) \propto G(\epsilon_{\mathrm{MB}}) \mathrm{e}^{-\beta_{\mathrm{eff}}(\beta, \dot{\gamma}) \epsilon_{\mathrm{MB}} N} \tag{6.3}$$

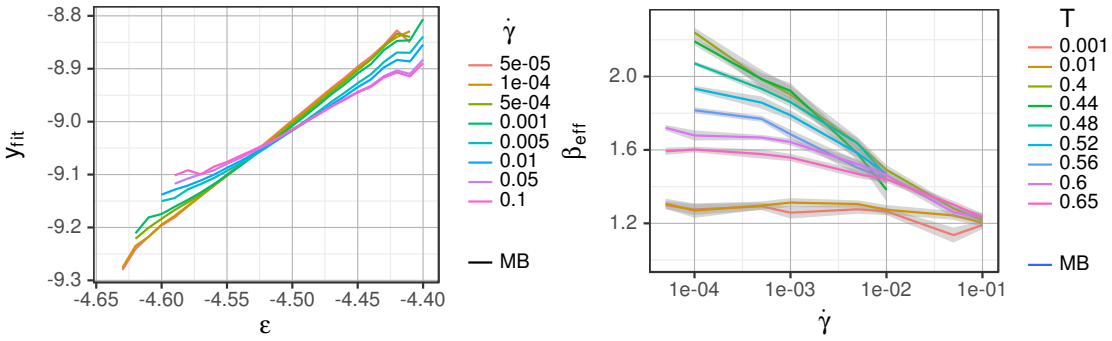

(a) $y_{\text{fit}}(\epsilon_{\text{MB}}, \beta, \dot{\gamma})$ (b) $\beta_{\text{eff}}(\beta, \dot{\gamma})$

Figure 6.6: (a) Fit function $y_{\text{fit}}(\epsilon_{\text{MB}}, \beta, \dot{\gamma})$ with $\beta = 2.0$, calculated via eq. (6.6) and data from the quiescent state with $\beta_0 = 2.0$. (b) Effective temperature $\beta_{\text{eff}}(\beta, \dot{\gamma})$ determined by a linear fit of the data shown in (a).

Dividing both sides with a distribution for a fixed temperature β_0 and $\dot{\gamma} = 0$ gives:

$$\frac{p(\epsilon_{\text{MB}}; \beta, \dot{\gamma})}{p(\epsilon_{\text{MB}}; \beta_0)} = \frac{\mathrm{e}^{-\beta_{\text{eff}}(\beta,\dot{\gamma})\epsilon_{\text{MB}}N}}{\mathrm{e}^{-\beta_0\epsilon_{\text{MB}}N}} \tag{6.4}$$

$$\Leftrightarrow \quad -\ln\left(\frac{p(\epsilon_{\text{MB}}; \beta, \dot{\gamma})}{p(\epsilon_{\text{MB}}; \beta_0)}\right) = \beta_{\text{eff}}(\beta, \dot{\gamma})\epsilon_{\text{MB}}N - \beta_0\epsilon_{\text{MB}}N \tag{6.5}$$

$$\Leftrightarrow \quad y_{\text{fit}}(\epsilon_{\text{MB}}, \beta, \dot{\gamma}) := -\frac{1}{N}\ln\left(\frac{p(\epsilon_{\text{MB}}; \beta, \dot{\gamma})}{p(\epsilon_{\text{MB}}; \beta_0)}\right) + \beta_0\epsilon_{\text{MB}} \tag{6.6}$$
$$= \beta_{\text{eff}}(\beta, \dot{\gamma})\epsilon_{\text{MB}}$$

If our hypothesis holds, we should have a linear dependence of the effective temperature on the energy, which can be verified in fig. 6.6a. With a linear fit on the data, we can determine $\beta_{\text{eff}}(\beta, \dot{\gamma})$, which is shown in fig. 6.6b.

In this plot, we have two asymptotic regimes, the temperature dominated and the shear-rate dominated. While in the completely temperature dominated regime, which can only be observed for temperatures $T > T_g$, we have $\beta_{\text{eff}} = \beta$. In the shear dominated regime the effective temperature shows logarithmic behavior in the shear rate $\dot{\gamma}$.

One additional thing to notice is the merge of all effective temperatures in a single point at $\dot{\gamma} = 5.42 \cdot 10^{-2}$ and $\beta_{\text{limit}} = 1.29$ [4]. The same value of β_{limit} has also be determined by [Kob and Andersen, 1995a] as the temperature, where the second neighbor peak in the van Hove correlation function $g_{pn}(r)$ splits. This split is a feature often observed in supercooled liquids, which leads us to the interpretation that this temperature marks the upper limit of the PEL influenced temperature range. A similar, but slightly higher value, was reported in [Schroer, 2015], analyzing the micro-rheology of supercooled liquids. In that work, the effective temperature of a system, where a single particle was pulled through with a constant force (which would translate to a constant stress in our case), collapsed to a single value at $\beta \approx \frac{1}{2T_c} = 1.15$. We note, that β_{limit} is also valid in the limit of small temperatures. So when looking at data in the flow regime at low

[4] We used linear interpolation of our data in the range $\dot{\gamma} \in [5 \cdot 10^{-05}, 1 \cdot 10^{-2}]$ and $T \in [0.001, 0.45]$, where we are clearly in the shear dominated regime and β_{eff} is linear in $\log \dot{\gamma}$. Using this interpolated data, we determined the mean crossing point of all straight lines by minimizing $\text{Var}(\vec{A} \log \dot{\gamma} + \vec{B})$.

temperature, as is usual in AQS simulations, we basically examine the upper limit of the energy landscape.

Comparing with literature, there have been very different approaches to define an effective temperature. Here, we report the works, which have used a similar Lennard-Jones system to compare the results. The first method from literature to define an effective temperature is explained in [Berthier and Barrat, 2002] and uses single-particle density fluctuations. Their effective temperature with $T_{\text{eff}} = 0.65$ for $T = 0.3$ and $\dot{\gamma} = 10^{-3}$ is slightly lower than ours. A similar value was reported in [Ilg and Barrat, 2007], which was extracted from simulations by replacing type B particles with dumbbells, each representing a two-state system. We note, that using the metabasin waiting time distribution for the definition of an effective temperature might have given very different results, as they represent the dynamics directly. However, this would have required the knowledge of the average metabasin barrier height at all temperatures and we have no direct access to this value. Therefore, in the following chapters, we will try to find a model, which can predict the waiting times and thereby describe dynamical properties.

6.3 Crossover between Temperature and Shear-Dominated Regime

In section 6.2, we have seen that there is a crossover between a temperature and a shear rate dominated regime. In this chapter, we will now analyze this transition in terms of the metabasin lifetime τ_{MB}.

The lower limit of shear rates available for metabasin analysis is $\dot{\gamma} = 5 \cdot 10^{-5}$, which is imposed by our current hardware used for simulation and analysis. The upper limit for generating useful information about the PEL is around $\dot{\gamma} = 0.01$ (see section 6.1 and section 6.2) As the waiting times start to deviate visibly from Arrhenius behavior at around $T = 0.625$ section 3.1.1, we use a slightly lower value of $T = 0.6$ as an upper limit. The lowest temperature can be determined looking at the effective temperatures in fig. 6.6b. Around $T = 0.41$, which matches the crossover in section 6.1, we have the steepest slope in $\beta_{\text{eff}}(\beta, \dot{\gamma})$. Looking at the effective temperature at our lowest possible shear rate of $\dot{\gamma} = 5 \cdot 10^{-5}$, we come up with $T = 0.42$, for which we are still in the shear rate dominated regime. To have a better view of the crossover, we decide to start with a slightly lower temperature and concentrate our detailed simulations to the range $T \in [0.38, 0.6]$.

Figure 6.7 shows the metabasin lifetimes in this crossover regime in great detail. In the limit of low temperatures, for all energies we see an exponential dependence of the waiting time on the shear rate. In section 6.3.1 we will describe in detail, why this is expected from the perspective of the sheared potential energy landscape. At higher temperatures/lower shear rates, we see the crossover to the temperature dominated regime. During the crossover and at energies ($\epsilon_{\text{MB}} \geq -4.5$), we see slightly increased metabasin times, compared to the lower shear rate limit. We will address this phenomenon to some degree later in section 6.3.7.

6.3.1 Crossover Model: Linearly Dropping Barriers

Our model to describe the crossover regime takes into account the properties of the sheared potential energy landscape (see section 3.2). Looking from the perspective of the PEL, we think of the system being trapped near an energy minimum, with barriers surrounding the minimum.

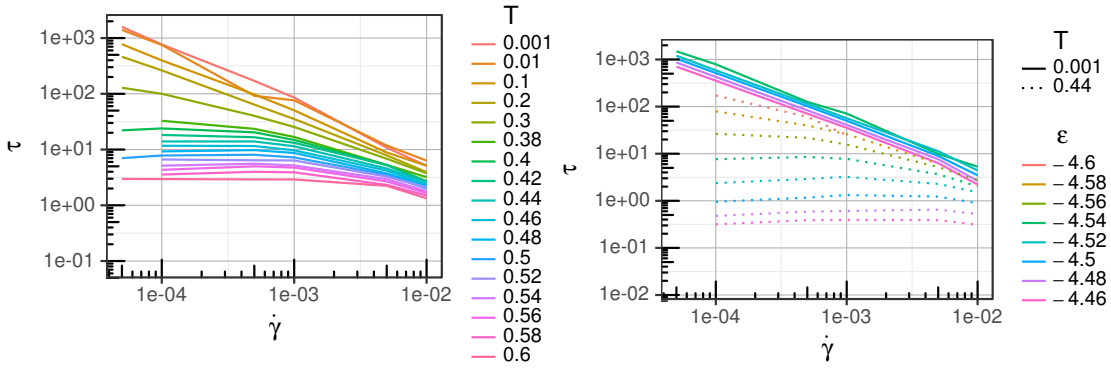

Figure 6.7: Metabasin lifetime $\langle \tau_{\mathrm{MB}} | \epsilon_{\mathrm{MB}}; \beta, \dot{\gamma} \rangle$ in the vicinity of the crossover between the temperature and the shear rate dominated regime. In (a) we show the dependence on the temperature for a metabasin single energy $\epsilon_{\mathrm{MB}} = -4.55$ and in (b) we show the energy-dependence for a few selected temperatures.

Although the energy landscape is highly multidimensional and non-linear, that potential energy near a barrier scales with $\Delta U = (\gamma_{\mathrm{c}} - \gamma)^{\frac{3}{2}}$ in the vicinity of a catastrophe at a critical γ_{c} [Maloney and Lacks, 2006]. This is a common scaling for a general fold catastrophe, as the minimum and saddle point merge, just before the barrier vanishes. We now assume, that at the beginning of our simulation, the system evolves in an arbitrary direction, corresponding to the eigenvectors of the lowest eigenvalues in an harmonic approximation. Despite shearing the system, the eigenvector to the lowest eigenvalue does not point into the shear direction [Gartner and Lerner, 2016b, Gartner and Lerner, 2016a], although they are changed by shear. Only very close to the catastrophe, the eigenvalues change and the eigenvector to the lowest eigenvalue now points into the direction of the barrier (see section 3.2 and [Maloney and Lacks, 2006]). Nevertheless, we can still assume, that the deformation only in the direction of this last eigenvector at the catastrophe looks very simple.

For example we could assume a simple $\sin(x)$ or $\sin^2(x)$ landscape, resembling in part the model in [Isner and Lacks, 2006], which was used to reproduce the results of cyclic shear [Fiocco et al., 2014]. Both show the characteristic fold catastrophe upon vanishing of the barrier. In section 6.3.7, we will see, that there is only a small difference between both models. Interestingly, we will see that both may be approximated by a simple linear scaling. Therefore, as for our first model, we assume a linear scaling of the energy barriers with the strain.

Here, we recall that the idea of dropping energy barriers has also been used in the so called *soft glassy rheology* (SGR) model [Sollich et al., 1997]. However, they assumed, that barriers would be dropping with a quadratic dependency in γ, as can be seen by the term $\frac{1}{2}k\gamma^2$. A much more similar approach was used in [Chattoraj et al., 2010], where the correct fold catastrophe scaling was used to determine a sharp flip distance at low temperatures, which effectively shifts the yield point by a $\Delta\gamma(\dot{\gamma}, T)$. Thereby, they could therefore correctly predict the stress dependence in the flow regime for temperatures below the glass transition. In contrast to their work, we are interested in higher temperatures in the crossover regime ($T \in [0.4, 0.6]$), so we have to use a complete scaling function.

As we explained earlier, we want to use a linear barrier scaling for our first crossover model:

$$V(\epsilon_{\mathrm{MB}}, t) = V_0(\epsilon_{\mathrm{MB}}) - \lambda(\epsilon_{\mathrm{MB}})\dot{\gamma}t \tag{6.7}$$

The mean barrier height is determined by the metabasin energy ϵ_{MB} in accord with the trap model [Monthus and Bouchaud, 1996], as discussed in section 3.1.1. This barrier is now lowered by shearing the system, i.e. tilting the energy landscape.

When we have relatively high temperatures, we can expect the transitions to be even further away from the critical γ_c than in [Chattoraj et al., 2010], so the exact scaling near the catastrophe may become negligible. The exact scaling is also mostly irrelevant, when we begin shearing the metabasin, as the change of the barrier is much smaller than the barrier height. Furthermore, small corrections may also be absorbed into the free parameter λ of the model. Another aspect, we did not incorporate into the model, is that after a transition, even when starting from the quiescent state, the stress is broadly distributed. We also neglect in our calculations, that the barrier might become negative at some point, which may results in unphysical behavior. This, however, only affects extreme cases at high shear rates and energies, i.e. very small energy barriers. In section 6.3.7 we will see by the use of numerical integration, that clamping $V \geq 0$ produces similar results for our parameter range.

Unfortunately, this model has one conceptual problem: Metabasins are a dynamic property of the energy landscape, so their size depends on the temperature and the shear rate, which in turn affects the barrier heights. This effect is not very pronounced in the temperature dominated regime (see section 3.1.2 and section 3.1.3), but for example, if we are at zero temperature and shear our system, our metabasins will most likely be consisting of a single MS, therefore the barrier height will be constant for all ϵ_{MB} (see section 3.1.1). On the other hand, in the temperature dominated regime, the activation energies show a linear dependence on ϵ_{MB} for energies $\epsilon_{\mathrm{MB}} \leq -4.5$ and are only constant for $\epsilon_{\mathrm{MB}} \geq -4.5$. So in principle, we would need some kind of effective potential in dependence of the effective temperature described in section 6.2. However, as we see in section 6.3.7, this model already produces good results for high energies and is equally applicable to MS statistics.

6.3.2 Constant Barriers

Before we start with our more complicated model, we will first describe the more simple model with a constant barrier, i.e. not time-dependent barrier height V, leading to Arrhenius behavior. In passing, we note that for simplicity we have dropped the energy dependence of the constants V, λ, Γ for easier notation. We use a simple rate model, where we have an ensemble of N systems, all starting from the first of two states and $n(t)$ specifies the number of system still in the first state.

$$\frac{\mathrm{d}}{\mathrm{d}t}n(t) = -\Gamma \mathrm{e}^{-\beta V} n(t) \tag{6.8}$$

$$\Rightarrow n(t) = N\mathrm{e}^{-\Gamma \mathrm{e}^{-\beta V} t} \tag{6.9}$$

As we model an activated process, the transition rate is dependent on the temperature and the height of the energy barrier. The probability to stay in the first state, and that the transition comes after t, is simply $P(t' \geq t) = \frac{n(t)}{N} = \mathrm{e}^{-\Gamma \mathrm{e}^{-\beta V} t}$ giving a jump probability at t of:

$$p(t) = \frac{\mathrm{d}}{\mathrm{d}t}P(t' \leq t) = \frac{\mathrm{d}}{\mathrm{d}t}\left(1 - P(t' \geq t)\right) = -\frac{\mathrm{d}}{\mathrm{d}t}P(t' \geq t) = \Gamma \mathrm{e}^{-\beta V}\mathrm{e}^{-\Gamma \mathrm{e}^{-\beta V} t} \tag{6.10}$$

This can be used to calculate the mean waiting time:

$$\begin{aligned}\langle\tau\rangle &= \int_0^\infty tp(t)\mathrm{d}t = -\int_0^\infty t\left(\frac{\mathrm{d}}{\mathrm{d}t}P(t'\geq t)\right)\mathrm{d}t = -\left[tP(t'\geq t)\right]_0^\infty + \int_0^\infty P(t'\geq t)\mathrm{d}t \\ &= \int_0^\infty \mathrm{e}^{-\Gamma\mathrm{e}^{-\beta V}t}\mathrm{d}t = -\frac{1}{\Gamma}\mathrm{e}^{\beta V}\left[\mathrm{e}^{-\Gamma\mathrm{e}^{-\beta V}t}\right]_0^\infty = \frac{1}{\Gamma}\mathrm{e}^{\beta V}\end{aligned} \tag{6.11}$$

We remark, that Γ and V may be dependent on additional constants, like ϵ_{MB}.

6.3.3 Time-Dependent Barriers

Now we extend the toy model from section 6.3.2 to support a general time-dependent barrier $V(t)$. The calculation proceeds in a very similar way, starting from a rate equation:

$$\frac{\mathrm{d}}{\mathrm{d}t}n(t) = -\Gamma\mathrm{e}^{-\beta V(t)}n(t) \tag{6.12}$$

$$\Leftrightarrow\frac{1}{n(t)}\frac{\mathrm{d}}{\mathrm{d}t}n(t) = \frac{\mathrm{d}}{\mathrm{d}t}\log n(t) = -\Gamma\mathrm{e}^{-\beta V(t)} \tag{6.13}$$

$$\Rightarrow n(t) = N\mathrm{e}^{-\int_0^t \Gamma\mathrm{e}^{-\beta V(t')}\mathrm{d}t'} = N\mathrm{e}^{-I(t)} \tag{6.14}$$

Again, the probability to stay in the first state is $P(t'\geq t) = \frac{n(t)}{N} = \mathrm{e}^{-I(t)}$, leading to a jump probability of:

$$p(t) = \frac{\mathrm{d}}{\mathrm{d}t}P(t'\leq t) = \frac{\mathrm{d}}{\mathrm{d}t}\left(1 - P(t'\geq t)\right) = -\frac{\mathrm{d}}{\mathrm{d}t}P(t'\geq t) = \mathrm{e}^{-I(t)}\frac{\mathrm{d}}{\mathrm{d}t}I(t) \tag{6.15}$$

Also, like in the previous case, we calculate the mean using integration by parts and leveraging $\lim_{t\to\infty} P(t'\geq t) = 0$:

$$\begin{aligned}\langle\tau\rangle &= \int_0^\infty tp(t)\mathrm{d}t = \int_0^\infty P(t'\geq t)\mathrm{d}t = \int_0^\infty \mathrm{e}^{-I(t)}\mathrm{d}t \\ &= \int_0^\infty \mathrm{e}^{-\int_0^t \Gamma\mathrm{e}^{-\beta V(t')}\mathrm{d}t'}\,\mathrm{d}t\end{aligned} \tag{6.16}$$

The last integrals cannot be simplified further and have to be solved with a specific model for $V(t)$.

6.3.4 Linearly Dropping Barriers

Finally, we are able to evaluate the mean metabasin lifetime for our model $V(t) = V_0 - \lambda\dot{\gamma}t$. First we evaluate the integral $I(t)$:

$$\begin{aligned} I(t) &= \int_0^t \Gamma \mathrm{e}^{-\beta V(t')}\mathrm{d}t' = \int_0^t \Gamma \mathrm{e}^{-\beta V_0 + \beta\lambda\dot{\gamma}t'}\mathrm{d}t' = \Gamma \mathrm{e}^{-\beta V_0}\int_0^t \mathrm{e}\beta\lambda\dot{\gamma}t'\mathrm{d}t' \\ &= \Gamma\frac{\mathrm{e}^{-\beta V_0}}{\beta\lambda\dot{\gamma}}\left[\mathrm{e}^{\beta\lambda\dot{\gamma}t'}\right]_0^t = \Gamma\frac{\mathrm{e}^{-\beta V_0}}{\beta\lambda\dot{\gamma}}\left(\mathrm{e}^{\beta\lambda\dot{\gamma}t}-1\right) \end{aligned} \tag{6.17}$$

Next, we solve eq. (6.16):

$$\begin{aligned} \langle\tau\rangle &= \int_0^\infty \mathrm{e}^{-\Gamma\frac{\mathrm{e}^{-\beta V_0}}{\beta\lambda\dot{\gamma}}\left(\mathrm{e}^{\beta\lambda\dot{\gamma}t}-1\right)}\mathrm{d}t = \mathrm{e}^{\frac{\Gamma}{\beta\lambda\dot{\gamma}}\mathrm{e}^{-\beta V_0}}\int_0^\infty \mathrm{e}^{-\frac{\Gamma}{\beta\lambda\dot{\gamma}}\mathrm{e}^{-\beta V_0}\mathrm{e}^{\beta\lambda\dot{\gamma}t}}\mathrm{d}t \\ &= \mathrm{e}^{\frac{\Gamma}{\beta\lambda\dot{\gamma}}\mathrm{e}^{-\beta V_0}}\left[\frac{1}{\beta\lambda\dot{\gamma}}\mathrm{Ei}\left(-\frac{\Gamma}{\beta\lambda\dot{\gamma}}\mathrm{e}^{-\beta V_0}\mathrm{e}^{\beta\lambda\dot{\gamma}t}\right)\right]_0^\infty \\ &= -\frac{1}{\beta\lambda\dot{\gamma}}\mathrm{e}^{\frac{\Gamma}{\beta\lambda\dot{\gamma}}\mathrm{e}^{-\beta V_0}}\mathrm{Ei}\left(-\frac{\Gamma}{\beta\lambda\dot{\gamma}}\mathrm{e}^{-\beta V_0}\right) \\ &= \frac{1}{\beta\lambda\dot{\gamma}}\mathrm{e}^{\frac{\Gamma}{\beta\lambda\dot{\gamma}}\mathrm{e}^{-\beta V_0}}\mathrm{e}^{-\frac{\Gamma}{\beta\lambda\dot{\gamma}}\mathrm{e}^{-V_0\beta}}\mathrm{U}\left(1,1,\frac{\Gamma}{\beta\lambda\dot{\gamma}}\mathrm{e}{-V_0\beta}\right) \\ &= \frac{1}{\beta\lambda\dot{\gamma}}\mathrm{U}\left(1,1,\frac{\Gamma}{\beta\lambda\dot{\gamma}}\mathrm{e}^{-V_0\beta}\right) \end{aligned} \tag{6.18}$$

For details about the exponential integral function Ei and Tricomi's confluent hypergeometric function U see appendix A. The notation using the hypergeometric function in eq. (6.18) has not only the advantage, that it looks much cleaner, but is also numerically much more stable than the Ei functions a few lines before for our range of values. We are are not interested in the asymptotic behavior of the waiting time for the shear and the temperature dominated regime.

6.3.5 Shear dominated regime

In case of the shear dominated regime, we have $\beta \to \infty$. With the use of eq. (A.5) in appendix A, we can now write:

$$\lim_{\beta\to\infty}\langle\tau\rangle = \lim_{\beta\to\infty}\frac{1}{\beta\lambda\dot{\gamma}}\mathrm{U}\left(1,1,\frac{\Gamma}{\beta\lambda\dot{\gamma}}\mathrm{e}^{-V_0\beta}\right) = \frac{V_0}{\lambda\dot{\gamma}} \tag{6.19}$$

This result gives us the correct $\langle\tau\rangle \propto \frac{V_0}{\dot{\gamma}}$ dependence. In the picture of the sheared energy landscape, the barrier height of the current metabasin $V_0(\epsilon_{\mathrm{MB}})$, which is dependent on the metabasin energy, is constantly lowered, proportional to $\dot{\gamma}$, as the landscape is sheared/tilted. We are now interested in the parameter λ. However, to determine λ, we have to know the barrier height $V_0(\epsilon_{\mathrm{MB}})$. In section 2.5.1 we described that the definition of the metabasin depends on the system trajectory. We have seen in section 3.1.2 and section 3.1.3, that there is only a small temperature dependence in the metabasin definition in the equilibrium. However at temperature far below T_g, the situation is much different. Here, we might see only few forward-backward jumps and in the zero temperature limit, the metabasins constructed from the trajectory will only contain a single MS. However, single minimized structures, which we can compare with inherent

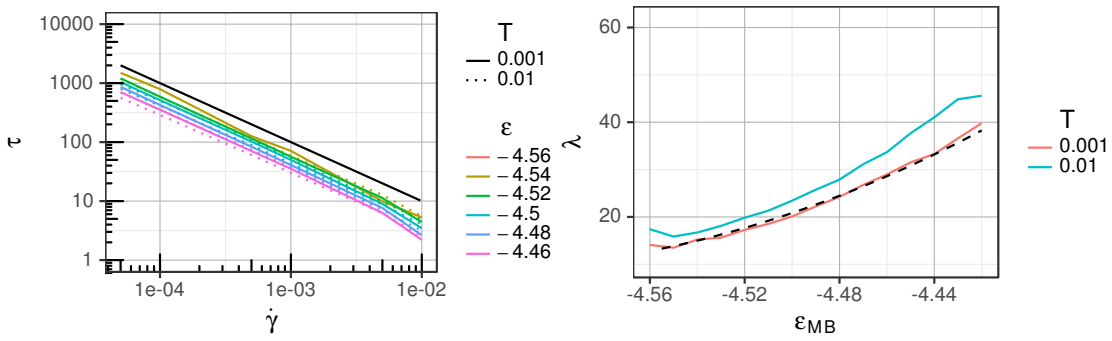

(a) $\langle \tau_{\mathrm{MB}} | \epsilon_{\mathrm{MB}}; T, \dot{\gamma} \rangle$ (b) $\lambda(\epsilon_{\mathrm{MB}}; T)$

Figure 6.8: (a) Metabasin lifetime at very low temperatures, which are used to determine λ. The black solid line acts as a guide to the eye and has a fixed slope of -1. (b) λ as calculated from a linear fit to the data in (a), assuming a fixed slope of -1 and using only data with $\dot{\gamma} \leq 5 \cdot 10^{-3}$. The dashed lines represents a polynomial fit of second order to $\lambda(\epsilon_{\mathrm{MB}})$, which is used for energies $\epsilon_{\mathrm{MB}} \geq -4.55$.

structures in the quiescent case, have a constant activation energy $V_0(\epsilon_{\mathrm{MB}})$ (see section 3.1.1). Using this activation energy, we can now fit the data, displayed in fig. 6.8a, to calculate λ. We remark that following our argumentation, for the crossover between the temperature and shear rate dominate regime, some kind of effective barrier height $V_0(\epsilon_{\mathrm{MB}}, T, \dot{\gamma})$ is needed, which is in turn dependent on the shear rate and the temperature.

As we can see in fig. 6.8, even for temperatures as low as $T = 0.001$ and $T = 0.01$ we see a clear difference in the calculated value of λ. In literature, this strong dependence is described well by [Chattoraj et al., 2010]. Going forward with our models, we use a polynomial fit of second order, to parameterize $\lambda(\epsilon_{\mathrm{MB}})$ using the lowest temperature $T = 0.001$, as it is shown in fig. 6.8b. However, we have to keep in mind, that our choice of lambda may not yet represent the $T \to 0$ limit. Fitting a non-constant $\lambda(\epsilon_{\mathrm{MB}})$ for a constant barrier height and seeing, that $\lambda(\epsilon_{\mathrm{MB}})$ decreases for small energies, is equivalent to non-constant decreasing energy barriers for smaller energies and a constant $\lambda(\epsilon_{\mathrm{MB}})$. Looking at fig. 3.6 in section 3.1.1, our data does not disagree with this assumption. However, our errors in are still too high, to put the calculated $V(\epsilon_{\mathrm{IS}})$ into the fit. Therefore, we will proceed with the polynomial fitted non-constant $\lambda(\epsilon_{\mathrm{MB}})$.

6.3.6 Temperature dominated regime

We will now look at the temperature dominated regime, which is found in the limit $\dot{\gamma} \to 0$. Using eq. (A.6) in appendix A, we write:

$$\lim_{\dot{\gamma}\to 0} \langle \tau \rangle = \frac{1}{\beta\lambda} \lim_{\dot{\gamma}\to 0} \frac{1}{\dot{\gamma}} \mathrm{U}\left(1, 1, \frac{1}{\dot{\gamma}} \frac{\Gamma}{\beta\lambda} \mathrm{e}^{-V_0\beta}\right) = \frac{1}{\Gamma} \mathrm{e}^{V_0\beta} \tag{6.20}$$

Fortunately, this is exactly the same Arrhenius result, we would expect in the case of constant barriers. As we are in the temperature dominated regime, we must be above the glass transition temperature T_g. Therefore, the barrier height is determined by the $V(\epsilon_{\mathrm{MB}})$, which can be calculated in the quiescent state (see section 3.1.1).

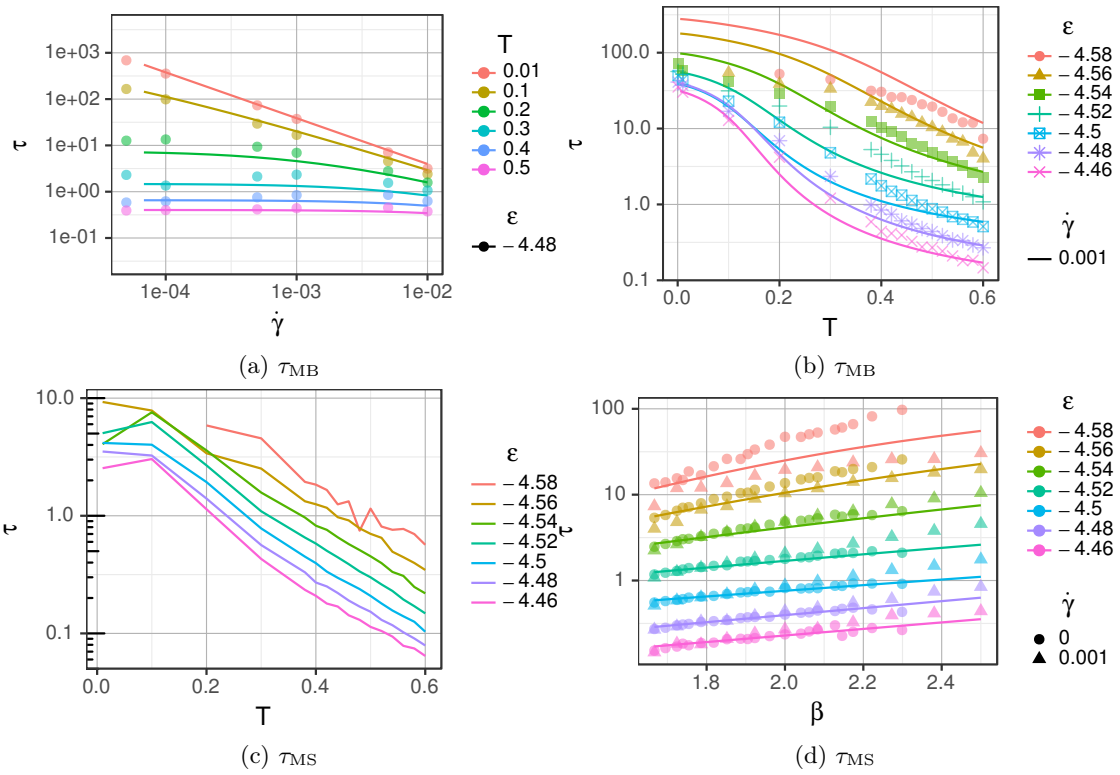

(a) τ_{MB} (b) τ_{MB}

(c) τ_{MS} (d) τ_{MS}

Figure 6.9: Comparison of metabasin lifetime (points) with the data generated from the model (lines). In (a) we show a few energies over a whole range of shear rates in the crossover regime. (b) shows the crossover for the shear rate $\dot{\gamma} = 0.001$ in the middle of our explored range. (c) shows the MS lifetimes τ_{MS} for the same parameter range as (b) and the shear rate $\dot{\gamma} = 0.001$. (d) compares data above T_g for $\dot{\gamma} = 0.001$ and $\dot{\gamma} = 0$.

6.3.7 Crossover regime

Using the fit of λ in section 6.3.5, we can now calculate the metabasin waiting times in the crossover regime in our model. We remark, that the model is very dependent on the effective metabasin barrier height $V(\epsilon_{\mathrm{MB}}, \dot{\gamma}, T)$. For energies $\epsilon_{\mathrm{MB}} < -4.5$ the barrier height changes strongly in dependence of the temperature and shear rate. However, for energies $\epsilon_{\mathrm{MB}} \geq -4.5$ the barrier height stays roughly constant at $V(\epsilon_{\mathrm{MB}}, \dot{\gamma}, T) \approx 1$ in the whole crossover region. Therefore, in fig. 6.9a we find that the model matches the data quite well for high energies.

In fig. 6.9b we select an intermediate shear rate within the crossover regime and see some substantial deviations in the slope at high temperatures, especially at high energies. The deviations in the zero temperature limit are expected, as we used the metabasin barrier height gathered at $T > T_g$ and not an effective barrier height. In the temperature range between $T = 0.4$ and $T = 0.6$, we see even for intermediate shear rates, that the waiting times follow perfect exponential behavior. This behavior is not caused by the construction of the metabasins, as it also appears in the single MS statistics (fig. 6.9c). Therefore, this has to be another temperature dependent effect, which makes the traversal of a MS longer at lower temperatures than our model predicts. In fig. 6.9d we see that the non-exponential form of the model results matches well the

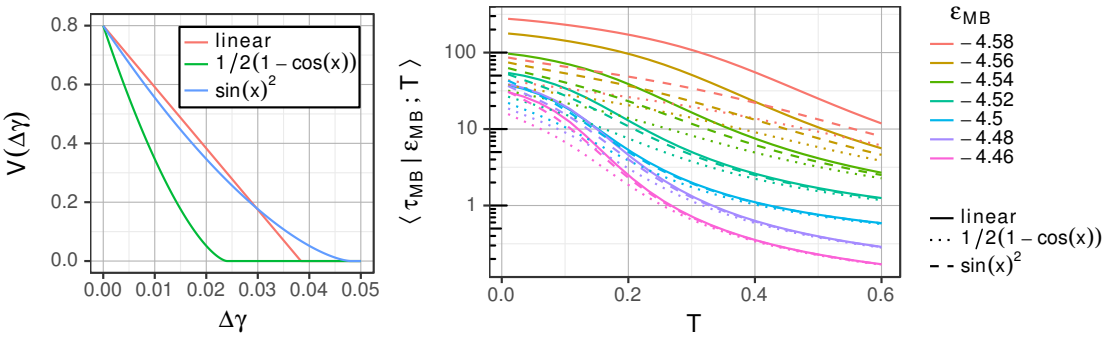

(a) (b)

Figure 6.10: Comparison of different models for the potential energy landscape. (a) Barrier height functions of the given potential. We calculated the height difference between the minimum at $x = 0$ and the adjacent the maximum with respect to the strain $\Delta\gamma = \dot{\gamma}t$. For all potentials, we used the following set of parameters: $\dot{\gamma} = 10^{-3}$, $T = 0.4$, $\epsilon_{\mathrm{MB}} = -4.5$. (b) Metabasin waiting time as calculated for different potentials at $\dot{\gamma} = 10^{-3}$.

Arrhenius behavior of unsheared simulations.

It could well be possible, that the shape of the energy landscape is relevant, as up until now, we have used only a model with constant drop rate λ. In general, various shapes are conceivable, for example $V(x) = \sin^2(x) - \lambda\Delta\gamma x$ or $V(x) = \frac{1}{2}(1 - \cos(x)) - \lambda\Delta\gamma x$, with $\Delta\gamma = \dot{\gamma}t$. The last term represents the tilt of our energy landscape. Conclusively, we check in fig. 6.10 the influence of different models on the waiting times. In fig. 6.10a we see the behavior of the energy barrier for all different models. By construction, they all show a different intersection with $V = 0$. This would require a different parameter λ, calibrated for each model to fit our data. As we are only interested in qualitative results, we skip this step and look directly at our waiting times in fig. 6.10b, which are all calculated for the same $\lambda(\epsilon_{\mathrm{MB}})$. We see immediately, that neither the model nor λ has much influence on the high temperature regime. Therefore, we have still the discrepancy between the data and the model in this regime. In the low temperature limit, the deviations in the waiting times between the models are mainly caused by our choice of λ. The influence of the model is best seen at $T \approx 0.2$, where the slope and the distance of τ_{MB} at different ϵ_{MB} depends strongly on the choice of the model.

In conclusion, our models can describe the crossover regime to some approximation, especially in relation to the variation of shear rates and at high energies. Further research is needed to analyze why all our models give the wrong exponential dependence for $T > T_g$ of the metabasin and minimized structure lifetimes on the temperature at intermediate shear rates.

6.3.8 Superposition Model

Another approach to describe the metabasin lifetime during the crossover is a simple superposition model. The basic principle is to add the mean transition caused by the shear and by the temperature to calculate the mean waiting time. Therefore, in this model, we simply add two

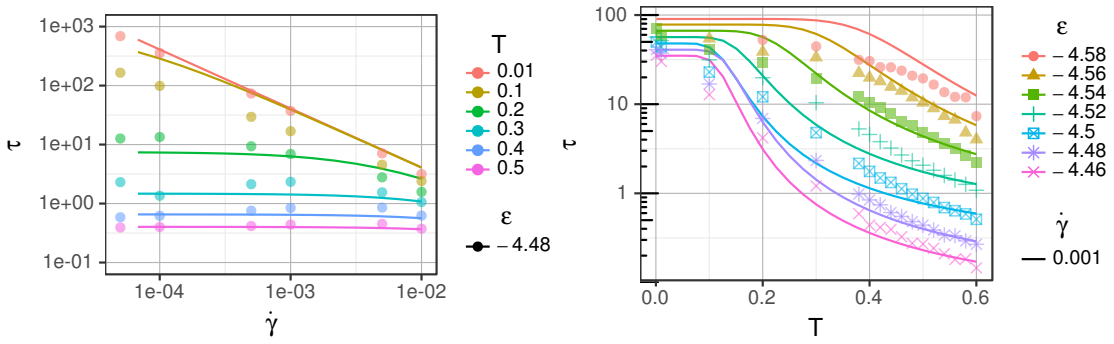

(a) (b)

Figure 6.11: Metabasin lifetimes for superposition model. To allow for a direct comparison with the results in section 6.3.7, we use the same parameters as in fig. 6.9.

rates, one specifying a jump rate for zero temperature and one for zero shear rate:

$$\langle \Gamma | \epsilon_{\mathrm{MB}}; T, \dot{\gamma} \rangle = \langle \Gamma | \epsilon_{\mathrm{MB}}; T = 0, \dot{\gamma} \rangle + \langle \Gamma | \epsilon_{\mathrm{MB}}; T, \dot{\gamma} = 0 \rangle \tag{6.21}$$

$$\Leftrightarrow \langle \tau | \epsilon_{\mathrm{MB}}; T, \dot{\gamma} \rangle = \frac{1}{\langle \Gamma | \epsilon_{\mathrm{MB}}; T, \dot{\gamma} \rangle} = \frac{1}{\frac{1}{\langle \tau | \epsilon_{\mathrm{MB}}; T=0, \dot{\gamma} \rangle} + \frac{1}{\langle \tau | \epsilon_{\mathrm{MB}}; T, \dot{\gamma}=0 \rangle}} \tag{6.22}$$

In fig. 6.11, we see the results of the superposition model in comparison with the data. The model parameters, namely the waiting times in the shear and temperature dominated regime, have been calculated via the previously determined parameter λ (section 6.3.5) and the energy barrier heights (section 3.1.1):

$$\langle \tau_{\mathrm{MB}} | \epsilon_{\mathrm{MB}}; T = 0, \dot{\gamma} \rangle = \frac{V(\epsilon_{\mathrm{MB}})}{\lambda(\epsilon_{\mathrm{MB}}) \dot{\gamma}} \tag{6.23}$$

$$\langle \tau_{\mathrm{MB}} | \epsilon_{\mathrm{MB}}; T, \dot{\gamma} = 0 \rangle = \frac{1}{\Gamma(\epsilon_{\mathrm{MB}})} \mathrm{e}^{\beta V(\epsilon_{\mathrm{MB}})} \tag{6.24}$$

Comparing the model with the data at different shear rates (fig. 6.11a), we see a relatively good agreement with the data. More details of the crossover can be seen in fig. 6.11b, where we compare at different temperatures. While the higher range of the temperatures shows similar deviations from the data as the previous model section 6.3.7, we see the transition of both regimes as a relatively sharp transition point, especially at high energies. However, this sharpness does not translate to the simulation data. Another problem of this model is, that it reproduces the low temperature regime with a constant, despite there being a strong temperature dependence in the vicinity of $T = 0$ (see [Chattoraj et al., 2010]). So apart from the simplicity of this model, we would prefer one of the cos or $\sin^2$ models from section 6.3.7 to describe the crossover.

6.4 Shear Modulus

In the flow regime, each single stress trajectory shows piecewise linear behavior, as pointed out in [Dubey et al., 2016b]. In their work, the authors argued, that the constant stress in the flow of a big system regime results from a superposition of small systems. While the shear modulus in the

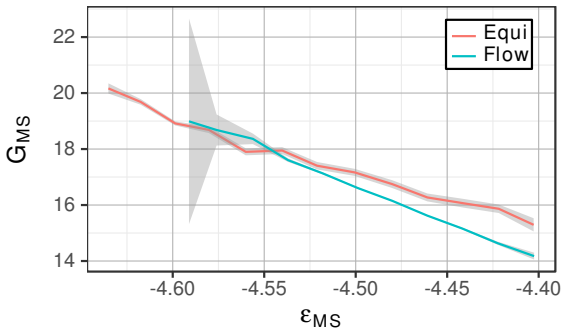

Figure 6.12: Shear modulus in the equilibrium and in the flow regime $\langle G|\epsilon_{\mathrm{MS}}\rangle$, calculated via AQS shear, starting from minimized structures with energy ϵ_{MS} in the trajectory. To increase statistics, especially at low energies, we combined data from temperatures at $T \in \{0.001, 0.005, 0.01\}$, $N = 130$, $\dot{\gamma} = 10^{-4}$.

flow regime is zero in the ensemble average, it is finite for each trajectory. Therefore, the average shear modulus is different than the shear modulus of the ensemble average. We point out, that even for our small system with $N = 130$, it may still be affected by the system size.

For $N = 130$ the linear ranges between plastic events are quite long, although at high stresses, we observe some non-linear behavior (see example trajectories in section 6.1). Here, we will determine the shear modulus using AQS shear, starting at *minimized structures*, which are generated from sample configurations in our trajectories. From these configurations we strain the system within a small interval $\Delta\gamma \leq 10^{-3}$ and determine the shear modulus via linear fit to the resulting stress-strain curve.

As one can see in fig. 6.12, the slope changes from the equilibrium to the flow regime. This is clear evidence, that the states in the flow regime differ from the states in thermal equilibrium despite having the same energies. We refer again to [Isner and Lacks, 2006], where this phenomenon is explained with a model system. In section 6.5, we will use this average shear modulus to estimate the viscosity.

6.5 Viscosity

At high shear rates, depending on the material, the effect of *shear thinning* or *shear thickening* can be observed, which means a decrease/increase in viscosity, as the shear rate is increased. It turns out, that our model glass former exhibits only shear thinning [Varnik and Henrich, 2006]. In simulations this can be measured by the apparent viscosity, which is defined via [Berthier and Barrat, 2002, Lacks, 2002]:

$$\eta = \frac{\sigma}{\dot{\gamma}} \tag{6.25}$$

In order to predict the viscosity, it is therefore sufficient to predict the stresses in the flow regime. But first, we clarify, that from the energy landscape perspective, we can only predict the structural part σ_{IS}, which is close to σ at low shear rates (see section 6.1). However, from [Lacks, 2001], we known already that contribution of the vibrational part to the viscosity is Newtonian

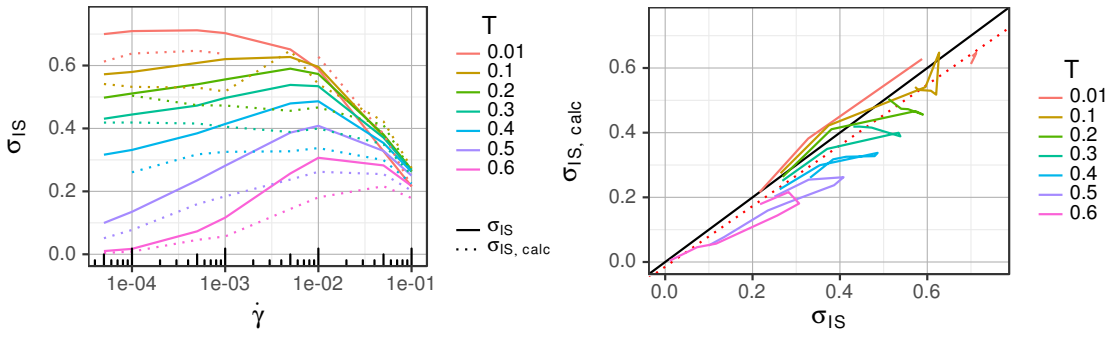

(a) (b)

Figure 6.13: Calculated IS stress compared with the actual IS stress. In (a) we plot against the shear rate $\dot{\gamma}$ and in (b) we show the direct comparison of the absolute values. We show simulation data for $N = 130$ and $\dot{\gamma} \in [5 \cdot 10^{-5}, 10^{-1}]$. In (b), the points for each colored line segment are ordered by the shear rate. The black solid line has a slope of 1 and shows where $\sigma_{\mathrm{IS,calc}} = \sigma_{\mathrm{IS}}$. The red dotted line represents a fit to the data with $\dot{\gamma} = 5 \cdot 10^{-5}$ and has a slope of 0.938(52) and an intercept of $-0.015(24)$.

and therefore shear rate independent. Therefore, the most interesting part is the shear thinning contribution of σ_{IS} and in particular during the crossover regime.

To describe σ_{IS}, we write down a simple model:

$$\langle \sigma_{\mathrm{IS}} \rangle = \frac{1}{2} \int \langle G | \epsilon_{\mathrm{MS}} = \epsilon_{\mathrm{MB}} \rangle \langle \tau_{\mathrm{MB}} | \epsilon_{\mathrm{MB}} \rangle_{\tau_{\mathrm{MB}}} \dot{\gamma} p(\epsilon_{\mathrm{MB}}) \mathrm{d}\epsilon_{\mathrm{MB}} \tag{6.26}$$

Basically, we average over an idealistic stress-strain curve, with the shear modulus determined at the base of the metabasin. For the length of the integration, we chose the distribution of waiting times, found in the flow regime. As we are interested in a time-average, we choose to average over the distribution $p(\epsilon_{\mathrm{MB}})$. Furthermore, we have to use the *time-weighted* average of τ_{MB}, denoted by $\langle ... \rangle_{\tau_{\mathrm{MB}}}$ (see section 3.1.1). This means, that at a fixed energy ϵ_{MB}, we determine the average of τ by weighting each τ with the length τ, to properly reflect the time average, as we have done in the analysis of $p(\epsilon_{\mathrm{MB}})$. The factor $\frac{1}{2}$ is added, as we are interested in the average stress of the whole interval.

The results can be seen in fig. 6.13 for various temperatures and shear rates. They are in quite reasonable agreement, even for high shear rates where the trajectory is far away from the energy landscape. However, we have made several assumptions, that differ from our actual numerical data of single trajectories. First, in our trajectories, we see that the stresses after a stress drop are distributed mostly around a positive value (see also section 3.2.7). As the average value for the initial stress after a stress drop is around $\sigma_{\mathrm{IS}} = 0.38$ for $T = 0.01$, this effect would be clearly visible in our data, but we see only very small deviations at this low temperature. Second, we neglect all possible non-linearity of the stress-strain curves. At high strains of a single MS, we see strong deviations from linearity, *reducing* the stress. However in our results, the actual stresses are even higher than what we have calculated. Still, we cannot exclude some combination of both effects.

Despite these strong differences, the model still appears to make good predictions. A possible explanation might be regarding our $N = 130$ system as a superposition of smaller subsystems.

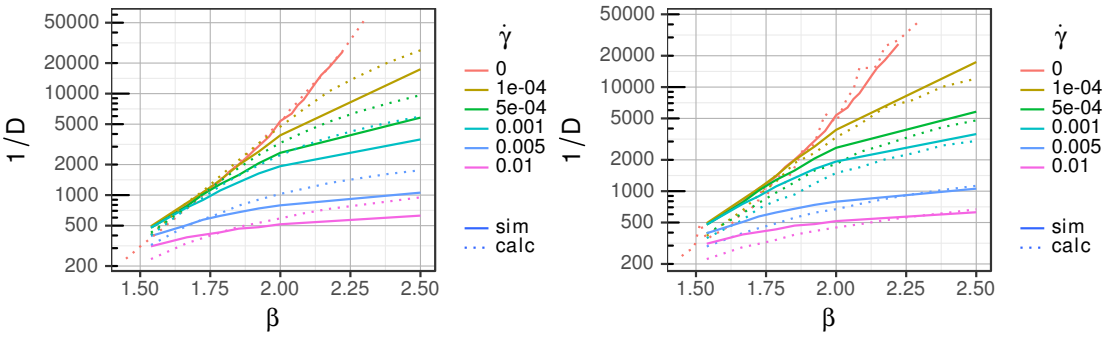

(a) Using $\langle \tau_{\mathrm{MB}} \rangle_{\phi}$ (b) Using $\frac{1}{2}\langle \tau_{\mathrm{MS}} \rangle_{p}$

Figure 6.14: Diffusion coefficient in the crossover regime using (a) the mean metabasin waiting time $\langle \tau_{\mathrm{MB}} \rangle_{\phi}$ and (b) the mean minimized structure relaxation time $\frac{1}{2}\langle \tau_{\mathrm{MS}} \rangle_{p}$. The constant coefficient a^2 was determined using only data from the quiescent state ($\dot{\gamma} = 0$) at temperatures $\beta \geq 1.6$. In (a) we find $a^2 = 0.259(20)$ and in (b) we find $a^2 = 0.278(76)$.

From tests, we know that the $N = 65$ system shows a much lower initial stress after a drop and higher fluctuations, while showing less non-linearity. In literature, we find that (at least in equilibrium) even the $N = 65$ system can be regarded as a superposition of 2-3 small subsystems [Heuer et al., 2005]. Therefore, it might be possible, that our model describes the smallest subsystem and the deviations seen in fig. 6.13 can be explained by some kind of coupling mechanism. We remark, that for a given shear rate, the strongest deviations occur always at the largest stresses.

6.6 Diffusion

Diffusion in the quiescent system can be explained by a continuous time random walk process among metabasins [Doliwa and Heuer, 2003c, Rubner and Heuer, 2008]. The basic idea is, that the system is trapped during some time within a metabasin and then exits randomly [Doliwa and Heuer, 2003d]. Therefore, only the motion between metabasins matters for the evaluation of the diffusion constant. As we want to compare the results from the quiescent system with the sheared system, we will only investigate diffusion in the z direction.

$$D = \frac{a^2}{2N\langle \tau_{\mathrm{MB}} \rangle_{\varphi}} \tag{6.27}$$

The metabasin lifetime is in this case computed from the distribution φ of metabasins, which we introduced in section 3.1.1. Due to the nature of the random walk, the complete temperature dependence is absorbed in the waiting time, and a^2 has no temperature dependence. In case of a sheared system, it would be favorable, to have an equally simple expression. In [Lacks, 2002], it was tried to use the stress σ instead of a waiting time/relaxation time. Thereby, the limiting cases of the temperature dominated and the shear dominated regime could be described. Additionally in [Lemaître and Caroli, 2009], the scaling of the diffusion coefficient with the strain rate at zero temperature has been successfully attributed to avalanches. However, this still leaves open the question of the crossover to the temperature dominated regime.

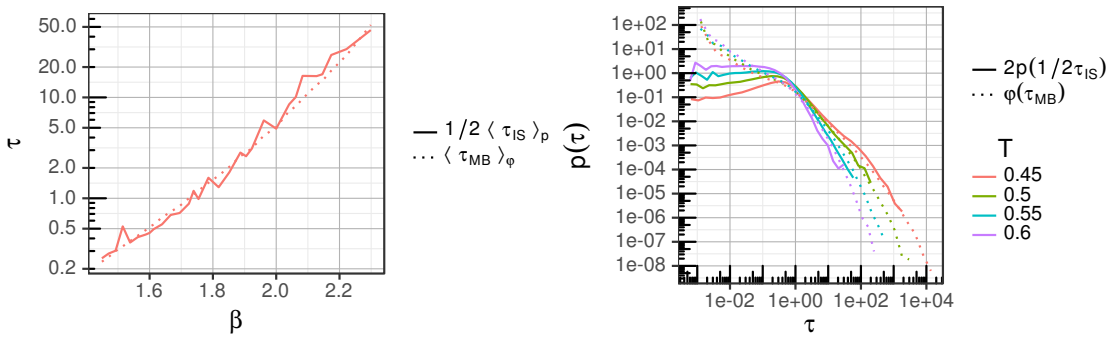

(a) Mean Waiting Times

(b) Waiting Time Distribution

Figure 6.15: (a) Mean waiting time and (b) distributions of waiting times for metabasins $\langle \tau_{\mathrm{MB}} \rangle_\phi$ and for the relaxation times of inherent structures $\frac{1}{2}\langle \tau_{\mathrm{IS}} \rangle_p$ in the quiescent system ($\dot{\gamma} = 0$) for various temperatures.

Our first ansatz uses eq. (6.27) with the definition of metabasins from section 3.2.5 using minimized structures instead of inherent structures for $\dot{\gamma} > 0$. The results can be seen in fig. 6.14a. While for the quiescent state ($\dot{\gamma} = 0$) we have a very good agreement for a constant a^2, there is still some significant temperature or strain rate dependence for $\dot{\gamma} > 0$. However, assuming a constant a^2, it would follow that we have overestimated the relevant timescale for diffusion by τ_{MB} and that there are multiple transitions, relevant for diffusion, within a single metabasin.

Only by chance, we found a similar agreement with a constant a^2 for the quiescent case by replacing $\langle \tau_{\mathrm{MB}} \rangle_\phi$ with another quantity: $\frac{1}{2}\langle \tau_{\mathrm{IS}} \rangle_p$. The quality of the agreement between both waiting times can be seen in fig. 6.15a. We note, that the physical property of $\frac{1}{2}\langle \tau_{\mathrm{IS}} \rangle_p$ is the relaxation time of a single IS. So if one chooses a random point in time, this would be the average remaining time in this inherent structure. Up until the time of this writing, the physical relevance of this agreement between $\langle \tau_{\mathrm{MB}} \rangle_\phi$ and $\frac{1}{2}\langle \tau_{\mathrm{IS}} \rangle_p$ is very unclear. The similarities, however, are even seen in the distributions (fig. 6.15b). In section 3.1.1 we showed that the tail of the distribution is most responsible for the average value, and this is, where both distributions overlap very well. We remark, that this agreement does *not* translate to the energy-resolved averages. Following this surprising and yet unexplained findings, we use $\frac{1}{2}\langle \tau_{\mathrm{IS}} \rangle_p$ to calculate the diffusion constant for the sheared system, replacing τ_{IS} with τ_{MS}. Quite remarkably, these results, shown in fig. 6.14b, are much better than using τ_{MB}, apart from systematic deviations at high temperatures. While one can argue, that the relaxation process of one minimized structures is the relevant process for diffusion in the sheared system, this still leaves open the question of the connection in the quiescent system. However, at this point, we have to leave further physical interpretation for future research.

6.7 Summary

In summary, we could show, that the description of the physical properties of sheared systems in the low temperature limit in terms of the potential energy landscape is possible for shear rates up to $\dot{\gamma} = 10^{-3}$. For higher shear rates, we notice that the ballistic regime during particle movement is responsible for deviations and the caging regime vanishes. In particular, we notice a completely different behavior in the vibrational part of the stress and the structural part. Furthermore, we

have found that the distances of the actual particle configurations and the inherent structures to the minimized structures are highly correlated. We concluded that minimized structures might still be a good candidate for a description in terms of the energy landscape at high shear rates.

For the description of the crossover regime between the shear rate and the temperature dominated regime, we started with the introduction of an effective temperature. Our definition, using the properties of the energy landscape, tells us, that mechanical rejuvenation brings us to energies comparable with temperatures of $T = 0.775$. This would be the upper bound of the energy landscape accessible by shear at zero temperature. We found that our definition of an effective temperature deviates much from literature values, so another approach using waiting times has to be used to describe viscosity or diffusion.

In order to explain the metabasin waiting times, as calculated on the basis of the minimized structures, we came up with a simple rate model. This model resembles the tilt of a fixed energy landscape into a specific direction and thereby neglects the formation of additional minima. The main input of this model are the barrier distribution for a given energy and a function, describing the drop of the energy barrier with strain. This function is dependent on the form of the energy landscape. We showed, that a model $\sin(x)$ and $\sin^2(x)$ landscape produce largely similar results and even a linear barrier drop function can be a valid approximation. With a linear barrier drop, the model is solvable analytically, while the other barrier drop functions require some integrals to be solved numerically. Although we assumed a constant metabasin barrier distribution for the whole crossover regime, the results from the model are in good agreement with our data. The highest discrepancies are in the middle of the crossover region, where we see a slightly wrong temperature dependence, calling for some future adjustments.

After modeling the waiting times in the crossover regime, we discussed key observables like the viscosity and the diffusion constant. We showed, that the structural part of the viscosity can be described in a good approximation with the knowledge of the energy dependence of the shear modulus and the typical metabasin relaxation time. The former was determined to be very non-linear with respect to the energy. We remark, that we could not use our model data here, as we have not yet calculated higher moments to predict the metabasin relaxation time. When analyzing the diffusion constant, we found some systematic deviations when using the metabasin waiting times and assuming an overall constant displacement per jump. This is expected, as the metabasins change their form when decreasing the temperature and jump distances will reduce to single MS jumps in the zero-temperature case. However, without understanding the physical origin, we noticed that using the *minimized structure relaxation time* and a constant displacement, we could provide a good estimation for diffusion constant in the whole crossover regime with slight systematic deviations at high temperatures.

Chapter 7

From Equilibrium to the Sheared System

In this chapter, we will focus mainly on characteristic observables for the sheared system, calculated from equilibrium fluctuations. Of particular interest are the shear stress, the shear modulus and the anisotropy, which we define later. As we have seen in the previous chapters, the energy landscape influences to a great deal the behavior during the overshoot or in the flow regime. Therefore, as the sheared energy landscape is connected to the equilibrium landscape, it seems natural, that some information can readily be extracted by looking at data gathered during equilibrium fluctuations. For example, this idea was followed in [Abraham and Harrowell, 2012], where the onset of viscous behavior was seen to be a direct consequence of residual shear stress, trapped in inherent structures. One key observable in this work are the stress fluctuations, as they are connected in the linear response regime to infinite frequency shear modulus G_∞ by:

$$G_\infty = \frac{V}{k_B T}\langle \sigma^2 \rangle \tag{7.1}$$

Therefore, we will first focus on the calculation of the stress distribution. To be precise, we will determine the distribution of σ_{IS}, which is connected to the plateau shear modulus G_p, which is the actual value measured by most experiments [Puosi and Leporini, 2012]. In simulations the equilibrium stress distribution is directly computable from the simulation data. However, in experiments the equilibrium $\langle \sigma_{\mathrm{IS}}^2 \rangle$ is more difficult to determine. It can either be derived indirectly from G_p or measured from the height of the shear stress autocorrelation function in step strain experiments.

Another way to calculate $\langle \sigma_{\mathrm{IS}}^2 \rangle$ is through knowledge about amorphous structure and the potential. As many amorphous materials share a common phenomenology of the glass transition and rheological properties, it is our central interest to gain insight about the influence of the structure. We will first derive the per-contact stress distribution using a method, that can be applied to other observables as well. Then, by using the two-contact distribution, we will show that also the per-particle distributions for the stress and all other observables can easily be calculated using numerical integration. Finally, we will be able to analyze the dependence of the system-wide distribution on the per-particle distributions. This method will not only be applied to the shear stress, but also to the shear modulus. We refer to table 7.1 for a short overview of

$\langle \sigma_{ij}^{pn} \rangle$	Average contact stress
$\langle (\sigma_{ij}^{pn})^2 \rangle$	Contact stress variance
$p(\sigma_{ij}^{pn})$	Contact stress distribution
$\langle \sigma_{ij}^{pn_1} \sigma_{ij}^{pn_2\prime} \rangle$	Stress covariance for distinct contacts of a single particle
$\langle \sigma_i^p \rangle$	Average particles stress
$\langle (\sigma_i^p)^2 \rangle$	Particles stress variance
$\langle \sigma_i^p \sigma_i^{n\prime} \rangle$	Stress covariance of distinct particles
$\langle 2V\sigma^p \rangle$	Contribution of type "p" particles to the system stress, scaled by volume
$\langle (2V\sigma)^2 \rangle$	System stress variance, scaled by volume
N_c^{AB}	Number of type B contacts for a given type A particle

Table 7.1: Description of commonly used variables in this chapter. The index p denotes the particle type and the index n the neighbor types. Numeric suffices are needed if two different contacts are involved. For readability, we often drop type indices, when calculations are performed for arbitrary particle-neighbor types. We remark, that only in the equilibrium the products given in this table are equivalent to covariances because the average values of the multiplicands are zero.

the common terminology, used in this section.

To further quantify the structural influence on the system stress, we look at the anisotropy of the strained system. In the equilibrium, the ensemble average of inherent structures $g(r)$ is totally isotropic. However, by averaging a sub-ensemble with a fixed residual stress, we find an anisotropy. A similar anisotropy has been reported before in start-up shear simulations [Koumakis et al., 2012, Koumakis et al., 2016, Shrivastav et al., 2016b, Denisov et al., 2015]. Our aim at this point is to analyze the connection of the anisotropy and the stress further, using the methods described earlier. We note, that both the anisotropy and the stress in equilibrium depend completely on the choice of the coordinate frame. Therefore, any connection between the structural relaxation and long-time persistent Eshelby events [Lemaître, 2014, Illing et al., 2016] are also subject to the coordinate frame [Chowdhury et al., 2016].

7.1 Single Contact Stress Distribution

In this section, we show that from knowledge of $g(r)$, assumed isotropy and full knowledge of the force field, we can in a straightforward way derive the single-contact stress distribution. In later sections, we will use the same formalism to calculate other observables and also use our results, to calculate the per-particle stress distribution.

7.1.1 Stress in Spherical Coordinates

The stress for the whole simulation box is defined as:

$$\sigma = \frac{1}{V} \sum_i \frac{p_{i,x} p_{i,y}}{m_i} - \frac{1}{V} \sum_{ij, i<j} r_{ij,x} F_{ij,y} \tag{7.2}$$

In this section we are interested only in the distribution of stress for the energy minima, so the first summand is zero. As the stress tensor is symmetric, we can write:

$$\sigma_{\mathrm{IS}} = -\frac{1}{V}\frac{1}{2}\sum_{ij} r_{ij,y}F_{ij,x} = \sum_{ij}\sigma_{ij} \tag{7.3}$$

For future simplification we regard the sum over i as the sum over all particles and the sum over j as the neighbors. Alternatively, one might think of σ_{ij} representing all the contacts in the system. The summation may then be split as a sum over all combinations of particle/neighbor types. In the following, we look at only one combination of particle/neighbor types.

Taking the ensemble average, we can rewrite the sum as an integral over the neighbor density $n_{pn}(r,\theta,\phi)$, switching to spherical coordinates for convenience. Thereby, we use $y = r\sin(\theta)\sin(\phi)$ and $F_x(r) = F(r)\sin(\theta)\cos(\phi)$:

$$\langle\sigma_{\mathrm{IS}}\rangle = -\frac{1}{2}\rho_p\int_0^\infty rF_{pn}(r)\sin^2(\theta)\frac{1}{2}\sin(2\phi)n_{pn}(r,\theta,\phi)r^2\sin\theta\mathrm{d}r\mathrm{d}\phi\mathrm{d}\theta \tag{7.4}$$

The constants ρ_p, ρ_n denote the the particle density of interest and the neighboring particle respectively. The functions $n_{pn}(r,\theta,\phi)$ is the neighbor density for a given particle/neighbor type combination, which follows directly from the definition of $g_{pn}(r,\theta,\phi)$:

$$n_{pn}(r,\theta,\phi) = g_{pn}(r,\theta,\phi)\rho_n \tag{7.5}$$

7.1.2 Deriving the Contact Stress Distribution

As we have seen in section 7.1.1, the stress is a sum over all contacts between particles. Now, we want to derive the distribution of a single particle contact. Since we are in equilibrium, we can assume all particles to be distributed isotropically. It does not matter that we have a small system, because we are looking at the distribution in the ensemble average over all possible configurations. The distribution over the particle contacts derives from eq. (7.5), which we divide by the average number of interacting particles. For simplicity, we drop the index np and remember to sum up later over all particle/neighbor type combinations. Due to isotropy, $n(r,\theta,\phi)$ is spherically symmetric, and therefore does not depend on the angles θ, ϕ. We also take into account that the force vanishes at the cutoff radius r_c, so there are no contacts with $r > r_c$.

$$p(r,\theta,\phi) = p(r) = \frac{\int_0^\pi\int_0^{2\pi} n(r)r^2\sin\theta\mathrm{d}\theta\mathrm{d}\phi}{\int_0^{r_c}\int_0^\pi\int_0^{2\pi} n(r)r^2\sin\theta\mathrm{d}r\mathrm{d}\theta\mathrm{d}\phi} = \frac{n(r)r^2}{\int_0^{r_c} n(r)r^2\mathrm{d}r}, \qquad r\in[0,r_c] \tag{7.6}$$

To have a uniform distribution over the surface, we use the following distribution, as derived in [Weisstein, c]:

$$p(\phi) = \frac{1}{2\pi} \tag{7.7}$$

$$p(\theta) = \frac{1}{2}\sin\theta \tag{7.8}$$

The mean stress for a single contact is then given by:

$$\langle \sigma_{ij} \rangle = -\int_0^{r_c}\int_0^{\pi}\int_0^{2\pi} rF(r)\sin^2(\theta)\frac{1}{2}\sin(2\phi)p_r(r)p_\theta(\theta)p_\phi(\phi)\mathrm{d}r\mathrm{d}\theta\mathrm{d}\phi = 0 \tag{7.9}$$

As we see, all contact stresses are zero, thus leading to a zero particle stress and to a zero system stress. We will use the integrand of formula eq. (7.9) to derive the distribution of the single contact stresses $p(\sigma_{ij})$, which is done via transformation of the probability densities $p(r)$, $p(\theta)$, $p(\phi)$.

In general, such a transformation is written as:

$$p_Y(y) = \sum_{x, f(x)=y} \frac{p_X(x)}{|f'(x)|} \tag{7.10}$$

We sum over all probabilities $p_X(x)$ where $f(x) = y$, taking into account the derivative of $f(x)$. For an injective function $f(x)$, this can also be written as:

$$p_Y(y) = \frac{p_X(f^{-1}(y))}{|f'(f^{-1}(y))|} = \left|\frac{\mathrm{d}f^{-1}(y)}{\mathrm{d}y}\right| p_X(f^{-1}(y)) \tag{7.11}$$

As an example, we first calculate for $y = \frac{1}{2}\sin(2\phi)$ using a uniform distribution of $\phi \in [0, 2\pi]$ and eq. (7.11):

$$p_y(y) = \frac{4}{\sqrt{1-4y^2}}\frac{1}{2\pi}, \qquad y \in [-\frac{1}{2}, \frac{1}{2}] \tag{7.12}$$

We have multiplied by 4, as we hit the $\sin(2\phi)$ four times, evaluating the inverse function at y. Similarly, we proceed with $z = \sin^2(\theta)$, using $p(\theta) = \frac{1}{2}\sin\theta$.

$$p_z(z) = \frac{2}{\sqrt{(1-z)z}}\frac{1}{2}\sqrt{z} = \frac{1}{\sqrt{(1-z)}}, \qquad z \in [0, 1] \tag{7.13}$$

Again, the factor 2 arises from the evaluation of the inverse function.

Calculating the product of two variables $Y = X_1X_2$ is done in a similar fashion:

$$p_Y(y) = \int p_{X_1}(x_1)p_{X_2}(y/x_1)\frac{1}{|x_1|}\mathrm{d}x_1 \tag{7.14}$$

Here we integrate over all density products, which have $x_2 = y/x_1$.

Using eq. (7.14), we can calculate the probability of the complete angular part $w = \sin^2(\theta)\frac{1}{2}\sin(2\phi)$:

$$p_w(w) = \int p_y(y)p_z(w/y)\frac{1}{|y|}\mathrm{d}y = \frac{1}{\pi}\int \frac{1}{|y|\sqrt{(1-4y^2)(1-\frac{w}{y})}}\mathrm{d}y, \qquad w \in [-\frac{1}{2}, \frac{1}{2}] \tag{7.15}$$

We do not solve this integral analytically here, but rather use a numeric adaptive quadrature algorithm [Jones et al., 2001]. The results can be seen in fig. 7.1a.

For the radial part $v = rF(r)$, we proceed similarly, using eq. (7.11). Therefore, we calculate the inverse of $v(r)$, which gives us 1 or 2 distances r, depending on v. As we have full knowledge of the mathematical form of our forces (see section 2.2), we can use the analytical derivative at these

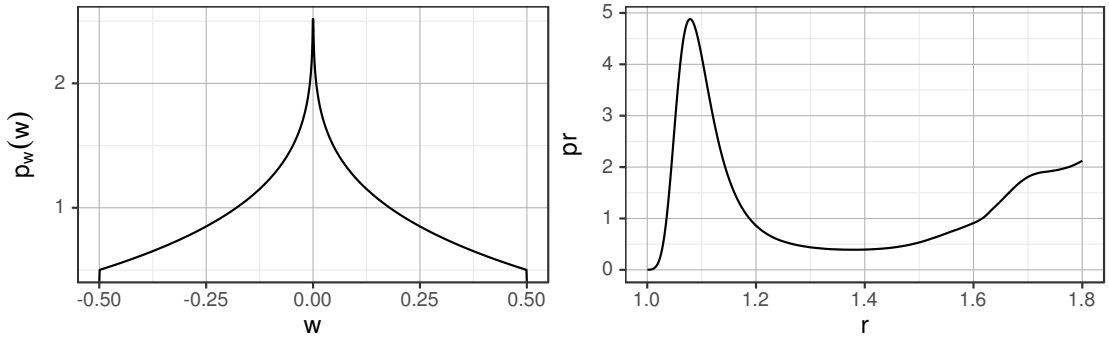

(a) $p\left(\sin(\theta)\frac{1}{2}\sin(2\pi)\right)$ (b) $p(r)$

(c) $rF(r)$ (d) $p\,(rF)$

Figure 7.1: Evaluation of the angular distribution $p_w(w)$ and the radial distribution $p_v(v)$. We show only results for contacts of A-type particles and neighbors. In (a) we see the distribution of the angular part, as evaluated from eq. (7.15). (b) shows the probability to have a contact of type A at distance r. (c) shows the function $rF(r)$, whose inverse has to be evaluated for the calculation of (d). In (d) the distribution of the radial component $p_v(v) = p(rF)$ is shown.

points to calculate $p_v(v)$. The form of $p_v(v)$ is shown in fig. 7.1d. Its first peak results from the second distance appearing for $v = rF > 0$ (compare fig. 7.1c). The height results from the low derivative near the cutoff. The second peak comes from the polynomial interpolation function, which was introduced to keep the second derivative zero at the cutoff r_c (see section 2.2). The third peak results from the peak in rF, where its derivative is zero, and no higher values can be found.

Again using eq. (7.14), we now finally calculate $p(\sigma_{ij})$ from $p_v(v)$ and $p_w(w)$.

$$p(\sigma_{ij}) = p(-rF\sin^2(\theta)\frac{1}{2}\sin(2\phi)) = p(-vw) = p(vw) = \int p_v(u/w)p_w(w)\frac{1}{|w|}\mathrm{d}w \tag{7.16}$$

The sign vanishes, as $p(w)$ is symmetric.

7.1.3 Comparison with simulation results

The distribution resulting from eq. (7.16) is shown in fig. 7.2a. For small stresses it follows a power-law behavior across 27 decades and a small exponential tail at high stresses ($\sigma_{ij} > 1.5$). We

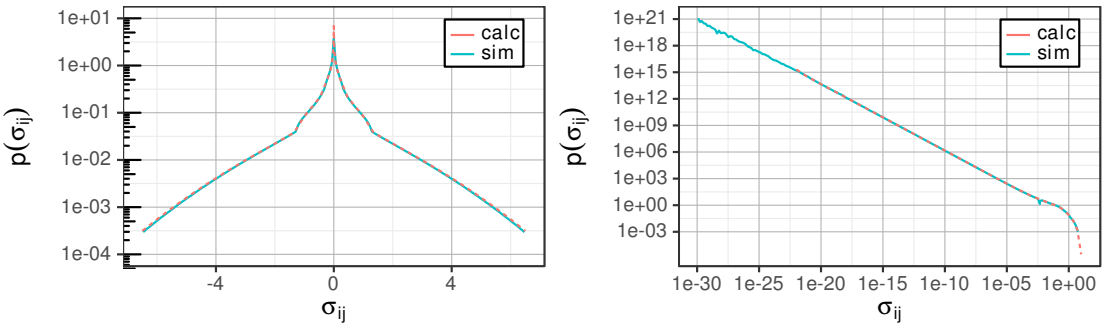

(a) Log-Normal (b) Log-Log

Figure 7.2: Stress contact distribution $p(\sigma_{ij})$ as determined via calculation (calc) and simulation (sim). In (a) we show in detail the tail of the distribution and in (b) we show the strong power-law behavior for small stresses.

see that the values from our calculation fit the real distribution perfectly, reproducing the special form of the crossover between power-law and exponential behavior. In passing, we note that we have interpolated our $g(r)$ data with a cubic spline for greater accuracy between bins.

Finally in this section, we can compare our equilibrium results with the flow regime of the sheared system. Figure 7.3 shows data from equilibrium simulations at $T = 0.5$ and from sheared simulations at $T = 0.01$ and $\dot{\gamma} = 10^{-4}$. As seen in section 6.1, the properties of the system are clearly dominated by the shear rate for the latter set of parameters. The overall distribution of system stresses differs significantly between the sheared and the non-sheared case. Therefore, we look at the stress contact distribution for fixed values of the system stress σ. However, the distributions for the equilibrium and the sheared system are indistinguishable by eye. Both times, we see the same power-law behavior for small stresses. The thinning of the data at low σ_{ij} has statistical reasons, as we have only a finite number of simulation data available. However, the tail of the σ_{ij} distribution shows a significant systematic shift to the right with increasing system stress σ. This shift look identical for both the sheared system and the system in equilibrium. Therefore we can say, that both the equilibrium and flow regime are indistinguishable in terms of the contact stress distribution.

7.2 Per-Particle and System Stress Distribution

We will now show how to calculate the per-particle and the system stress distribution in equilibrium using our knowledge of the contact stress distribution. The method we derive here, will later be used not only to calculate the distribution of stresses, but also the affine contribution to the shear modulus in section 7.3 and the anisotropy in section 7.5.

7.2.1 Two-Contact Distribution

To calculate the distribution of the stress for a single particle and other observables, we need the distribution of two contacts:

$$p(r_1, r_2, \cos\alpha) = p(r_2, \cos\alpha | r_1) p(r_1) \tag{7.17}$$

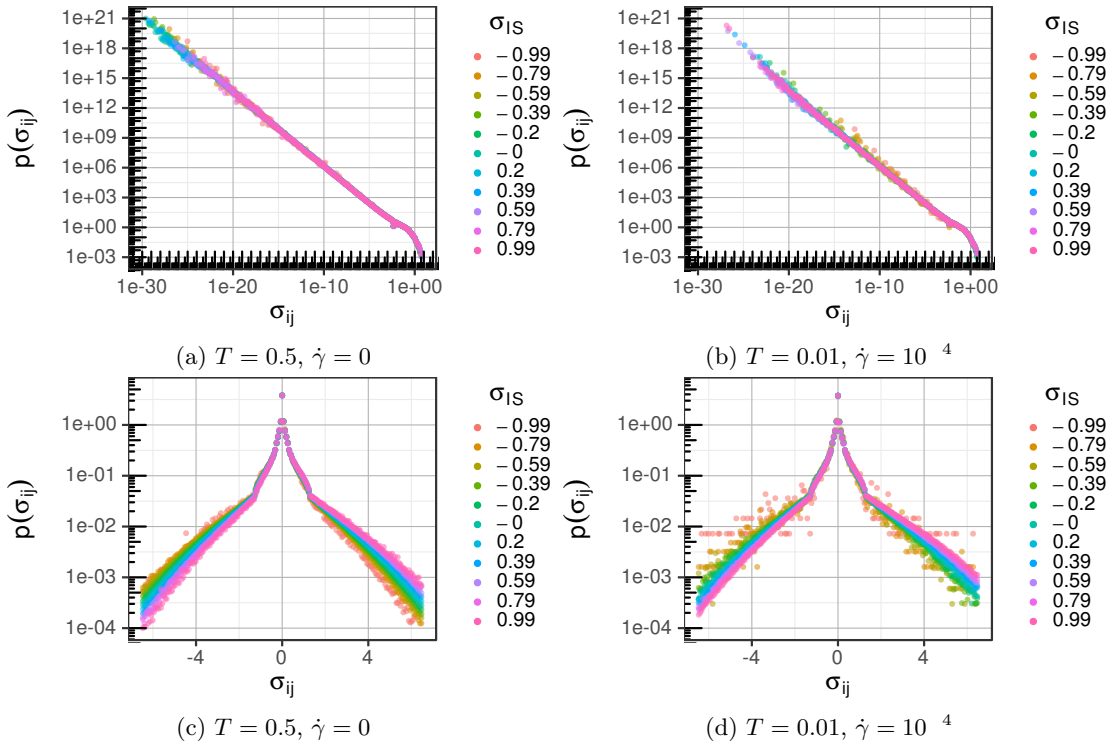

(a) $T = 0.5$, $\dot{\gamma} = 0$ (b) $T = 0.01$, $\dot{\gamma} = 10^{-4}$

(c) $T = 0.5$, $\dot{\gamma} = 0$ (d) $T = 0.01$, $\dot{\gamma} = 10^{-4}$

Figure 7.3: Stress contact distribution of particle/neighbor type A-A contacts for a fixed system stress $p(\sigma_{ij}|\sigma)$. (a) and (c) shows equilibrium data from simulations at $T = 0.5$, $\dot{\gamma} = 0$ while (b) and (d) shows data from the flow regime of simulations with $T = 0.01$, $\dot{\gamma} = 10^{-4}$.

This distribution contains the full information, as it has rotational symmetry around the r_1 axis following isotropy in equilibrium. Therefore, we only need the distances from the two contacts and the angle α between them. In contrast to the previous definition of $p(r)$, which was tailored specifically to spherical coordinates and contained a r^2 dependency, we this time use a plain volume probability density for $p(r_2, \cos\alpha|r_1)$ and have to take care about the correct volume element while integrating. However, the distribution $p(r_1)$ is the single stress distribution, we derived in section 7.1.2.

We determine an approximation of p by binning equilibrium simulation data at $T = 0.5$, $N = 130$ using 128 bins for each variable and limiting out data to the interaction range $r \in [0.75, 1.8 = r_c]$. In fig. 7.4 we see the usual first neighbor shell at approximately the same distance across all angles. The upper limit in $\cos\alpha$ is caused by two neighboring particles having a minimum distance. Looking at the case of $r_1 = 1.1$, we see a maximum $\cos\alpha = 0.5$ for small r_2, as in this case the three particles describe an equilateral triangle with an angle of $\frac{\pi}{3}$. Increasing r_2, the second neighbor start to move above the first neighbor, keeping the minimum distance of 1, thereby decreasing the angle α between both neighbors. At $r_1 = 1.6$ in our second example this effect is not so pronounced, as the first neighbor is far away and the second neighbor moves around its shell keeping the angle approximately constant. Another feature present in both plots are several parallel straight blue lines. These lines correspond to the splitting in the second neighbor peak, seen also in $g(r)$ (see section 7.4.1).

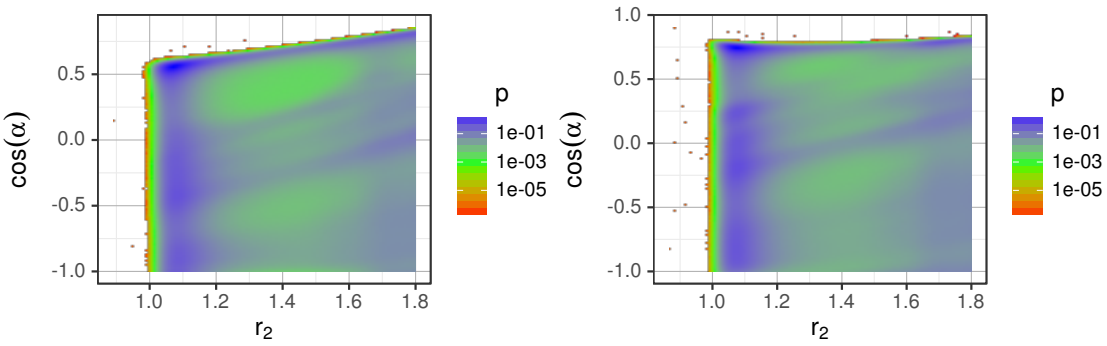

(a) $r_1 = 1.1$ (b) $r_1 = 1.6$

Figure 7.4: Probability $p(r_2, \cos\alpha | r_1)$ to find a type A-A contact with length r_2 at the angle α to another contact with length r_1. We show the data generated through binning of equilibrium data for two contact distances r_1.

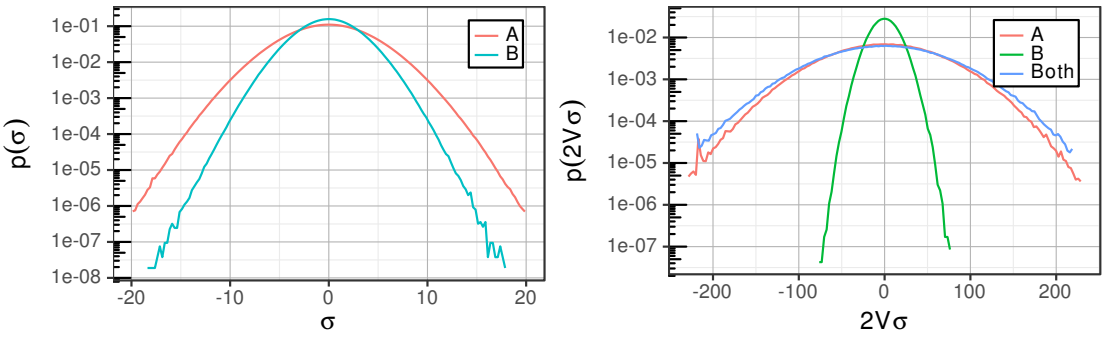

(a) Particle (b) System

Figure 7.5: Stress distribution of inherent structures in equilibrium at $T = 0.5$, $N = 130$. (a) Particle stress distribution $p(\sigma_i)$ with $\sigma_i = \sum_j \sigma_{ij} = -\sum_{ij} r_{ij,y} F_x(r_{ij})$. (b) Unscaled system stress distribution $p(2V\sigma)$ with $2V\sigma = \sum_i \sigma_i$.

7.2.2 Particle Distribution

We will now use the contact distribution to calculate basic properties of the stress distribution, i.e. mean value and variance, for a single particle. As this procedure is very generic, we will use it later to calculate other properties. In fig. 7.5, we see that the per particle distribution is mostly Gaussian as expected from the central limit theorem. Typical type A particles have 20.589 neighbors, while a full system with $N = 130$ consists of 104 particles of type A, therefore netting 1070.64 A-A contacts. A Gaussian distribution is fully characterized by its mean value and variance, as all higher moments can be expressed by the first and second. Therefore, we will now show how the variance is calculated from the basic contact stress distribution. These are also the only variables we need later for the calculation of the system stress.

To simplify notation, we will drop the type index of the particle, as the calculation is identical for type A and type B particles. Rather, the type index only denotes the neighbor type. As an

example, we will do the calculation first for same-types contacts only, before continuing with the more complicated version for a mixture of A-A and A-B contacts.

The variance of a sum of random variables can be rewritten in terms of the covariance:

$$\mathrm{Var}(\sum_i X_i) = \sum_{ij} \mathrm{Cov}(X_i, X_j) = \sum_i \mathrm{Var}(X_i) + \sum_{i \neq j} \mathrm{Cov}(X_i, X_j) \tag{7.18}$$

$$= N_c \mathrm{Var}(X) + N_c(N_c - 1)\mathrm{Cov}(X, X') \tag{7.19}$$

In the current case, all random variables are equally distributed, so we could drop the index in the variance calculation. Computing the covariance, we can choose any two distinct contacts. We have to be careful about the number of the contacts N_c, as it is also randomly distributed. The mean value is calculated as follows:

$$\langle \sum_{i=1}^{N_c} X_i \rangle = \langle \langle \sum_{i=1}^{N_c} X_i | N_c \rangle \rangle_{N_c} = \langle N_c \langle X \rangle \rangle_{N_c} = \langle X \rangle \langle N_c \rangle \tag{7.20}$$

The variance calculates a bit more difficult, using the law of total variance:

$$\mathrm{Var}(\sum_{i=1}^{N_c} X_i) = \langle \mathrm{Var}(\sum_{i=1}^{N_c} X_i | N_c) \rangle_{N_c} + \mathrm{Var}_{N_c}(\langle \sum_{i=1}^{N_c} X_i | N_c \rangle) \tag{7.21}$$

$$= \langle N_c \rangle \mathrm{Var}(X) + (\langle (N_c)^2 \rangle - \langle N_c \rangle)\mathrm{Cov}(X, X') + \mathrm{Var}(N_c)\langle X \rangle^2 \tag{7.22}$$

Next, we will look at the case, where we have a mixture of two types of contacts, with the number of contacts N_c^A and N_c^B both randomly distributed. First, we start again with the mean value:

$$\langle \sum_{i=1}^{N_c^A} X_i^A + \sum_{i=1}^{N_c^B} X_i^B \rangle = \langle \langle N_c^A \langle X^A \rangle + N_c^B \langle X^B \rangle | N_c^A, N_c^B \rangle \rangle_{N_c^A, N_c^B} \tag{7.23}$$

$$= \langle X^A \rangle \langle N_c^A \rangle + \langle X^B \rangle \langle N_c^B \rangle \tag{7.24}$$

The variance however, requires a more complex application of the law of total variance, as the numbers of contacts are by no means independent. Using the short notation $Y = \sum_{i=1}^{N_c^A} X_i^A + \sum_{i=1}^{N_c^B} X_i^B$,

we can write:

$$\begin{aligned}
\mathrm{Var}(Y) &= \langle \mathrm{Var}_Y(Y|N_c^A, N_c^B)\rangle_{N_c^A,N_c^B} && (7.25)\\
&\quad + \langle \mathrm{Var}_{N_c^B}(\langle Y|N_c^A, N_c^B\rangle|N_c^A)\rangle_{N_c^A}\\
&\quad + \mathrm{Var}_{N_c^A}(\langle Y|N_c^A\rangle)\\
\langle \mathrm{Var}_Y(Y|N_c^A, N_c^B)\rangle_{N_c^A,N_c^B} &= \langle N_c^A\rangle \mathrm{Var}(X^A) + \langle N_c^B\rangle \mathrm{Var}(X^B) && (7.26)\\
&\quad + (\langle (N_c^A)^2\rangle - \langle N_c^A\rangle)\mathrm{Cov}(X^A, X^{A\prime})\\
&\quad + (\langle (N_c^B)^2\rangle - \langle N_c^B\rangle)\mathrm{Cov}(X^B, X^{B\prime})\\
&\quad + 2\langle N_c^A \langle N_c^B|N_c^A\rangle_{N_c^A}\mathrm{Cov}(X^A, X^B)\\
\langle Y|N_c^A, N_c^B\rangle &= N_c^A\langle X^A\rangle + N_c^B\langle X^B\rangle && (7.27)\\
\mathrm{Var}_{N_c^B}(\langle Y|N_c^A, N_c^B\rangle|N_c^A) &= \mathrm{Var}_{N_c^B}(N_c^A\langle X^A\rangle + N_c^B\langle X^B\rangle|N_c^A) && (7.28)\\
&= \langle X^B\rangle^2 \mathrm{Var}_{N_c^B}(N_c^B|N_c^A) && (7.29)\\
\langle Y|N_c^A\rangle &= N_c^A\langle X^A\rangle + \langle N_c^B|N_c^A\rangle\langle X^B\rangle && (7.30)\\
\mathrm{Var}_{N_c^A}(\langle Y|N_c^A\rangle) &= \mathrm{Var}_{N_c^A}(N_c^A\langle X^A\rangle) && (7.31)\\
&\quad + \mathrm{Var}_{N_c^A}(\langle N_c^B|N_c^A\rangle\langle X^A\rangle)\\
&\quad + 2\mathrm{Cov}(N_c^A\langle X^A\rangle, \langle N_c^B|N_c^A\rangle\langle X^B\rangle)\\
&= \langle X^A\rangle^2 \mathrm{Var}(N_c^A) + && (7.32)\\
&\quad + \langle X^B\rangle^2 \mathrm{Var}_{N_c^A}(\langle N_c^B|N_c^A\rangle_{N_c^B})\\
&\quad + 2\langle X^A\rangle\langle X^B\rangle \mathrm{Cov}(N_c^A, \langle N_c^B|N_c^A\rangle_{N_c^B})\\
\mathrm{Var}_{N_c^A}(\langle N_c^B|N_c^A\rangle) &= \langle \langle N_c^B|N_c^A\rangle^2\rangle_{N_c^A} - (\underbrace{\langle \langle N_c^B|N_c^A\rangle\rangle_{N_c^A}}_{\langle N_c^B\rangle})^2 && (7.33)\\
\mathrm{Cov}(N_c^A, \langle N_c^B|N_c^A\rangle) &= \langle N_c^A\langle N_c^B|N_c^A\rangle\rangle_{N_c^A} - \langle N_c^A\rangle \underbrace{\langle N_c^B|N_c^A\rangle_{N_c^A}}_{\langle N_c^B\rangle} && (7.34)
\end{aligned}$$

In this derivation, we have added a prime ($'$), if two same typed contacts specify different neighbors. In section 7.5.2, we will also need the expectation value of $\langle YW\rangle$, where W is defined similarly to Y, but using other variables $Y_i^{A,B}$. Using conditional means, we are able to express

the product via:

$$\langle YW\rangle = \langle\langle YZ|N_c^A, N_c^B\rangle_{N_c^B}|N_c^A\rangle_{N_c^A} \tag{7.35}$$

$$= \langle\langle \sum_i^{N_c^A}\sum_j^{N_c^A} X_i^A Y_j^A + \sum_i^{N_c^A}\sum_j^{N_c^B} X_i^A Y_j^B \tag{7.36}$$
$$+ \sum_i^{N_c^B}\sum_j^{N_c^A} X_i^B Y_j^A + \sum_i^{N_c^B}\sum_j^{N_c^B} X_i^B Y_j^B |N_c^A, N_c^B\rangle_{N_c^B}|N_c^A\rangle_{N_c^A}$$

$$= \langle\langle N_c^A\langle X^A Y^A\rangle + N_c^A(N_c^A-1)\langle X^A Y^{A\prime}\rangle \tag{7.37}$$
$$+ N_c^A N_c^B\langle X_c^A Y_c^B\rangle + N_c^A N_c^B\langle X^B Y^A\rangle$$
$$+ N_c^B(N_c^B-1)\langle X^B Y^{B\prime}\rangle +$$
$$+ N_c^B\langle X^B Y^B\rangle |N_c^A, N_c^B\rangle_{N_c^B}|N_c^A\rangle_{N_c^A}$$

$$= \langle N_c^A\rangle\langle X^A Y^A\rangle + (\langle (N_c^A)^2\rangle - \langle N_c^A\rangle)\langle X^A Y^{A\prime}\rangle \tag{7.38}$$

$$+ \langle N_c^A\langle N_c^B|N_c^A\rangle_{N_c^B}\rangle_{N_c^A}\langle X^A Y^B\rangle \tag{7.39}$$
$$+ \langle N_c^A\langle N_c^B|N_c^A\rangle_{N_c^B}\rangle_{N_c^A}\langle X^B Y^A\rangle$$
$$+ (\langle (N_c^B)^2\rangle - \langle N_c^B\rangle)\langle X^B Y^{B\prime} + \langle N_c^B\rangle\langle X^B Y^B\rangle$$

The relevant values for the N_c^A and N_c^B distributions are found in table 7.2.

We now come back to the original problem, the single particle stress distribution. Calculating per particle stress variance, all terms involving the contact stress mean will vanish. However, in our derivation, we have included all terms, as they are of interest in the determination of other observables, as the energy, the pressure and the shear modulus, all of which have a non-vanishing mean.

With a zero mean stress, the only term remaining is given in eq. (7.26), we must now calculate the stress contact variance and covariance using spherical coordinates and the corresponding distributions. The variance is derived easily from the radial distribution:

$$\left\langle \sigma_{ij}^2\right\rangle = \left\langle (yF_x)^2\right\rangle = \int_0^{r_c}\int_0^{\theta}\int_0^{2\pi} (rF(r)\sin^2\theta\frac{1}{2}\sin(2\phi))^2 p(r)p(\theta)p(\phi)\mathrm{d}r\mathrm{d}\theta\mathrm{d}\phi \tag{7.40}$$

$$= \frac{1}{16\pi}\int_0^{r_c}\int_0^{\theta}\int_0^{2\pi} (rF(r))^2\sin^5\theta\sin^2(2\phi)p(r)\mathrm{d}r\mathrm{d}\theta\mathrm{d}\phi \tag{7.41}$$

$$= \frac{1}{15}\int_0^{r_c} (rF(r))^2 p(r)\mathrm{d}r \tag{7.42}$$

The covariance calculates similarly, although now we have to take into account two distinct contacts. The angle between contacts $\cos\alpha$ is expressed in spherical coordinates as:

$$\cos\alpha = \frac{\boldsymbol{r}_1\boldsymbol{r}_2}{|r_1 r_2|} = \sin\theta_1\sin\theta_2\cos\phi_1\cos\phi_2 + \sin\theta_1\sin\theta_2\sin\phi_1\sin\phi_2 + \cos\theta_1\cos\theta_2 \tag{7.43}$$

	Part. Type	Neigh. Type 1	Neigh. Type 2	Result
$\langle N_c^1 \rangle$	A	A		20.58865(12)
	A	B		5.83156(11)
	B	A		23.32383(22)
	B	B		6.15554(23)
$\mathrm{Var}(N_c^1)$	A	A		3.00570(29)
	A	B		2.60834(25)
	B	A		2.65116(52)
	B	B		2.71463(53)
$\langle N_c^1 \langle N_c^2 \vert N_c^1 \rangle_{N_c^2} \rangle_{N_c^1}$	A	A	B	119.91570
	A	B	A	119.91594
	B	A	B	143.03361
	B	B	A	143.03348
$\langle \langle N_c^2 N_c^2 \vert N_c^1 \rangle_{N_c^1}$	A	A	B	34.01604
	A	B	A	423.90467
	B	A	B	37.99976
	B	B	A	544.10313
$\langle \mathrm{Var}_{N_c^2}(N_c^2 \vert N_c^1) \rangle_{N_c^1}$	A	A	B	2.57803
	A	B	A	2.98872
	B	A	B	2.59098
	B	B	A	2.50870
$\mathrm{Var}_{N_c^1}(\langle N_c^2 \vert N_c^1 \rangle_{N_c^2})$	A	A	B	0.00892
	A	B	A	0.01196
	B	A	B	0.10906
	B	B	A	0.10197
$\mathrm{Cov}(N_c^1, \langle N_c^2 \vert N_c^1 \rangle_{N_c^2})$	A	A	B	-0.14833
	A	B	A	-0.14810
	B	A	B	-0.53721
	B	B	A	-0.53734

Table 7.2: Statistics for the number of neighbors for given particle type and neighbor types. The values listed have been extracted from simulations at $T = 0.5$ and $N = 130$.

Part. Type	Neigh. Type	Result
A	A	0.801335
A	B	0.244349
B	B	0.033898

(a) Variance: $\langle(\sigma_{ij}^{pn})^2\rangle$

Part. Type	Neigh. Type 1	Neigh. Type 2	Result
A	A	A	-0.009145(15)
A	A	B	-0.002438(11)
A	B	B	0.0000750(31)
B	A	A	0.0022322(54)
B	A	B	-0.0005517(20)
B	B	B	-0.00050188(49)

(b) Covariance: $\langle\sigma_{ij}^{pn_1}\sigma_{ij}^{pn_2}\rangle$

Table 7.3: Contact stress variance for a single contact (a) and covariance for two distinct contacts (b) in dependence of the particle/neighbor types. The variance values in (a) were calculated using $p(r)$ by integrating analytically over the angular parts. The covariance values in (b) were computed via Monte-Carlo integration over the whole integral including angular parts. The necessary two-contact probability was determined using the method described in section 7.2.1. We have omitted the values for obvious symmetries.

Therefore, we make use of the two contacts distribution, we introduced in section 7.2.1 and integrate over all degrees of freedom.

$$\mathrm{Cov}(\sigma_{ij},\sigma'_{ij}) = \left\langle \sigma_{ij}\sigma'_{ij}\right\rangle \tag{7.44}$$

$$= \int_0^{r_c}\int_0^{r_c}\int_0^{\pi}\int_0^{\pi}\int_0^{2\pi}\int_0^{2\pi} r_1 F(r_1) r_2 F(r_2) \sin^2\theta_1 \sin^2\theta_2 \frac{1}{2}\sin(2\phi_1)\frac{1}{2}\sin(2\phi_2) \tag{7.45}$$
$$r_2^2 \sin\theta_2 p(r_2,\cos\alpha|r_1)p(r_1)p(\theta_1)p(\phi_1)\mathrm{d}r_1\mathrm{d}r_2\mathrm{d}\theta_1\mathrm{d}\theta_2\mathrm{d}\phi_1\mathrm{d}\phi_2$$

This lengthy integral is hard to transform further [1]. Therefore we employ a Monte Carlo integration scheme [Peter Lepage, 1978], which evaluates the integral to reasonable accuracy already within minutes. For this purpose, we binned the function $p(r_2,\cos\alpha|r_1)$ with 128 bins in each variable and used linear interpolation for values between bins. The results from evaluating the stress covariances between contacts using this method are listed in table 7.3b. All these results are given with the statistical error of the Monte Carlo scheme. However, due to the binning and interpolation, there may be a significant systematic error, which is different for each function, we integrate over. The accuracy of the two-contact distribution can be tested by integrating over $p(r_2,\cos\alpha|r_1)p(r_1)p(\theta_1)p(\phi_1)$, which, being a probability density, should result in the value 1. Here, we are able to achieve an accuracy of approximately 98%.

Using eq. (7.26), we can calculate the variance looking up the contact variances in table 7.3a and the covariances in table 7.3b. For type A particles, this results in a per particle variance

[1] After a weekend of transformations, we got $\cos\alpha$ as an integration variable, so that only the outermost three integrals would need numeric data. However, we still found no analytic expression for the inner three integrals and even inexact numerical computation of these took several minutes.

Part. Type	Result
A	13.8068(13)
B	6.9270(14)

(a) Particle Stress Variance: $\langle(\sigma_i^p)^2\rangle$

Part. Type	Neigh. Type	Result
A	A	20.04290(30)
A	B	2.103373(42)
B	A	8.41359(17)
B	B	0.940347(15)

(b) Particle Stress Covariance: $\langle\sigma_i^p, \sigma_j^p\rangle$

Part. Type	Result
A	3491.7(35)
B	204.4(20)
Combined	4121.5(41)

(c) System Stress Variance: $\langle(2V\sigma^p)^2\rangle$

Table 7.4: (a) Stress variance per particle for both particle types. Listed values are gathered directly from equilibrium simulations at $T = 0.5$, $N = 130$. (b) Stress covariance for different particles. We determined these values by integrating over $\mathrm{Cov}(\sigma_i^p, \sigma_j^p|r)$ using eq. (7.47). (c) Stress variance for the whole system.

of $\langle(\sigma^A_{i,\mathrm{calc}})^2\rangle = 13.61$, which is in very good agreement with $\langle(\sigma^A_{i,\mathrm{sim}})^2\rangle = 13.81$, extracted from simulation data. Similarly, we arrive at equally good values for type B particles: $\langle(\sigma^B_{i,\mathrm{calc}})^2\rangle = 6.91$ and $\langle(\sigma^B_{i,\mathrm{sim}})^2\rangle = 6.92$. From the values of the single-contact variances, we see that most of the contribution for the stress variance of both type A and type B particles comes from the interaction with type A neighbors [2]. Thus, for the approximation of the particle stresses, it would suffice to only use type A particles.

7.2.3 System Stress Distribution

Calculating the stress distribution directly for the whole system would require the two-contact probability for two arbitrary contacts in the system, i.e. not necessarily belonging to a single particle. This function would be dependent on the distance between the originating particles and the orientations of both contacts. However, without a proper model for this function, which reduces some degrees of freedoms by analytical expressions, the amount of data needed to represent this function numerically via histogram and interpolation is too large for current computers. We hope, that current research on icosahedra [Hirata et al., 2013] and [Ding et al., 2014] may provide additional insight into the form of the the two contact distribution. In this section, we need to resort to inter-particle correlations, directly extracted from simulation data, to determine the stress of the whole system. These correlation functions have to be derived from simulation data for each observable. For the stress, we define $C_{pn}(r) \coloneqq \langle\sigma_i\sigma_j|r = |r_i - r_j|\rangle$, where the left and right σ are of the specified particle types p and n. As we simulate in three dimensions and use periodic boundaries, the radius r is limited to $\frac{1}{2}\sqrt{3}L$, if we refrain from taking periodic copies into account. Starting at $\frac{L}{2}$, the statistical error of $C_{pn}(r)$ increases, as

[2] Using only the variances with $pn = pA$ and the covariances with $pn_1n_2 = pAA$ we calculate $\langle\sigma_i^A\rangle = 12.78$ and $\langle\sigma_i^B\rangle = 6.85$.

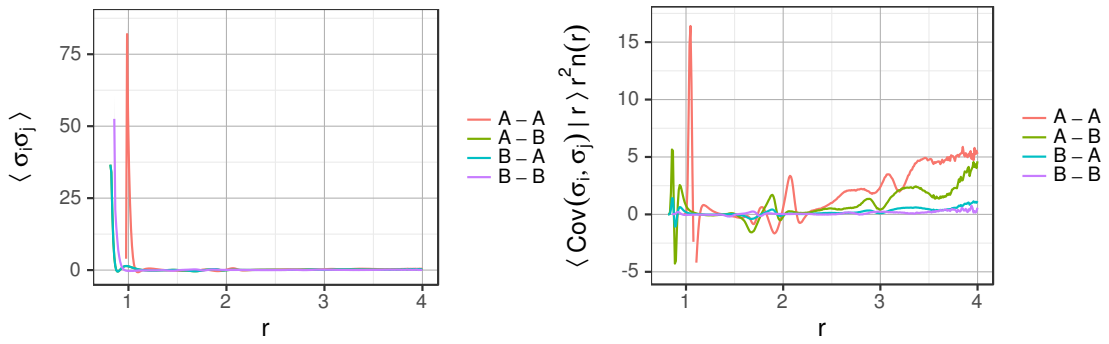

(a) $\langle \sigma_i \sigma_j | r \rangle$ (b) $\mathrm{Cov}(\sigma_i, \sigma_j | r) r^2 n(r)$

Figure 7.6: Stress-stress correlation and covariance for particles of different types, calculated from simulation data of inherent structures in equilibrium at $T = 0.5$.

the spherical sampling shell is restricted to the first periodic neighbor box [3]. Looking at fig. 7.6, this is also the point, where the covariance systematically increases towards positive values. At this point, it would be interesting to study the influence of different box sizes in this region, as we see a systematic positive deviation is probably being caused by finite size effects. From [Chowdhury et al., 2016], we know that the stress variance from the corners is about as big as the stress variance from the particle-particle interactions. However, we have to leave the question of finite size scaling open for future research.

Using the function $C_{pn}(r)$, we can now calculate the sum of the covariances for single particles via:

$$\langle \mathrm{Cov}(\sigma_i, \sigma_j) | r = |r_i - r_j| \rangle = C_{pn}(r) - (\langle \sigma_i \rangle)^2 = C_{pn}(r) \tag{7.46}$$

$$\left\langle \sum_{j \neq i} \mathrm{Cov}(\sigma_i, \sigma_j) \right\rangle = \int_V \langle \mathrm{Cov}(\sigma_i, \sigma_j) | r = |r_i - r_j| \rangle \, n_{pn}(r) \mathrm{d}V \tag{7.47}$$

Ideally, the covariance would drop to zero for large distances and we could use an infinite integration volume V. However, as we simulate small systems, the range we can reliably calculate $C_{pn}(r)$ is limited and we have to account for finite size effects. Therefore, we calculate the sum by integrating over exactly the first periodic neighbor box, taking into account the interaction of all distinct particles exactly once. Similar to the previous covariance integral in section 7.2.2, we solve this integral using Monte-Carlo integration.

Using the numerical data shown in fig. 7.6, we can now use eq. (7.18) to calculate the stress variance for our system. In addition, we use our previously calculated particle variances. For type A particles we get a variance of $\langle (2V\sigma_{calc})^2 \rangle = \langle (\sum_i \sigma_i)^2 \rangle = 3501.5$, which is in perfect agreement with the variance computed directly from simulation data $\langle (2V\sigma_{sim})^2 \rangle = 3491.7$. The same calculations apply to type B particles, where we get a similar good result: $\langle (2V\sigma_{calc})^2 \rangle = 204.5$ compared to $\langle (2V\sigma_{sim})^2 \rangle = 204.4$. We can even compute the stress variance for the sum of all

[3] The first periodic neighbor box includes all particles in our simulation exactly once at their nearest position to the position of the particle in question, while taking periodic boundary conditions into account.

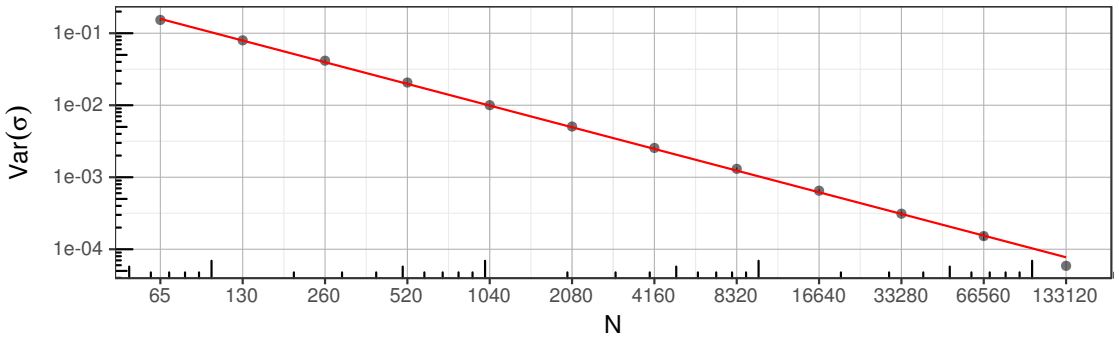

Figure 7.7: Stress variance scaling for inherent structure in equilibrium simulations at $T = 0.5$. The solid red line represents a fit with a fixed slope of -1 and a calculated intercept of 10.29.

stresses using the following equation:

$$\langle (2V\sigma_{calc})^2 \rangle = N_A \mathrm{Var}(\sigma_i^A) + N_B \mathrm{Var}(\sigma_i^B) + N_A \left\langle \sum_{j \neq i} \mathrm{Cov}(\sigma_i^A, \sigma_j^A) \right\rangle \tag{7.48}$$

$$+ \quad N_B \left\langle \sum_{j \neq i} \mathrm{Cov}(\sigma_i^B, \sigma_j^B) \right\rangle + 2N_A \left\langle \sum_{j \neq i} \mathrm{Cov}(\sigma_i^A, \sigma_j^B) \right\rangle \tag{7.49}$$

This leads to a value of $\langle (2V\sigma_{calc})^2 \rangle = 4143.5$, which is equally in very good agreement with variance extracted directly from simulations $\langle (2V\sigma_{sim})^2 \rangle = 4121.5$. As we see from the numbers, the larger part of the variance is contained in the covariances, especially in the particle-particle covariance. Therefore, we think that more research is needed to better understand the structural arrangement of the particles. We remark, that one of the current favored models to explain structure in glasses uses the icosahedron as the basic structure element [Ding et al., 2014, Hirata et al., 2013, Doye et al., 2003, Doye et al., 1999].

As previously noted, it is important to study the finite size scaling of the particle-particle correlation function. We note that our equation eq. (7.48) already includes the correct finite size scaling for the stress variance, namely a trivial $\frac{1}{N}$ power law dependence on the system size, which has been reported in [Abraham and Harrowell, 2012]. However, this only holds, if $C_{pn}(r)$ drops to zero for large distances, which makes $\langle \sum_{j \neq i} \mathrm{Cov}(\sigma_i, \sigma_j) \rangle$ a constant. As the particle ratio between particle types is fixed, we have $N_A \propto N$ and $N_B \propto N$ as well as $V \propto N$, which reproduces the power law scaling. For our small system, $C_{pn}(r)$ does not yet reduce to zero, but looking at the data presented in [Abraham and Harrowell, 2012], the scaling is already present at particle counts as low as $N \approx 250$. In fig. 7.7 we plot the stress variance scaling for our own data and see, that the variance scales with $\frac{1}{N}$ for system sizes as low as $N = 65$. This result is really good in terms of finite size effects for the interpretation of our results, but also somewhat unexpected from evaluation of our covariance function. We remark at this point, that for the normal shear stress, i.e. not for inherent structures, but rather measured during the normal trajectory, there exists a crossover to another variance scaling in dependence on the system size and the temperature [Hentschel et al., 2010].

For future research, it might be of interest to study the stress-stress covariance in dependence of energy $\langle C_{pn}(r) | \epsilon_{\mathrm{IS}} \rangle$, as the particle movement is dominated by hopping between inherent structures, whose energy distribution is dependent on the temperature. Also, the effect of strain

on $C_{pn}(r)$ has to be determined. Together with a known IS energy distribution of Gaussian shape (see section 6.2) in the flow regime, it might be possible to give a prediction of the covariance under shear $\langle C_{pn}(r); \dot{\gamma} \rangle$ and therefore the stress distribution.

7.3 Shear Modulus

Similar to the calculations in section 7.1.2, we now calculate the affine contribution to the shear modulus from equilibrium data. The shear modulus is normally defined by taking the ensemble average of all trajectories and taking the derivative. Assuming we calculate the modulus at an infinitesimal small interval, we can take the average of the shear modulus of all trajectories. For a single trajectory, the shear modulus in the IS trajectory is defined as:

$$G = \frac{\mathrm{d}}{\mathrm{d}\gamma}\sigma(\gamma) = -\frac{1}{V}\frac{1}{2}\sum_{ij}\frac{\mathrm{d}}{\mathrm{d}\gamma}r_{ij,y}F_{ij,x} \tag{7.50}$$

For convenience, we will drop the indices for some part of the calculations, while only looking at the summands $\frac{\mathrm{d}}{\mathrm{d}\gamma}yF_x(r)$. The derivative with respect to γ can be transformed as a derivative in the $x-y$ coordinate system, when looking at the change of the coordinates doing an affine transformation in the $x-y$ plane, i.e y is constant.

$$\mathrm{d}x = y\mathrm{d}\gamma \Rightarrow \frac{\mathrm{d}x}{\mathrm{d}\gamma} = y \tag{7.51}$$

Therefore, we can rewrite our expression for G and transforming spherical coordinates:

$$\frac{\mathrm{d}}{\mathrm{d}\gamma}yF_x(r) = y\frac{\mathrm{d}F_x(r)}{\mathrm{d}x}\frac{\mathrm{d}x}{\mathrm{d}\gamma} = y^2\frac{\mathrm{d}F_x(r)}{\mathrm{d}x} = r^2\sin^2\theta\sin^2\phi\frac{\mathrm{d}F_x(r)}{\mathrm{d}x} \tag{7.52}$$

$$= r^2\sin^2\theta\sin^2\phi\left(\frac{\partial F(r)\sin\theta\cos\phi}{\partial r}\frac{\mathrm{d}r}{\mathrm{d}x} + \frac{\partial F(r)\sin\theta\cos\phi}{\partial\theta}\frac{\mathrm{d}\theta}{\mathrm{d}x}\right. \tag{7.53}$$

$$\left. + \frac{\partial F(r)\sin\theta\cos\phi}{\partial\phi}\frac{\mathrm{d}\phi}{\mathrm{d}x}\right)$$

Next, we have to solve the derivations of the transformation functions:

$$\frac{\mathrm{d}\phi}{\mathrm{d}x} = \frac{\mathrm{d}}{\mathrm{d}x}\sin^{-1}\left(\frac{y}{\sqrt{x^2+y^2}}\right) = -\frac{xy}{\sqrt{\frac{x^2}{x^2+y^2}(x^2+y^2)^{\frac{3}{2}}}} \tag{7.54}$$

$$= -\frac{r^2\sin^2\theta\frac{1}{2}\sin(2\phi)}{\sqrt{\frac{r^2\sin^2\theta\cos^2\phi}{r^2\sin^2\theta}(r^2\sin^2\theta)^{\frac{3}{2}}}} = -\frac{r^2\sin^2\theta\frac{1}{2}\sin(2\phi)}{r^3\left|\cos\phi\right|\left|\sin\theta\right|^3} \tag{7.55}$$

$$= -\frac{1}{2r}\frac{\sin(2\phi)}{\left|\cos\phi\right|\left|\sin\theta\right|^3} \tag{7.56}$$

$$\tag{7.57}$$

$$\frac{\mathrm{d}\theta}{\mathrm{d}x} = \frac{\mathrm{d}\theta}{\mathrm{d}x}\cos^{-1}\left(\frac{z}{r}\right) = \frac{\mathrm{d}\theta}{\mathrm{d}x}\cos^{-1}\left(\frac{z}{\sqrt{x^2+y^2+z^2}}\right) = \frac{r^2\frac{1}{2}\sin(2\theta)\cos\phi}{r^3\sqrt{1-\frac{r^2\cos^2\theta}{r^2}}} \tag{7.58}$$

$$= \frac{1}{2r}\frac{\sin(2\theta)\cos\phi}{\sin\theta} \tag{7.59}$$

$$\tag{7.60}$$

$$\frac{\mathrm{d}r}{\mathrm{d}x} = \frac{\mathrm{d}}{\mathrm{d}x}\sqrt{x^2+y^2+z^2} = \frac{1}{2}\frac{1}{r}2x = \frac{1}{r}r\sin\theta\cos\phi \tag{7.61}$$

$$= \sin\theta\cos\phi \tag{7.62}$$

Putting all intermediate solutions together, we solve eq. (7.52):

$$\frac{\mathrm{d}}{\mathrm{d}\gamma}yF_x(r) = r^2\frac{\partial F(r)}{\partial r}\sin^4\theta\frac{1}{4}\sin^2(2\phi) + rF(r)\frac{1}{2}\sin(2\theta)\frac{\cos\theta\sin^2\theta}{|\sin(\theta)|}\cos^2\phi\sin^2\phi \tag{7.63}$$

$$+ rF(r)\frac{1}{2}\sin(2\phi)\frac{\sin^3\phi}{|\cos\phi|\,|\sin\phi|}\sin^3\theta \tag{7.64}$$

$$= r^2\frac{\partial F(r)}{\partial r}\frac{1}{4}\sin^4\theta\sin^2(2\phi) + rF(r)\frac{1}{8}\frac{\sin(2\theta)\cos\theta\sin^2\theta}{|\sin\theta|}\sin^2(2\phi) \tag{7.65}$$

$$+ rF(r)\frac{1}{2}\frac{\sin(2\phi)\sin^3\phi}{|\cos\phi|\,|\sin\phi|}\sin^3\theta \tag{7.66}$$

Now we return to the sum over all particles and take the ensemble average, as we have done in section 7.1.2. Thereby, we replace the sum by an integral over the neighbor density. The shear modulus written as integral over particle densities is written as:

$$G_{pn} = -\rho_p\int_0^{r_c}\int_0^{\pi}\int_0^{2\pi}\left[\frac{\mathrm{d}}{\mathrm{d}\gamma}yF_x(r)\right]r^2\sin\theta n_{pn}(r,\theta,\phi)\mathrm{d}r\mathrm{d}\theta\mathrm{d}\phi \tag{7.67}$$

$$= -\rho_p\frac{\pi}{15}\int_0^{r_c}\left[4r^2\frac{\partial F(r)}{\partial r} + rF(r)\right]r^2 n_{pn}(r)\mathrm{d}r \tag{7.68}$$

$$G = \frac{1}{2}\sum_{p,n\in\{A,B\}}G_{pn} \tag{7.69}$$

In the second equation, we have evaluated the angular integrals and in the third equation we have corrected for the fact that every neighbor is counted twice in $n(r)$ for same particle types. By numerical evaluation of the integrals, we arrive at a value of $G_{\mathrm{calc}} = 44.91$ for the contribution of the affine transformation, which is much above $G_{\mathrm{sim}} = 18.75$, we measure in our simulations (see fig. 4.8c). To verify this result, we have calculated the shear modulus for pure affine transformations in a few example trajectories, and found a similar difference. This discrepancy arises from non-affine contributions to the movement of the particles, which greatly reduces the stress in the system, thereby leading to a lower shear modulus. We discussed this effect in the introduction to chapter 4.

In section 7.4, we will see, how an applied strain changes the neighbor density, introducing anisotropy to the system. So as an alternative to calculating the inverse of the Hessian matrix, maybe the derivative of $n(r,\theta,\phi)$ with respect to γ provides a good starting point for a correction term.

7.4 Radial Distribution

The radial distribution functions gives us insight into the arrangement of the particles. In equilibrium, this distribution is assumed to be isotropic, therefore only dependent on the distance

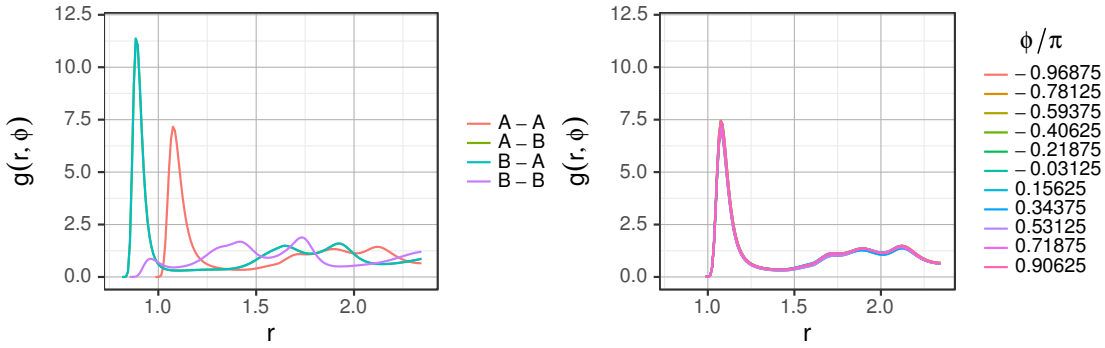

(a) $\langle g_{pn}(r) \rangle$ (b) $\langle g_{AA}(r)|\phi \rangle$

Figure 7.8: Inherent structure radial distribution function $g_{pn}(r)$, (a) for a given particle and neighbor type and (b) for a given angle ϕ in the x-y plane and type A particles and neighbors. Both quantities are determined from equilibrium simulations at $T = 0.5$, $N = 130$.

of the neighbors. Characteristic for supercooled fluids is the appearance of a split in the second neighbor shell, appearing at temperatures lower than $T \approx 0.8$ [Kob and Andersen, 1995a]. We remark, that we have seen this split also in the two-contact distribution for a single particle in section 7.2.1. However, as we shear the system, the system becomes anisotropic [Koumakis et al., 2016]. In section 7.5, we will analyze this anisotropy for the sheared system. Here, we look at the radial distribution function and its anisotropy during equilibrium fluctuations.

7.4.1 Radial Distribution Function

The radial distribution function $g_{pn}(r)$ is defined by normalizing the neighbor density $n_{pn}(r)$ by the mean density ρ_n of the overall system. The indices pn denote the particle type and the neighbor type under investigation. The function $g_{pn}(r)$ is shown for different particle types in fig. 7.8. Clearly visible is the different position of the first neighbor shell for the different particle-neighbor combinations. The distributions for $g_{AB} = g_{BA}$ overlap completely due to scaling by the neighbor density. In fig. 7.8 we also see very well the isotropy of $g_{pn}(r)$, showing only very minor fluctuations due to our constrained sample size, consisting of 2048 equilibrium runs at $T = 0.5$ with 1000 uncorrelated data points each.

7.4.2 Anisotropy in Equilibrium Fluctuations

Due to fluctuations when simulating in equilibrium at $T = 0.5$, the system visits many different IS during its trajectory. As our system size is small at $N = 130$, there is always a remaining shear stress in the system, which would vanish in the limit of large N. In particular, the residual inherent structure stress fluctuations follow a power law in N [Abraham and Harrowell, 2012], which we have also derived in section 7.2.3. However, looking at small subsets of a big system, there would still remain a residual local stress in the inherent structures [Abraham and Harrowell, 2012]. At non-zero shear, we expect to have anisotropy in the radial distribution function $\langle g(r)|\phi, \sigma \rangle$ with respect to the angle ϕ in the shear plane. For colloidal systems during start-up shear, this anisotropy has been extensively studied by [Koumakis et al., 2016]. Shear causes a compression axis to appear at $\phi = \frac{3\pi}{2}$ and an extension axis at $\phi = \frac{\pi}{2}$. At these axes, the

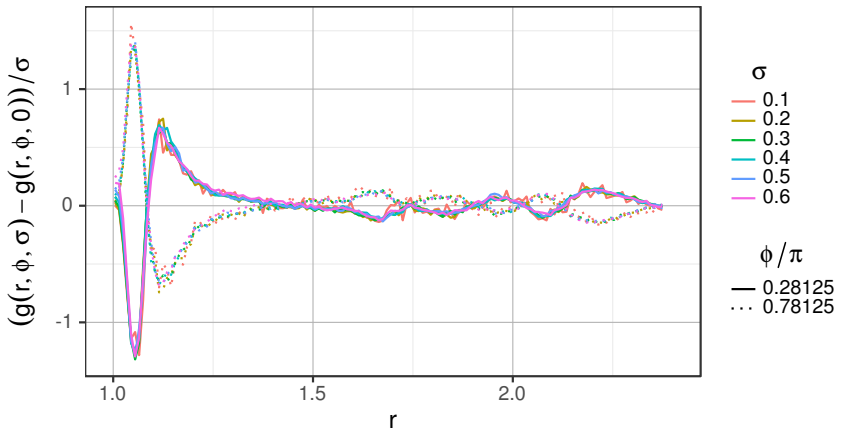

Figure 7.9: Angular dependence of the inherent stress radial distribution function $\langle g_{AA}(r)|\phi,\sigma\rangle$ at different stresses σ. Shown are the compression axis at $\phi = \frac{3\pi}{2}$ and the extension axis at $\phi = \frac{\pi}{2}$. As the differences are between the axes are small, we plot the difference to the zero-stress distribution on each axis, scaled by the inverse system stress: $\frac{1}{\sigma}\left[\langle g_{AA}(r)|\phi,\sigma\rangle - \langle g_{AA}(r)|\phi,\sigma=0\rangle\right]$. The distribution was measured in thermal equilibrium at $T = 0.5$, $N = 130$.

particles are most compressed or extended than in the mean $\langle g(r)\rangle$. In fig. 7.9, we show that this effect is also present for the inherent structure radial distribution function during equilibrium simulation, as there are residual stresses. We find, that the first and second neighbor peak both show the same compression/extension behavior, which is linearly correlated with the amount of accumulated stress in the inherent structures.

To complete this analysis, we show that the compression/extension effect is caused by a rather complicated movement of the neighboring particles. Therefore, we show the average displacement field of neighbors from the zero-stress minimized structure to the inherent structure in equilibrium simulations in fig. 7.10. We see that there is larger particle movement on the compression axis than on the extension axis. Both times, the angular part seems higher in size than the radial part. We remark, that the particle trajectory, starting at the MS with zero temperature, can be described analytically by use of the inverse Hessian matrix [Lemaître and Maloney, 2006]. For comparison, we show data from the flow regime in fig. 7.11 with a similar average shear stress. However, we note here, that the stress fluctuations in the flow regime are quite high, which means that the average displacement field looks different than one obtained in equilibrium. The difference between both is mainly seen in the amplitude of the displacement, but not the direction.

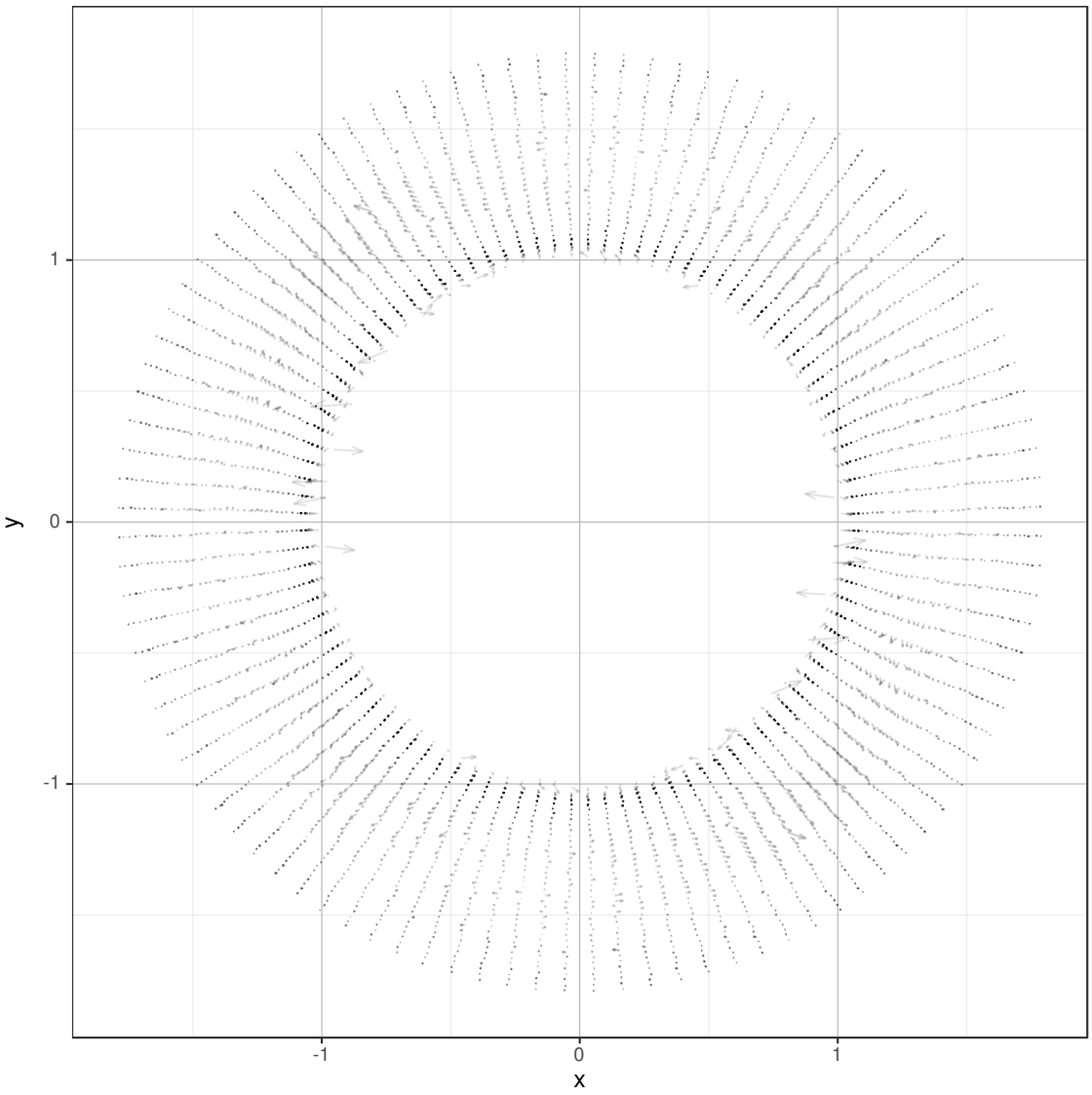

Figure 7.10: Displacement vectors of neighboring particles between the MS and IS in equilibrium data ($T = 0.5$, $N = 130$, $\dot{\gamma} = 0$) for a fixed IS stress of $\sigma = 0.7$, which is comparable to the stress in the flow regime at low temperature. We show the average over a small volume around the x-y plane, limited by $\left|\theta - \frac{\pi}{2}\right| \leq \frac{\pi}{50}$. The alpha value is proportional to the number of particles per bin.

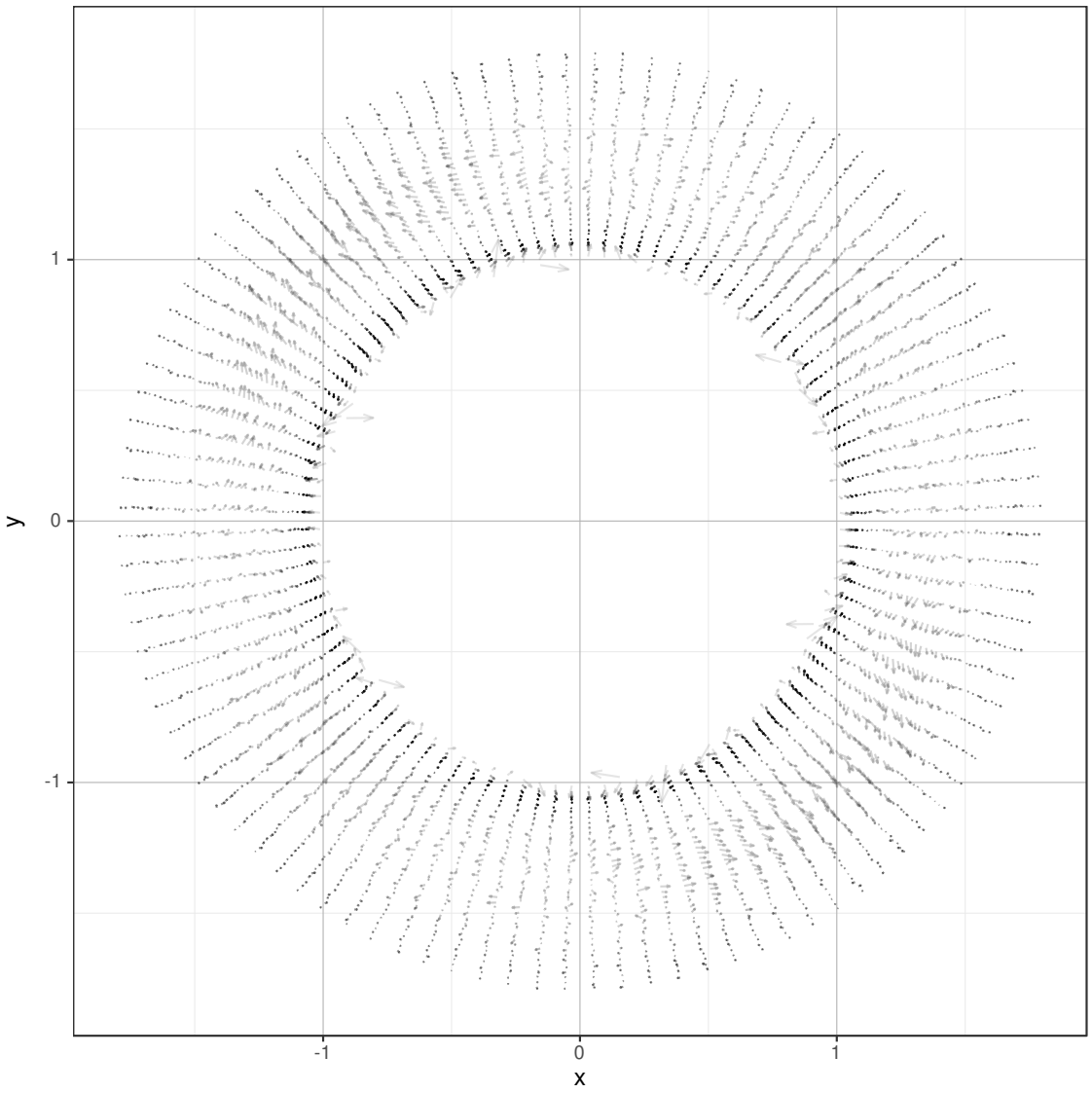

Figure 7.11: Displacement vectors of neighboring particles between the MS and IS in the flow regime ($T = 0.01$, $N = 130$, $\dot{\gamma} = 10^{-4}$). As in fig. 7.10, we show the average over a small volume around the x-y plane, limited by $\left|\theta - \frac{\pi}{2}\right| \leq \frac{\pi}{50}$. The alpha value is proportional to the number of particles per bin.

7.5 Anisotropy

In section 7.4.2, we determined that we see anisotropic behavior in the inherent structure radial distribution function $\langle g(r)|\phi,\sigma\rangle$, which is dependent on the residual IS stresses. We will now define a scalar value, characterizing this anisotropy, which does not depend on the inter-particle potential and determine its behavior in equilibrium, under shear and its relation to the shear stress. As there is are two orthogonal symmetry axes in $\langle g(r)|\phi,\sigma\rangle$ with respect to ϕ, we define the anisotropy for a particle-particle contact as follows:

$$A_{ij} \coloneqq \frac{1}{2} r \sin(2\phi) \sin^2\theta, \qquad r \in [0, r_{\min_1}] \tag{7.70}$$

We will now motivate each term in this definition. The anisotropy with respect to ϕ is accommodated for by the $\sin(2\phi)$, where particles on the extension axis are weighted by $+1$ and on the compression axis by -1. Assuming there are two particles, one on the compression axis and one on the extension axis at the same distance, they cancel each other out by summing over both contacts. However, adding a slight anisotropy, where the particle on the compression axis is closer than the other, this produces a positive discrepancy. We weigh this difference linearly in r, so we have a direct measure of the compression/extension in relation to the distance, the particles are compressed or extended. Without a weight, we would count the difference in the average number of particles on the compression/extension axes. The connection between the anisotropy and the movement of the particles becomes more clear, if we look at a small perturbation of a particles position from its stable equilibrium point:

$$(r_0 + \Delta r)\sin(2(\phi_0 + \Delta\phi)) \approx r_0 \sin(\phi_0) + 2\Delta\phi r_0 \cos 2\phi_0 + \Delta r \sin 2\phi_0 \tag{7.71}$$

On the compression and extension axes, a small perturbation in ϕ can be neglected, as well as a small change in distance for the x- and y-axes. Using the MS as our unsheared reference point and looking at the small displacement between the IS and the MS, we find that in the ensemble average, due to the symmetry in fig. 7.11, the $\cos(2\phi)$ term vanishes. Due to isotropy of the MS, also the first term vanishes in the ensemble average. This leaves us just with the compression and extension, which is most relevant on the diagonals:

$$\langle r \sin(2\phi)\rangle \approx \langle \Delta r \sin(2\phi_0)\rangle \tag{7.72}$$

As the compression and extension axes may extend for several neighbor shells, our results would scale with the included volume. Therefore, we limit the anisotropy in our calculations to the first neighbor shell, which is bounded by the first minimum in $g(r)$ at $r_{\min_1}$. Furthermore, this specific limit has the advantage, that the number of particles changes only slightly during compression/extension and thereby has a lower impact on A_{ij} than the movement of the particles. In particular, if choosing the r_c as upper limit, this would be just at the position of the second neighbor peak, directly resulting in a negative correlation between the stress and the anisotropy due to the change of particles on the axes. At last, we introduce a weight with respect to the z axis, which favors particles on the xy-plane. Otherwise, particles with high r and $\vec{r}$ perpendicular to the xy-plane could introduce a huge change in ϕ by very small particle movements. We chose the weight $\sin^2\theta$ exactly as in contact stress (see section 7.1.1):

$$\sigma_{ij} = -\frac{1}{2} r F(r) \sin(2\phi) \sin^2\theta = -F(r) A_{ij}(r,\theta,\phi) \tag{7.73}$$

In this equation, we see that the stress and the anisotropy differ only by the multiplication with the force $F(r)$, which implicitly solves the problem at high radii, as the $F(r)$ becomes zero at r_c.

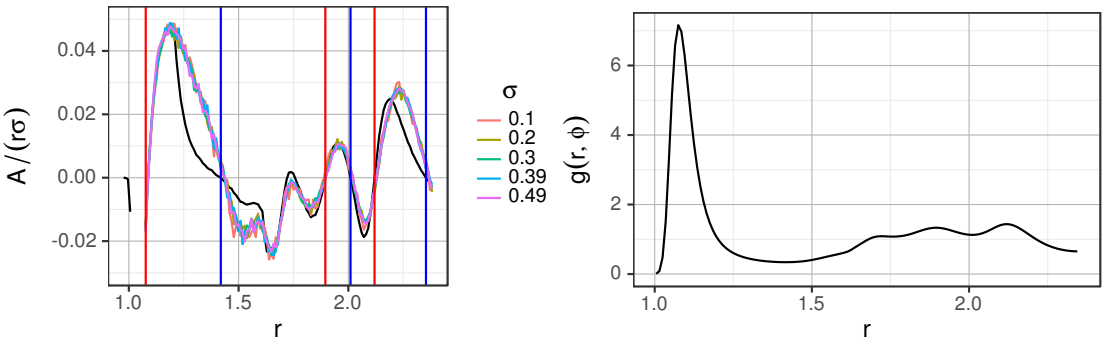

(a) $\frac{1}{r\sigma}\langle A_{ij}|r,\sigma\rangle$ (b) $g(r)$

Figure 7.12: (a) Radial dependence of A_{ij} for a fixed σ. Blue vertical lines mark the positions of the minima of $g(r)$ and red lines the maxima. The black line shows the derivative of $g(r)$, which has been scaled with the factor $-4 \cdot 10^{-3}$. (b) Radial distribution function $g(r)$. Both values were determined for inherent structures in equilibrium simulations at $T = 0.5$, $N = 130$.

However, we want the anisotropy to be a purely structural quantity, which can easily be extracted from experimental data without the requirement of the exact knowledge of the underlying force. Due to this additional factor, we expect significant deviations between the anisotropy and the stress in a single observation. However we will see in section 7.5.2, that there is a very strong correlation between the stress and the anisotropy in the ensemble average.

To get a measure of the anisotropy at a given radius, we average $\frac{1}{r}A_{ij}(r,\phi,\theta)$ over both angles, removing the radial weight. As we integrate over ϕ, we see a positive anisotropy at a given r, if there is a higher average number of particles on the extension axis than on the compression axis. At $\sigma > 0$, the particles move outwards on the extension axis and inwards on the compression axis. So compared with the average $g(r)$, we have a decreased number of particles before the first neighbor peak on the extension axis and an increased number beyond. The opposite is true for the compression axis (see fig. 7.9). So we expect a positive value for the anisotropy before the first neighbor peak and a negative value beyond. This is exactly, what we see in fig. 7.12. At every minimum/maximum in $g(r)$, we see a change of sign in $\frac{1}{r}\langle A_{ij}|r\rangle$. We reason, that the same has to be true for $\langle\sigma_{ij}|r\rangle$, as it has the same radial dependency. Furthermore, we see a perfect linear scaling of the anisotropy with the system stress, we averaged the anisotropy for. We remark, that we have seen the same scaling with σ in $\langle g(r)|\phi,\sigma\rangle$ in section 7.4.2. For future research, it might be interesting to determine the energy-dependence of A_{ij}, which would be interesting in terms of the PEL analysis of both the quiescent and the sheared system.

7.5.1 Anisotropy Distribution

As the anisotropy and the stress are similar in many ways, we now want to apply our calculation from section 7.2 to the anisotropy, to analyze the anisotropy distribution in the same way. From symmetry, we know that the mean anisotropy for a single contact in equilibrium must be zero due to isotropy:

$$\langle A_{ij}\rangle = \frac{1}{4\pi}\int_0^{r_{\min_1}}\int_0^{\pi}\int_0^{2\pi} r\frac{1}{2}\sin(2\phi)\sin^2\theta\sin\theta p(r)\mathrm{d}r\mathrm{d}\theta\mathrm{d}\phi = 0 \tag{7.74}$$

However, the variance of the contact-anisotropy is non-zero and calculated via:

$$\langle A_{ij}^2 \rangle = \frac{1}{4\pi} \int_0^{r_{\min_1}} \int_0^{\pi} \int_0^{2\pi} r^2 \frac{1}{4} \sin^2(2\phi) \sin^4\theta \sin\theta p(r) \mathrm{d}r \mathrm{d}\theta \mathrm{d}\phi \tag{7.75}$$
$$= \frac{1}{15} \int_0^{r_{\min_1}} r^2 p(r) \mathrm{d}\phi$$

The results can be found in *table* 7.5*a*. We remark, that for a radial weight of 1 instead of r, we would have $A_{ij} = \frac{1}{15}$ for all particle-neighbor combinations.

The two-contact anisotropy covariance can also be calculated by evaluating:

$$\mathrm{Cov}(\sigma_{ij}, \sigma'_{ij}) = \left\langle \sigma_{ij} \sigma'_{ij} \right\rangle \tag{7.76}$$
$$= \int_0^{r_c} \int_0^{r_c} \int_0^{\pi} \int_0^{\pi} \int_0^{2\pi} \int_0^{2\pi} r_1 \frac{1}{2} \sin(2\phi_1) \sin^2\theta_1 r_2 \frac{1}{2} \sin(2\phi_2) \sin^2\theta_2 \tag{7.77}$$
$$r_2^2 \sin\theta_2 p(r_2, \cos\alpha | r_1) p(r_1) p(\theta_1) p(\phi_1) \mathrm{d}r_1 \mathrm{d}r_2 \mathrm{d}\theta_1 \mathrm{d}\theta_2 \mathrm{d}\phi_1 \mathrm{d}\phi_2$$

Due to the number of nested integrals, we evaluate this equation using Monte-Carlo integration. The results are shown in table 7.5c.

The distributions for the by-particle anisotropy and the system anisotropy are shown in fig. 7.13. As the particle- and system-anisotropy are defined as the sum over many contacts, both distributions are Gaussian. The mean values for both distributions are zero, as the mean anisotropy for a contact is zero.

$$\langle A_i^p \rangle = \langle N_c^{pA} \rangle \langle A_{ij}^{pA} \rangle + \langle N_c^{pB} \rangle \langle A_{ij}^{pB} \rangle = 0 \tag{7.78}$$
$$\langle A^p \rangle = N^{pA} \langle A_i^{pA} \rangle + N^{pB} \langle A_i^{pB} \rangle = 0 \tag{7.79}$$

However the per particle variance can be calculated in the same was as the stress in section 7.2.2:

$$\langle (A_i^p)^2 \rangle = \langle N_c^{pA} \rangle \langle (A_{ij}^{pA})^2 \rangle + \langle N_c^{pB} \rangle \langle (A_{ij}^{pB})^2 \rangle \tag{7.80}$$
$$+ (\langle (N_c^{pA})^2 \rangle - \langle N_c^{pA} \rangle) \langle A_{ij}^{pA} A_{ij}^{pA\prime} \rangle$$
$$+ (\langle (N_c^{pB})^2 \rangle - \langle N_c^{pB} \rangle) \langle A_{ij}^{pB} A_{ij}^{pB\prime} \rangle$$
$$+ 2 \langle N_c^{pA} \langle N_c^{pB} | N_c^{pA} \rangle_{N_c^{pB}} \rangle_{N_c^{pA}} \langle A_{ij}^{pA} A_{ij}^{pB} \rangle$$
$$\tag{7.81}$$

Together with the covariance values values given in table 7.5c, we arrive at $\langle (A_{i,calc}^A)^2 \rangle = 0.032610$ and $\langle (A_{i,calc}^B)^2 \rangle = 0.043773$. However, the expected value for the type A particles differ significantly from the results extracted directly from the simulations (see table 7.6a). Looking at eq. (7.80) the first two summands are completely fixed and only the calculation of the covariance gives room for error. In contrast to the calculation of the by-particle stress variance, in this case the contact-covariance is of the same order as the contact-variance. Therefore, any error to the calculated covariance is more visible. Looking at the values of the expected contact covariance and the calculated value, we see an overestimation of approximately 6%. Multiplying the

Part. Type	Neigh. Type	Result
A	A	0.04883764
A	B	0.01820559
B	B	0.00344327

(a) Anisotropy Contact

Variance: $\langle A_{ij}^{pn} \rangle$

Part. Type	Neigh. Type	Result
A	A	0.10805245(93)
A	B	0.01005931(15)
B	A	0.04023706(61)
B	B	0.01178047(16)

(b) Anisotropy Particle

Covariance: $\langle \sum_j A_i^p A_j^n \rangle$

Part. Type	Neigh. Type 1	Neigh. Type 2	Result
A	A	A	-0.00231884(96)
A	A	B	-0.00046972(55)
A	B	B	-0.00078475(12)
B	A	A	-0.00074336(24)
B	A	B	-0.000051663(51)
B	B	B	-0.0000203804(47)

(c) Anisotropy Contact Covariance: $\langle A_{ij}^{pn_1} A_{ij}^{pn_2} \rangle$

Table 7.5: (a) Anisotropy variance for a single contact between two particles, calculated by numerical integration. (b) Anisotropy covariance between particles, calculated also by Monte-Carlo integration over the r dependent mean covariance $C_{pn}(r)$. (c) Anisotropy covariance between individual contacts for a single particle, calculated by Monte-Carlo integration over the two-contact distribution (see eq. (7.76)).

Part. Type	Result
A	0.098384(5)
B	0.045160(4)

(a) Anisotropy Particle

Variance: $\langle (A_i^p)^2 \rangle$

Part. Type	Result
A	21.362(11)
B	1.48109(73)
Combined	24.936(12)

(b) Anisotropy System

Variance: $\langle (A^p)^2 \rangle$

Table 7.6: (a) Anisotropy variance for individual particles and (b) anisotropy variance for the whole system. Both values are determined directly from equilibrium simulation data at $T = 0.5$, $N = 130$.

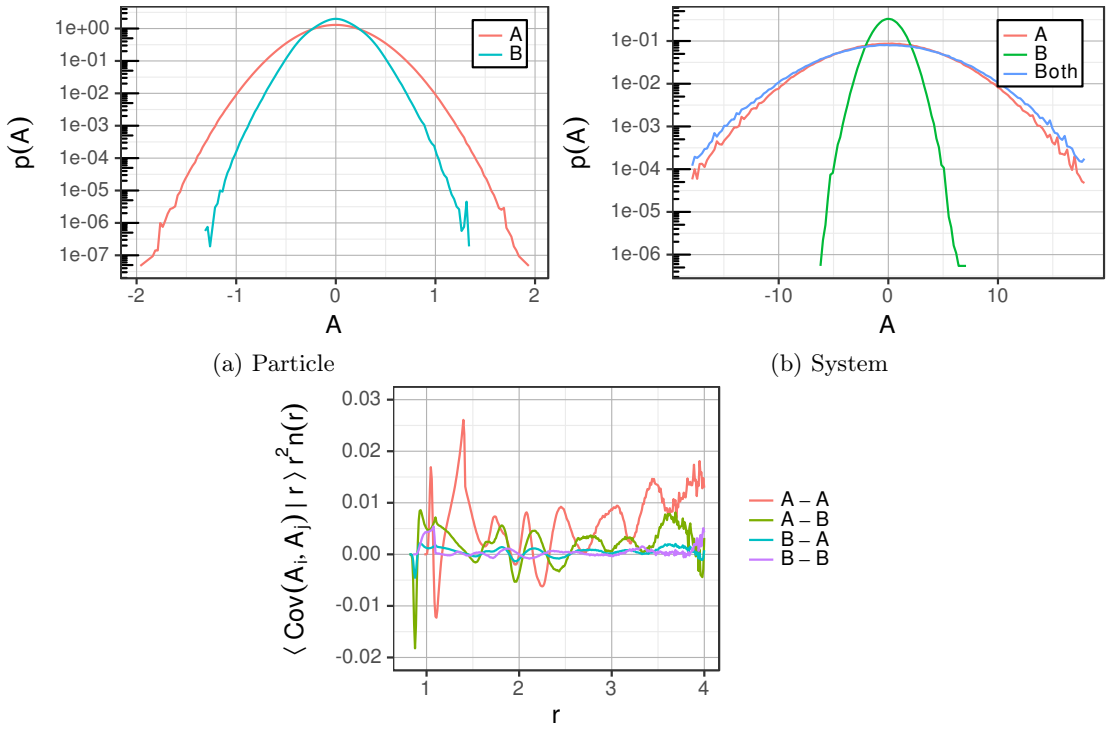

(a) Particle

(b) System

(c) Particle-Particle Covariance

Figure 7.13: Anisotropy distribution for a single particle (a) and for the whole simulation box (b). (c) shows the particle-particle anisotropy covariance, computed up to half of the simulation box length $\frac{L}{2}$.

anisotropy covariance with a factor of 0.94, we arrive at much better estimate of the by-particle anisotropy variance for type A particles, while the results for type B particles get slightly worse: $\langle (A^A_{i,calc,94\%})^2 \rangle = 0.097357$ and $\langle (A^B_{i,calc,90\%})^2 \rangle = 0.067893$. However, most of the contribution for the system anisotropy comes from type A particles, as we will see. The error in the covariance calculation stems from the fact, that we use a fixed grid with linear approximation to estimate $p(r_2, \cos\alpha | r_1)$, as described in section 7.2.1. The influence of this error on each calculated variable is different, as the calculated overall probability by integration over $p(r_2, \cos\alpha | r_1) p(r_1)$ is underestimated by approximately 2%. In passing, we note that changing the covariance values by 10% would change our estimates for the particle stress variance only slightly. A better interpolation scheme would be the use of a radial basis function (RBF) interpolation [Buhmann, 2003]. However, the memory requirement for this method could not be met by our hardware.

Giving a good estimate for the system anisotropy variance proves again more difficult than the particle variance, as we experience finite size effects. The r dependent mean particle-particle anisotropy covariance is shown in fig. 7.13c. As in section 7.2.3, we integrate over the first periodic neighbor box using Monte-Carlo integration. This results in the estimations for the covariances, given in table 7.5b. Using these covariance values, we can estimate the system

anisotropy by:

$$\langle (A^p)^2 \rangle = N^A \mathrm{Var} A_i + N^A \left\langle \sum_{j \neq i} \mathrm{Cov}(A_i^{pA}, A_j^{pA}) \right\rangle \tag{7.82}$$

$$\begin{aligned} \langle (A)^2 \rangle = {} & N^A \mathrm{Var} A_i + N^A \left\langle \sum_{j \neq i} \mathrm{Cov}(A_i^{AA}, A_j^{AA}) \right\rangle \\ & + N^B \mathrm{Var} A_i + N^B \left\langle \sum_{j \neq i} \mathrm{Cov}(A_i^{BB}, A_j^{BB}) \right\rangle \\ & + 2N^A \left\langle \sum_{j \neq i} \mathrm{Cov}(A_i^{AA}, A_j^{AB}) \right\rangle \end{aligned} \tag{7.83}$$

The calculated values using the 94% covariance results from above are: $\langle (A^A_{calc,94\%})^2 \rangle = 21.370$, $\langle (A^B_{calc,94\%})^2 \rangle = 2.070$ and $\langle (A_{calc,94\%})^2 \rangle = 25.532$. Compared with the real results in table 7.6b this is again a very good estimate for the anisotropy variance for the whole system. In this calculation, our previous error in the estimation of the type B particle anisotropy variance has little influence on the result, as its contribution is only around 7%.

7.5.2 Stress-Anisotropy Correlation in the Ensemble Average

From definition eq. (7.70), we may indeed expect some connection between the anisotropy and the stress in the ensemble average. In fig. 7.14, we see a very strong, potentially linear, correlation. We also see a similar overshoot, as in the stress trajectory and a constant anisotropy as we reach the steady state in the flow regime. We remark, that for a single IS trajectory, the anisotropy curve shows much more jumps than the energy, the stress or other observables. These are caused by fluctuations in the number of contacts in the first neighbor shell. A possible way to counter this effect would be the introduction of a dampening term similar to the force in eq. (7.73). However, this is not necessary for the current work, because the fluctuations are already small, as we chose the cutoff at the first minimum of $g(r)$.

In the regime of high shear rates, we find that the trajectory and IS ensemble averaged flow anisotropy behaves also completely similar. However, one distinguishing feature between the anisotropy and the stress is seen in the MS trajectory. While the stresses in all MS must be zero (see section 3.2.3), there is a small, but finite, positive anisotropy remaining for minimized structures. Hence, we keep a memory of our previous shear direction in our system, which is not visible in common observables like the energy, stress or pressure. For future studies, it might be intriguing examine the physical origin of this residual anisotropy and check for a connection to the two-state shear transformation zone formalism [Langer, 2001]. The basic idea in this model is the existence zones with two different directions. These directions could then be associated with the sign of the residual anisotropy.

To analyze the connection between anisotropy and stress further, we look at the combined density $p(\sigma, A)$, which we have plotted in fig. 7.15a. As previously, we scale system stress by $2V$, so that $2V\sigma$ is a plain sum of particle stresses. While we see very large fluctuations, the mean system stress clearly shows a strong linear dependence on the anisotropy (see fig. 7.15d).

So to find the slope of the linear connection between the system stress and the system anisotropy,

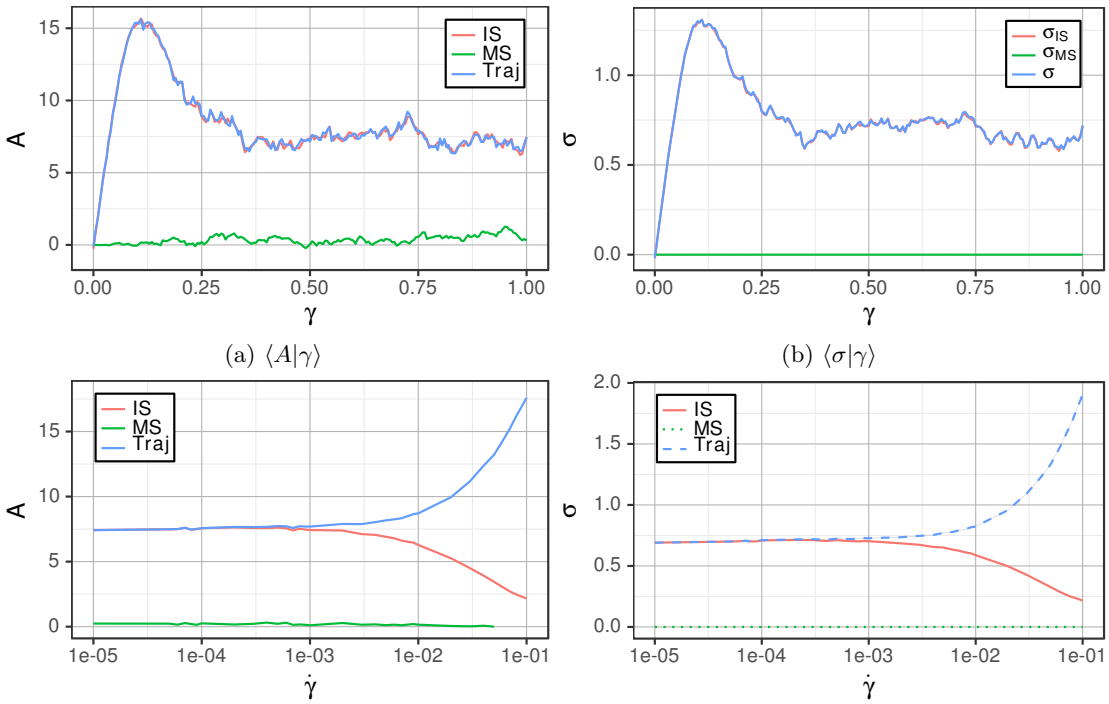

(a) $\langle A|\gamma\rangle$ (b) $\langle\sigma|\gamma\rangle$

(c) $\langle A|\dot{\gamma}\rangle$ (d) $\langle\sigma|\dot{\gamma}\rangle$

Figure 7.14: Connection between anisotropy (a,c) and stress (b,c) in the ensemble average over 128 independent runs at $T = 0.01$, $N = 130$, $\dot{\gamma} = 10^{-4}$ using 6 different shear directions (see section 2.6.2). (a,b) compare the anisotropy/stress with respect to γ at the start of our simulations. (c,d) compare the mean anisotropy/stress in the flow regime.

we have to calculate the covariances between σ and A, since:

$$\langle\sigma|A\rangle = mA \quad \Leftrightarrow \quad \langle\sigma A|A\rangle = mA^2 \tag{7.84}$$

$$\Rightarrow \quad \langle\sigma A\rangle = m\langle A^2\rangle \quad \Leftrightarrow \quad m = \frac{\langle\sigma A\rangle}{\langle A^2\rangle} \tag{7.85}$$

Luckily, we already calculated the anisotropy variance in section 7.5.1.

In strong contrast the linear stress-anisotropy connection for system-wide value, the mean particle stress $\langle\sigma_i|A_i\rangle$ shows a very non-linear dependency on the anisotropy, as shown in fig. 7.15b. However, this does not hinder us from following the same calculations as before, starting with the one- and two-contact stress-anisotropy covariance, which is calculated using integration over

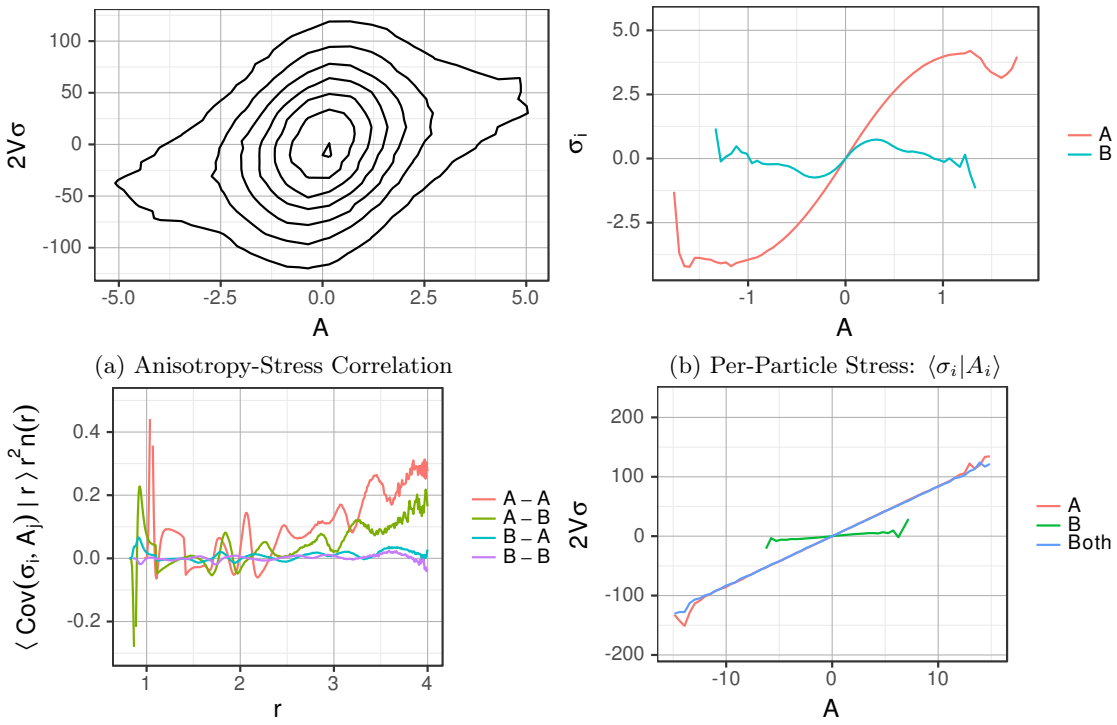

(a) Anisotropy-Stress Correlation

(b) Per-Particle Stress: $\langle \sigma_i | A_i \rangle$

(c) Per-Particle Stress-Anisotropy Covariance: $\mathrm{Cov}(\sigma_i, A_j | r) n(r)$

(d) Mean System Stress: $\langle \sigma | A \rangle$

Figure 7.15: (a) Contours for the probability density of inherent structure with a given system anisotropy and stress. (b) Mean value of particle stress for a given particle anisotropy: $\langle \sigma_i | A_i \rangle$. (c) Covariance between particle stress and anisotropy for different particles, multiplied by particle density: $\mathrm{Cov}(\sigma_i, A_j | r) n(r)$. (d) Mean value of system stress for a given system anisotropy: $\langle \sigma | A \rangle$.

the probability densities:

$$\begin{aligned}
\mathrm{Cov}(\sigma_{ij}, A_{ij}) &= \langle \sigma_{ij} A_{ij} \rangle && (7.86)\\
&= -\frac{1}{4\pi} \int_0^{r_c} \int_0^{\pi} \int_0^{2\pi} r F(r) \sin^2\theta \frac{1}{2} \sin(2\phi) \sin(2\phi) \sin\theta p(r) \mathrm{d}r \mathrm{d}\theta \mathrm{d}\phi \\
&= -\frac{1}{6} \int_0^{r_c} r F(r) p(r) \mathrm{d}r \\
\mathrm{Cov}(\sigma_{ij}, A'_{ij}) &= \langle \sigma_{ij} A'_{ij} \rangle && (7.87)\\
&= \int_0^{r_c} \int_0^{r_c} \int_0^{\pi} \int_0^{\pi} \int_0^{2\pi} \int_0^{2\pi} r_1 F(r_1) \sin^2\theta \frac{1}{2} \sin(2\phi_1) \sin(2\phi_2) && (7.88)\\
&\qquad r_2^2 \sin\theta_2 p(r_2, \cos\alpha | r_1) p(r_1) p(\theta_1) p(\phi_1) \mathrm{d}r_1 \mathrm{d}r_2 \mathrm{d}\theta_1 \mathrm{d}\theta_2 \mathrm{d}\phi_1 \mathrm{d}\phi_2
\end{aligned}$$

Again, we solve the first integral using an adaptive quadrature algorithm and the second via Monte-Carlo integration. The results can be seen in table 7.7. Using these values, we can

Part. Type	Neigh. Type	Result
A	A	-0.0828325
A	B	0.00203300
B	B	-0.0021569

(a) Anisotropy-Stress Contact Covariance: $\langle \sigma_{ij}^{pn} A_{ij}^{pn} \rangle$

Part. Type	Neigh. Type	Result
A	A	1.254296(16)
A	B	0.1393022(19)
B	A	0.403599(10)
B	B	-0.00545858(90)

(b) Anisotropy-Stress Particle Covariance: $\langle \sum_j \sigma_i^p A_j^n \rangle$

Part. Type	Neigh. Type 1	Neigh. Type 2	Result
A	A	A	0.0051389(32)
A	A	B	0.0022368(20)
A	B	A	0.0000536(22)
A	B	B	-0.00063073(50)
B	A	A	0.00007052(98)
B	A	B	-0.00008214(20)
B	B	A	0.00002752(38)
B	B	B	-0.000165277(40)

(c) Anisotropy-Stress Contact Covariance: $\langle \sigma_{ij}^{pn_1} A_{ij}^{pn_2} \rangle$

Table 7.7: Stress-anisotropy covariance for one contact (a), between two particles (b) and between two distinct contacts (c) in dependence of the particle/neighbor types. The covariance values in (b) and (c) were computed via Monte-Carlo integration. For (b) we have used simulation data to directly determine the integrand $\langle \sigma_i A_j | r \rangle$. The necessary two-contact probability for (c) was determined using the method described in section 7.2.1.

compute the covariance between σ_i and A_i for a given particle type:

$$\begin{aligned} \langle \sigma_i A_i \rangle = &\langle N_c^A \rangle \langle \sigma_{ij}^A A_{ij}^A \rangle + \langle N_c^B \rangle \langle \sigma_{ij}^B A_{ij}^B \rangle \\ &+ (\langle (N_c^A)^2 \rangle - \langle N_c^A \rangle) \langle \sigma_{ij}^A A_{ij}^{A\prime} \rangle \\ &+ (\langle (N_c^B)^2 \rangle - \langle N_c^B \rangle) \langle \sigma_{ij}^B A_{ij}^{B\prime} \rangle \\ &+ \langle N_c^A \langle N_c^B | N_c^A \rangle_{N_c^B} \rangle_{N_c^A} \langle \sigma_{ij}^A A_{ij}^B \rangle \\ &+ \langle N_c^A \langle N_c^B | N_c^A \rangle_{N_c^B} \rangle_{N_c^A} \langle \sigma_{ij}^B A_{ij}^A \rangle \end{aligned} \tag{7.89}$$

This results in $\langle (\sigma_i^A A_i^A)_{calc,94\%} \rangle = 0.509247$ for type A particles and $\langle (\sigma_i^B A_i^B)_{calc,94\%} \rangle = 0.083098$ for type B particles. As in section 7.5.1, we have used a factor of 0.94 to correct the covariance. Both values are very close to the values directly extracted from the simulation, which are given in table 7.8a.

For a single particle type, the covariance for the whole system can be calculated using:

$$\begin{aligned} \langle 2V\sigma A \rangle = \langle \sum_{ij} \sigma_i A_j \rangle &= \sum_i \langle \sigma_i A_i \rangle + \sum_{i \neq j} \langle \sigma_i A_j \rangle \\ &= N \langle \sigma_i A_i \rangle + N \langle \sum_{j \neq i} \sigma_i A_j \rangle \end{aligned} \tag{7.90}$$

(7.91)

Part. Type	Result
A	0.512203(43)
B	0.098399(37)

(a) Anisotropy-Stress Particle Covariance: $\langle \sigma_i^p A_i^p \rangle$

Part. Type	Result
A	181.36(12)
B	2.4290(62)
Combined	208.89(14)

(b) Anisotropy-Stress System Covariance: $\langle 2V\sigma^p A^p \rangle$

Table 7.8: (a) Stress-Anisotropy covariance for individual particles and (b) for the whole system. Both values are determined directly from equilibrium simulation data at $T = 0.5$, $N = 130$.

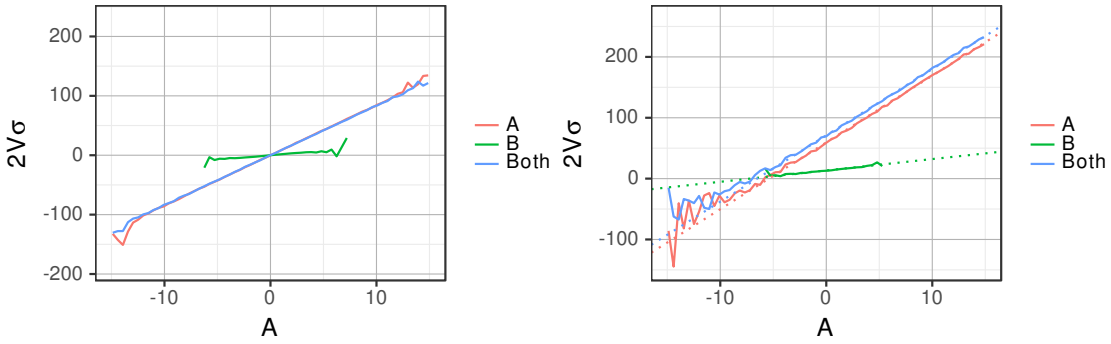

(a) $T = 0.5$, $\dot{\gamma} = 0$ (b) $T = 0.01$, $\dot{\gamma} = 10^{-4}$

Figure 7.16: Mean value of system stress for a given system anisotropy in the trajectory of inherent structures: $\langle \sigma | A \rangle$ for (a) the equilibrium at $T = 0.5$, $\dot{\gamma} = 0$ and (b) the flow regime at $T = 0.01$, $\dot{\gamma} = 10^{-4}$.

The corresponding r dependent covariance function $\mathrm{Cov}(\sigma_i, A_j | r)$, used to calculate the two-particle covariance, is shown in fig. 7.15c. Like the other covariances, we notice finite size effects in these functions, forcing us to integrate over the first periodic neighbor box instead of the whole volume. For type A particles, we calculate a stress-anisotropy covariance $\langle (2V\sigma A)_{calc} \rangle = 183.41$ and $\langle (2V\sigma A)_{calc} \rangle = 2.0186$ for type B particles. The covariance including all particles is calculated as: $\langle (2V\sigma A)_{calc} \rangle = 210.41$. Again, all values are in very good agreement to simulation data (see table 7.8b).

Finally, this lets us approximate the slope of $2V\sigma$ against A. We find a value of $m_{\mathrm{calc}} = 8.24$, which is in reasonable agreement with the fitted slope of $m_{\mathrm{fit}} = 8.44$. Dividing by $2V$, we arrive at a factor of $3.80 \cdot 10^{-2}$ between the stress and the anisotropy in the ensemble average.

This result is valid for IS during in thermal equilibrium without shear. However, looking again at fig. 7.14, where we compare at $T = 0.01$ and $\dot{\gamma} = 10^{-4}$, we see a factor of around 10^{-1}. Therefore, there has to be an additional effect, which sets in, when we shear our system. This can also be seen at the height of the overshoot, which is bigger in case of the anisotropy compared to the overshoot of the stress. We remark, that a change in the number of contacts can be ruled out, as it changes less than 2% between the equilibrium and the flow regime. Figure 7.16 shows a comparison of the system stress for a given anisotropy for the equilibrium and the sheared system. Even for the sheared system, we see a linear dependence between the stress and the anisotropy with a slightly changed slope. However, we now find a non-zero intercept for the

sheared system. We remark, that in the opposite case $\langle A|\sigma\rangle$ the intercept is still zero. This shows, that there is yet another contribution to the system stress, resulting from shear, that is not captured by our definition of the anisotropy.

7.6 Summary

In summary, we could show that the per-contact distributions for key observables are easily computable in spherical coordinates using just the interaction potential and the neighbor density. As an example, we determined the power-law behavior and the exponential tails of the per-contact stress distribution with perfect accuracy. With the addition of the the single-particle two-contact distribution, one can then calculate the contact-contact covariances, and with them the moments of the per-particle distributions. As these are Gaussian, the first two moments suffice to describe the distribution. In the calculation of the single-particle variances, we found that the contribution of the covariances for distinct contacts is at least as high as the variance, showing the strong contribution of the amorphous structure. Therefore a high accuracy in the numerical calculation is necessary, especially if both have different signs.

The extension of this method to calculate the moments of the system-wide distributions is computationally more difficult, as it requires the use of the two-contact distribution for arbitrary contacts. Due to computational limitations, we had to measure the particle-particle covariances directly in the simulations. For future research, it might be interesting to model the radial covariance functions instead of measuring them for every observable, as they contain key information for the system size scaling of the observables. In the computation of the stress variance, we also found that the radial covariance functions contribute a large part.

As an application of this method, we calculated the affine contribution of the shear modulus, starting with the expression of the modulus in spherical coordinates. This affine contribution is approximately twice as big as the real shear modulus. A better approximation of the real shear modulus may be achieved by measuring or modeling the derivative of the neighbor density with an applied strain.

Looking at the radial distribution of the neighbors, we found that the changes on the compression and extension axes scale perfectly with the current residual stress in the system. Using the MS as reference point, we also looked at the actual average displacement between the IS and MS configurations. This showed the expected symmetry and provided a detailed view on the particle movements towards the compression and extension axes.

In the final part of this chapter, we defined an anisotropy observable, based on our previous observations, which can be computed without the knowledge of the interaction potential but otherwise resembles closely the definition of the stress. We found, that just like the radial distribution, the radial contribution to the anisotropy also scales linearly with the system stress. This linear scaling also translates well into the sheared system, where we observe a very good agreement between the anisotropy and the stress at the overshoot and in the flow regime. We see that this linear behavior is mostly caused by the particle covariances, as the per-particle stress-anisotropy dependence is highly non-linear. Furthermore, we found that going over from the equilibrium to the sheared system in the flow regime, the stress-anisotropy dependence stays linear with only a slight change in the slope. However, we now notice a finite stress at zero anisotropy, showing a shear-induced effect that is not captured by our definition of the anisotropy.

Chapter 8

Summary

In summary, we could show that the sheared potential energy landscape has a huge effect on the dynamics. In the quiescent system the dynamics can be described as a hopping process between *inherent structures* (IS) and *metabasins* (MB). For the description of the sheared system, we introduced the new concept of *minimized structures* (MS), which is basically an extension to the inherent structures in the quiescent state. They are defined similar to the IS, but also allow the energy minimization to change the Lees-Edwards boundary conditions, which is equivalent to an *athermal quasistatic* (AQS) simulation in the direction of zero stress. This definition is motivated by the need for a stable reference point, as due to an applied shear strain, inherent structures are continuously changing between plastic events. Defining metabasins via hopping between MS allowed us to transfer this concept to the sheared system, describing not only the limiting cases of high shear rate and high temperature, but also the crossover between both in terms of metabasin waiting times.

We have seen, that there are also plastic events possible during a single MS. We called these events IS transitions, as they correspond to vanishing inherent structures. Comparing IS transitions to MS transitions, we came to the conclusion, that IS transitions are more local and small, as in general, they show only small energy and stress drops and have a smaller number of contacts involved in the transition. Nevertheless, the stress drops of IS transitions suffice, to cause a small stress overshoot in the ensemble average within a *single* MS. This overshoot however differs from the real overshoot, by having 33% higher flow stress after the overshoot. We noticed a striking resemblance of the stress drop distribution in the sheared system and the energy drop distribution in the quiescent system, showing again the strong influence of the energy landscape. Via the assumption, that the part of the system with low stresses and another random part is resetting its stress during a transition, we reproduced this stress drop distribution with a small toy model.

Next, we looked at the sheared PEL during the stress overshoot and yielding. In particular, we looked at the statistics of the first MS transition. We found, that there are two kinds of MS transitions, one of which has no significant influence on key observables, like the energy and the form of the stress overshoot. From the data, it was easy to identify an average crossover position, which was slightly lower than the position of the overshoot maximum. Furthermore, we identified a strong dependence on the starting energy. This corresponds to the observation, that the properties of the sheared system depends on the initial glass preparation, as often reported in literature. Looking at the MS jump distance for different system sizes, we found

that the system size scaling changes at the crossover point. This provided a link to systems under cyclic shear, which show a crossover point, where the avalanche statistics also change their system size scaling. With regard to yielding, we concluded that the crossover marks the average onset of irreversible transitions, which is accompanied with a large stress drop. However, we note that MS transitions are not necessarily irreversible under shearing backward, as we saw in cyclic simulations, that limit cycles can form up to very high oscillations amplitudes at small system sizes. Using a toy-model, we could reproduce the form of the overshoot by just using the statistics of MS transitions, showing that IS transitions add only minor corrections to the height and position in the case of low start energies.

One major strength of the predictive power of MS transitions can be seen in cyclic shear simulations. Here, we could show that information about the MS energies at the reversal point suffices to perfectly predict the overshoot height. Also in good agreement with data, we could predict the shear modulus at the reversal point. We could attribute the discrepancy to MS transitions, which are reversible at shearing backwards. In the analysis of limit cycles in cyclic AQS simulations, we found that the difficulty to find a cycle shows a power-law behavior in $\gamma_{\max}$ with a divergence at $\gamma_{\mathrm{nl}} = 0.231$, as measured by the average number of cycles needed to reach a limit cycle. The highest average MS energy of trajectories in limit cycles was found to be -4.55, which was reached at a similar value of $\gamma_{\max} = 0.22$. Adding a small temperature by using MD simulations, we found that the limit cycles were easily broken. The number of cycle repetitions, until breaking the cycle, showed a crossover position, that was similar to the previously found crossover position in the MS transitions, hinting at some structural origin. Furthermore, we examined the reversibility of the first MS transition, finding that the average onset of irreversible transitions is at the same position. Using the reversibility probability, we found a simple method to approximate the value of $\gamma_{\max}$, beyond which no limit cycles can be found in cyclic AQS simulations. Normally, due to diverging simulation times, this value is difficult to determine accurately. In addition, we also found a simple expression for the probability to be already in a limit cycle at the start of the simulation with respect to $\gamma_{\max}$.

We also looked at the flow regime, with a focus on the crossover between temperature and shear rate dominated regime, at both limiting cases quite well understood. Our investigation of the flow curve showed a decreased influence of the inherent structures at the higher shear rates $\dot{\gamma} > 10^{-3}$, which is caused mainly by ballistic movement. Nevertheless, we found that the energy landscape in terms of minimized structures still plays a major role. The position in the energy landscape can be easily expressed by an effective temperature, which can be extracted from the metabasin energies. We concluded that mechanical rejuvenation by an applied shear at zero temperatures brings us to the upper limit of the energy landscape influenced regime, which is at $T_{\mathrm{eff}} \approx 0.775$. Then, we investigated different rate models for the description of the metabasin waiting times in the crossover regime. With these simple models, we were already able to achieve very good agreements at high energies, where the barrier sizes are constant. However, at low energies and at intermediate shear rates, the models showed some weaknesses due to a still missing description of the effective metabasin energy barriers. We hope that our results might inspire future work in this direction.

Using the now accessible metabasin waiting times in the sheared system, we could give an expression for the structural contribution of the viscosity, which causes shear thinning behavior. Basically, we assumed a stress-strain curve with the length of a metabasin, starting from zero stress, with an energy dependent shear modulus. Despite many oversimplifications, we could already achieve a good agreement between our model expression and the simulation data. We were also able to approximate the diffusion constant in the crossover regime. It turned out that

using the metabasin waiting times produced a systematically too small diffusion constant and that the MS relaxation times provided a much better fit to the data. However, we concluded, that more research is necessary to understand this behavior in detail.

Also, we explored the stress and other key observables in the equilibrium, as even in equilibrium fluctuations there is still a residual stress in the inherent structures. Using some calculus, we were able to derive the stress distribution for individual contacts in spherical coordinates with just using isotropy, $g(r)$ and knowledge of the force field. Then, we showed how to derive the moments of the Gaussian per-particle distribution in a straight forward calculation, using two-contact distribution for a single particle. Using this method, it is equally easy to calculate the distribution of the per-particle energy, pressure and the affine contribution of the shear modulus. For the affine contribution of the shear modulus, we found that it overestimates the real shear modulus approximately by a factor of 2. The extension to the system had been done via particle-particle correlation functions, showed massive finite size effects. Nevertheless, we could reproduce perfect $\frac{1}{N}$ system size scaling, which we could also see in our mathematical expressions. Overall, we found that most contribution to the per-particle and system variances came from type A particles.

As a stressed system shows structural anisotropy with respect to the chosen coordinate system, we defined a purely structural contact anisotropy mathematically, which can also be extracted from experiments without knowledge of the force field. We found an anisotropy overshoot and an anisotropy flow curve, which were nearly identical to the stress overshoot and the stress flow curve. Within both the equilibrium and the flow regime at low temperature, we found a linear connection between the stress and the anisotropy in the fluctuations. However, when going over from the quiescent system in equilibrium to the low temperature flowing system, there appeared an offset in the stress dependence on the overshoot. We concluded, that this is the result of another structural contribution not yet captured by our definition.

Overall, we could see that the concept of the extended potential energy landscape $V(\mathbf{x}, \gamma)$ gave us many new insights into the description and understanding of the sheared system. The γ dependence at vanishing energy barriers, having the functional form of a fold catastrophe, led to the simple picture of a tilted PEL. This picture helped us to understand, how points in the extended PEL are connected with each other and how to find minimized structures as stable reference points. This in turn helped us to easily explain hysteresis effects, which lead to limit cycles in cyclic shear and are also the key aspect in the process of yielding. It also provided us the central idea for our model to explain the change in waiting times in the crossover between shear and temperature dominated regime.

In this work, we focused mainly on small systems, which already includes much of the phenomenology of large systems. However, some effects, like shear bands, are only present in large systems. To extend our findings from the small system to the large system, PEL based elasto-plastic models on the mesoscopic scale are actively being researched. As such models have successfully been applied to the quiescent system [Rehwald and Heuer, 2012], we hope they apply similarly to the sheared PEL. In particular, these models are expected to show shear bands and characteristic avalanche-like scaling behavior.

Appendix A

Exponential Integral and Hypergeometric Function

In section 6.3.4 we made use of the exponential integral function Ei and the confluent hypergeometric function of the second kind U. The use of these functions was necessary to write the integrals in a more simple form, which could then be evaluated numerically. In this chapter, we give a short overview of some mathematical transformations of these functions, which were needed during the calculations. These and other properties of these functions are found in [Weisstein, a] and [Weisstein, b] as well as mathematics textbooks.

The connection between the exponential integral Ei and U given by:

$$U(1,1,x) = \Gamma(0,x)\mathrm{e}^{x} = -\mathrm{Ei}(-x)\mathrm{e}^{x} \tag{A.1}$$

Here, $\Gamma(0,x)$ is the upper gamma function. We note in passing, that this relation holds only for positive x.

The definition of the exponential integral is given by:

$$\mathrm{Ei}(x) \coloneqq -\int_{-x}^{\infty} \frac{\mathrm{e}^{-t}}{t}\mathrm{d}t \tag{A.2}$$

By the use of substitution ($-t = a\mathrm{e}^{ux}$), it follows that:

$$\int \mathrm{e}^{a\mathrm{e}^{ux}}\mathrm{d}x = \frac{1}{u}\mathrm{Ei}\left(a\mathrm{e}^{ux}\right) \tag{A.3}$$

Especially useful is the limiting/asymptotic behavior for small and large arguments:

$$\lim_{x\to-\infty} \mathrm{Ei}(x) = 0 \tag{A.4}$$

$$\lim_{x\to\infty} \mathrm{U}(1,1,\frac{c}{x}\mathrm{e}^{-ax}) = a \tag{A.5}$$

$$\lim_{x\to0} \frac{1}{x}\mathrm{U}(1,1,\frac{c}{x}) = \frac{1}{c} \tag{A.6}$$

$$\tag{A.7}$$

And also the Taylor expansions for small x:

$$\mathrm{U}(1,1,\frac{c}{x}) = \frac{x}{c} - \frac{x^2}{c^2} + 2\frac{x^3}{c^3} + \mathcal{O}(x^4) \tag{A.8}$$

$$\mathrm{U}(1,1,\frac{c}{x}\mathrm{e}^{-ax}) = \frac{x}{c} + (ac-1)\frac{x^2}{c^2} + \frac{(2-ac)^2}{2}\frac{x^3}{c^3} + \mathcal{O}(x^4) \tag{A.9}$$

Appendix B

Bibliography

[Abraham and Harrowell, 2012] Abraham, S. and Harrowell, P. (2012). The origin of persistent shear stress in supercooled liquids. *J. Chem. Phys.*, 137(1):014506.

[Argon, 1979] Argon, A. (1979). Plastic deformation in metallic glasses. *Acta Metall.*, 27(1):47–58.

[Berthier and Barrat, 2002] Berthier, L. and Barrat, J.-L. (2002). Nonequilibrium dynamics and fluctuation-dissipation relation in a sheared fluid. *J. Chem. Phys.*, 116(14):6228.

[Berthier and Biroli, 2011] Berthier, L. and Biroli, G. (2011). Theoretical perspective on the glass transition and amorphous materials. *Reviews of Modern Physics*, 83(2):587–645.

[Berthier et al., 2005] Berthier, L., Chandler, D., and Garrahan, J. P. (2005). Length scale for the onset of fickian diffusion in supercooled liquids. *Europhysics Letters (EPL)*, 69(3):320–326.

[Bonn et al., 2017] Bonn, D., Denn, M. M., Berthier, L., Divoux, T., and Manneville, S. (2017). Yield stress materials in soft condensed matter. *Rev. Mod. Phys.*, 89(3).

[Büchner and Heuer, 2000] Büchner, S. and Heuer, A. (2000). Metastable States as a Key to the Dynamics of Supercooled Liquids. *Phys. Rev. Lett.*, 84(10):2168–2171.

[Buhmann, 2003] Buhmann, M. D. (2003). *Radial basis functions: theory and implementations*, volume 12. Cambridge university press.

[Chattoraj et al., 2010] Chattoraj, J., Caroli, C., and Lemaître, A. (2010). Universal, additive effect of temperature on the rheology of amorphous solids. *Phys. Rev. Lett.*, 105(26):266001.

[Chowdhury et al., 2016] Chowdhury, S., Abraham, S., Hudson, T., and Harrowell, P. (2016). Long range stress correlations in the inherent structures of liquids at rest. *J. Chem. Phys.*, 144(12):124508.

[Chung and Lacks, 2012a] Chung, Y. G. and Lacks, D. J. (2012a). Atomic Mobility in a Polymer Glass after Shear and Thermal Cycles. *J. Phys. Chem. B*, 116(48):14201–14205.

[Chung and Lacks, 2012b] Chung, Y. G. and Lacks, D. J. (2012b). Atomic mobility in strained glassy polymers: The role of fold catastrophes on the potential energy surface. *J. Polym. Sci., Part B: Polym. Phys.*, 50(24):1733–1739.

[Denisov et al., 2015] Denisov, D. V., Dang, M. T., Struth, B., Zaccone, A., Wegdam, G. H., and Schall, P. (2015). Sharp symmetry-change marks the mechanical failure transition of glasses. *Sci. Rep.*, 5(1):14359.

[Denny et al., 2003] Denny, R. A., Reichman, D. R., and Bouchaud, J.-P. (2003). Trap Models and Slow Dynamics in Supercooled Liquids. *Phys. Rev. Lett.*, 90(2):025503.

[Ding et al., 2014] Ding, J., Cheng, Y.-Q., and Ma, E. (2014). Full icosahedra dominate local order in cu64zr34 metallic glass and supercooled liquid. *Acta Materialia*, 69:343–354.

[Divoux et al., 2016] Divoux, T., Fardin, M. A., Manneville, S., and Lerouge, S. (2016). Shear banding of complex fluids. *Annu. Rev. Fluid Mech.*, 48(1):81–103.

[Doliwa and Heuer, 2003a] Doliwa, B. and Heuer, A. (2003a). Energy barriers and activated dynamics in a supercooled Lennard-Jones liquid. *Phys. Rev. E*, 67(3):031506.

[Doliwa and Heuer, 2003b] Doliwa, B. and Heuer, A. (2003b). Finite-size effects in a supercooled liquid. *J. Phys. Condens. Matter*, 15(11):S849–S858.

[Doliwa and Heuer, 2003c] Doliwa, B. and Heuer, A. (2003c). Hopping in a supercooled Lennard-Jones liquid: Metabasins, waiting time distribution, and diffusion. *Phys. Rev. E*, 67(3):030501.

[Doliwa and Heuer, 2003d] Doliwa, B. and Heuer, A. (2003d). What does the potential energy landscape tell us about the dynamics of supercooled liquids and glasses? *Phys. Rev. Lett.*, 91(23):235501.

[Doye et al., 1999] Doye, J. P. K., Miller, M. A., and Wales, D. J. (1999). The double-funnel energy landscape of the 38-atom lennard-jones cluster. *J. Chem. Phys.*, 110(14):6896–6906.

[Doye et al., 2003] Doye, J. P. K., Wales, D. J., Zetterling, F. H. M., and Dzugutov, M. (2003). The favored cluster structures of model glass formers. *J. Chem. Phys.*, 118(6):2792.

[Dubey et al., 2016a] Dubey, A. K., Hentschel, H. G. E., Procaccia, I., and Singh, M. (2016a). Statistics of plastic events in post-yield strain-controlled amorphous solids. *Phys. Rev. B*, 93(22):224204.

[Dubey et al., 2016b] Dubey, A. K., Procaccia, I., Shor, C. A., and Singh, M. (2016b). Elasticity in amorphous solids: Nonlinear or piecewise linear? *Phys. Rev. Lett.*, 116(8):085502.

[Evans and Morriss, 1984a] Evans, D. J. and Morriss, G. P. (1984a). Nonlinear-response theory for steady planar couette flow. *Phys. Rev. A*, 30(3):1528–1530.

[Evans and Morriss, 2013] Evans, D. J. and Morriss, G. P. (2013). *Statistical Mechanics of Nonequilibrium Liquids*. Elsevier. Google-Books-ID: SSESBQAAQBAJ.

[Evans and Morriss, 1984b] Evans, D. J. and Morriss, O. P. (1984b). Non-newtonian molecular dynamics. *Computer Physics Reports*, 1(6):297–343.

[Eyring, 1936] Eyring, H. (1936). Viscosity, plasticity, and diffusion as examples of absolute reaction rates. *J. Chem. Phys.*, 4(4):283–291.

[Falk and Langer, 1998] Falk, M. L. and Langer, J. S. (1998). Dynamics of viscoplastic deformation in amorphous solids. *Phys. Rev. E*, 57(6):7192–7205.

[Fiocco et al., 2013] Fiocco, D., Foffi, G., and Sastry, S. (2013). Oscillatory athermal quasistatic deformation of a model glass. *Phys. Rev. E*, 88(2):020301.

[Fiocco et al., 2014] Fiocco, D., Foffi, G., and Sastry, S. (2014). Encoding of Memory in Sheared Amorphous Solids. *Phys. Rev. Lett.*, 112(2):025702.

[Frenkel and Smit, 2001] Frenkel, D. and Smit, B. (2001). *Understanding molecular simulation: from algorithms to applications*, volume 1. Academic press.

[Gartner and Lerner, 2016a] Gartner, L. and Lerner, E. (2016a). Nonlinear modes disentangle glassy and goldstone modes in structural glasses. *SciPost Physics*, 1(2).

[Gartner and Lerner, 2016b] Gartner, L. and Lerner, E. (2016b). Nonlinear plastic modes in disordered solids. *Phys. Rev. E*, 93(1):011001.

[Ghosh et al., 2017] Ghosh, A., Budrikis, Z., Chikkadi, V., Sellerio, A. L., Zapperi, S., and Schall, P. (2017). Direct observation of percolation in the yielding transition of colloidal glasses. *Phys. Rev. Lett.*, 118(14):148001.

[Gough, 2009] Gough, B. (2009). *GNU scientific library reference manual*. Network Theory Ltd.

[Hentschel et al., 2010] Hentschel, H. G. E., Karmakar, S., Lerner, E., and Procaccia, I. (2010). Size of plastic events in strained amorphous solids at finite temperatures. *Phys. Rev. Lett.*, 104(2):025501.

[Herschel and Bulkley, 1926] Herschel, W. H. and Bulkley, R. (1926). Konsistenzmessungen von gummi-benzollösungen. *Kolloid-Zeitschrift*, 39(4):291–300.

[Heuer, 2008] Heuer, A. (2008). Exploring the potential energy landscape of glass-forming systems: from inherent structures via metabasins to macroscopic transport. *J. Phys.: Condens. Matter*, 20(37):373101.

[Heuer et al., 2005] Heuer, A., Doliwa, B., and Saksaengwijit, A. (2005). Potential-energy landscape of a supercooled liquid and its resemblance to a collection of traps. *Phys. Rev. E*, 72(2):021503.

[Hirata et al., 2013] Hirata, A., Kang, L. J., Fujita, T., Klumov, B., Matsue, K., Kotani, M., Yavari, A. R., and Chen, M. W. (2013). Geometric frustration of icosahedron in metallic glasses. *Science*, 341(6144):376–379.

[Ilg and Barrat, 2007] Ilg, P. and Barrat, J.-L. (2007). Driven activation vs. thermal activation. *Europhysics Letters (EPL)*, 79(2):26001.

[Illing et al., 2016] Illing, B., Fritschi, S., Hajnal, D., Klix, C., Keim, P., and Fuchs, M. (2016). Strain pattern in supercooled liquids. *Phys. Rev. Lett.*, 117(20):208002.

[Isner and Lacks, 2006] Isner, B. A. and Lacks, D. J. (2006). Generic Rugged Landscapes under Strain and the Possibility of Rejuvenation in Glasses. *Phys. Rev. Lett.*, 96(2):025506.

[Jaiswal et al., 2016] Jaiswal, P. K., Procaccia, I., Rainone, C., and Singh, M. (2016). Mechanical Yield in Amorphous Solids: A First-Order Phase Transition. *Phys. Rev. Lett.*, 116(8):085501.

[Jiang et al., 2015] Jiang, M. Q., Wilde, G., and Dai, L. H. (2015). Origin of stress overshoot in amorphous solids. *Mech. Mater.*, 81:72–83.

[Johnson and Samwer, 2005] Johnson, W. L. and Samwer, K. (2005). A universal criterion for plastic yielding of metallic glasses with a (t/tg) 2/3 temperature dependence. *Phys. Rev. Lett.*, 95(19):195501.

[Jones et al., 2001] Jones, E., Oliphant, T., Peterson, P., et al. (2001). SciPy: Open source scientific tools for Python.

[Karmakar et al., 2009] Karmakar, S., Dasgupta, C., and Sastry, S. (2009). Growing length and time scales in glass-forming liquids. *Proceedings of the National Academy of Sciences*, 106(10):3675–3679.

[Karmakar et al., 2010a] Karmakar, S., Lemaître, A., Lerner, E., and Procaccia, I. (2010a). Predicting plastic flow events in athermal shear-strained amorphous solids. *Phys. Rev. Lett.*, 104(21):215502.

[Karmakar et al., 2010b] Karmakar, S., Lerner, E., and Procaccia, I. (2010b). Statistical physics of the yielding transition in amorphous solids. *Phys. Rev. E*, 82(5):055103.

[Kawasaki and Berthier, 2016] Kawasaki, T. and Berthier, L. (2016). Macroscopic yielding in jammed solids is accompanied by a nonequilibrium first-order transition in particle trajectories. *Phys. Rev. E*, 94(2):022615.

[Kob and Andersen, 1994] Kob, W. and Andersen, H. C. (1994). Scaling behavior in the β - relaxation regime of a supercooled lennard-jones mixture. *Phys. Rev. Lett.*, 73(10):1376–1379.

[Kob and Andersen, 1995a] Kob, W. and Andersen, H. C. (1995a). Testing mode-coupling theory for a supercooled binary Lennard-Jones mixture I: The van Hove correlation function. *Phys. Rev. E*, 51(5):4626–4641.

[Kob and Andersen, 1995b] Kob, W. and Andersen, H. C. (1995b). Testing mode-coupling theory for a supercooled binary Lennard-Jones mixture. II. Intermediate scattering function and dynamic susceptibility. *Phys. Rev. E*, 52(4):4134–4153.

[Koumakis et al., 2012] Koumakis, N., Laurati, M., Egelhaaf, S. U., Brady, J. F., and Petekidis, G. (2012). Yielding of hard-sphere glasses during start-up shear. *Physical Review Letters*, 108(9):098303.

[Koumakis et al., 2016] Koumakis, N., Laurati, M., Jacob, A. R., Mutch, K. J., Abdellali, A., Schofield, A. B., Egelhaaf, S. U., Brady, J. F., and Petekidis, G. (2016). Start-up shear of concentrated colloidal hard spheres: Stresses, dynamics, and structure. *J. Rheol.*, 60(4):603–623.

[Lacks, 2001] Lacks, D. J. (2001). Energy landscapes and the non-newtonian viscosity of liquids and glasses. *Phys. Rev. Lett.*, 87(22):225502.

[Lacks, 2002] Lacks, D. J. (2002). Stokes-einstein-like relation for athermal systems and glasses under shear. *Phys. Rev. E*, 66(5):051202.

[Lacks and Osborne, 2004] Lacks, D. J. and Osborne, M. J. (2004). Energy landscape picture of overaging and rejuvenation in a sheared glass. *Phys. Rev. Lett.*, 93(25):255501.

[Langer, 2001] Langer, J. S. (2001). Microstructural shear localization in plastic deformation of amorphous solids. *Phys. Rev. E*, 64(1):011504.

[Lees and Edwards, 1972] Lees, A. W. and Edwards, S. F. (1972). The computer study of transport processes under extreme conditions. *J. Phys. C Solid State Phys.*, 5(15):1921–1928.

[Leishangthem et al., 2017] Leishangthem, P., Parmar, A. D. S., and Sastry, S. (2017). The yielding transition in amorphous solids under oscillatory shear deformation. *Nat. Commun.*, 8:14653.

[Lemaître, 2002] Lemaître, A. (2002). Rearrangements and dilatancy for sheared dense materials. *Phys. Rev. Lett.*, 89(19):195503.

[Lemaître, 2014] Lemaître, A. (2014). Structural relaxation is a scale-free process. *Phys. Rev. Lett.*, 113(24):245702.

[Lemaître and Caroli, 2009] Lemaître, A. and Caroli, C. (2009). Rate-Dependent Avalanche Size in Athermally Sheared Amorphous Solids. *Phys. Rev. Lett.*, 103(6):065501.

[Lemaître and Maloney, 2006] Lemaître, A. and Maloney, C. (2006). Sum rules for the quasi-static and visco-elastic response of disordered solids at zero temperature. *J. Stat. Phys.*, 123(2):415–453.

[Liu et al., 2016] Liu, C., Ferrero, E. E., Puosi, F., Barrat, J.-L., and Martens, K. (2016). Driving Rate Dependence of Avalanche Statistics and Shapes at the Yielding Transition. *Phys. Rev. Lett.*, 116(6):065501.

[Malandro and Lacks, 1999] Malandro, D. L. and Lacks, D. J. (1999). Relationships of shear-induced changes in the potential energy landscape to the mechanical properties of ductile glasses. *J. Chem. Phys.*, 110(9):4593.

[Maloney and Lemaître, 2004a] Maloney, C. and Lemaître, A. (2004a). Subextensive scaling in the athermal, quasistatic limit of amorphous matter in plastic shear flow. *Phys. Rev. Lett.*, 93(1):016001–1.

[Maloney and Lemaître, 2004b] Maloney, C. and Lemaître, A. (2004b). Universal breakdown of elasticity at the onset of material failure. *Phys. Rev. Lett.*, 93(19).

[Maloney and Lacks, 2006] Maloney, C. E. and Lacks, D. J. (2006). Energy barrier scalings in driven systems. *Phys. Rev. E*, 73(6):061106.

[Maloney and Lemaître, 2006] Maloney, C. E. and Lemaître, A. (2006). Amorphous Systems in Athermal, Quasistatic Shear. *Phys. Rev. E*, 74(1):016118.

[Martens et al., 2012] Martens, K., Bocquet, L., and Barrat, J.-L. (2012). Spontaneous formation of permanent shear bands in a mesoscopic model of flowing disordered matter. *Soft Matter*, 8(15):4197.

[Martyna et al., 1992] Martyna, G. J., Klein, M. L., and Tuckerman, M. (1992). Nosé–Hoover chains: The canonical ensemble via continuous dynamics. *J. Chem. Phys.*, 97(4):2635–2643.

[Monthus and Bouchaud, 1996] Monthus, C. and Bouchaud, J.-P. (1996). Models of traps and glass phenomenology. *J. Phys. A. Math. Gen.*, 29(14):3847–3869.

[Mosayebi et al., 2014] Mosayebi, M., Ilg, P., Widmer-Cooper, A., and Del Gado, E. (2014). Soft Modes and Nonaffine Rearrangements in the Inherent Structures of Supercooled Liquids. *Phys. Rev. Lett.*, 112(10):105503.

[Nosé, 1984] Nosé, S. (1984). A molecular dynamics method for simulations in the canonical ensemble. *Mol. Phys.*, 52(2):255–268.

[Parisi et al., 2017] Parisi, G., Procaccia, I., Rainone, C., and Singh, M. (2017). Shear bands as manifestation of a criticality in yielding amorphous solids. *Proc. Natl. Acad. Sci.*, page 201700075.

[Patinet et al., 2016] Patinet, S., Vandembroucq, D., and Falk, M. L. (2016). Connecting local yield stresses with plastic activity in amorphous solids. *Phys. Rev. Lett.*, 117(4):045501.

[Peter Lepage, 1978] Peter Lepage, G. (1978). A new algorithm for adaptive multidimensional integration. *J. Comput. Phys.*, 27(2):192–203.

[Picard et al., 2004] Picard, G., Ajdari, A., Lequeux, F., and Bocquet, L. (2004). Elastic consequences of a single plastic event: A step towards the microscopic modeling of the flow of yield stress fluids. *Eur. Phys. J. E*, 15(4):371–381.

[Procaccia et al., 2017] Procaccia, I., Rainone, C., and Singh, M. (2017). Mechanical failure in amorphous solids: Scale free spinodal criticality. *arXiv preprint arXiv:1704.05285*.

[Puosi and Leporini, 2012] Puosi, F. and Leporini, D. (2012). Communication: Correlation of the instantaneous and the intermediate-time elasticity with the structural relaxation in glass-forming systems.

[Regev et al., 2015] Regev, I., Weber, J., Reichhardt, C., Dahmen, K. A., and Lookman, T. (2015). Reversibility and criticality in amorphous solids. *Nat. Commun.*, 6:8805.

[Rehwald, 2012] Rehwald, C. (2012). *Die Energielandschaft glasbildender Systeme*. PhD thesis.

[Rehwald and Heuer, 2012] Rehwald, C. and Heuer, A. (2012). How coupled elementary units determine the dynamics of macroscopic glass-forming systems. *Phys. Rev. E*, 86(5):051504.

[Rehwald et al., 2010] Rehwald, C., Rubner, O., and Heuer, A. (2010). From Coupled Elementary Units to the Complexity of the Glass Transition. *Phys. Rev. Lett.*, 105(11):117801.

[Rodney and Schuh, 2009] Rodney, D. and Schuh, C. (2009). Distribution of thermally activated plastic events in a flowing glass. *Phys. Rev. Lett.*, 102(23):235503.

[Rottler and Robbins, 2003] Rottler, J. and Robbins, M. O. (2003). Shear yielding of amorphous glassy solids: Effect of temperature and strain rate. *Phys. Rev. E*, 68(1):011507.

[Rottler and Robbins, 2005] Rottler, J. and Robbins, M. O. (2005). Unified description of aging and rate effects in yield of glassy solids. *Phys. Rev. Lett.*, 95(22):225504.

[Rottler and Warren, 2008] Rottler, J. and Warren, M. (2008). Deformation, yield and ageing in glassy solids. *The European Physical Journal Special Topics*, 161(1):55–63.

[Rubner and Heuer, 2008] Rubner, O. and Heuer, A. (2008). From elementary steps to structural relaxation: A continuous-time random-walk analysis of a supercooled liquid. *Phys. Rev. E*, 78(1):011504.

[Salerno et al., 2012] Salerno, K. M., Maloney, C. E., and Robbins, M. O. (2012). Avalanches in strained amorphous solids: Does inertia destroy critical behavior? *Phys. Rev. Lett.*, 109(10).

[Salerno and Robbins, 2013] Salerno, K. M. and Robbins, M. O. (2013). Effect of inertia on sheared disordered solids: Critical scaling of avalanches in two and three dimensions. *Phys. Rev. E*, 88(6).

[Sastry et al., 1998] Sastry, S., Debenedetti, P. G., and Stillinger, F. H. (1998). Signatures of distinct dynamical regimes in the energy landscape of a glass-forming liquid. *Nature*, 393(6685):554–557.

[Schrøder et al., 2000] Schrøder, T. B., Sastry, S., Dyre, J. C., and Glotzer, S. C. (2000). Crossover to potential energy landscape dominated dynamics in a model glass-forming liquid. *J. Chem. Phys.*, 112(22):9834–9840.

[Schroer, 2015] Schroer, C. F. E. (2015). *Microrheology of Supercooled Liquids: From the Potential Energy Landscape to Nonlinear Response*. PhD thesis.

[Schroer and Heuer, 2013] Schroer, C. F. E. and Heuer, A. (2013). Anomalous Diffusion of Driven Particles in Supercooled Liquids. *Phys. Rev. Lett.*, 110(6):067801.

[Schroer and Heuer, 2015] Schroer, C. F. E. and Heuer, A. (2015). Understanding the nonlinear dynamics of driven particles in supercooled liquids in terms of an effective temperature. *J. Chem. Phys.*, 143(22):224501.

[Shi et al., 2013] Shi, Z., Debenedetti, P. G., and Stillinger, F. H. (2013). Relaxation processes in liquids: Variations on a theme by Stokes and Einstein. *J. Chem. Phys.*, 138(12):12A526.

[Shrivastav et al., 2016a] Shrivastav, G. P., Chaudhuri, P., and Horbach, J. (2016a). Heterogeneous dynamics during yielding of glasses: Effect of aging. *J. Rheol.*, 60(5):835–847.

[Shrivastav et al., 2016b] Shrivastav, G. P., Chaudhuri, P., and Horbach, J. (2016b). Yielding of glass under shear: A directed percolation transition precedes shear-band formation. *Phys. Rev. E*, 94(4):042605.

[Sollich et al., 1997] Sollich, P., Lequeux, F., Hébraud, P., and Cates, M. E. (1997). Rheology of Soft Glassy Materials. *Phys. Rev. Lett.*, 78(10):2020–2023.

[Spaepen, 1977] Spaepen, F. (1977). A microscopic mechanism for steady state inhomogeneous flow in metallic glasses. *Acta Metall.*, 25(4):407–415.

[Stillinger, 1995] Stillinger, F. H. (1995). A topographic view of supercooled liquids and glass formation. *Science*, 267(5206):1935–1939.

[Stillinger and Weber, 1983] Stillinger, F. H. and Weber, T. A. (1983). Dynamics of structural transitions in liquids. *Phys. Rev. A*, 28(4):2408–2416.

[Tsamados et al., 2009] Tsamados, M., Tanguy, A., Goldenberg, C., and Barrat, J.-L. (2009). Local elasticity map and plasticity in a model Lennard-Jones glass. *Phys. Rev. E*, 80(2):026112.

[Utz et al., 2000] Utz, M., Debenedetti, P. G., and Stillinger, F. H. (2000). Atomistic Simulation of Aging and Rejuvenation in Glasses. *Phys. Rev. Lett.*, 84(7):1471–1474.

[Varnik et al., 2004] Varnik, F., Bocquet, L., and Barrat, J.-L. (2004). A study of the static yield stress in a binary Lennard-Jones glass. *J. Chem. Phys.*, 120(6):2788.

[Varnik and Henrich, 2006] Varnik, F. and Henrich, O. (2006). Yield stress discontinuity in a simple glass. *Phys. Rev. B*, 73(17):174209.

[Wang, 2012] Wang, W. H. (2012). The elastic properties, elastic models and elastic perspectives of metallic glasses. *Prog. Mater Sci.*, 57(3):487–656.

[Wang et al., 2003] Wang, W. H., Wen, P., Zhao, D., Pan, M., and Wang, R. J. (2003). Relationship between glass transition temperature and debye temperature in bulk metallic glasses. *Journal of materials research*, 18(12):2747–2751.

[Weisstein, a] Weisstein, E. W. Confluent Hypergeometric Function of the Second Kind.

[Weisstein, b] Weisstein, E. W. Exponential Integral.

[Weisstein, c] Weisstein, E. W. Sphere Point Picking.

[Widmer-Cooper and Harrowell, 2006] Widmer-Cooper, A. and Harrowell, P. (2006). Predicting the Long-Time Dynamic Heterogeneity in a Supercooled Liquid on the Basis of Short-Time Heterogeneities. *Phys. Rev. Lett.*, 96(18):185701.

[Widmer-Cooper et al., 2008] Widmer-Cooper, A., Perry, H., Harrowell, P., and Reichman, D. R. (2008). Irreversible reorganization in a supercooled liquid originates from localized soft modes. *Nat. Phys.*, 4(9):711–715.

[Zhang et al., 2007] Zhang, B., Bai, H., Wang, R., Wu, Y., and Wang, W. (2007). Shear modulus as a dominant parameter in glass transitions: ultrasonic measurement of the temperature dependence of elastic properties of glasses. *Physical Review B*, 76(1):012201.

Danksagung

Zuerst möchte ich meinem Doktorvater Prof. Dr. Andreas Heuer danken, der mich während meiner Promotion stets auf vielerlei Weise unterstützt hat und dessen zahlreiche innovative Ideen mich immer wieder vorangebracht haben. Insbesondere danke ich ihm für die ausführlichen Diskussionen, die maßgeblich zum Verständnis der Ergebnisse beigetragen haben und seinen kritischen Blick auf die Ergebnisse.

Außerdem möchte ich Prof. Dr. Nikos Doltsinis für die Übernahme des Zweitgutachtens danken und ebenso Prof. Dr. Gerhard Wilde dafür, dass er als Drittprüfer für meine Disputation zur Verfügung steht.

Besonders danken möchte ich auch Dr. Oliver Rubner, dass er mir sein Vertrauen entgegengebracht hat und mich die Administration des Arbeitskreis-Clusters "Bagheera" übernehmen ließ. Durch diese Aufgabe habe ich viel IT-Wissen für meine weitere Zukunft erlernen können und ohne unsere Umstrukturierungen und Aufrüstungen des Clusters wäre meine Dissertation in dieser Form nicht möglich gewesen. An dieser Stelle möchte ich auch Hendrik Feldhues für seine lockere Art in unseren teils langen IT-Planungs-Diskussionen bedanken. Für Ihre organisatorische Hilfe, insbesondere in Fragen der Bürokratie möchte ich hier außerdem Andrea Staubermann dankend erwähnen.

Beim gesamten Arbeitskreis möchte ich mich für die angenehme Arbeitsatmosphäre bedanken, insbesondere für die schöne Zeit auf unseren gemeinsamen Tagungen oder unsere "Lan-Party". Insbesondere geht mein Dank an meinen Bürokollegen Lawrence Smith für die vielen anregenden Diskussionen über die neusten Ergebnisse, die mich sehr oft auf neue Ideen brachten und zu einem tieferen Verständnis führten. Weiterhin möchte ich mich auch bei meinen beiden anderen Bürokollegen, Katharina Ferling und Dr. Diddo Diddens bedanken für unsere Gespräche jenseits von Forschung und IT.

Ich danke meinen Eltern, die mich dazu ermutigt haben mein Studium zu beginnen und mir auf meinem Weg in jeder Situation bedingungslosen Rückhalt gewährt haben. Dank ihrer Unterstützung konnte ich Physik als zusätzlichen Diplomstudiengang belegen und mich jederzeit sorglos auf die Wissenschaft konzentrieren. Schließlich danke ich meiner Freundin Yureshika Rüskamp, dass sie auch in schwierigen Zeiten immer für mich da war und mich insbesondere in den letzten Wochen dieser Arbeit mit viel Geduld unterstützt hat.